Quantum-Enhanced Precision Measurement and Information Processing with Integrated Photonics

Nicholas Thomas-Peter
Balliol College, Oxford

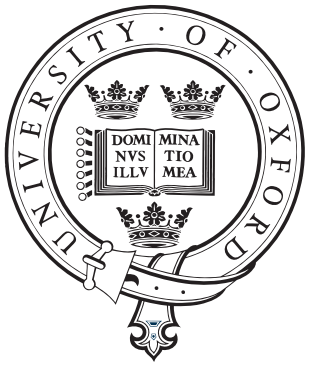

Submitted for the degree of Doctor of Philosophy
Hillary term 2012

Supervised by
Prof. Ian A. Walmsley

Clarendon Laboratory
University of Oxford
United Kingdom

Quantum-Enhanced Precision Measurement and Information Processing with Integrated Photonics

Nicholas Thomas-Peter
Balliol College, Oxford

Submitted for the degree of Doctor of Philosophy
Hilary term 2012

Abstract

Photons have proven to be an effective test-bed for the fundamental concepts and elements of quantum-enhanced technologies. As systems become increasingly complex, however, practical considerations make the traditional approach of bulk optics and free-space propagation progressively more difficult. The major obstacles are the physical space necessary to realise and operate such a complex system, its stability, and maintaining low losses. In order to address these issues, quantum optical technologies can take a cue from their classical counterparts and look towards an integrated architecture to provide miniaturisation, greatly enhanced stability, less alignment, and low loss interfaces between different system components.

In this thesis the feasibility of chip-based waveguides as a platform for metrology and information processing will be explored. In Part I, the necessary criteria for a metrology system to out-perform its classical counterpart will be investigated. It will be found that loss is a major barrier to this aim and, critically, that it is unlikely to have been achieved to date by any experiment which consumes resources of a fixed photon number. The issue of loss will be addressed by developing a scalable heralded source of a class of entangled photonic states which are both robust to losses and practically feasible to prepare. A novel tomographic technique will be developed to characterize these states and it will be explicitly demonstrated how it is possible to beat some bounds on classical performance without being able to out-perform a comparable classical system. Finally, a proof of principle demonstration of a waveguide-based interferometer with an integrated phase-shifter will be undertaken. It will be shown that the device preserves quantum interference, making it suitable for use in quantum-enhanced metrology applications.

In Part II, integrated optics in the context of information processing will be discussed. First, a novel characterization technique will be developed which enables the behaviour of complex circuits to be predicted. The technique is independent of loss in the device being characterized. A method of simulating these circuits will be outlined that takes advantage of the computational speed-up available from parallelisation and sparse matrix operations. A key increase in complexity for integrated photonic systems will be demonstrated by showing quantum interference of three photons from two separate sources in eight spatial modes. The resulting interference has a visibility which beats all possible classical interference visibilities for similar circuits. Finally, a fully integrated waveguide-coupled photon-number-resolving detector will be developed and demonstrated. This proof of concept demonstration will show good resolution of different photon number events. The device will be modelled and routes to high efficiency operation will be explored.

To Mum and Dad.

Thank you.

Acknowledgements

Throughout my DPhil, I have relied on many people, all of whom are in some way responsible for getting me here. There are too many to thank everyone individually, but I will do my best. My first thanks are to my supervisor, Ian. Thank you for taking me on, and for persevering with me even when I wasn't the most attentive student. You have taught me a great deal, certainly about physics, but also about life and leadership, even when you haven't been meaning to.

My second thanks are to the Post-docs who have looked after me over my Ultrafast career. Jeff, for spending time in the lab teaching me, Brian, for continuing Jeff's work and especially for helping me to keep at least one eye on physics and, over the second half of my DPhil, Nathan. You gave me the freedom to run with my ideas, encouraged my curiosity in interesting projects, helped me to see the larger picture of what I was doing, asked (lots) of awkward questions, and forced me to think properly about things, even when I didn't want to. My thanks also go to the other Post-docs: Animesh, for his theoretical assistance and ability to identify the critical path in investigating a problem; Adam, for many invaluable discussions regarding Matlab and having a seemingly endless library of incredibly useful functions; Josh, for all the tea, of course, but perhaps even more importantly for your incredible ability to know something about almost everything and your patience in explaining it.

Next, to the other students I've worked with. To Hendrik, for being a fantastic lab-buddy and an endless source of advice (especially about last-minute travel plans). To

Team Integrated Photonics: Ben, Justin, and most recently Peter. I have so much enjoyed morning breakfast meetings, and working with you to move the integrated photonics projects forwards. I've been amazed at how much we've achieved over the past eighteen months thanks to your hard work and I can't wait to see what happens over the next few years for the integrated photonics (sub-sub-)group.

I would not have continued on to the DPhil without Balliol, my home for the last nine years. My undergraduate physics tutors, Jon Hodby, Chris Palmer, David Lucas, and Armin Reichold. I owe a lot to your understanding and support (sometimes by means of Haribo and Jaffa Cakes) in physics when I was being pulled in other directions by rowing. Especially, to Douglas, for your support, friendship, and the opportunities that I have had to work with you over the years.

Now I come to the non-physics people. A special thank you must go first and foremost to Hannah. You have had to bear the brunt of the difficulties and disappointments I have had during my DPhil, especially in finishing. Thank you for your extraordinary patience, your love, the endless list of things you do for me, and your uncanny ability to know whether to give me a supportive hug or send me back to work. It's finally done. Thank you also to the Smith-Willis family, you have taken me in and looked after me as one of your own over the last three months. I am forever grateful.

Finally, my family. To Han and David, for being trail-blazers in life. Your advice has been so very helpful over the past couple of years as I've struggled to decide what to do next and the achievements you both make with alarming regularity are a continuing inspiration. Lastly to my parents, to whom this thesis is dedicated. You have done more for me over the last 27 years than I could possibly thank you for but it is safe to say that I would not be who I am or where I am without all your hard work.

Author's publications

Journal publications

1. P. S. Salter, A. Jesacher, J. B. Spring, B. J. Metcalf, N. Thomas-Peter, R. D. Simmonds, N. K. Langford, I. A. Walmsley, and M. J. Booth. "**Adaptive slit beam shaping for direct laser written waveguides**" *Optics Letters*, **37**, 470 (2012).

2. T. Gerrits, N. Thomas-Peter, J. C. Gates, A. E. Lita, B. J. Metcalf, B. Calkins, N. A. Tomlin, A. .E. Fox, A. Lamas Linares, J. B. Spring, N. K. Langford, R. P. Mirin, P. G. R. Smith, I. A. Walmsley, and S. W. Nam. "**On-chip, photon-number-resolving, telecommunication-band detectors for scalable photonic information processing**" *Physical Review A*, **84**, 060301(R) (2011).

3. A. Datta, L. Zhang, N. Thomas-Peter, U. Dorner, B. J. Smith, and I. A. Walmsley. "**Quantum Metrology with Imperfect States and Detectors**" *Physical Review A*, **83**, 063836 (2011).

4. N. Thomas-Peter, B. J. Smith, A. Datta, L. Zhang, U. Dorner, and I. A. Walmsley. "**Real-World Quantum Sensors: Evaluating Resources for Precision Measurement**" *Physical Review Letters*, **107**, 113603 (2011).

5. N. Thomas-Peter, N. K. Langford, A. Datta, L. Zhang, B. J. Smith, J. B. Spring, B. J. Metcalf, H. B. Coldenstrodt-Ronge, M. Hu, J. Nunn, and I. A. Walmsley. "**Integrated Photonic Sensing.**" *New Journal of Physics*, **13**, 055024 (2011).

6. B. J. Smith, D. Kundys, N. Thomas-Peter, P. G. R. Smith, and I. A. Walmsley. "**Phase-Controlled Integrated Photonic Circuits**" *Optics Express*, **17**, 13516 (2009).

7. A. P. Worsley, Worsley, H. B. Coldenstrodt-Ronge, J.S. Lundeen, P. J. Mosley, B. J. Smith, G. Puentes, N. Thomas-Peter, and I. A. Walmsley. "**Absolute efficiency estimation of photon-number-resolving detectors using twin beams.**" *Optics Express*, **17**, 4397 (2009).

Conferences

1. N. Thomas-Peter, B. J. Smith, D. Kundys, P. G. R. Smith, and I. A. Walmsley. "**Phase-Controlled Photonic Quantum Circuits in Laser Written Integrated Optics**" *Conference on Lasers & Electro-Optics/Quantum Electronics & Laser Science Conference*, May 2010.

2. B. J. Smith, N. Thomas-Peter, and I. A. Walmsley. "**Two-Photon Interference and Commutation Relations**" *Conference on Lasers & Electro-Optics/Quantum Electronics & Laser Science Conference*, May 2010.

3. H. B. Coldenstrodt-Ronge, A. P. Worsley, J. S. Lundeen, A. Feito, K. L. Pregnell, C. Silberhorn, P. J. Mosley, B. J. Smith, G. Puentes, N. Thomas-Peter, T. C Ralph, J. Eisert, M. B. Plenio, and I. A. Walmsley. "**Full Characterization of Quantum Optical Detectors**" *Conference on Lasers & Electro Optics & The Pacific Rim Conference on Lasers and Electro-Optics*, September 2009.

4. G. Puentes, L. Zhang, H. B. Coldenstrodt-Ronge, O. Cohen, B. J. Smith, N. Thomas-Peter, and I. A. Walmsley. "**Components for Multi-Photon Non-Classical State Preparation and Measurement**" *XIX Conference on Laser Spectroscopy*, June 2009.

5. N. Thomas-Peter, B. J. Smith, and I. A. Walmsley. "**Tomography of a Heralded N00N State with Losses**" *Conference on Lasers & Electro-Optics/Quantum Electronics & Laser Science Conference*, June 2009.

Contents

Acknowledgements **vii**

Author's publications **ix**

List of Figures **xv**

List of Tables **xix**

List of abbreviations **xxi**

I Precision Measurement **1**

1 Introduction **3**
1.1 Part I outline 4
1.2 Previous work 5
1.3 Single parameter estimation in the absence of loss 7
1.3.1 Fisher Information and the Cramér-Rao Bound 8
1.3.2 Classical limits on precision: the Standard Quantum Limit 11
1.3.3 Comparing classical and quantum strategies 14
1.4 Resource counting in the presence of loss 16
1.4.1 The Standard Interferometric Limit (SIL) 17
1.4.2 States for quantum-enhanced metrology 21
1.4.3 Super-resolution and super-sensitivity 26
1.5 Including real-world imperfections 33
1.5.1 Device transmission efficiency 34
1.5.2 State preparation efficiency 37
1.5.3 Detection efficiency 38
1.5.4 Beam splitter imperfections 41

2 Heralded Holland-Burnett state generation and characterization **45**
2.1 A heralded source of Holland-Burnett states 45
2.2 Interference experiments 50
2.2.1 Polarization interferometry 50

2.2.2 Quality control by Hong-Ou-Mandel interference . . . 52
2.2.3 Post selected quantum interference . . . 56
2.3 State characterization . . . 58
2.3.1 Tomographic reconstruction . . . 63
2.3.2 Evaluating the state for precision measurement . . . 66

3 Integrated photonic sensing 69
3.1 The integrated platform . . . 70
3.1.1 Waveguide structure . . . 70
3.1.2 Beamsplitters . . . 73
3.1.3 Phase shifters . . . 74
3.2 Hong-Ou-Mandel interference at an integrated Mach-Zehnder interferometer 76
3.2.1 The MZI as a programmable beamsplitter . . . 76
3.2.2 Observing Hong-Ou-Mandel interference . . . 78
3.3 Controllable quantum interference . . . 82

II Information Processing 87

4 Introduction 89
4.1 Part II outline . . . 90
4.2 Background . . . 91
4.2.1 Qubits and the controlled-NOT gate . . . 91
4.2.2 Results in the field . . . 95
4.3 Linear optics quantum computation . . . 96
4.3.1 The KLM scheme . . . 98
4.3.2 One-way quantum computing . . . 102
4.3.3 The state of the art in linear optics quantum computation . . . 104
4.4 Coping with imperfections . . . 105
4.4.1 Programmable beamsplitters revisited . . . 105
4.4.2 Perfectly programmable beamsplitters . . . 109

5 Characterization and simulation of linear optical circuits 111
5.1 Estimating reflectivity . . . 112
5.1.1 Naive reflectivity characterization . . . 113
5.1.2 Loss independent reflectivity characterization . . . 114
5.1.3 Camera-based characterization . . . 116
5.2 Linear optical circuit simulation . . . 123
5.2.1 Method . . . 124
5.2.2 Predicting interference visibilities . . . 133

6 Three photon quantum interference in an integrated device 139
6.1 The circuit . . . 140
6.1.1 The Ralph-White controlled sign-flip gate . . . 142
6.1.2 Operation under the cluster state single qubit rotation interpretation 145
6.1.3 Operation under the teleportation interpretation . . . 149
6.2 The device . . . 151

6.2.1 Characterization . . . 152
6.3 Two-photon interference . . . 160
6.4 Three-photon interference . . . 169

7 Integrated Transition Edge Sensors 177
7.1 Superconducting transition edge sensors . . . 178
7.2 Evanescently-coupled photon counting detectors . . . 181
7.3 Device structure . . . 182
7.4 Modelling a simple device . . . 184
7.5 Experimental testing . . . 188
7.5.1 Model verification by absorption measurement . . . 188
7.5.2 Measurement of a weak coherent state and efficiency characterization 193
7.6 Geometry optimization . . . 199

8 Conclusion 203
8.1 Summary . . . 204
8.2 Outlook . . . 209
8.2.1 Femtosecond writing in bulk silica . . . 209
8.2.2 Further work . . . 210
8.2.3 Future challenges . . . 212

Bibliography 213
*

List of Figures

1.1 A general, lossless two mode interferometer. 7
1.2 A lossless Mach-Zehnder interferometer. 11
1.3 A general two mode interferometer and a Mach-Zehnder interferometer with losses. 18
1.4 Comparison of the quantum Fisher information of Holland-Burnett, N00N, and optimal states as a function of single arm transmissivity. 36
1.5 Feasibility region for beating the standard quantum limit using HB(2) and HB(4) states. 40
1.6 The effect of beamsplitter imperfections on the effective phase operator and Fisher information when performing phase estimation with Holland-Burnett states. 44

2.1 Polarization-based Holland-Burnett state generation and characterization scheme. 48
2.2 The four possible outcomes when two photons impinge upon a beam splitter. 53
2.3 Raw and background-subtracted polarization Hong-Ou-Mandel interference. 55
2.4 Post-selected quantum interference of photonic states by scanning the relative phase between the two modes in the integrated Mach-Zehnder interferometer. 57
2.5 A typical scheme used to perform state tomography. 60
2.6 The reconstructed and perfect density matrices for a heralded HB(2) state including lower photon numbers. 65

3.1 A cross-section of the waveguide structure. 71
3.2 Schematic of the UV-waveguide writing process. 72
3.3 Experimental scheme for testing an integrated Mach-Zehnder interferometer. 78
3.4 Two-photon Hong-Ou-Mandel interference through a waveguide Mach-Zehnder interferometer 82
3.5 Two-photon Holland-Burnett state interference through a waveguide Mach-Zehnder interferometer 83

4.1 Linear optical networks to implement the KLM nonlinear sign flip and controlled sign flip. 99

4.2 Two examples of cluster states. 102
4.3 Values of the beamsplitter reflectivities in a Mach-Zehnder interferometer for which a specified effective reflectivity can be reached. 108
4.4 A perfectly programmable beamsplitter design. 109

5.1 Schematic of a device consisting of a single beam splitter with input and output coupling efficiencies modelled by beam splitters. 113
5.2 Experimental scheme used to compare reflectivity characterization techniques. 117
5.3 The sequence of image analysis applied to the images of scatter from the output modes of the beamsplitter to be characterized. 120
5.4 A direct comparison of naive photodiode, loss-independent photodiode, and loss-independent camera reflectivity characterization techniques. 122
5.5 A generic linear optical circuit with product state inputs. 124

6.1 Schematic of the three qubit waveguide circuit. 140
6.2 Schematic of the Ralph-White controlled sign-flip gate, its circuit picture representation with the circuit picture representation of two concatenated sign-flip gates. 143
6.3 Circuit picture representations of the full linear optical circuit under the cluster state single qubit rotation and teleportation interpretations. 146
6.4 Transmission of the chip when light is coupled into each accessible input mode. 154
6.5 The characterized beamsplitter reflectivities and their ideal values. 157
6.6 Measured effective reflectivity of the three central Mach-Zehnder interferometers as a function of the square of the applied voltage. 159
6.7 Experimental scheme for generating the photon pairs. 161
6.8 Filtered and unfiltered marginal spectra for the downconverted photon pairs. 163
6.9 Two-photon coincidence rates measured at the output of the device when photons were launched into pairs of input modes while their relative arrival time was scanned. 165
6.10 A comparison of measured two-photon interference visibilities with the expected two-photon interference visibilities based on the circuit characterization, and the classical limit on visibility. 167
6.11 Heralded three-fold rates as a function of τ_2. 171
6.12 Comparison of the measured, theoretically expected, and classical three photon interference visibilities. 172

7.1 Schematic of the evanescently coupled photon counting detector. 181
7.2 The cross sectional structure of the tungsten transition edge sensor based evanescently-coupled photon counting detector. 182
7.3 Microscope image of the fabricated TES on the optical waveguide. The TES dimension is $25\,\mu\text{m} \times 25\,\mu\text{m} \times 40\,\text{nm}$. The tungsten TES bisects the waveguide in the centre. The niobium wiring attaches top and bottom of the TES and exits off the chip to the right. Additional arrows simply serve as alignment marks and guide. 183
7.4 Simulated mode parameters for a simple superconducting transition edge sensor based evanescently coupled photon counting detector. 187

7.5 Schematic of a sample fabricated in order to measure the modal alpha underneath the tungsten, testing the validity of the predictions of the model. 188
7.6 Schematic of experimental scheme for characterizing the absorption of a waveguide with a strip of tungsten above it. 189
7.7 Reflection spectra for the TE and TM mode when coupling in the forward and backward direction. 190
7.8 Logarithm of the ratio of forward- and backward- coupling reflected intensities for each Bragg grating with the theoretical fit. 192
7.9 Schematic of experimental scheme used to measure a weak coherent state with the prototype evanescently-coupled photon-counting detector. 194
7.10 Experimental results obtained by measuring a weak coherent state with the evanescently-coupled photon counting detector. 195
7.11 Estimated total absorption of the TM mode for different detector geometries. 202

List of Tables

4.1 Classical truth table for the controlled-NOT gate. 94
4.2 Truth table for the controlled-NOT gate with superposition inputs as the control. 94

6.1 Extracted phase shifter parameters. 160

7.1 Extracted fibre-pigtail-waveguide transmission $\eta_{A/B}$ and TES detection efficiency η_{TES}. 198

List of abbreviations

Abbreviation	Description
FI	Fisher Information
CRB	Cramér-Rao Bound
QFI	Quantum Fisher Information
QCRB	Quantum Cramér-Rao Bound
SQL	Standard Quantum Limit
MZI	Mach-Zehnder interferometer
SIL	Standard Interferometric Limit
HL	Heisenberg Limit
HB	Holland-Burnett
PNRD	photon number resolving detector
PDC	parametric down-converter
APD	avalanche photodiode
BBO	beta barium borate
KDP	potassium dihydrogen phosphate
FPBS	fibre-coupled polarizing beam splitter
QWP	quarter-wave plate
HWP	half-wave plate
SMF	single-mode fibre
PBS	polarizing beam splitter
H	horizontal polarization
V	vertical polarization
HOM	Hong-Ou-Mandel
D	diagonal polarization
A	anti-diagonal polarization
R	right circular polarization
L	left circular polarization
LN	lithium niobate
CW	continuous wave
UV	ultraviolet
FHD	flame-hydrolysis deposition
EDX	energy dispersive X-ray
VGA	v-groove assembly
CNOT	controlled-NOT
CZ	controlled-σ_z
KLM	Knill, Laflamme, and Milburn

LOQC	linear optics quantum computation
PMF	polarization maintaining fibre
ROI	region of interest
POVM	positive operator valued measure
CS	controlled sign-flip
TES	transition edge sensor
InGaAs	indium gallium arsenide
ECPCD	evanescently-coupled photon counting detector
SQUID	superconducting quantum interference device
TE	transverse electric field
TM	transverse magnetic field
ASE	amplified spontaneous emission
DR	dilution refrigerator

Part I

Precision Measurement

Chapter 1

Introduction

Measurement is central to all experimental sciences as the connection between theoretical understanding and the real world. Improving our ability to measure physical parameters is therefore critical to increasing our understanding of the physical world. Improved tools enable new science to be uncovered and new science leads to technological advances. These in turn enable further improvements in measurement, leading to yet more rigorous tests of fundamental understanding.

In physics, measurement is cast in the form of estimating the value of a parameter of a system of interest. Physical examples of the parameter of interest may be length, time, mass, charge, and density, among others. A probe, a separate system under the control of the experimenter, is prepared in a known state and allowed to interact with the system. This interaction must result in the probe evolving into a state which is dependent on the value of the parameter of interest. The state of the probe is then measured. Each time this process is repeated, one data point is collected. These data points come from an underlying probability distribution and hence their value is described a random variable.

An estimate of the parameter is then derived from the data using an estimator. An estimator can be any function of the data. Since the data values are random variables, the value of the estimator is also a random variable with an associated probability distribution, the distribution of estimates.

The utility of a measurement can be assessed using several criteria, however, there are two with which scientists are largely concerned. The first is accuracy or bias. This is the difference between the mean of the distribution of estimates and the true value of the parameter as the number of estimates becomes large. The second is precision. This is the standard deviation of the distribution of estimates and gives a measure of 'how close' an estimate is likely to be to the true value. All other things being equal, estimators with zero bias and small standard deviation (high precision) are more desirable.

Extending this, quantum-enhanced metrology aims to employ probe states which, through their quantum mechanical behaviour, allow one to estimate a parameter of interest with precision beyond what is possible using classical resources [1]. The key characteristic which enables these probe states to achieve an enhancement in precision is entanglement [2], or correlations in the state that are stronger than can be explained with classical physics alone.

1.1 Part I outline

This thesis is presented in two parts. Part I continues the discussion so far, concentrating on the issue of quantum-enhanced metrology while Part II, which begins with Chapter 4, discuses quantum-enhanced information processing.

The remainder of this chapter will consist of a summary of work in the field of quantum-

enhanced precision measurement, briefly for several different physical systems and in more depth for systems using photons. The discussion will be centred on strategies using resources of fixed photon number. This will be followed by an introduction to the problem of parameter estimation in the absence of loss and a discussion of how quantum and classical strategies are compared. The problem will then be generalised to situations including loss and it will be shown that careful consideration of the resources consumed is critical in order to prove any enhancement. Moreover, it will be shown that it is unlikely that most of the optical experiments performed to date have achieved it.

In Chapter 2, a scheme for producing a class of state that is robust to losses will be proposed and demonstrated and a novel technique will be developed to characterize it. Using this source, it will be explicitly demonstrated that improper characterization of device efficiencies can result in the conclusion that classical limits have been beaten while a more complete characterization suggests that they have not.

The final chapter of Part I contains a proof of principle demonstration of an integrated platform for quantum-enhanced metrology. The ability of the device to preserve quantum properties of light is demonstrated and this is used to observe and control post-selected quantum interference.

1.2 Previous work

No mention has so far been made of a specific physical implementation of quantum-enhanced metrology. Several instantiations exist, each with advantages and disadvantages. Trapped ions[3] have provided extremely high precision in measurements of frequency using single ion optical clocks[4]. Although extremely impressive, there is no entanglement

involved in these measurements. The use of entangled trapped ions to improve spectroscopic sensitivity has, however, been proposed [5–10] and demonstrated [8,9,11–13]. Indeed the largest entangled states to date have been created using trapped ions, where 14 Calcium ions were entangled in a Greenberger-Horne-Zeilinger state [14]. Precision measurement using Bose-Einstein condensates (BECs) is also a promising possibility due to the large numbers of particles that can be prepared in a quantum-mechanically identical state. There has been extensive theoretical work in the area [15–19], as well as promising experimental results [20,21]. The ability to coherently split and interfere BECs has, however, only relatively recently been demonstrated [22,23]. Progress in Mach-Zehnder type interferometry has even been made using superconducting qubits [24,25].

In what follows, the discussion will be restricted to optical sensing where a single parameter of interest is mapped onto an optical phase. The interaction will be limited to linear metrology where the phase acquired depends linearly on the intensity of the probe state and only resources of fixed total photon number will be considered. This excludes protocols employing so called 'squeezed' states [26–30], which do not have a fixed total photon number. Such an exclusion is necessary both because its inclusion would require more discussion than can be reasonably accomplished here, and because it is not yet clear how to compare these two classes of state. Specifically, the role of post-selection and its impact is unclear in the context of squeezed states.

Several proof of principle experiments aimed at quantum-enhanced metrology in this restricted class have been performed to date [31–39]. These typically rely on utilizing a signature of non-classical behaviour in measurement outcomes which is not affected by preparation, device, or detection efficiencies. It is then claimed that the presence of such a

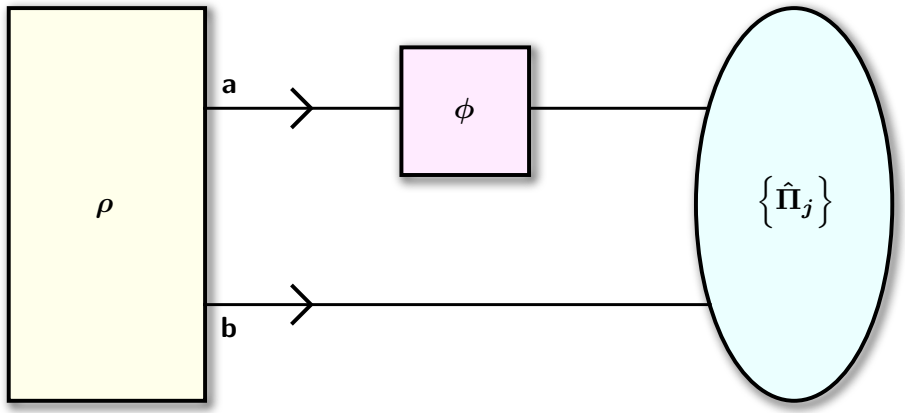

Figure 1.1: A general, lossless two mode interferometer. The state $\boldsymbol{\rho}$ is prepared at the input in modes **a** and **b**. The phase $\boldsymbol{\phi}$ to be estimated is applied to mode **a** in the interferometer. At the output a measurement is performed, the outcomes of which are represented by the operators $\boldsymbol{\{\hat{\Pi}_j\}}$.

signature is sufficient to prove that the system could in principle out-perform its classical counterpart if it were to be used in a full phase-estimation protocol. Recent work has shown, however, that practical imperfections such as loss, decoherence, state-preparation and detector inefficiency make it difficult to deliver true quantum enhancements in metrology[40–46]. The discrepancy between the experimental results and the theoretical analysis stems from differences in how the consumed resources are counted. This critical issue will be discussed in more detail in Section 1.4.

1.3 Single parameter estimation in the absence of loss

Figure 1.1 depicts a general two-mode interferometer with no losses. In the optical case, these modes are usually either two orthogonal polarizations or two spatially separated paths. To estimate the phase ϕ, a state ρ is prepared in modes a and b. This state then evolves into the state $\rho(\phi)$ due to interaction with the phase-shifting element. Finally, a measurement is performed at the interferometer output and the particular outcome is re-

corded. Measurements are described by a set of operators, $\{\hat{\Pi}_j\}$, where each element in the set is associated with a different outcome. The elements of the set are Hermitian positive semi-definite, and they must sum to the identity. This prepare, evolve, measure process is repeated ν times and the phase ϕ is estimated from the ν outcomes. The precision with which ϕ can be estimated depends on both the state, ρ, and the measurements performed, $\{\hat{\Pi}_j\}$. This makes intuitive sense since a state that experiences a larger change as a result of the phase ϕ and measurements which are better able to distinguish this change should give a more precise estimate. There exists, however, a rigorous way of quantifying this through the Fisher Information (FI)[47] and the Cramér-Rao Bound (CRB)[48,49].

1.3.1 Fisher Information and the Cramér-Rao Bound

When a measurement, $\{\hat{\Pi}_j\}$, with several possible outcomes enumerated by j, is made on $\rho(\phi)$, each outcome has an associated probability, $p_j(\phi)$. The outcome is therefore a classical random variable X with a point-mass probability distribution function $f_X(x;\phi)$,

$$f_X(x;\phi) = \begin{cases} p_1(\phi) & \text{if } x = x_1 \\ \vdots & \vdots \\ p_j(\phi) & \text{if } x = x_j \end{cases} \tag{1.1}$$

where the x_j are arbitrary values associated with each measurement outcome and the probabilities $p_j(\phi)$ are given by the Born rule[50],

$$p_j(\phi) = \mathrm{Tr}\{\rho(\phi)\hat{\Pi}_j\}. \tag{1.2}$$

The score function of the random variable X is then defined to be[51]

$$s_X(x;\phi) = \frac{1}{f_X(x;\phi)} \frac{\partial f_X(x;\phi)}{\partial \phi}. \tag{1.3}$$

It is a normalized measure of how much the probabilities of the measurement outcomes change for a change in ϕ. The FI is then defined as the variance of the score function,

$$F(\phi) = \mathbb{V}(s_X(x;\phi)) = \mathbb{E}(s_X^2(x;\phi)) - (\mathbb{E}(s_X(x;\phi)))^2, \tag{1.4}$$

where $\mathbb{E}(\cdot)$ denotes the expectation. Intuitively, this means that if a change in ϕ is associated with a *certain* change in $p_j(\phi)$ (small variance), a large amount of information about ϕ has been gained whereas if the associated change in $p_j(\phi)$ is very *uncertain* (large variance), a small amount of information about ϕ has been obtained. The expectation of the score function is zero since

$$p_i(\phi) = 1 - \sum_{j \neq i} p_j(\phi). \tag{1.5}$$

Hence the FI is defined as the expectation of the square of the score function,

$$F(\phi) = \sum_j \frac{1}{p_j(\phi)} \left(\frac{\partial p_j(\phi)}{\partial \phi} \right)^2. \tag{1.6}$$

Finally, the precision with which ϕ can be estimated is determined by the CRB[52],

$$\Delta\phi \geq \frac{1}{\sqrt{\nu F(\phi)}} = \Delta\phi_{\mathrm{CRB}}. \tag{1.7}$$

This bound can be achieved for a large number of trials ν and an unbiased estimator, such as a maximum likelihood estimator.

The CRB is bounded from below by the Quantum Cramér-Rao Bound (QCRB), which is independent of the measurement and depends only on the state used,

$$\Delta\phi \geq \frac{1}{\sqrt{\nu F(\phi)}} \geq \frac{1}{\sqrt{\nu F_Q(\phi)}} = \Delta\phi_{\mathrm{QCRB}}, \tag{1.8}$$

where $F_Q(\phi) = F_Q(\rho(\phi))$ is the Quantum Fisher Information (QFI)[52–55]. The QFI is found by maximizing the FI over all possible measurements $\hat{\Pi}_i$. Note that in general both the FI and the QFI depend on the value of the parameter ϕ. A method for obtaining this maximum was developed by Braunstein and Caves[55], who showed that there always exists a measurement that saturates the QCRB. The operator representing this optimal measurement, called the symmetric logarithmic derivative, is obtained by applying a superoperator to the derivative of the density matrix with respect to the parameter ϕ[55]. It is important to note two things. First, that the symmetric logarithmic derivative does not uniquely saturate the CRB and second, that there is currently no recipe for physically constructing a measurement device which implements the symmetric logarithmic derivative. For pure states, the QFI is given by

$$F_{\mathrm{Q}}(\phi) = 4(\langle\psi_\phi|\,\psi_\phi\rangle - |\,\langle\psi|\,\psi_\phi\rangle|^2), \tag{1.9}$$

where $|\psi_\phi\rangle \equiv d\,|\psi\rangle\,/d\phi$.

Given a particular input state ρ and measurement with outcomes $\{\hat{\Pi}_j\}$, the CRB gives the precision that can be achieved in estimating a parameter, ϕ. The QCRB gives the

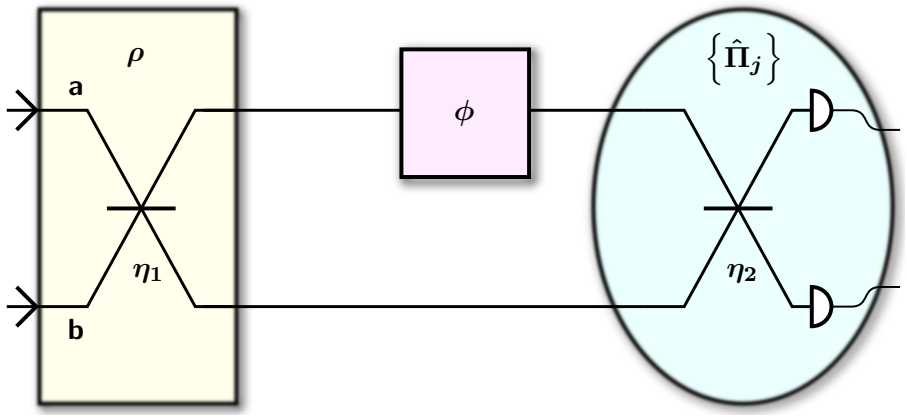

Figure 1.2: A lossless Mach-Zehnder interferometer. Modes **a** and **b** interfere at the first beam splitter which has reflectivity $\boldsymbol{\eta_1}$ (1/2 in the ideal case) before the relative phase $\boldsymbol{\phi}$ is applied to mode **a**. The two modes then interfere again at the second beam splitter, with reflectivity $\boldsymbol{\eta_2}$ (1/2 in the ideal case) before being detected at the output ports. Everything to the left of, and including, beam splitter 1 is considered as preparing the state $\boldsymbol{\rho}$ while everything to the right of, and including, beam splitter 2 is considered as part of the measurement.

best possible precision achievable with a given input state ρ.

1.3.2 Classical limits on precision: the Standard Quantum Limit

In order to assess whether a particular protocol is 'better' than its classical counterpart, it is important to define classical limits to the precision that can be achieved with given resources. In the absence of loss, this limit is called the Standard Quantum Limit (SQL). The SQL is the best precision that can be achieved in an estimate of a parameter using N independent photons. It can be derived using several methods, however, perhaps the most instructive in this instance is to consider the Mach-Zehnder interferometer (MZI) in Figure 1.2. In what follows and throughout this thesis, familiarity with Dirac notation is assumed. The operator $\hat{a}^\dagger$ is the creation operator for a photon in mode a and $\hat{b}^\dagger$ is the creation operator for a photon in mode b. The action of a creation operator on a mode is

to add one more excitation to that mode so that, for example,

$$\hat{a}^\dagger |n\rangle = \sqrt{n+1}\,|n+1\rangle\,, \tag{1.10}$$

where $|n\rangle$ represents a Fock state containing n photons. Similarly, the annihilation operator $\hat{a}$ acting on mode a reduces the number of excitations so that

$$\hat{a}\,|n\rangle = \sqrt{n}\,|n-1\rangle\,. \tag{1.11}$$

To calculate the evolution of a photon through the MZI shown in Figure 1.2, and hence calculate the associated FI, it is necessary to know the effect of a phase shifter and a beamsplitter on the creation operator. The action of a phase shift ϕ on a mode is to implement the transformation $\hat{a}^\dagger \rightarrow e^{i\phi}\hat{a}^\dagger$ while a beamsplitter transforms a creation operator in one input mode into a superposition of creation operators in both output modes. The exact ratio in the superposition is determined by the reflectivity of the beamsplitter, η, so that for the first beamsplitter in Figure 1.2, the two input modes evolve as

$$\begin{aligned}\hat{a}^\dagger &\rightarrow \sqrt{\eta_1}\hat{a}^\dagger + \sqrt{1-\eta_1}\hat{b}^\dagger,\\ \hat{b}^\dagger &\rightarrow \sqrt{1-\eta_1}\hat{a}^\dagger - \sqrt{\eta_1}\hat{b}^\dagger.\end{aligned} \tag{1.12}$$

The minus sign in the evolution of $\hat{b}^\dagger$ is due to the π phase shift that occurs when light reflects off one side of all beamsplitters. Throughout this thesis, the convention will be adopted that this phase shift occurs when light is reflected from the 'bottom' of the

beamsplitter.

All the components necessary to calculate the evolution of a state through the MZI of Figure 1.2 are now in place. A single photon launched into mode a of the interferometer evolves as follows where the three steps represent passing through the first beamsplitter, phase shifter, and second beamsplitter respectively.

$$\hat{a}^\dagger |\text{vac}\rangle \rightarrow \frac{1}{\sqrt{2}}(\hat{a}^\dagger + \hat{b}^\dagger) |\text{vac}\rangle , \tag{1.13}$$

$$\rightarrow \frac{1}{\sqrt{2}}(e^{i\phi}\hat{a}^\dagger + \hat{b}^\dagger) |\text{vac}\rangle , \tag{1.14}$$

$$\rightarrow \frac{1}{2}\left[(e^{i\phi}+1)\hat{a}^\dagger + (e^{i\phi}-1)\hat{b}^\dagger\right] |\text{vac}\rangle . \tag{1.15}$$

In order to calculate the FI for this output state, the probabilities associated with the two possible outcomes must be obtained as a function of ϕ. The operators corresponding to the two possible outcomes, detection of the photon in mode a or detection of the photon in mode b, are

$$\hat{\Pi}_\text{a} = |1,0\rangle\langle 1,0| , \tag{1.16}$$

$$\hat{\Pi}_\text{b} = |0,1\rangle\langle 0,1| , \tag{1.17}$$

where $|m,n\rangle$ denotes a state with m photons in mode a and n photons in mode b. The associated probabilities are easy to calculate since the Fock basis is orthonormal, meaning that $\langle n|m\rangle = \delta_{n,m}$ where $\delta_{n,m}$ is the Kronecker delta. The probabilities, which are given

by the Born rule, are then

$$p_{\mathrm{a}}(\phi) = \frac{1}{2}(1+\cos\phi), \tag{1.18}$$

$$p_{\mathrm{b}}(\phi) = \frac{1}{2}(1-\cos\phi). \tag{1.19}$$

The square of the derivatives of $p_{\mathrm{a}}(\phi)$ and $p_{\mathrm{b}}(\phi)$ are both $(\sin^2\phi)/4$ so that the FI for each single photon is given by

$$F(\phi) = \sum_j \frac{1}{p_j(\phi)}\left(\frac{\partial p_j(\phi)}{\partial\phi}\right)^2 \tag{1.20}$$

$$= \frac{1}{2}\left[\frac{1}{1+\cos\phi}+\frac{1}{1-\cos\phi}\right]\sin^2\phi \tag{1.21}$$

$$= 1. \tag{1.22}$$

However, the total FI for the N photons sent through the MZI is $F_N(\phi) = N$ since, for independent events, $F_N(\phi) = NF(\phi)$[51]. The FI for N uncorrelated photons in the absence of loss is therefore $F^{\mathrm{SQL}} = N$. Finally, the precision that can be obtained for ν trials, each of which involves sending N completely uncorrelated photons, one at a time, into mode a of the MZI with vacuum in mode b is limited by the CRB which, in this case, is referred to as the SQL,

$$\Delta\phi \geq \frac{1}{\sqrt{\nu N}} = \Delta\phi_{\mathrm{SQL}}. \tag{1.23}$$

1.3.3 Comparing classical and quantum strategies

With the CRB, QCRB, and SQL all now defined, the thresholds for deeming a quantum-enhanced metrology protocol to be 'better' than its classical counterpart can be set as

follows. In the absence of loss, a device can be said to beat its classical counterpart for the same resources if

$$\Delta\phi_{\mathrm{CRB}} < \Delta\phi_{\mathrm{SQL}}. \tag{1.24}$$

This inequality expresses that the precision achievable using the particular state and detector combination employed in the device must be smaller than the precision achievable using a classical state of the same resources and a classical detector.

A second statement can also be made. The device is, in principle, capable of outperforming its classical counterpart for the same resources if

$$\Delta\phi_{\mathrm{QCRB}} < \Delta\phi_{\mathrm{SQL}}. \tag{1.25}$$

This inequality expresses that the state prepared is capable of providing greater precision than a classical state, if optimal measurements on that state were performed.

In each of these descriptions, the phrase 'for the same resources' has been carefully used. Several schools of thought exist. It is important to note that in the absence of loss these schools are completely equivalent, however, when loss is considered, they can differ significantly. The prevalent school of thought is that only the N_{d} photons which are detected at the output of an interferometer should be considered as consumed resources. This is a form of post-selection and can lead to an extreme underestimate of the number of photons passing through the interferometer. The second school is that all photons which are created and intended to be sent through the interferometer should be counted as resources, regardless of whether they make it to the output. As will be shown theoretically in Section 1.5 and experimentally in the Chapter 2, this leads to extremely stringent

constraints on the allowable inefficiencies in the system.

The argument for using this second resource accounting strategy relies on the situations in which quantum-enhanced metrology may be employed. In the case where the physical system being probed is unaffected by the light passing through it, the practical reality is that it is much more straight-forward to use a standard laser and a MZI. This is because the SQL can be made arbitrarily small by using more and more photons. It is only when the sample one wishes to probe is destroyed or affected by the total number of photons sent through it, such as with a fragile biological specimen or state of matter such as a Bose-Einstein condensate, that the increased precision achievable with quantum-enhanced metrology becomes desirable. In this situation it is therefore problematic if photons are lost by scattering off or being absorbed in the sample as they will not be detected at the output, giving no information about the phase, but will damage the sample in the process. The post-selector continues, unaware that the sample may have been damaged, and tries again. In the event that transmission through the system is small, the measurement may be attempted many times before the desired N_{d} event is detected, by which time the sample has been damaged and the information gained about the phase is no longer useful.

1.4 Resource counting in the presence of loss

Much of the above discussion is based on the assumption of no photon loss and ideal beam splitters inside the MZI. In any practical attempt to produce a device that will outperform its classical counterpart, these assumptions will certainly no longer be true. As will be shown, real-world imperfections, and especially loss, very quickly destroy the ability of a device to beat any classical limit. The precise effect of loss depends on how the state being

used evolves under that loss. In order to discuss these effects, it is therefore necessary to introduce first the classical bounds that can be reached in the presence of loss, followed by specific quantum states which can be used in quantum-enhanced metrology.

1.4.1 The Standard Interferometric Limit (SIL)

Figure 1.3a shows a general two mode interferometer with real world imperfections. There are three stages at which loss can compromise precision: in the preparation of the probe state, interaction of the state with the phase shifting element, and in measurement. These are characterized by the efficiencies ξ_{g}, ξ_{i}, and ξ_{m} respectively. ξ_{g} is the generation or heralding efficiency. It is the probability that we have generated the desired state given some signal that the generation step has been carried out. This signal may be as simple as knowledge that a light pulse has been emitted by a laser, or it may be the detection of one or more photons to herald the generation of others[56–58]. ξ_{i} is the interaction efficiency, the probability that the probe state, once generated, is transmitted through the two modes reaching the interferometer. Finally, ξ_{m} is the measurement efficiency, the probability that the measurement is made.

In general, states of multiple photons can retain phase sensitivity even after experiencing loss of one or more photons. It is also true that the state after loss depends on the form of the state before loss. It is therefore necessary to introduce a specific model of loss in order to assess its impact. This model is shown in Figure 1.3b. Loss at all stages is modelled by beam splitters in the arms of the MZI. Note that in contrast to other beam splitters, where *reflectivities* will be referred to with the symbol η_α, loss or efficiency will be referred to with the symbol ξ_α representing a *transmissivity*. This is to maintain

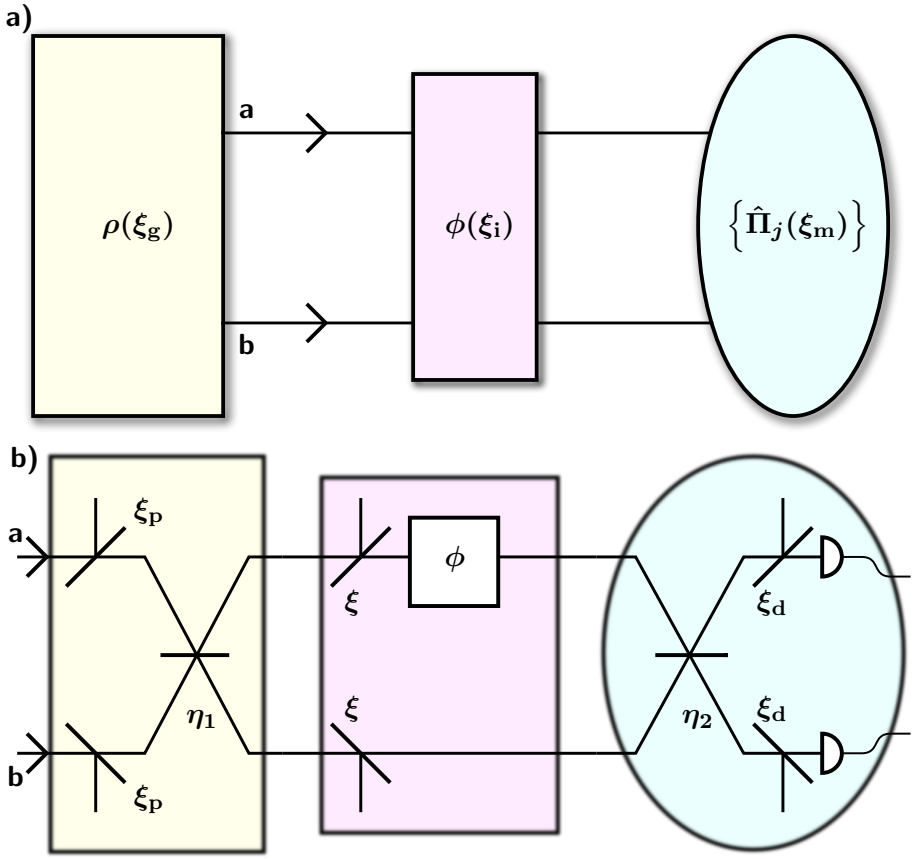

Figure 1.3: a) A general two mode interferometer with losses. The efficiencies $\boldsymbol{\xi_g}$, $\boldsymbol{\xi_i}$, and $\boldsymbol{\xi_m}$ characterize state generation, interaction with the phase shifting element, and measurement respectively. The phase shifting element has been extended across both modes to indicate that, although the phase shift is only applied to mode **a**, the efficiency $\boldsymbol{\xi_i}$ can involve both modes. b) A MZI with balanced loss in state preparation, interaction with the phase shifting element, and detection. The efficiencies are modelled by beamsplitters with *transmissivity* $\boldsymbol{\xi_p}$, $\boldsymbol{\xi}$, and $\boldsymbol{\xi_d}$ respectively, where one of the output ports of the beamsplitter is not monitored. The first and second beam splitters of the MZI have *reflectivities* $\boldsymbol{\eta_1}$ and $\boldsymbol{\eta_2}$ respectively. In the ideal case, $\boldsymbol{\eta_1 = \eta_2 = 1/2}$.

consistency with the literature where beamsplitters are frequently characterized by their reflectivity, while it is customary to have an efficiency (associated with a loss) run from 0 to 1 where 1 is perfect efficiency. The beam splitters of transmissivity ξ_{p} model the efficiency in state preparation. As will be discussed in Section 1.4.2, the coherent mixing of two spatial modes on a beam splitter is not sufficient to prepare an arbitrary state for quantum enhanced metrology, however, it is sufficient both to observe how a classical N photon resource behaves, and to prepare a class of states which will be the focus of the discussion in Part I of this thesis. It will therefore suffice for now. The beamsplitters of transmissivity ξ model the efficiency of interaction, and the beamsplitters of transmissivity ξ_{d} model the efficiency of measurement, or detection. Again, as with state preparation, it is not in general sufficient to mix the two spatial modes of the MZI coherently on a beamsplitter in order to saturate the CRB. As will be shown, however, it is sufficient for the situations considered here.

The Standard Interferometric Limit (SIL) is the precision achievable in estimating the phase ϕ using a MZI with non-unit transmission and detection efficiencies with a coherent state of unknown phase and average photon number N at one input and vacuum at the other[40]. Coherent states of unknown phase, or phase-averaged coherent states, can be prepared perfectly since a coherent state, $|\alpha\rangle$, with average photon number $N = |\alpha|^2$, evolves under a loss ξ_{p} to become the coherent state $\left|\sqrt{\xi_{\mathrm{p}}}\alpha\right\rangle$, with average photon number $\xi_{\mathrm{p}}N$[59]. Therefore, by calibration of the loss ξ_{p}, a coherent state with arbitrary photon number can still be prepared and ξ_{p} can be ignored. The behaviour of this state can still be mimicked by tracking the evolution of single photons through the MZI in Figure 1.3, as in Section 1.3.2. In contrast to that analysis, however, for every photon sent into the

MZI there are now four possible outcomes. Either the detector monitoring mode a fires, the detector monitoring mode b fires, neither of the detectors fire, or both of them do. In the absence of noise, the probability of both firing is zero and the other three outcomes have the probabilities

$$p_{\mathrm{a}}(\phi) = \frac{\xi\xi_{\mathrm{d}}}{2}(1+\cos\phi), \tag{1.26}$$

$$p_{\mathrm{b}}(\phi) = \frac{\xi\xi_{\mathrm{d}}}{2}(1-\cos\phi), \tag{1.27}$$

$$p_0(\phi) = 1 - p_{\mathrm{a}}(\phi) - p_{\mathrm{b}}(\phi) = 1 - \xi\xi_{\mathrm{d}}. \tag{1.28}$$

Since p_0 does not depend on ϕ, the value of p_0 does not give any information about the phase. The QFI is therefore scaled by $\xi\xi_{\mathrm{d}}$, the new pre-factor in p_{a} and p_{b}, giving a QCRB of

$$\Delta\phi \geq \frac{1}{\sqrt{\nu\xi\xi_{\mathrm{d}}N}} = \Delta\phi_{\mathrm{SIL}}, \tag{1.29}$$

where $\Delta\phi_{\mathrm{SIL}}$ is the Standard Interferometric Limit. Note that this is the QCRB rather than the CRB because the combination of a beamsplitter of reflectivity $1/2$ and two single photon sensitive detectors is still the optimal measurement under balanced loss.

In order to compare the precision obtainable with a given input state with the best practical precision obtainable with a classical device using the same interferometer and detectors, one can therefore compare $\Delta\phi_{\mathrm{CRB}}$ with $\Delta\phi_{\mathrm{SIL}}$. If the inequality $\Delta\phi_{\mathrm{SIL}} > \Delta\phi_{\mathrm{CRB}}$ holds, then a particular (imperfect) device will outperform its (imperfect) classical counterpart. Since in this inequality the number of trials is the same for both the classical and quantum cases, it may be expressed in terms of the FI only so that in order for the

device to outperform its classical counterpart, the following inequality must hold:

$$\eth = \frac{F}{F^{\mathrm{SIL}}} > 1. \tag{1.30}$$

1.4.2 States for quantum-enhanced metrology

There are primarily three classes of state which have been explored for use in quantum-enhanced metrology with fixed total resources.

N00N states

The first, and the most widely studied, is the N00N state[7,31–39,60–64].

$$|N::0\rangle_{\pm} = \frac{1}{\sqrt{2}}(|N,0\rangle_{\mathrm{a,b}} \pm |0,N\rangle_{\mathrm{a,b}}). \tag{1.31}$$

This path entangled state is an equal superposition of N photons in mode a and 0 photons in mode b with 0 photons in mode a and N photons in mode b. If this state is launched into the general lossless two mode interferometer shown in Figure 1.1, the portion of the state with N photons in mode a picks up a phase shift of $N\phi$. Calculation of the symmetric logarithmic derivative reveals that an optimal measurement for the N00N state are those which project it onto the basis $\{|N::0\rangle_{+}, |N::0\rangle_{-}\}$. The probabilities corresponding to these outcomes are

$$p_{\pm}(\phi) = \frac{1}{2}(1 \pm \cos N\phi). \tag{1.32}$$

This leads to a QFI of $F_{\mathrm{Q}}(\phi) = N^2$ and hence the achievable precision is bounded by the QCRB,

$$\Delta\phi \geq \frac{1}{\sqrt{\nu N}} = \Delta\phi_{\mathrm{HL}}. \tag{1.33}$$

The limit is written as equal to $\Delta\phi_{\mathrm{HL}}$ to denote that this is in fact the Heisenberg Limit (HL), the tightest known bound on precision in linear metrology [1,2]. Since the N00N state is, in principle, capable of saturating the tightest known bound to precision, it has been extremely well studied and several experiments have claimed to have beaten the SQL using them [31,35,38,64].

There is, however, a major drawback to N00N states. Under the loss of even a single photon, the resulting state is completely insensitive to phase. The intuitive explanation of this is that if a photon is lost, it must have been lost from the mode which contains N photons. Hence, if all of the possible loss modes from modes a and b were monitored, an observer would be able to tell which component of the superposition the state was in, collapsing it into that component. Critically, it is enough that an observer, even in principle, could have known which mode carried N photons to collapse the state. The resulting state, which carries 0 photons in one mode and $N-1$ photons in the other, is then measured at the output, however, the outcome of the measurement is no longer affected by the phase ϕ since there is no interference. The remaining $N-1$ photons therefore give no information about ϕ. Further to this, N00N states require not only the generation of N or more photons but the manipulation of these photons by means of a complex linear optical network [31,33,57,58,65–68]. The output of these networks is probabilistic since it relies on detection and/or non-detection of ancillary photons and the success probability usually decreases exponentially with increasing photon numbers. Schemes which can, in

principle, generate N00N states with high probability require either a high nonlinearity [69] or actively controlled cavities [70], which challenge current technology.

Optimal states

The second class of states are the so-called optimal states [40,71]. Optimal states are not maximally entangled like N00N states, however, this fact makes them less sensitive to loss. They take the form

$$|\psi\rangle = \sum_{k=0}^{N} A_k \, |k, N-k\rangle_{\mathrm{a,b}} \, , \tag{1.34}$$

where the A_k are a function of the loss in the system and are chosen specifically to maximize the QFI [71]. As an example, consider a two photon state and an interferometer containing a phase shifting element with a transmissivity of $\xi = 0.45$. The general form of a two photon state input state is

$$|\psi\rangle = A_2 \, |2,0\rangle + A_1 \, |1,1\rangle + A_0 \, |0,2\rangle \, . \tag{1.35}$$

The coefficients of the three terms making up the state are found by maximizing the F_{Q} subject to the constraints $|A_0|^2 + |A_1|^2 + |A_2|^2 = 1$ and $A_i \geq 0$. For $\xi = 0.45$ this gives $A_2 = 0.7570$, $A_1 = 0.3740$, and $A_0 = 0.5357$, yielding $F_Q = 1.6035$. In contrast, the QFI for a N00N state in the same situation is 0.405.

Although these states achieve the best possible precision for a given efficiency, its specific value must be known before hand. The form of the state which must be generated is then dependent on the value of the loss. In addition, there is currently no known general recipe for generating these states or implementing the corresponding ideal measurements.

Despite these difficulties, however, a proof of principle experiment has been performed [71] in which a known loss was introduced in a post-selected way and the optimal two-photon state was prepared, demonstrating their robustness.

Holland-Burnett states

The final and less widely studied class of states are the Holland-Burnett (HB) or twin-Fock states [72], which we denote HB($N = 2K$), where $K \in \{1, 2, 3, \ldots\}$. These can be prepared by sending K photons to both inputs of a 50:50 beam splitter. The state of the field after the beamsplitter and the phase shifter in Figure 1.2 is then

$$|\mathrm{HB}(2K)\rangle = \sum_{n=0}^{K} A_n \, |2n, 2K-2n\rangle \,, \qquad A_n = \frac{\sqrt{(2n)!(2K-2n)!}}{2^K n!(K-n)!} e^{2in\phi}. \tag{1.36}$$

This notation differs slightly from the standard notation, where the state is specified by N, the size of the Fock states impinging on either side of the beamsplitter at which the state is created, and there are a total of $N_{\mathrm{tot}} = 2N$ photons. This is done so that N has a consistent meaning for N00N and HB states.

The HB state has a similar structure to the optimal states, with the notable difference that the method for preparing them is known, universal, and practically feasible. In addition, their performance is not drastically diminished in the presence of losses [15,73–75], making them significantly more practical than N00N states.

Equation 1.9 can be used to calculate the QFI for the HB state in the absence of loss,

$$|\psi_\phi\rangle = \sum_{n=0}^{K} 2inA_n \,|2n, 2K-2n\rangle\,, \tag{1.37}$$

$$\langle\psi_\phi|\,\psi_\phi\rangle = K(3K+1)/2, \tag{1.38}$$

$$\langle\psi|\,\psi_\phi\rangle = iK. \tag{1.39}$$

The QFI and QCRB are therefore

$$F_{\mathrm{Q}} = 2K(K+1) = N(\frac{N}{2}+1), \tag{1.40}$$

$$\Delta\phi_{\mathrm{QCRB}} = \frac{1}{\sqrt{\nu N(N/2+1)}}. \tag{1.41}$$

The quadratic behaviour of the QFI with N shows that Heisenberg scaling is reached. When there is no loss, the HB state does not achieve the same precision as the N00N state which will out-perform it by a constant factor of $\sqrt{2}$.

Following the evolution of the state, interfering the two modes on the second beamsplitter shown in Figure 1.2, yields

$$|\psi_{\mathrm{out}}\rangle = \frac{1}{K!}\left(\frac{ie^{i\phi}\sin\phi}{2}\right)^K \left((\hat{\mathrm{a}}^\dagger)^2 + (\hat{\mathrm{b}}^\dagger)^2 - 2i\hat{\mathrm{a}}^\dagger\hat{\mathrm{b}}^\dagger\cot\phi\right)^K |\mathrm{vac}\rangle\,. \tag{1.42}$$

The expansion of the operators gives

$$N!\left(\sum_{\mathcal{K}} \frac{(-2i\cot\phi)^{k_3}}{k_1!k_2!k_3!}(\hat{\mathrm{a}}^\dagger)^{2k_1+k_3}(\hat{\mathrm{b}}^\dagger)^{2k_2+k_3}\right)|\mathrm{vac}\rangle\,, \tag{1.43}$$

where $\mathcal{K} = \{(k_1,k_2,k_3)|k_i \in \mathbb{Z}^+, k_1+k_2+k_3 = K\}$. Projecting the two modes onto the Fock

states $|n\rangle|2K-n\rangle$ gives the associated probabilities $p_n(\phi) = \frac{n!}{(2K-n)!}\left[P_K^{K-n}(\cos\phi)\right]^2$, where $0 \leq n \leq K$, and $P_K^l(\cdot)$ are the Legendre polynomials. The expression for $K \leq n \leq 2K$, is obtained by substituting $n \to 2K-n$. Perhaps surprisingly, by a continuation of this train of analysis, one can show that a beamsplitter and two photon number resolving detectors (PNRDs) that project onto the state $|K\rangle|K\rangle$ are sufficient to attain the Heisenberg scaling in the absence of loss[41].

1.4.3 Super-resolution and super-sensitivity

There are two effects attributed to quantum behaviour in interferometry: phase super-resolution and phase super-sensitivity. Historically these effects have been used to determine whether or not a quantum enhancement of phase estimation had been achieved. However, as will be shown later, the observation of these phenomena may not properly account for all resources needed to truly go beyond what is possible classically. Nonetheless, their importance in the development of the field is such that it is necessary to introduce them.

Phase super-resolution is the sinusoidal variation of an N_d-fold detection signal, the rate at which N_d events occur simultaneously, as a function of interferometer phase ϕ. This signal is said to show super-resolution if the variation displays an N_d-times increase in oscillation rate. It has been shown, however, that this can be observed using only classical input states of light and projective measurements[60]. Recently, the visibility of such super-resolving fringes was also shown to be able to distinguish between quantum and classical input states of a MZI[61]. This signature of quantum behaviour does not, however, quantify improved performance beyond classical interferometry.

Phase super-sensitivity, a commonly employed measure of performance, is defined as reduced phase uncertainty compared to that possible with classical resources [60]. The model introduced in a paper by Resch et al. [60] incorporates experimental imperfection through 'efficiency' and visibility parameters ξ' and V, by means of a phenomenological model of an $N_{\rm d}$-fold detected coincidence signal. Here, ξ' is the proportion of the input state ρ that can lead to an $N_{\rm d}$-fold detection event. Note that this immediately restricts the applicability of the analysis to cases where a particular photon number event is being post-selected and all others are ignored. In fact, the Authors state that their argument is based on the comparison of a N00N state scheme with a classical scheme that consumes the same amount of energy. The visibility is then required to satisfy $\xi' V^2 N_{\rm d} > 1$ in order for the measurement to be regarded as 'super-sensitive'.

In order to clarify the use of this criteria it is first necessary to briefly outline the argument followed by Resch et al. and then compare it to an analysis based on consideration of the QFI. Resch et al. argue that estimating a phase with a N00N state amounts to measuring $N_{\rm d}$-fold coincidence events of an observable $\hat{A}$ which take the form $\langle \hat{A} \rangle = \frac{1}{2}(1 - V \cos N_{\rm d}\phi)$, giving

$$\frac{d\langle \hat{A} \rangle}{d\phi} = \frac{N_{\rm d} V}{2} \sin N_{\rm d}\phi. \tag{1.44}$$

Then, for small deviations about a particular value of ϕ, the precision with which ϕ can be estimated, $\Delta\phi$, is given by

$$\Delta\phi = \frac{\Delta\hat{A}}{d\langle \hat{A} \rangle / d\phi} = \frac{2\Delta\hat{A}}{N_{\rm d} V \sin N_{\rm d}\phi}. \tag{1.45}$$

Now, if the device has an 'efficiency' ξ', $N_{\rm tot} = N_{\rm d}/\xi'$ photons are consumed on average for each $N_{\rm d}$ event. Here, ξ' is the probability that the whole $N_{\rm d}$ photon N00N state is transmitted and detected. The obtained precision should therefore be compared with a classical strategy that consumes $N_{\rm tot}$ photons. The best possible classical strategy has no loss and so the precision is bounded by the SQL, $\Delta\phi_{\rm SQL} = \sqrt{\xi'/N_{\rm d}}$. Then, in order to be 'better than classical,'

$$\Delta\phi_{\rm SQL} > \Delta\phi, \tag{1.46}$$

$$\Longrightarrow \frac{\xi'}{N_{\rm d}} > \frac{4(\Delta\hat{A})^2}{N_{\rm d}^2 V^2 \sin^2 N_{\rm d}\phi}. \tag{1.47}$$

The Authors then state that for an observable which is bounded between 0 and 1, the worst case is $\Delta\hat{A} = 1/2$ so that at the point of minimum uncertainty for the N00N state scheme,

$$\xi' V^2 N_{\rm d} > 1 \tag{1.48}$$

must be satisfied in order for a N00N state scheme to beat its classical counterpart. Further, Resch et al. assume that a supply of N00N states is available on demand – that is, that they can be prepared with a probability of one.

An alternative analysis based on the QFI proceeds as follows. Since there is no known arbitrary N00N state generation scheme, one must be considered which has a heralding or generation efficiency $\xi_{\rm g}$. It is assumed that the non-unit heralding efficiency arises as a result of loss or the probabilistic nature of the generation scheme. Under this assumption, any states generated in failure cannot result in an $N_{\rm d}$-fold detection event.

In a N00N scheme experiment using a general two mode interferometer with imperfect

efficiency, an N-fold detection event corresponds to projection onto an N-photon $N00N$ state, $|N::0\rangle_{\pm} = (|N,0\rangle \pm |0,N\rangle)/\sqrt{2}$. This measurement set has three possible outcomes: $j = \pm$ (detection of $|N::0\rangle_{\pm}$) and $j = 0$ (otherwise). In the absence of loss, the probabilities associated with these measurement outcomes are as described in Section 1.4.2. In practice, however, it is impossible with current technology to realize lossless single-mode sensors and this can lead to degraded interference due to unmeasured distinguishing information of the input state. Measurement outcomes therefore typically have probabilities

$$p_{\pm}(\phi) = f[1 \pm V\cos(N\phi)]/2, \tag{1.49}$$

and $p_0(\phi) = 1 - p_+(\phi) - p_-(\phi)$, where f and V both depend upon the presence of distinguishing information in the input state. f is also related to the probability that an input state leads to an N-fold detection event, and V is the fringe visibility. The FI for this configuration is given by

$$F(\phi) = fN^2V^2\frac{\sin^2(N\phi)}{1 - V^2\cos^2(N\phi)}, \tag{1.50}$$

where we have made use of the first derivatives of $p_{\pm}(\phi)$ with respect to ϕ,

$$\frac{\partial p_{\pm}(\phi)}{\partial\phi} = \mp\frac{f}{2}NV\sin(N\phi). \tag{1.51}$$

Note that the denominator in Equation. (1.50) is greater than or equal to $\sin^2(N\phi)$ for $0 \leq V \leq 1$, which sets a bound on the FI,

$$F(\phi) \leq fV^2N^2. \tag{1.52}$$

The phase uncertainty that can be achieved with ν trials is therefore bounded by the CRB

$$\Delta\phi \geq \frac{1}{\sqrt{\nu f} NV}. \tag{1.53}$$

As in the previous analysis, this precision can be compared with the best possible classical strategy that consumes the same energy. Such a strategy will consume an N photon resource per trial but will experience no inefficiencies. Comparison should therefore be with the SQL, implying that in order to demonstrate precision beyond the SQL,

$$V \geq \frac{1}{\sqrt{fN}} = V_{\text{th}}^{(\text{SQL})}. \tag{1.54}$$

This is not the only comparison that can be made, however. If it is assumed that the same channel and detectors are used in both classical and quantum schemes, the achievable quantum precision should be compared with the SIL, implying that

$$V \geq \sqrt{\frac{\xi\xi_{\text{d}}}{fN}} = V_{\text{th}}^{(\text{SIL})}. \tag{1.55}$$

For the general lossy two-mode interferometer, f can be straightforwardly calculated as the probability that the N00N state is produced, transmitted, and detected, $f = \xi_{\text{g}}(\xi\xi_{\text{d}})^N$. By comparing Equation 1.54 to Equation 1.48, it can be seen that an equivalent bound has been reached with $\xi' = f$. There is a significant advantage, however. Although, when correctly applied, Equation 1.48 provides a helpful bound, it is useful only when using a scheme under which all phase information is lost if any photons are lost. In contrast, the analysis based on the FI and QFI is much more general and allows the objective

comparison of different schemes. As well as this, it provides a route to a perhaps more useful comparison between practical devices, Equation 1.55.

The usual application of these bounds deviates significantly from what is outlined above. It is common practice to set $f = \xi_{\text{intrinsic}}$, the fraction of the expected input state which could lead to a particular N-fold detection event, and all other efficiencies are set to 1 [31,35,37,38,64,76]. This significantly underestimates the resources consumed and the threshold on V. The impact of such an analysis is emphasised by a simple example. A single parametric down-converter (PDC) emits a superposition of zero photons, one pair of photons, two pair etc [59]. Consider such a photon source in a typical configuration, pumped using a pulsed laser system with a repetition rate 80 MHz and probability of producing one pair per pump pulse ~ 0.03. Now, if the two output modes of the PDC are degenerate, they can be interfered on a beam splitter with reflectivity 1/2. If two pairs were generated, the state after the beam splitter is

$$\sqrt{\frac{3}{4}}\,|4::0\rangle_{\text{a,b}} + \frac{1}{\sqrt{4}}\,|22\rangle_{\text{a,b}}\,. \tag{1.56}$$

A measurement can be performed on this state which is only sensitive to the $|4::0\rangle$ portion [35], but is only successful, in the ideal case, with probability 1/2. The post-selector sets $f = 3/4 \times 1/2$, the average probability (over the phase ϕ) that the idealised input state leads to the particular 4-fold detection event, and obtains the visibility threshold $V_{\text{th}}^{(\text{SQL})} = 0.82$. Note that this analysis implicitly sets N equal to $N_{\text{d}} = 4$, the number of detected photons, and only counts as a trial the number of times the N_{d} event occurred. In any practically realisable device, this is not the case due to photon loss. The number of

trials will be significantly larger than those which lead to N_{d}-fold events and, in the case of PDC-based photon sources, there is a comparatively larger probability of generating one pair of photons than two pairs.

A 'worst case scenario' analysis requires information about the probability of producing two pairs per pump pulse to be incorporated. In the worst case scenario, the source is viewed as a $|4::0\rangle_{\mathrm{a,b}}$ generator with generation efficiency $\xi_{\mathrm{g}} = 0.03^2 \times 3/4$, the probability of producing two pairs per pulse times the fraction of the state which could lead to the 4-fold detection event. Even assuming perfect transmission through the device and a deterministic detection scheme, this leads to the visibility threshold $V_{\mathrm{th}}^{(\mathrm{SQL})} = 19.25$. As visibilities greater that 1 are unphysical, this analysis implies that it is not possible to beat the best possible classical counterpart of this system.

Although the worst case scenario is perhaps unfair, it serves as a stark indication of the effect of resource accounting on the conclusion of whether or not a metrology system has truly out performed its classical counterpart. It is also the case that both of these analyses are limited by considering only a particular measurement outcome which consists of a 4-fold detection event. This is because they were originally envisaged as thresholds on visibility for N00N-state schemes where loss renders the lower photon number portions of the state insensitive to phase. The CRB and QCRB analyses give a more general method to quantify the resources consumed in an experiment and compare quantum with classical strategies. These quantities are derived from the density matrix of the *input* state to the interferometer through the FI and QFI respectively. To ascertain the best performance of a given quantum strategy, one must therefore know the density matrix ρ of the input probe state as prepared, as well as the device transmission and detector efficiency. The average

photon number of the input state can then be calculated from ρ, giving N. Note that although the HL is defined for states of fixed total photon number and the SQL is defined for states of fixed mean photon number, these are interchangeable here. This is because the SQL is also the precision that can be obtained by N single photons propagating in turn through a MZI, as in Section 1.3.2. These photons are completely independent and all correlation functions of order greater than 1, are zero. In this way, they mimic the behaviour of a classical state. For a more general discussion of these issues, see Escher et al.[77]

The FI of ρ is calculated in combination with a model of the particular detection scheme used which has a known efficiency. The CRB then takes into account information from all detector outcomes and all parts of the input state rather than a particular outcome corresponding to a particular N_{d}-fold detection event. Comparison with the SQL or SIL then reveals whether the scheme beats the best possible or the best practical classical counterpart respectively. Calculation of the QCRB based on the QFI and comparison with the SQL reveals whether the input state combined with the most optimal, although perhaps unknown, detection scheme is capable of beating the best possible classical counterpart which consumes the same energy.

1.5 Including real-world imperfections

Imperfections are present in every real-world device. If quantum-enhanced technologies are ultimately to prove their worth, they must be able to overcome the likely imperfections. Theoretical strategies to overcome common imperfections in quantum information processing have been developed, however, there has been comparatively less attention paid

to overcoming imperfections in metrology schemes. The analysis laid out above based on the CRB and the QCRB provides a consistent, device independent way of comparing different strategies, even in the presence of real-world imperfections. Here, the effect of inefficiencies in state preparation, propagation, and detection on whether a device beats its classical counterpart are considered.

1.5.1 Device transmission efficiency

Analysis of the performance of HB(N) states in interferometry in the presence of losses begins with Equation (1.36). Here, only loss in a single arm of the interferometer is considered so that only the beamsplitter labelled ξ in the same arm as the phase shifter in Figure 1.3 is present. Loss in both arms can be treated similarly, but requires numerical analysis and hence perhaps provides less insight into its effects. The state after loss is

$$\begin{aligned}
|\psi\rangle &= \frac{1}{2^K}\sum_{n=0}^{K}\sum_{m=0}^{2n} C_n B_{n,m}\,|2n-m\rangle\,|2N-2n\rangle\,|m\rangle_{\mathrm{e}}\,,\\
C_n &= \frac{(2n)!}{n!}\frac{\sqrt{(2K-2n)!}}{(K-n)!}e^{2in\phi},\\
B_{n,m} &= \frac{\xi^{n-m/2}(1-\xi)^{m/2}}{\sqrt{(2n-m)!\;m!}},
\end{aligned} \tag{1.57}$$

where m is the number of photons lost to the environment mode, labelled e. Since this mode is to be traced over, the state can be rewritten as

$$|\psi\rangle = \sum_{m=0}^{2K} |\psi_m\rangle |m\rangle_{\mathrm{e}},$$
$$|\psi_m\rangle = \begin{cases} \frac{1}{2^K} \sum_{k=0}^{K-\lceil \frac{m}{2} \rceil} C_{k+\lceil \frac{m}{2} \rceil} B_{k+\lceil \frac{m}{2} \rceil, m} |2k\rangle_{\mathrm{a}} |2K-2k\rangle_{\mathrm{b}} & \text{for } m \text{ even} \\ \frac{1}{2^K} \sum_{k=0}^{K-\lceil \frac{m}{2} \rceil} C_{k+\lceil \frac{m}{2} \rceil} B_{k+\lceil \frac{m}{2} \rceil, m} |2k+1\rangle_{\mathrm{a}} |2K-2k-1\rangle_{\mathrm{b}} & \text{for } m \text{ odd} \end{cases} \tag{1.58}$$

where $\lceil \cdot \rceil$ denotes rounding up to the nearest integer. Evaluating the QFI for the lossy states in Equation (1.58) is simplified by their block diagonal form. Setting $\left|\tilde{\psi}_m\right\rangle = |\psi_m\rangle / \sqrt{\mathfrak{N}_m}$, with $\mathfrak{N}_m = \langle \psi_m | \psi_m \rangle$, enables the QFI for the lossy state to be written as $F_{\mathrm{Q}} = \sum_{m=0}^{2K} \mathfrak{N}_m F_{\mathrm{Q}}(\left|\tilde{\psi}_m\right\rangle)$. Here $F_{\mathrm{Q}}(\left|\tilde{\psi}_m\right\rangle)$ is given by Equation (1.9), where

$$\left\langle \tilde{\psi}_m^{(\phi)} \middle| \tilde{\psi}_m^{(\phi)} \right\rangle = \frac{4}{\mathfrak{N}_m 2^{2K}} \sum_{k=0}^{K-\lceil \frac{m}{2} \rceil} \left(k + \left\lceil \frac{m}{2} \right\rceil\right)^2 \left| C_{k+\lceil \frac{m}{2} \rceil} \right|^2 \left| B_{k+\lceil \frac{m}{2} \rceil, m} \right|^2, \tag{1.59}$$

$$\left\langle \tilde{\psi}_m \middle| \tilde{\psi}_m^{(\phi)} \right\rangle = \frac{2i}{\mathfrak{N}_m 2^{2K}} \sum_{k=0}^{K-\lceil \frac{m}{2} \rceil} \left(k + \left\lceil \frac{m}{2} \right\rceil\right) \left| C_{k+\lceil \frac{m}{2} \rceil} \right|^2 \left| B_{k+\lceil \frac{m}{2} \rceil, m} \right|^2. \tag{1.60}$$

To consider some specific cases, for $N = 2$ ($K = 1$),

$$F_{\mathrm{Q}}^{(N=2)} = 8 \frac{\xi^2}{1+\xi^2}, \tag{1.61}$$

which is identical to that obtained for two-photon N00N states in Dorner et al.[40]. This is as expected, since HB(2) states and two photon N00N states are equivalent. For higher photon numbers, N00N and HB(N) states differ. HB(N) states are much more resilient to losses than the corresponding N00N states with the same number of photons, and track the

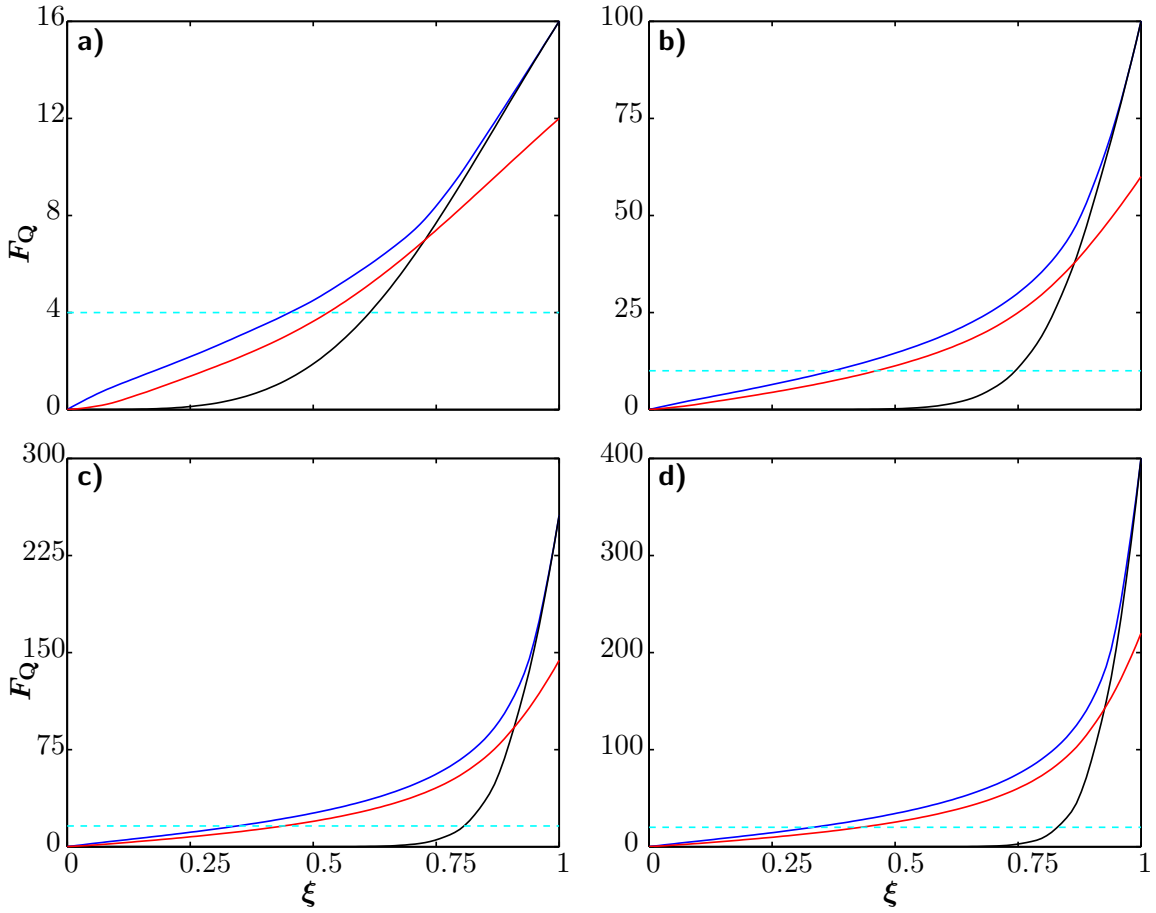

Figure 1.4: Quantum Fisher information for phase estimation as a function of the transmissivity of one arm, ξ, for a) 4, b) 10, c) 16, and d) 20 input photons. In each graph, the dashed cyan: standard quantum limit, blue: optimal states [40], red: HB states, black: N00N states.

behaviour of the optimal states. This is demonstrated in Figure 1.4 where N00N states, optimal states, and HB states are compared as a function of ξ for $N = 4$, 10, 16, 20 in a), b), c), and d) respectively. As N increases, the threshold ξ for which N00N states beat the SQL also increases while the threshold for which optimal and HB states beat the SQL reduces. The difference in robustness between the HB and N00N states therefore becomes more prominent for increasing N, highlighting the benefit of using HB states. In contrast, the discrepancy between HB states and optimal states is both smaller and much less sensitive on N.

1.5.2 State preparation efficiency

The second source of imperfections that can be included in an analysis of the performance of HB(N) states is in their preparation. In this section the effect of only state preparation efficiencies is considered. Imperfections of this type are, as in the previous section, modelled by inserting a fictitious beamsplitter at the two inputs shown in Figure 1.3b with a transmissivity of ξ_{p}. It is then assumed that two perfectly pure and indistinguishable Fock states, $|K\rangle$, are launched into each of these inputs and so imperfection arises from loss. Such a beamsplitter implements the transformation

$$|K\rangle \to \rho \equiv \sum_{n=0}^{K} \binom{K}{n} \xi_{\mathrm{p}}^{n} (1-\xi_{\mathrm{p}})^{K-n} \, |n\rangle\langle n| \, . \tag{1.62}$$

The state after the first beam splitter of the MZI is then $U(\rho_{\mathrm{a}} \otimes \rho_{\mathrm{b}})U^{\dagger}$, where $U = e^{i\pi(\hat{\mathrm{a}}^{\dagger}\hat{\mathrm{b}}+\hat{\mathrm{a}}\hat{\mathrm{b}}^{\dagger})/4}$. Here, U is the operator representing the action of the beamsplitter. In general, $U_{\mathrm{a,b}}(\theta) = e^{i\theta(\hat{\mathrm{a}}^{\dagger}\hat{\mathrm{b}}+\hat{\mathrm{a}}\hat{\mathrm{b}}^{\dagger})}$ where $\xi_{\mathrm{p}} = \cos^2\theta$. After the phase accumulation operator, given by $P = e^{i\phi\hat{\mathrm{a}}^{\dagger}\hat{\mathrm{a}}}$, and the final beamsplitter operator are applied, the output state is

$$\rho_{\mathrm{out}} = U(P \otimes \mathbb{1}_b)U(\rho_a \otimes \rho_b)U^{\dagger}(P \otimes \mathbb{1}_b)^{\dagger}U^{\dagger}. \tag{1.63}$$

Number resolving measurements on the two modes at the interferometer output then give the probabilities $p_{mn} = \langle m,n| \, \rho_{\mathrm{out}} \, |m,n\rangle$. Note that the number of photons in the interferometer can now be less than N and that $p_{mn} = 0$ if $m+n > 2K$. The resulting FI is, in general, a function of the phase to be estimated ϕ but its maximum is always attained for $\phi = 0$, giving by $F_{\xi_{\mathrm{p}}}^{(\mathrm{max})} = 2K(K+1)\xi_{\mathrm{p}}^{K+1}$. This is the QFI for a perfect HB

state, Equation 1.40, scaled by ξ_{p}^{K+1}. It is interesting to note that the power of ξ is not $N = 2K$. It is difficult to compare this effect across N00N and optimal states since the preparation loss is specific to the state generation scheme.

1.5.3 Detection efficiency

Now the scenario of imperfect detection, in addition to imperfect preparation and transmission loss, will be considered. This situation can be modelled, once again, by placing beam splitters in front of perfectly number resolving detectors with transmissivity ξ_{d}. Though obtainable analytically in terms of hyper-geometric functions, the form of the expressions for the FI in the general case is verbose and brings little insight. A simple case, however, is found for $\phi = 0$ and $\xi = 1$ where

$$F_{\xi_{\mathrm{p}},\xi_{\mathrm{d}}}(\phi = 0) = 2N(N+1)(\xi_{\mathrm{p}}\xi_{\mathrm{d}})^{N+1}, \tag{1.64}$$

showing the symmetry of the FI under exchange of ξ_{p} and ξ_{d}.

More generally, by denoting the loss modes in Figure 1.3 as e_1 to e_6, remembering that in the situation considered here the beamsplitter coupling mode a with mode e_4 has transmissivity 1, and adopting the abbreviation $X \circ Y = XYX^{\dagger}$, the state after the first beamsplitter may be written as

$$\rho_1 = U_{\mathrm{a,b}}(1/2) \circ (\rho_{\mathrm{a}} \otimes \rho_{\mathrm{b}}), \tag{1.65}$$

where the ρ_α were defined in the previous section. After phase evolution, propagation loss,

and the second beamsplitter, the state may be written as

$$\rho_2 = \mathrm{Tr}_{\mathrm{e}_3}\left\{U_{\mathrm{a,b}}(1/2)\circ U_{\mathrm{a,e_3}}(\xi)\circ(P_{\mathrm{a}}(\phi)\otimes\mathbb{1}_{\mathrm{b}}\otimes\mathbb{1}_{\mathrm{e}_3})\circ(\rho_1\otimes|0\rangle_{e_3}\langle 0|)\right\}. \tag{1.66}$$

Finally, after detection losses, projection onto $|m,n\rangle$ gives the probabilities

$$p_{m,n}(\phi) = \langle m,n|\,\mathrm{Tr}_{\mathrm{e_5,e_6}}\left\{(U_{\mathrm{a,e_5}}(\xi_{\mathrm{d}})\otimes U_{\mathrm{b,e_6}}(\xi_{\mathrm{d}}))\circ(\rho_2\otimes|0\rangle_{e_5}\langle 0|\otimes|0\rangle_{e_6}\langle 0|)\right\}|m,n\rangle\,. \tag{1.67}$$

Note that since $p_{m,n}(\phi) = p_{n,m}(\phi)$, $\sum_{m,n} p_{m,n}(\phi) = 1$, and $p_{m,n}(\phi) = 0$ for $m+n > 2K$, there are $(N+1)^2$ independent probabilities. From these probabilities, the FI can be calculated according to Equation 1.6.

Consideration of the cases $N = 2$ ($K = 1$) and $N = 4$ ($K = 2$) will demonstrate the benefit of these results, including the identification of regimes within which a quantum advantage in metrology can be unambiguously demonstrated. For HB(2) states, the FI is given by

$$F^{(N=2)}(\xi_{\mathrm{p}},\xi,\xi_{\mathrm{d}},\phi) = \frac{8\xi_{\mathrm{p}}^2\xi_{\mathrm{d}}^2\xi^2(1+\xi^2)\sin^2(2\phi)}{1+\xi^4-2\xi^2\cos(4\phi)}, \tag{1.68}$$

which is maximized for $\phi = \pi/4$, giving

$$F^{(N=2)}(\xi_{\mathrm{p}},\xi,\xi_{\mathrm{d}}) = \frac{8\xi_{\mathrm{p}}^2\xi_{\mathrm{d}}^2\xi^2}{1+\xi^2}. \tag{1.69}$$

To find values of ξ_{p}, ξ, and ξ_{d} for which a device will outperform its classical counterpart, the value $\eth_{N=2}$ can be calculated using Equation 1.30, giving

$$\eth_{N=2} = \frac{4\xi_{\mathrm{p}}^2\xi_{\mathrm{d}}\xi}{1+\xi^2} > 1. \tag{1.70}$$

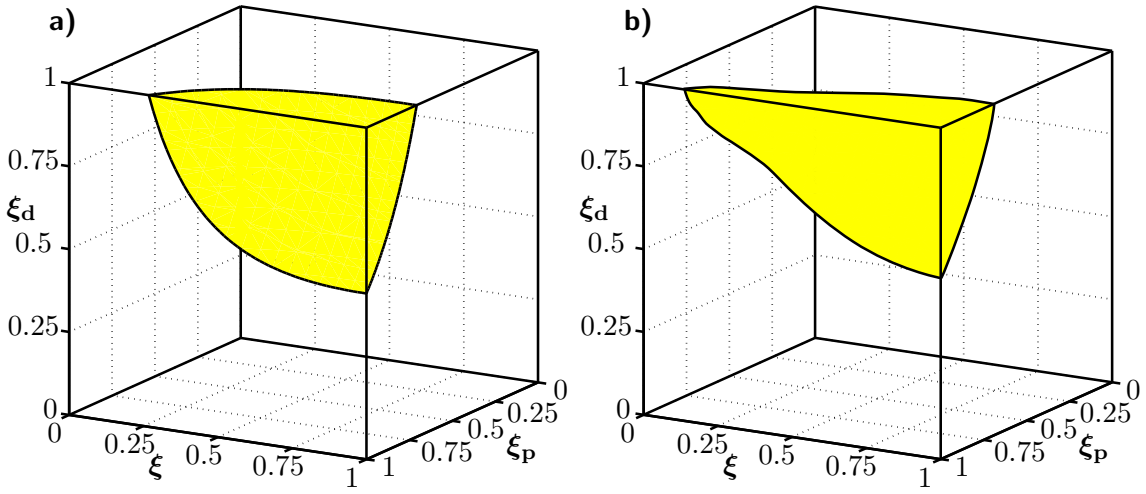

Figure 1.5: Feasibility region for beating the standard quantum limit using a) HB(2) states and b) HB(4) states. The bottleneck in beating the standard quantum limit is the detector imperfection, followed by the preparation imperfection and lastly, losses in the interferometer.

This inequality, the boundary of which is shown in Figure 1.5a, demonstrates exactly the tradeoffs in state preparation, interferometer construction, and detection imperfection when attempting to outperform classical interferometry with HB(2) states. Interestingly, note that if $\xi_d < 0.5$, there is no way to beat the SIL with HB(2) states, thereby rendering moot any discussion about the nature of the source and the interferometer.

For HB(4) states, the FI is significantly more complicated. The question of quantum enhancement is again addressed by $\eth_{N=4} = F^{(N=4)}(\xi_p, \xi, \xi_d)/(4\xi\xi_d)$, where the right hand side is maximized over ϕ. The boundary of the region in which a quantum enhancement can be achieved was calculated numerically and is shown in Figure 1.5b. It was found numerically that $\eth_2(0.687, 1, 1) \approx \eth_2(1, 0.135, 1) \approx \eth_2(1, 1, 0.547) \approx 1$, where the notation $\eth_2(\xi_p, \xi, \xi_d)$ has been used.

In general, higher photon states are more resilient to losses in the interferometer but they also put stricter demands on ξ_p and ξ_d. Thus, with increasing photon numbers, the feasibility region shrinks along the two axes denoting the preparation and detection

imperfections and extends along the axis denoting loss in the interferometer.

To experimentally realize an improvement over its classical counterpart, quantum phase estimation with HB states requires high-quality state preparation and detection in addition to low-loss interferometers. In a realistic experiment with 95% interferometer transmission, and 60% detection efficiency (at the high end for commercially available Silicon avalanche photodiodes), the HB(2) state preparation must be better than $\xi_{\mathrm{p}} \geq 0.91$, which is beyond the current state of the art [78]. Utilizing the highest-efficiency PNRDs available, with detection efficiencies approaching 0.98 [79], relaxes the preparation of the HB(2) state to $\xi_{\mathrm{p}} \geq 0.71$, which has recently been demonstrated [78], however, the necessary elements have not to date been demonstrated in a single experiment.

1.5.4 Beam splitter imperfections

The reflectivities of the two beamsplitters labelled η_1 and η_2 in Figure 1.3b affect the fidelity of the HB state produced and the measurement scheme which is implemented respectively, limiting the FI that can be obtained. Here, the effect of these beamsplitter reflectivities on the precision obtainable in estimating ϕ when there are no losses is considered.

It is helpful to begin by defining the angular momentum operators in the Schwinger

representation as

$$\hat{J}_x = \frac{1}{2}(\hat{a}^\dagger \hat{b} + \hat{a}\hat{b}^\dagger), \tag{1.71}$$

$$\hat{J}_y = \frac{1}{2i}(\hat{a}^\dagger \hat{b} - \hat{a}\hat{b}^\dagger), \tag{1.72}$$

$$\hat{J}_z = \frac{1}{2}(\hat{a}^\dagger \hat{a} - \hat{b}^\dagger \hat{b}), \tag{1.73}$$

$$\hat{J}^2 = \hat{J}_x^2 + \hat{J}_y^2 + \hat{J}_z^2. \tag{1.74}$$

In a basis defined by the mutual eigenbasis of $\hat{J}^2$ and $\hat{J}_z$, the ideal input state $|N\rangle_a |N\rangle_b$ appears as $|N, 0\rangle$. In this picture, the phase operator is[80]

$$\hat{P}(\phi) = e^{i\phi \hat{J}_z}, \tag{1.75}$$

while a beamsplitter is given by

$$\hat{B}(\theta) = e^{-2i\theta \hat{J}_x}, \tag{1.76}$$

where $\cos^2\theta = \eta_1$, the input beamsplitter reflectivity. The effective phase operator is then given by

$$\begin{aligned} \tilde{P}(\phi) &= \hat{B}(\theta)\hat{P}(\phi)\hat{B}(\theta)^\dagger \\ &= e^{i\phi(\cos 2\theta \hat{J}_z - \sin 2\theta \hat{J}_y)}, \end{aligned} \tag{1.77}$$

where the commutation relations of the angular momentum operators have been used.

For a beamsplitter with reflectivity $\eta_1 = 1/2$, $\theta = \pi/4$, and the net effect of the beamsplitter and the phase shift is a rotation about the $-\hat{J}_y$ axis. In general, the axis

of rotation is given by (1.77), and given that the input state points along the z-axis, the radius of rotation shrinks by a factor of $\sin 2\theta = 2\sqrt{\eta_1(1-\eta_1)} \leq 1$, as depicted in Figure 1.6a. The net effect is to suppress the phase picked up by the state $|N\rangle_{\mathrm{a}} |N\rangle_{\mathrm{b}}$. This suppression of the effective phase picked up by the state manifests itself in the QFI so that for the state created by the first beamsplitter, the QFI is given by

$$F_{\mathrm{Q}} = 4N(N+1)\eta_1(1-\eta_1). \tag{1.78}$$

This is consistent with the idea that the best attainable precision is provided by an input beamsplitter with reflectivity $\eta_1 = 1/2$. In that case, as shown in Section 1.4.2, the best precision can be attained, in the lossless case, with a second beamsplitter of reflectivity $\eta_2 = 1/2$ and PNRDs. In every other case, however, there remains the issue of attaining the reduced bound provided by Equation (1.78).

Allowing for a general beamsplitter at the detection end makes the calculation somewhat involved, so only the $|1\rangle_a |1\rangle_b$ case is considered here. Then the classical FI, F, as a function of the input beamsplitter η_1 and output beamsplitter η_2 is shown in Figure 1.6b, assuming that perfect PNRDs are used. As expected, the peak FI is found at $\eta_1 = \eta_2 = 1/2$, corresponding to the ideal case. Any deviation from this point results in a reduction of the FI, however, the dependence is relatively weak with deviations of ± 0.05 in both beamsplitters resulting in a FI of ~ 3.7. It is only when significant imperfections are present so that one of the beamsplitters has a reflectivity of > 0.8 does the CRB finally drop below the SQL of 2.

In the subsequent two chapters, methods for creating and characterizing heralded

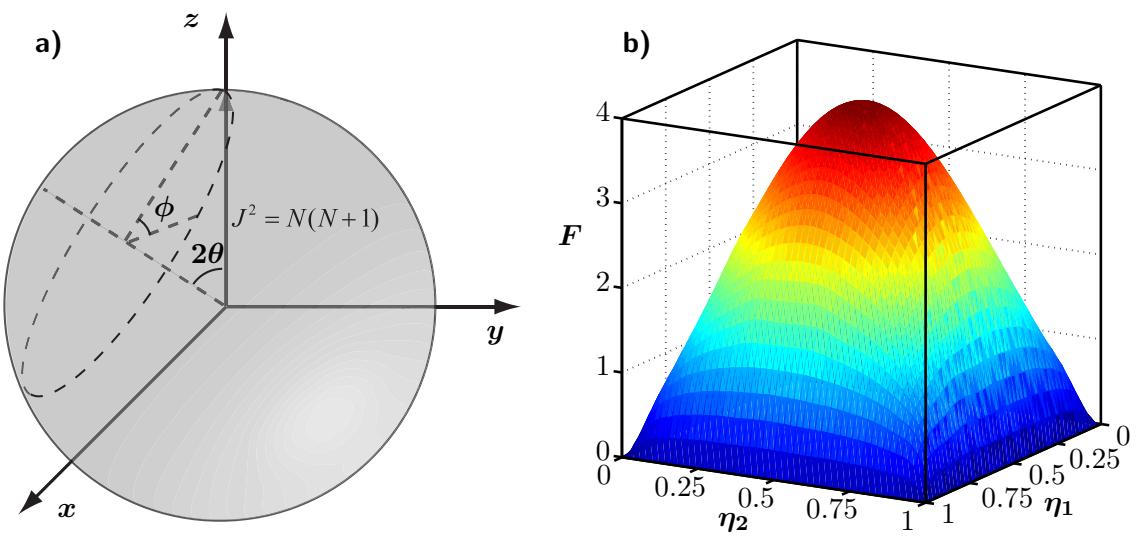

Figure 1.6: a) Depiction of the effect of varying η_1 on the effective phase operator. b) The Fisher information, F, of the state generated by $|1\rangle_a |1\rangle_b$ impinging on a beam splitter of reflectivity η_1 when two photon number resolving detection is made after a beam splitter of reflectivity η_2. For each η_1, η_2 combination, F was maximized over the phase ϕ.

polarization Holland-Burnett states will be demonstrated and an integrated device for preparing and manipulating path-based HB states will be presented. Such a device will be central to developing measurement schemes which show a palpable enhancement over their classical counterparts.

Chapter 2

Heralded Holland-Burnett state generation and characterization

If photonic Holland-Burnett states are to be practically useful, an easy to realise scheme for their generation is required. In this chapter, a scheme will be demonstrated which will ultimately allow high efficiency, heralded generation of arbitrary Holland-Burnett states using feasible and currently available technology. A novel tomographic technique for fully characterizing these heralded states will also be introduced which allows their utility for precision measurement to be objectively assessed.

2.1 A heralded source of Holland-Burnett states

HB states are generated by interfering two K photon Fock states on a beam splitter with $\eta = 1/2$. The problem is therefore reduced to the generation of two indistinguishable K photon Fock states. As discussed in Section 1.4, a critical component of being able to compare a quantum and classical strategy is an accurate enumeration of the resources

consumed. This is equivalent to requiring a signal that a state has been prepared, and an accurate characterization of the prepared state.

The signal that a state has been prepared can take several forms. In the simplest case, it can be given by a photodiode observing pulses being emitted from the laser which pumps the source. This will typically significantly overestimate the number of trials in a metrology scheme since photon sources are frequently probabilistic with the probability of generating one or more photons per pump pulse being $<< 1$. Sources based on PDC, however, can provide a signal which gives a more accurate enumeration of the number of trials undertaken.

The output of a PDC source is a coherent superposition of pairs of photons, so that one pump pulse can produce no pairs, a single pair, two pairs et cetera[59]. If the PDC emits into two perfectly distinguishable modes, orthogonal polarizations for example, then a perfectly efficient photon number resolving detector detecting K photons in one of the modes, *heralds* the presence of K photons in the other mode. There is, however, a complication. In general, the spectra of the two photons are correlated due to conservation of energy and momentum. The implication of this is that when one photon is detected using a non-spectrally selective detector such as the commonly used avalanche photodiode (APD), no spectral information about the herald photon is obtained so the spectral modes of the heralded photon must be traced over, leaving it in a spectrally mixed state. This mixedness degrades the quantum interference necessary to produce HB states using two such heralded sources[56].

The traditional approach to resolving this problem is to apply tight spectral filters to one or both modes emitted by the PDC, however, this can dramatically reduce the effective

pair generation rate and reduce preparation efficiencies which, as discussed in Section 1.5, severely reduces the ability of a quantum scheme to out-perform its classical counterpart. An alternative solution relies on careful control of the phase-matching function in order to remove spectral-temporal correlations between the photon pairs, allowing spectrally pure heralded Fock states to be produced[56,78,81–88]. These schemes have the significant advantage that spectral filtering is not required in order to achieve high visibility quantum interference and hence there is, in principle, no barrier to achieving high efficiency and brightness pure Fock state sources.

The scheme used to generate heralded HB states is shown in Figure 2.1a. In contrast to the description above, this scheme produces polarization-based HB states, however, they behave completely analogously to the path-based equivalent. The state is obtained by combining two orthogonally polarized $K = N/2$-photon Fock states at a polarizing beam splitter. In principle this source, with the use of photon-number-resolving heralding detectors[79,89], generates ideal HB states of arbitrary N. To experimentally examine realistic quantum sensors based on HB states, however, it is instructive to implement the simplest scheme in which increased precision can in principle be shown: a scheme employing HB(2) states.

A mode-locked Ti:Sapphire laser system operating at 80 MHz provides 100 fs duration pulses centred at a wavelength of 830 nm with an average power of 2.38 W (Laser). These pulses were focused using a 7.5 cm lens (L1) into beta barium borate (BBO) for second harmonic generation (SHG) to a wavelength of 415 nm and the output was collimated using a 10 cm lens (L2). Residual infrared radiation was filtered using two dichroic mirrors (LPDMs) and a blue glass filter (BG), resulting in an average UV power of 600 mW. The

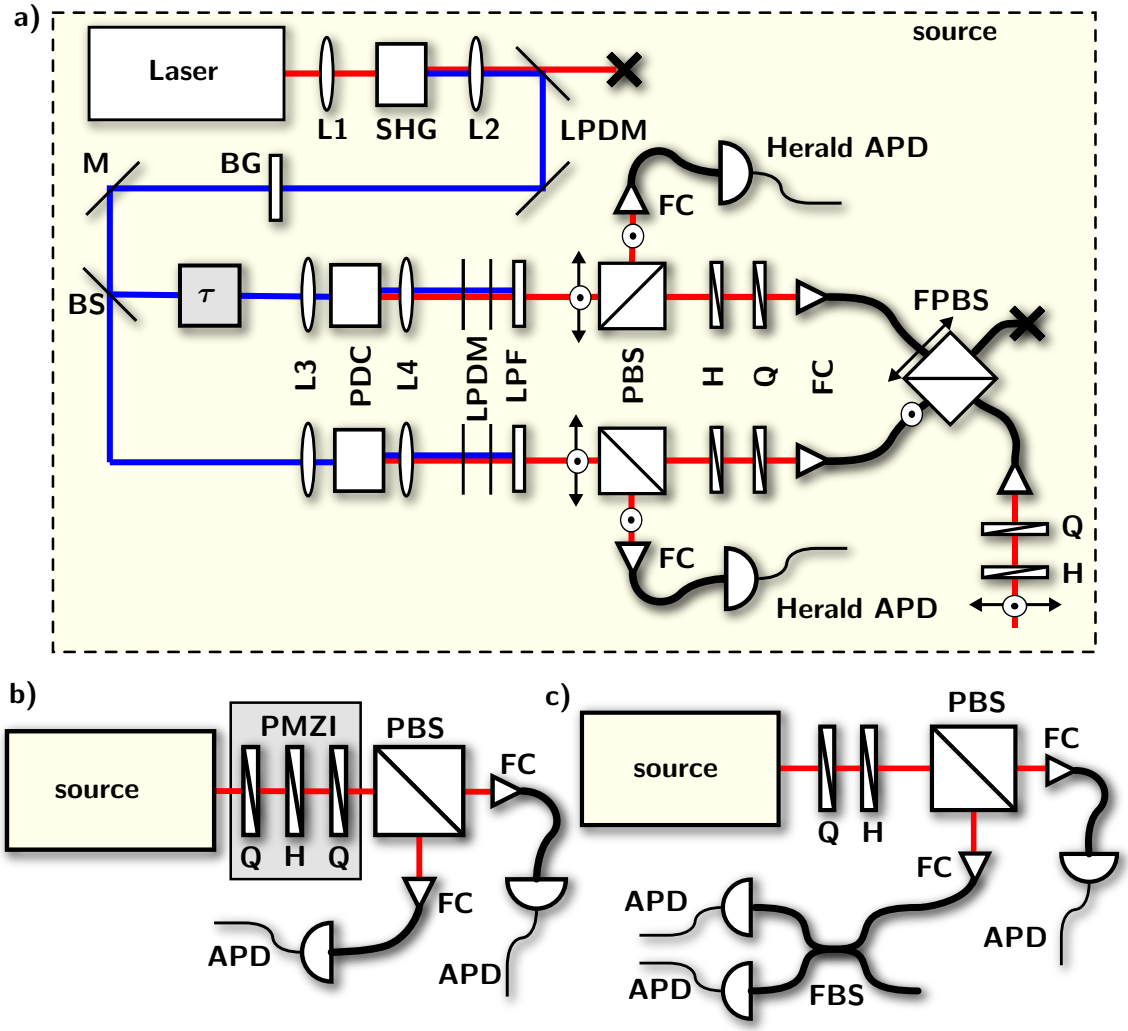

Figure 2.1: Scheme for generating and characterizing heralded HB states. a) State generation based on two parametric downconverters (**PDC**). Half- (**H**) and a quarter-wave plates (**Q**) after each polarizing beam splitter (**PBS**) adjust the polarizations to combine photons at a fibre polarizing beam splitter (**FPBS**). Coincidence detection between heralding avalanche photodiodes (**Herald APD**) signals HB state preparation at the output of the FPBS. b) Applying a phase shift ϕ between $\pm 45°$ polarizations using a quarter-, half-, quarter- wave plate combination. Coincidence detection between the **APDs** implements the optimal measurement for HB(2) state. c) Polarization tomography using a quarter- and half-wave plate followed by a PBS. Outputs are coupled into single-mode fibre (**FC**) with the reflected mode split by a 50:50 fibre beam splitter (**FBS**) for partial number resolution.

UV pulses were then split at a 50:50 beam splitter (BS), with one output mode delayed by an optical delay line (τ). The pulses were then used to concurrently pump two potassium dihydrogen phosphate (KDP) crystals (PDC) which were oriented for type-II collinear parametric downconversion [56]. The input was focused using a 25 cm lens (L3) and the output collimated with a 15 cm lens before undergoing filtering to reject the pump light using two long-pass dichroic mirrors (LPDM) and a long-pass interference filter (LPF). In this configuration, the two cones into which the daughter photons were emitted intersect at a single point in a direction collinear with the pump beam. The photon pairs generated in each KDP crystal were orthogonally polarized and central wavelength degenerate at 830 nm, but had different bandwidths. A polarizing beam splitter (PBS) was used to split the modes and the vertically polarized mode of each source was detected by a fibre-coupled APD (herald APD). This served as the herald signal for a photon being created in a horizontal mode. Single photons were typically heralded with an efficiency of 0.18 in this experimental configuration.

The heralded modes were coupled (FC) into the input fibres of a fibre-coupled polarizing beam splitter (FPBS). In order to combine the two heralded modes into a single spatial mode, each mode was blocked in turn while one of the outputs of the FPBS was minimized by adjusting a quarter-wave plate (QWP) and a half-wave plate (HWP). This both rotated the polarization of one of the heralded modes to be orthogonal to the other and pre-compensated both modes for polarization rotations occurring in the non-polarization maintaining input single-mode fibre (SMF). The mode emitted from the output fibre of the FPBS was collimated before being passed through another QWP/HWP combination to compensate for polarization effects in the FPBS output SMF. These wave

plates were aligned by minimizing the power in the transmitted mode of a polarizing beam splitter (PBS) when the horizontally polarized input mode was unblocked and the vertically polarized input mode was blocked.

Preparation of the HB(2) state was signalled by a coincidence detection event between the two heralding detectors. When a single photon was registered at each herald detector, the state that was in principle heralded (in the absence of loss and with perfect polarization compensation) was $|1,1\rangle_{\mathrm{HV}}$ where $|n,m\rangle_{\mathrm{HV}}$ denotes n (m) horizontally (vertically) polarized photons. Written in the 45° rotated basis, this is equivalent to the HB(2) state $(|2,0\rangle_{\mathrm{DA}} - |0,2\rangle_{\mathrm{DA}})/\sqrt{2}$, where D and A denote the diagonal polarization (D) (+45°) and anti-diagonal polarization (A) (−45°) respectively.

2.2 Interference experiments

As already discussed, quantum enhanced metrology is based, like its classical counterpart, on interference. Here, the polarization interferometry scheme is introduced and its use in observing quantum interference is explained. The indistinguishability of the heralded single photons is then tested by means of Hong-Ou-Mandel interference and finally, post-selected quantum interference fringes which are characteristic of the HB(2) state are presented.

2.2.1 Polarization interferometry

In order to implement a phase shift between the two arms (polarizations) of the interferometer, a sequence of a QWP(0) HWP(θ) QWP(0) was inserted, as shown in Figure 2.1b. QWP(α) and HWP(α) denote a quarter- and half-wave plate aligned with their fast axis

at angle α to the horizontal axis respectively. It is straight forward to see the effect of this wave plate combination by propagating the Jones vectors for horizontal polarization (H) and vertical polarization (V) through it [90]. Beginning with the H mode,

$$\begin{pmatrix} 1 \\ 0 \end{pmatrix} \rightarrow \begin{pmatrix} 1 & 0 \\ 0 & i \end{pmatrix} \begin{pmatrix} \cos 2\theta & \sin 2\theta \\ \sin 2\theta & -\cos 2\theta \end{pmatrix} \begin{pmatrix} 1 & 0 \\ 0 & i \end{pmatrix} \begin{pmatrix} 1 \\ 0 \end{pmatrix}, \tag{2.1}$$

$$= \begin{pmatrix} \cos 2\theta \\ i \sin 2\theta \end{pmatrix}. \tag{2.2}$$

Similarly for the V mode,

$$\begin{pmatrix} 0 \\ 1 \end{pmatrix} \rightarrow \begin{pmatrix} i \sin 2\theta \\ \cos 2\theta \end{pmatrix}. \tag{2.3}$$

It can now be seen that by setting $\theta = 0$, the wave plate combination can be made to do nothing or, by setting $\theta = \pi/8$, H and V can be converted to right circular polarization (R) and left circular polarization (L) respectively. Moreover, by expressing D and A polarizations in terms of H and V by $|D\rangle = (|H\rangle + |V\rangle)/\sqrt{2}$ and $|A\rangle = (|H\rangle - |V\rangle)/\sqrt{2}$, it can be seen that

$$|D\rangle \rightarrow \frac{1}{\sqrt{2}} \begin{pmatrix} \cos 2\theta + i \sin 2\theta \\ \cos 2\theta + i \sin 2\theta \end{pmatrix} = e^{i2\theta} |D\rangle, \tag{2.4}$$

$$|A\rangle \rightarrow \frac{1}{\sqrt{2}} \begin{pmatrix} \cos 2\theta - i \sin 2\theta \\ -(\cos 2\theta - i \sin 2\theta) \end{pmatrix} = e^{-i2\theta} |A\rangle. \tag{2.5}$$

A relative phase shift between the D and A modes of $\phi = 4\theta$ can therefore be introduced by rotating the HWP.

To align the wave plates, the following procedure was followed. First, the two QWPs were inserted and only the H input was unblocked. Then, transmission through the PBS was minimized by alternately adjusting first one, then the other QWP. This resulted in the QWPs being aligned such that their fast axes were parallel to each other and at 45° to the horizontal. With the QWPs in this position, H was rotated to V which was then completely reflected at the PBS. The QWPs were then rotated by 45° in the same direction so that their optical axes lay either along the horizontal or vertical. In this configuration no rotation occurs at either wave plate. Finally, the HWP was inserted between the QWPs and again the transmission through the PBS was minimized. This occurred when the HWP fast axis was at 45° to the horizontal so that $\mathrm{H} \rightarrow \mathrm{H} \rightarrow \mathrm{V} \rightarrow \mathrm{V}$ at each of the wave plates. From this configuration, rotating the HWP introduces a phase between the A and D modes which comprise the HB state. The state was then analysed in the $\{\mathrm{H}, \mathrm{V}\}$ basis by the PBS and the outputs of the PBS coupled into SMF connected to two APDs.

2.2.2 Quality control by Hong-Ou-Mandel interference

The effect of distinguishability and mixedness in the heralded Fock states used to generate the HB state is to degrade the quantum interference that is critical for its creation. Distinguishability may enter in the spatial, spectral, temporal or polarization degrees of freedom. Although it is difficult to separate the effects of distinguishability and mixedness, a lower bound on the average purity of two heralded single-photon sources can be set by observing the visibility of the Hong-Ou-Mandel (HOM) interference [91] between them [56]. Since this inherently quantum interference effect is critical to many quantum-enhanced

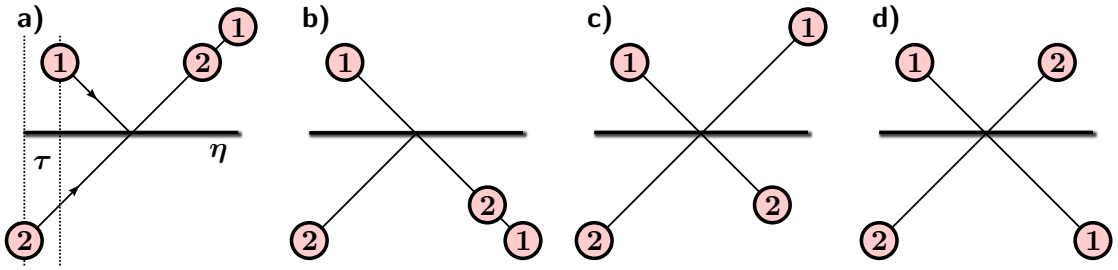

Figure 2.2: The four possible outcomes when two photons impinge upon a beam splitter of reflectivity $\boldsymbol{\eta}$ with a relative arrival time of $\boldsymbol{\tau}$. The photons are indistinguishable apart from their relative arrival time and the labels **1** and **2** are only to indicate the path of each photon. a) Photon **1** is reflected and photon **2** is transmitted. b) Photon **1** is transmitted and photon **2** is reflected. c) Both photons are reflected. d) Both photons are transmitted.

metrology schemes as well as quantum information processing with linear optics, a brief overview is useful.

Figure 2.2 shows the four possible outcomes when two photons impinge on a beam splitter of reflectivity η from either side with a relative arrival time of τ. If the photons are indistinguishable in spatial mode, spectra, arrival times, and polarization, then outcomes c and d occur with the same amplitude but a π phase difference due to the phase obtained by one mode upon reflection at the beam splitter. Their amplitudes therefore interfere destructively leaving only outcomes a and b. If the photons are completely distinguishable, as a result of a large time delay, τ, for example, then this destructive interference will not occur and outcomes c and d will persist. Consider the two spatial modes shown in Figure 2.2 with creation operators $\hat{\mathrm{a}}_0^\dagger$ and $\hat{\mathrm{b}}_\tau^\dagger$, where the subscript indicates the relative temporal mode. Then, continuing the convention of a π phase shift occurring upon reflection of the bottom mode, after propagation through the beam splitter, these creation operators become $\sqrt{\eta}\hat{\mathrm{a}}_0^\dagger + \sqrt{1-\eta}\hat{\mathrm{b}}_0^\dagger$ and $\sqrt{1-\eta}\hat{\mathrm{a}}_\tau^\dagger - \sqrt{\eta}\hat{\mathrm{b}}_\tau^\dagger$ respectively. Hence the input

state $\hat{a}_0^\dagger \hat{b}_\tau^\dagger |\text{vac}\rangle$ evolves as

$$\hat{a}_0^\dagger \hat{b}_\tau^\dagger |\text{vac}\rangle \rightarrow (\sqrt{\eta}\hat{a}_0^\dagger + \sqrt{1-\eta}\hat{b}_0^\dagger)(\sqrt{1-\eta}\hat{a}_\tau^\dagger - \sqrt{\eta}\hat{b}_\tau^\dagger) |\text{vac}\rangle \quad (2.6)$$

$$= [\sqrt{\eta(1-\eta)}(\hat{a}_0^\dagger \hat{a}_\tau^\dagger - \hat{b}_0^\dagger \hat{b}_\tau^\dagger) - \eta \hat{a}_0^\dagger \hat{b}_\tau^\dagger - (1-\eta)\hat{a}_\tau^\dagger \hat{b}_0^\dagger] |\text{vac}\rangle , \quad (2.7)$$

where the four terms in the output state are the four outcomes shown in Figure 2.2. From this it can be seen that if $\eta = 1/2$ and $\tau = 0$, then $\hat{a}_0^\dagger \hat{b}_\tau^\dagger = \hat{a}_\tau^\dagger \hat{b}_0^\dagger$ with equal amplitude and opposite sign such that they cancel. Hence, if detection events of one click in mode a and one click in mode b are monitored while the time delay, τ, between the modes is scanned through 0, the rate of these events should, in the ideal case, drop to zero at $\tau = 0$ so that the visibility of this interference is 1. This is the Hong-Ou-Mandel interference effect. In contrast, the classical limit to the visibility of this interference is 50% [92]. This occurs when two phase-averaged coherent states of equal amplitude are interfered as above.

In order to obtain this interference for the two polarization modes discussed in Section 2.1, the HWP must be rotated to 22.5°. In this configuration, H evolves to R and V evolves to L as H → H → D → R and V → V → A → L respectively. Although the first QWP doesn't effect any change to the polarization, it is a necessary part of the second part of the experiment in which full interference fringes are measured. Leaving it in place during the observation of HOM ensures that the experiment is well aligned and the components are not introducing any distinguishability. It can now be seen that since

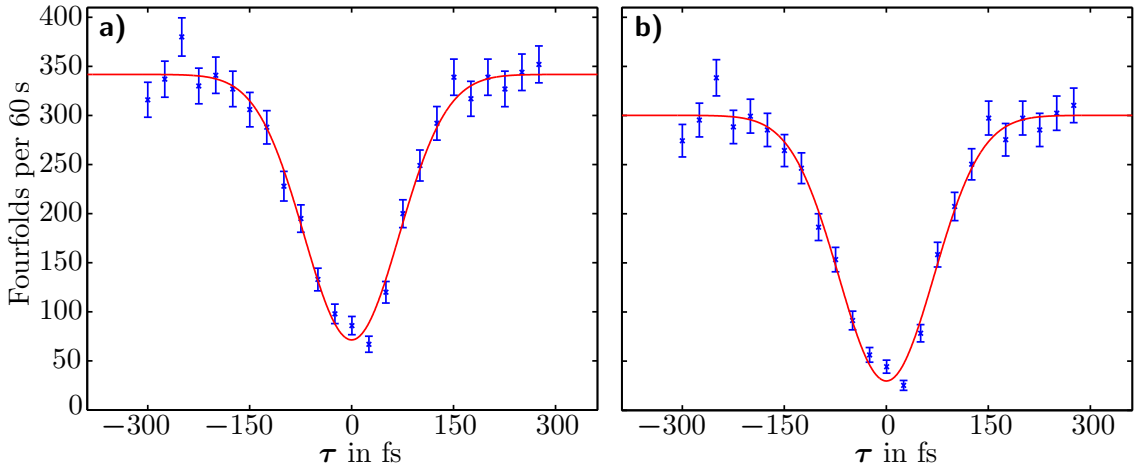

Figure 2.3: Coincidence counts between the two output ports of a polarizing beam splitter when the relative arrival time (τ) of two heralded single photons in R and L modes impinging upon it at one input port is scanned. a) Raw. b) With higher photon number contributions removed. The error bars in each plot are theoretical and derived from Poissonian counting statistics.

$|11\rangle_{\mathrm{RL}}$ can be written as

$$|11\rangle_{\mathrm{RL}} = \frac{1}{2}(\hat{a}^\dagger + i\hat{b}^\dagger)(\hat{a}^\dagger - i\hat{b}^\dagger)\,|\mathrm{vac}\rangle\,, \tag{2.8}$$

$$= \frac{1}{2}(\hat{a}^\dagger\hat{a}^\dagger + \hat{b}^\dagger\hat{b}^\dagger)\,|\mathrm{vac}\rangle\,, \tag{2.9}$$

$$= \frac{1}{\sqrt{2}}(|20\rangle_{\mathrm{HV}} + |02\rangle_{\mathrm{HV}}), \tag{2.10}$$

where $\hat{a}^\dagger$ and $\hat{b}^\dagger$ are now creation operators for photons in H and V respectively, analysing the state in the $\{\mathrm{H}, \mathrm{V}\}$ basis reveals the desired HOM interference.

The quality of the heralded single photon Fock states produced by the source shown in Figure 2.1 was tested by observing the coincidence counts in 60s as the relative arrival time of the UV pump pulses was scanned through zero delay. Coincidence counting was performed by field-programmable gate array (FPGA) electronics using a coincidence window of 3 ns.

Figure 2.3a shows the raw measured counts with the theoretical fit which gives a

visibility of $80 \pm 3\%$. A PDC does not just produce a single pair of photons, however, and so the coincidence signal is contaminated by those events where either PDC produces two or more pairs. The relative probability of these events is small but their effect is amplified by inefficiencies in the system [93,94]. Since the average purity of the heralded single photons is the only parameter of interest, the number of these higher order contributions occurring during each 60s sample can be estimated and subtracted. This is achieved by blocking the heralded photon from one PDC while leaving the herald unblocked. A four-fold event can then only occur when the partially blocked PDC produces one or more pairs and the fully unblocked PDC produces two or more pairs. By swapping the partial block to the other PDC and summing the two measured four-fold counts in 300 s, the total higher photon contribution in 60s can be estimated and subtracted from the measurement.

Figure 2.3b shows the background subtracted measurement. The theoretical fit gives a visibility of $90 \pm 3\%$, setting a lower bound on the average heralded photon purity and distinguishability, and an upper bound for the multi-photon fringe visibility achievable in a full HB state experiment. The residual impurity is partly intrinsic [56] and partly due to imperfect compensation of the optical fibre birefringence.

2.2.3 Post selected quantum interference

Positioning the time delay between the UV pump pulses to be at the minimum of the measured HOM interference ensured that the heralded single photons were maximally indistinguishable. At this delay, which ideally would result in complete indistinguishability, the heralded HB(2) state is generated in the $\{\mathrm{D}, \mathrm{A}\}$ basis, as discussed in Section 2.1. After generation, the heralded HB states were launched into the sequence of three wave plates

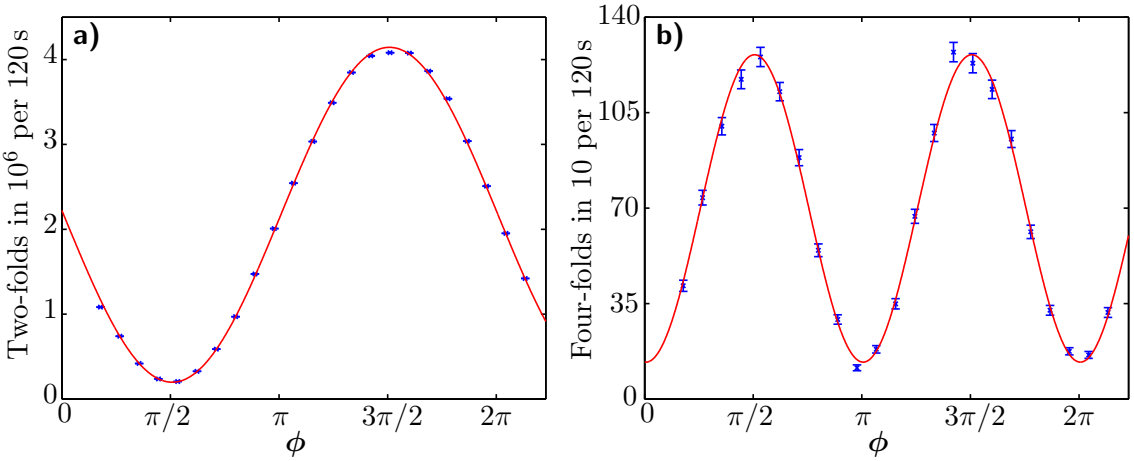

Figure 2.4: Post-selected quantum interference of photonic states by scanning the relative phase between D and A modes in the interferometer. a) Single-photon (classical) interference. b) Two-photon (HB state) interference. Error bars are derived from Poissonian statistics and contributions from multiple PDC pair emissions are removed.

described in Section 2.2.1 in order to introduce a relative phase between the D and A modes, dependent on the angle of the HWP, before being analysed in the $\{\mathrm{H}, \mathrm{V}\}$ basis.

Figure 2.4a shows the detection count-rate phase-dependence for heralded single-photon states with a theoretical fit showing a visibility of $90.9 \pm 0.5\%$. The remaining visibility is a result of imperfect polarization compensation for the effects of the output FPBS SMF. Figure 2.4b shows the detection count-rate phase dependence for the heralded HB(2) states. The theoretical fit shows a visibility of $80.6 \pm 1.5\%$ ($76.4 \pm 1.4\%$ raw) which is consistent with the bound on the state purity set by the visibility of the HOM interference.

It is important to note that the HB state interference observed is, in part, post-selected. Only events which consist of both a herald signal, given by a coincidence between the two herald detectors, and detection of two photons at the output of the polarization interferometer are recorded. The herald signal does not guarantee that the HB(2) state will be detected at the output of the interferometer. Instead, either one-click or zero-click detection events may occur at the output. In general, these lower click detection events

may contain information about the phase. Hence, their contribution to the heralded state must be characterized in order to assess its utility for quantum-enhanced metrology. The following section presents a scheme for tomographically reconstructing a state including these lower photon number components.

2.3 State characterization

In general, a state tomography experiment can be described by a set of M_α detection apparatus settings, labelled here with α, each of which has associated with it a set of M_γ outcomes, labelled here with γ, so that $M_\alpha M_\gamma$ measurements are made. In photonic experiments, the outcomes are usually a particular combination of physical detectors firing simultaneously ("in coincidence"). The measurements implemented are modelled by a set of positive operator value measure (POVM) elements $\{\hat{\Pi}_\gamma\}_\alpha$. In this scheme, the outcomes for each setting are complete so that for every α,

$$\sum_\gamma \hat{\Pi}_\gamma = \mathbb{1}. \tag{2.11}$$

The settings must be chosen so that the POVM elements span the space of states, allowing reconstruction of any state in the space. In general there are optimal ways to choose both the settings and the amount of time spent measuring at each setting, which is sometimes referred to as optimal experiment design [95–98].

Once the settings have been chosen, the measurements are performed, usually with a fixed time spent at each α. In this time, the number of events corresponding to each outcome γ are recorded, giving a set of counts $\{m_\gamma\}_\alpha$. The probability that any state, ρ,

could produce the observed counts is then given by the likelihood function,

$$\mathcal{L} = p(\{m_{\alpha\gamma}\}|\rho), \tag{2.12}$$

where $\{m_{\alpha\gamma}\}$ denotes the set of all measured counts at all settings. We discuss here the most common state reconstruction technique, maximum likelihood estimation, where the estimated ρ is determined by maximizing the value of the likelihood function [99,100].

The exact form of $\mathcal{L}$ is dependent upon the system generating the state. With heralded state generation, the number of times that the state has been prepared for each setting, m_α, is known so that for each herald signal a result is collected. The number of heralds limits the values of m_γ so that $\mathcal{L}$ is most appropriately described by a multinomial distribution,

$$\mathcal{L} = \prod_{\alpha\gamma} C_\alpha(\{m_\gamma\}_\alpha) p_{\alpha\gamma}^{m_{\alpha\gamma}}, \tag{2.13}$$

where C_α is a multinomial factor which accounts for the number of ways the observed m_γ could have occurred for each setting and $p_{\alpha\gamma} = tr(\rho\hat{\Pi}_{\alpha\gamma})$. Since m_α is known for each setting, only $M_\gamma - 1$ measurement results, are independent variables in the maximum likelihood optimization. This can be expressed as the constraint equation

$$\sum_\gamma m_{\alpha\gamma} = m_\alpha. \tag{2.14}$$

The maximization can then be performed directly using an iterative technique [100].

If m_α is large and $p_{\alpha\gamma}$ is small, the multinomial form can be approximated by a product

of $M_\alpha(M_\gamma - 1)$ Gaussian distributed variables,

$$\mathcal{L} = \prod_{\alpha\gamma} \frac{1}{\sqrt{2\pi\sigma_{\alpha\gamma}^2}} \exp\{-\frac{(m_{\alpha\gamma} - m_\alpha p_{\alpha\gamma})^2}{2\sigma_{\alpha\gamma}^2}\}, \tag{2.15}$$

where $\sigma_{\alpha\gamma} = m_\alpha p_{\alpha\gamma}(1-p_{\alpha\gamma}) \approx m_\alpha p_{\alpha\gamma}$ for small $p_{\alpha\gamma}$. Current devices typically exhibit high loss, so that the vacuum component of any heralded state will contain a large population. While this might be expected to invalidate the assumption of small $p_{\alpha\gamma}$, the choice of which outcome probability is the "dependent variable" for each measurement setting is still free. Using the corresponding constraint equation, the vacuum term can be eliminated, leaving only the lower probability terms which still satisfy the small p approximation. Expressing the likelihood function in this form ultimately allows one to express the problem in a weighted least-squares form which can be converted into a semi-definite program so that the well developed tools of convex optimization can be employed [101,102].

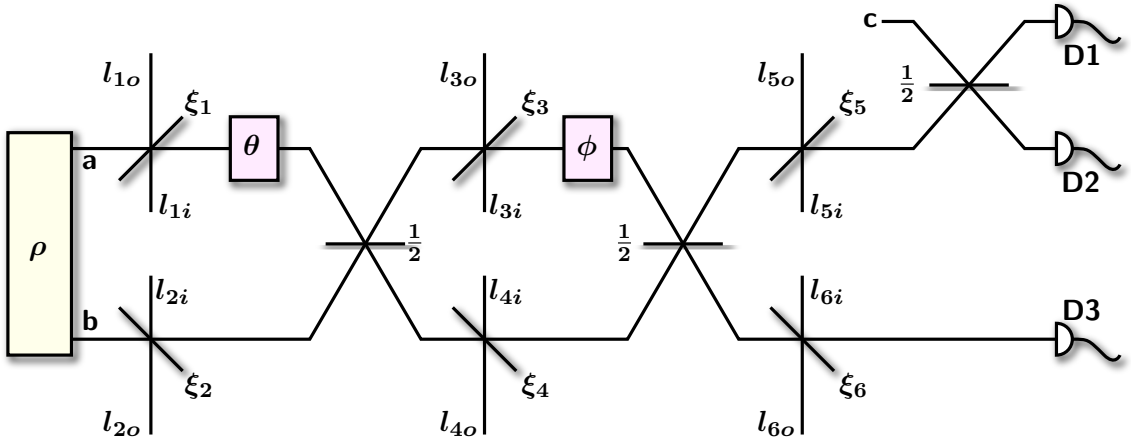

Figure 2.5: A typical scheme used to perform state tomography on $\boldsymbol{\rho}$. $\boldsymbol{\rho}$ is assumed to be a single polarization photonic state in two spatial modes. A MZI and two phase shifters allow a tomographically complete set of measurements to be made. Detection is performed by avalanche photodiodes (**D1**-**D3**). The spatial modes which lead to detectors are labelled **a**, **b**, and **c** while loss modes are labelled $\boldsymbol{l_{1i}}$-$\boldsymbol{l_{6i}}$ and $\boldsymbol{l_{1o}}$-$\boldsymbol{l_{6o}}$.

A necessary part of this optimization is knowledge of the POVM elements which model

the particular outcomes observed. Since all photon number subspaces must be reconstructed, measurements are needed which access each of them. In the case of a perfectly efficient, perfectly photon number resolving device, it can be precisely known which photon number subspace is being projected onto. In the presence of any loss, however, even photon number resolving detectors project onto multiple photon number subspaces since registering a single photon could be due to, for example, two photons where one is lost. The exact value of the loss in the measurement device specifies the mixture of photon number subspaces being projected onto and hence must be known if a state is to be accurately reconstructed.

As an example, the device shown in figure 2.5 will be considered. This device provides tomographic measurements suitable for characterizing the HB(2) state. The detectors used are perfect APDs which have a POVM set of $\{|0\rangle\langle 0|, \mathbb{1} - |0\rangle\langle 0|\}$ meaning that they either don't fire and therefore project onto the vacuum, or they fire in which case at least one photon was present but it is not known how many. This device is insensitive to coherences between components in different photon number subspaces. Fortunately, however, these coherences cannot affect the measurement statistics in our system, or indeed in any system comprised of imperfect state preparation, lossy linear optical interactions, and inefficient detection. This is true because all linear optical components conserve photon number by definition (i.e. they operate only within each photon number subspace), loss is always incoherent, and photon counting detectors project onto incoherent mixtures of components from within these different subspaces. A state reconstructed in this way therefore provides sufficient information to predict all measurement outcomes of any subsequent system acting on that state using linear optical interactions and photon counting measurement.

For the system in figure 2.5, there are five possible outcomes: no clicks; a click at either

of detector 1 (D1) or detector 2 (D2); a click at detector 3 (D3); a click at D1 and D2; a click at D1 and D3 or D2 and D3. These are labelled $\hat{\Pi}_{\gamma}^{(\mathrm{out})}$ where $\gamma = 1$ to 5. Losses in the system are modelled by beam splitters with transmissivities ξ_1 to ξ_6. Detector inefficiencies are incorporated into the losses directly before the detectors (ξ_5 and ξ_6)[103]. The modes leading to detectors are labelled a, b, and c while the loss modes are labelled l_{1o} to l_{6o} for the "outer" modes and l_{1i} to l_{6i} for the "inner" modes. Typically, the projectors for the detectors are back propagated and expressed in terms of projectors at the input of the measurement device and the ξ_i are set to 1. If losses are considered, however, one must back propagate both the click projectors for the APDs and identity projectors for each of the outer loss modes since they are not monitored. The output POVM set is given by the projectors

$$\hat{\Pi}_1^{(\mathrm{out})} = \mathbb{1}_{l_{1o}} \otimes ... \otimes \mathbb{1}_{l_{6o}} \otimes |0\rangle_{\mathrm{a}}\langle 0| \otimes |0\rangle_{\mathrm{b}}\langle 0| \otimes |0\rangle_{\mathrm{c}}\langle 0|\,, \tag{2.16}$$

$$\hat{\Pi}_2^{(\mathrm{out})} = \mathbb{1}_{l_{1o}} \otimes ... \otimes \mathbb{1}_{l_{6o}} \otimes [(\mathbb{1} - |0\rangle_{\mathrm{a}}\langle 0|) \otimes |0\rangle_{\mathrm{b}}\langle 0| + |0\rangle_{\mathrm{a}}\langle 0| \otimes (\mathbb{1} - |0\rangle_{\mathrm{b}}\langle 0|)] \otimes |0\rangle_{\mathrm{c}}\langle 0|\,, \tag{2.17}$$

$$\hat{\Pi}_3^{(\mathrm{out})} = \mathbb{1}_{l_{1o}} \otimes ... \otimes \mathbb{1}_{l_{6o}} \otimes |0\rangle_{\mathrm{a}}\langle 0| \otimes |0\rangle_{\mathrm{b}}\langle 0| \otimes (\mathbb{1} - |0\rangle_{\mathrm{c}}\langle 0|)\,, \tag{2.18}$$

$$\hat{\Pi}_4^{(\mathrm{out})} = \mathbb{1}_{l_{1o}} \otimes ... \otimes \mathbb{1}_{l_{6o}} \otimes (\mathbb{1} - |0\rangle_{\mathrm{a}}\langle 0|) \otimes (\mathbb{1} - |0\rangle_{\mathrm{b}}\langle 0|) \otimes |0\rangle_{\mathrm{c}}\langle 0|\,, \tag{2.19}$$

$$\hat{\Pi}_5^{(\mathrm{out})} = \mathbb{1}_{l_{1o}} \otimes ... \otimes \mathbb{1}_{l_{6o}} \otimes [(\mathbb{1} - |0\rangle_{\mathrm{a}}\langle 0|) \otimes |0\rangle_{\mathrm{b}}\langle 0| + |0\rangle_{\mathrm{a}}\langle 0| \otimes (\mathbb{1} - |0\rangle_{\mathrm{b}}\langle 0|)] \otimes (\mathbb{1} - |0\rangle_{\mathrm{c}}\langle 0|)\,. \tag{2.20}$$

By expanding the photon-number modes as $|n\rangle\langle n| = (1/n!)a^{\dagger n}\,|0\rangle\langle 0|\,a^n$, these ideal POVM elements can then be propagated backwards through the lossy circuit to determine the complete POVM elements for the overall measurement apparatus, represented by $\hat{\Pi}_{\alpha\gamma}^{(\mathrm{in})}$. The back-propagated projectors, however, can be dramatically simplified using *a priori*

knowledge of the system. In the situation considered in Section 2.1, this amounts to knowledge that the input loss modes l_{1i} to l_{6i} contain only the vacuum, and that the state ρ contains no more than two photons. The back-propagated projectors can therefore be *conditioned* using this information, which can be summarised by the following projector:

$$\hat{P} = (|0\rangle_{\mathrm{b}}\langle 0| + |1\rangle_{\mathrm{b}}\langle 1| + |2\rangle_{\mathrm{b}}\langle 2|) \otimes (|0\rangle_{\mathrm{c}}\langle 0| + |1\rangle_{\mathrm{c}}\langle 1| + |2\rangle_{\mathrm{c}}\langle 2|) \otimes |0\rangle\langle 0|_{l1i} \otimes ... \otimes |0\rangle\langle 0|_{l6i}\,. \quad (2.21)$$

This allows the final measurement POVM elements to be calculated according to:

$$\hat{\Pi}_{\alpha\gamma} = \hat{P}\hat{\Pi}^{(\mathrm{in})}_{\alpha\gamma}\hat{P}. \quad (2.22)$$

When the transmissivities ξ_1 to ξ_4 are pair-wise symmetric so that $\xi_1 = \xi_2$ and $\xi_3 = \xi_4$, the situation is further simplified. This is because the total population in the loss modes is not a function of the phases θ, ϕ since every possible path to the detectors experiences the same loss regardless of the phase settings. This approximation corresponds to the situation considered here where loss does not typically depend on the polarization mode occupied.

2.3.1 Tomographic reconstruction

For the source shown in Figure 2.1a, the heralded state populates two polarization modes in a single transverse spatial mode. To perform state tomography on a state of this form, either the two polarization modes must be deterministically separated and matched using a PBS followed by appropriate wave plates, in which case the measurement device shown in Figure 2.5 can be used, or the device shown in Figure 2.1c can be employed. In this

device, a HWP is followed by a QWP, the angles of which determine the measurement implemented. The wave plate combination is followed by a PBS with the transmitted mode coupled into a SMF-coupled APD and the reflected mode coupled into a single-mode fibre beam splitter (50:50) with outputs connected to fibre-coupled APDs.

The wave plate settings used to analyse the state were, $\{\theta, \phi\}$, were $\{0°, 0°\}$, $\{0°, 11.25°\}$, $\{0°, 22.5°\}$, $\{0°, 45°\}$, $\{22.5°, 0°\}$, $\{22.5°, 22.5°\}$, $\{22.5°, 45°\}$, and $\{45°, 22.5°\}$, where θ and ϕ are the angles of the QWP and HWP respectively. These measurements form an over-complete set on the whole space. Again, the measurement outcomes, including two-, one-, and zero- click events, were recorded conditionally on observing a herald event consisting of a coincidence between the two herald detectors in Figure 2.1. Although these measurements are sufficient to estimate the effect of entanglement of the photons with hidden or experimentally inaccessible degrees of freedom such as multiple spectral modes[104,105], the situation considered here is one with a single spectral mode. This allows for comparison with previous work on super-resolution and super-sensitivity as well as straightforward estimation of f in Equation 1.54 which is essential for determining whether the sensor has out-performed its classical counterpart.

Figure 2.6a shows the reconstructed density matrix of the heralded state, obtained by maximum likelihood estimation[106] using the measurement outcomes. The heralded state has populations of 0.686, 0.277, and 0.037 in the zero-, one-, and two-photon subspaces giving an average photon number of 0.35. This state has an overlap of 0.031 with the ideal 2-photon HB state,

$$\rho_{\mathrm{HB}(2)} = \frac{1}{2}(|2,0\rangle_{\mathrm{DA}} - |0,2\rangle_{\mathrm{DA}})(\langle 2,0|_{\mathrm{DA}} - \langle 0,2|_{\mathrm{DA}}), \tag{2.23}$$

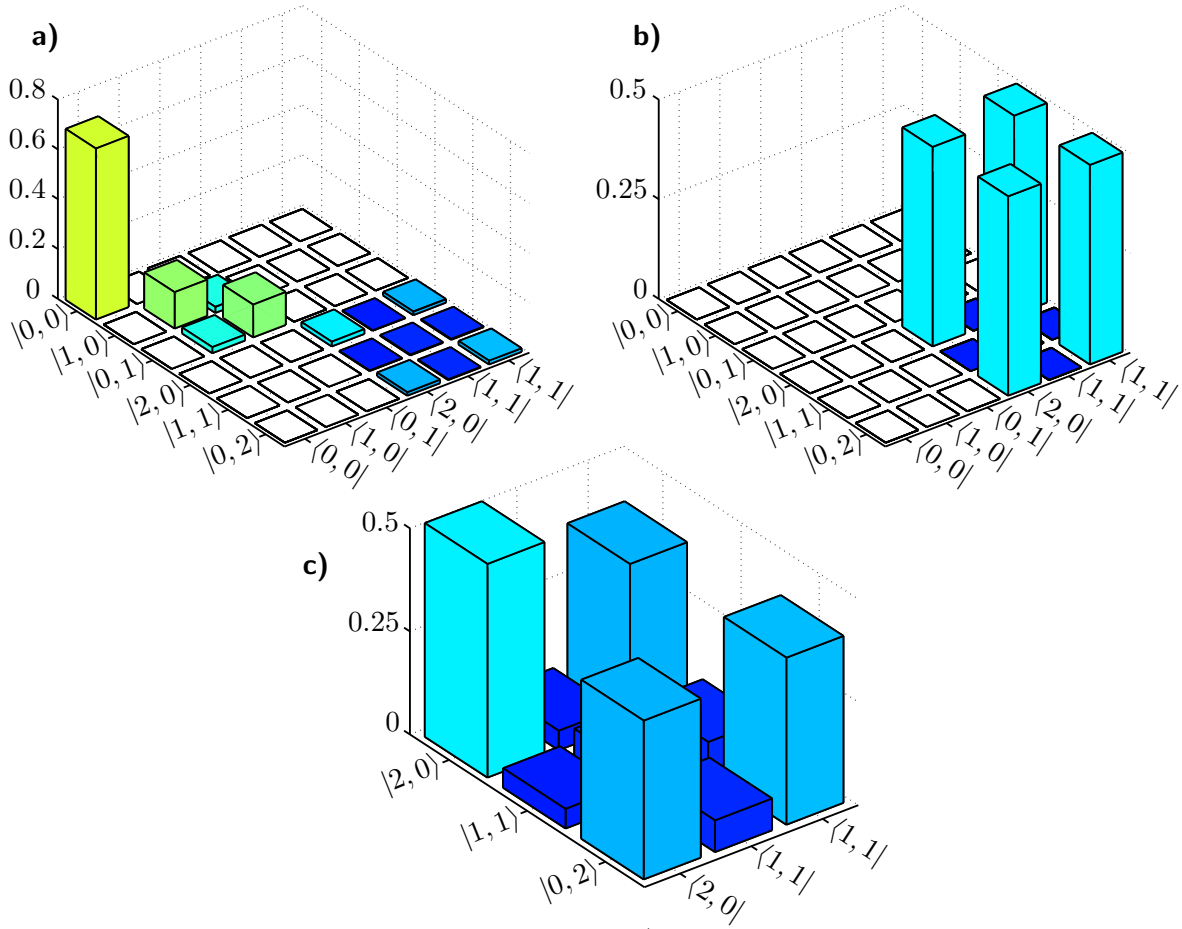

Figure 2.6: Reconstructed heralded quantum state. a) The absolute value of the density matrix including vacuum, one-, and two-photon subspaces. b) The ideal HB(2) state including lower photon number subspaces. c) An enlargement of the two-photon subspace where the scale has been re-normalized assuming that only the two-photon subspace is populated. $|m,n\rangle$ denotes m diagonally polarized photons and n anti-diagonally polarized photons.

shown in Figure 2.6b, while the re-normalized two photon subspace, shown in Figure 2.6c has an overlap of 0.85. The latter of these overlaps is consistent with the visibility of the HOM interference measured in Section 2.2.2.

The difference between the density matrix obtained in this way and that which would have been obtained in post-selection is clear. The state reconstructed under post-selection would have an apparent average photon number of 2 as only those events where two photons are detected are considered. In reality, even with this state of the art heralded source, the average number of photons in the heralded state is nearly 6 times smaller as a result of inefficiencies in state preparation, ξ_{p}, resulting in less than 4% of the state being in the 2-photon subspace.

2.3.2 Evaluating the state for precision measurement

With the heralded state completely characterized, its use for precision measurement tasks can now be evaluated. For $N = 2$, HB and $N00N$ states are equivalent and Equation 1.55 can be applied. Using post-selection, only data resulting in 2-fold outcomes are recorded, ξ, ξ_{d} and f are set to 1, and $N = 2$, yielding a threshold visibility $V_{\mathrm{th}} = 1/\sqrt{2}$. The measured fringe visibility significantly exceeds this bound and so by this analysis super-sensitivity is achieved, beating the SQL. If the post-selected two-photon subspace is re-normalized and $\xi_{\mathrm{g}} = 0.85$ is used while still neglecting ξ and ξ_{d}, a threshold of $V_{\mathrm{th}} = 0.77$ is obtained. The measured fringe visibility also exceeds this threshold, again demonstrating super-sensitivity and beating the SQL. Since the whole state including lower photon number subspaces is known, however, the correct ξ_{g}, given by the overlap of the reconstructed state with the HB(2) state, can be calculated as $\xi_{\mathrm{h}} = 0.031$. Applying the bound

in[60] leads to $V_{\text{th}} = 4.02$, which is unphysical. So, by this analysis, the SQL cannot be beaten.

The above thresholds are based on post-selection and re-normalization or neglect both channel transmissivity and detector efficiencies, significantly underestimating the resources required to reach a given precision. Heralding a characterized state affords a complete reckoning of the resources used by counting all states put into the interferometer. f and ξ can then be estimated experimentally, allowing V_{th} to be calculated according to Equation 1.55. f is determined from the ratio of four-fold coincidences to heralding events, giving $f = 0.0047 \pm 0.0001$ and $\xi\xi_{\text{d}} = \sqrt{f/\xi_{\text{g}}} = 0.39$. For our detector $\xi_d = 0.45$, giving $\xi = 0.87$, resulting in $V_{\text{th}} = \sqrt{\xi/Nf} = 9.57$. This is an even higher threshold on visibility, showing that the SIL cannot be beaten.

The analyses above are based on the FI and are valid only for states where a single measurement outcome is observed, such as with N00N states. However, since the full density matrix has been reconstructed, the analysis outlined in Section 1.4.1 can be applied. The QFI is given by[54]

$$F_Q = 2\sum_{k,l} \frac{(p_k - p_l)^2}{p_k + p_l} |\langle\psi_k|\hat{n}|\psi_l\rangle|^2, \tag{2.24}$$

where $\hat{n}$ is the photon number operator in the sensor arm of the interferometer, and $\{p_k\}$ and $\{|\psi_k\rangle\}$ are the eigenvalues and corresponding eigenvectors of the reconstructed density matrix. For the reconstructed state, $F_Q = 0.079$, giving a QCRB $\Delta\phi \geq 3.56/\sqrt{\nu}$. For a classical state with the same average photon number as the reconstructed state, $\Delta\phi_{\text{SIL}} = 1.81/\sqrt{\nu}$, showing again that, despite the implications of the post selected and

re-normalized analyses, the classical limits to precision can never be surpassed with this state and arbitrary measurements.

Going beyond the classical performance limit with realistic quantum sensors requires stringent bounds on throughput, probe-state preparation and detection efficiencies. For heralded $N00N$ states, $f = \xi_{\mathrm{h}}(\xi\xi_{\mathrm{d}})^N$ must satisfy $f \geq \xi/NV^2$. For the ideal two-photon situation ($V = 1$) this implies $\xi_{\mathrm{h}}\xi\xi_{\mathrm{d}}^2 \geq 1/2$. This benchmark for heralded two-photon states provides a challenging goal which must be achieved in order to surpass the classical limit. Even for perfect detectors ($\xi_{\mathrm{d}} = 1$), this would require $\xi_{\mathrm{h}}\xi \geq 1/2$. Conversely, perfect preparation and transmission ($\xi_{\mathrm{h}}\xi = 1$) implies that detectors must have $\xi_{\mathrm{d}} \geq 1/\sqrt{2}$. The above criteria have not yet been demonstrated together in a single experiment.

These results clearly demonstrate the impact of losses on the ability of a quantum sensor to outperform its classical counterpart. If this practical roadblock is to be overcome, it is necessary to develop a low-loss, adaptable platform for quantum-enhanced sensing. This platform is likely to be waveguide based with integrated phase shifting elements. In the next chapter, we will test the viability of such a platform for precision measurement.

Chapter 3

Integrated photonic sensing

Waveguides are structures in which the time-independent solutions of the electromagnetic wave equation are invariant along the length of the structure [90]. If the electromagnetic field is prepared in a superposition of these solutions, it therefore propagates without change, avoiding the diffraction associated with propagating a beam in free-space. Optical waveguides are usually, although by no means exclusively, formed by a region with a refractive index that is higher than that of the surrounding material. This guiding of electromagnetic waves has proved to be incredibly successful in classical photonics where, for example, optical fibres have been used to transmit information over long distance with losses below the $0.2\,\mathrm{dB\,km^{-1}}$ level [107].

By constructing a waveguide-based sensor, straightforward low-loss integration with waveguide-based non-classical light sources [78,84,88,108–120] and integrated detectors [121–125] is ultimately achievable. Such an approach hopes to reduce or remove the major sources of inefficiency in photonic technologies which, in the work presented in the previous chapter, resulted in the device being unable to outperform its classical counterpart.

In this chapter, the fabrication, characterization and performance of integrated beam-splitting and phase shifting elements will be discussed. The low loss and programmable nature of these devices makes them both ideal for generating the HB state discussed above and a promising candidate for future experiments that will truly beat the SQL.

3.1 The integrated platform

A multitude of material platforms exist for producing integrated devices and which one is chosen depends upon the wavelength of operation, active or passive requirements, desired switching speed, tolerable losses, and many others. Perhaps the most widely employed materials are silica due to the already mentioned ability to draw it into flexible, long, and extremely uniform fibres, and lithium niobate (LN) due to its excellent $\chi^{(2)}$ optical nonlinearity, electro- and acousto-optic properties. Methods to produce waveguides vary widely and include lithographically defining and etching rib-like structures [126], in-diffusing lithographically patterned metals such as Titanium [127], proton-exchange [128], annealed proton-exchange [129] or reverse proton-exchange [130], and direct laser writing techniques either with femtosecond pulsed laser systems for direct material modification [131,132] or with continuous wave (CW) systems for modification of a photo-sensitive layer [133,134].

3.1.1 Waveguide structure

Figure 3.1 shows the basic waveguide structure of integrated devices used for experiments described in this thesis. The host slab waveguides are fabricated by flame-hydrolysis deposition (FHD) [135], utilizing 6" diameter silicon wafers with an 18 μm thick thermal-oxide silica layer which acts as an under-clad. The thermal-oxide layer relieves unwanted

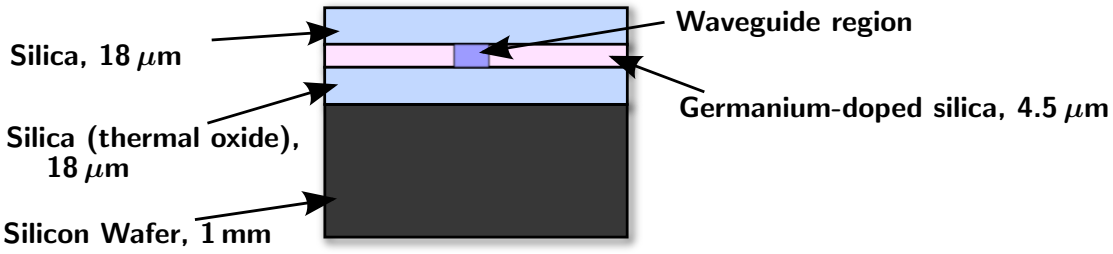

Figure 3.1: A cross-section of the waveguide structure. A 1 mm thick Silicon substrate is topped with an 18 μm silica thermal oxide layer, a 4.5 μm photosensitive layer of germanium doped silica, and an 18 μm top layer of silica.

stress, and therefore birefringence, due to lattice mismatch. Two layers of doped silica are then deposited on top of this substrate. These layers consist of a 4.5 μm thick photosensitive germanium-doped silica layer ($\approx$ 0.5 % atomic mass, measured by energy dispersive X-ray (EDX) spectroscopy), and an 18 μm thick top silica layer. Both layers are also doped with boron and phosphorous to closely match their refractive indices while ensuring successively lower melting points to enable deposition without melting previously deposited layers. The photo-induced index change is therefore the dominant contribution to optical guiding. The wafer is subsequently diced into chips with typical widths of 10 mm and lengths of 25 mm to 70 mm depending on requirements. Once diced, the chips are hydrogen loaded at high pressure to increase the photosensitivity of the germanium [136]. The individual waveguides are written by focusing a CW ultraviolet (UV) laser with a wavelength of 244 nm into the Ge-doped layer and moving the chip transversely to the surface normal with computer-interfaced 2D motion control, as depicted in Figure 3.2.

The core of the waveguide is formed by a local change in refractive index of the Ge-doped planar silica layer that is proportional to the local fluence of the UV light, and is roughly $\delta n \approx 4 \times 10^{-3}$ [137,138]. The vertical extent of the refractive index contrast is

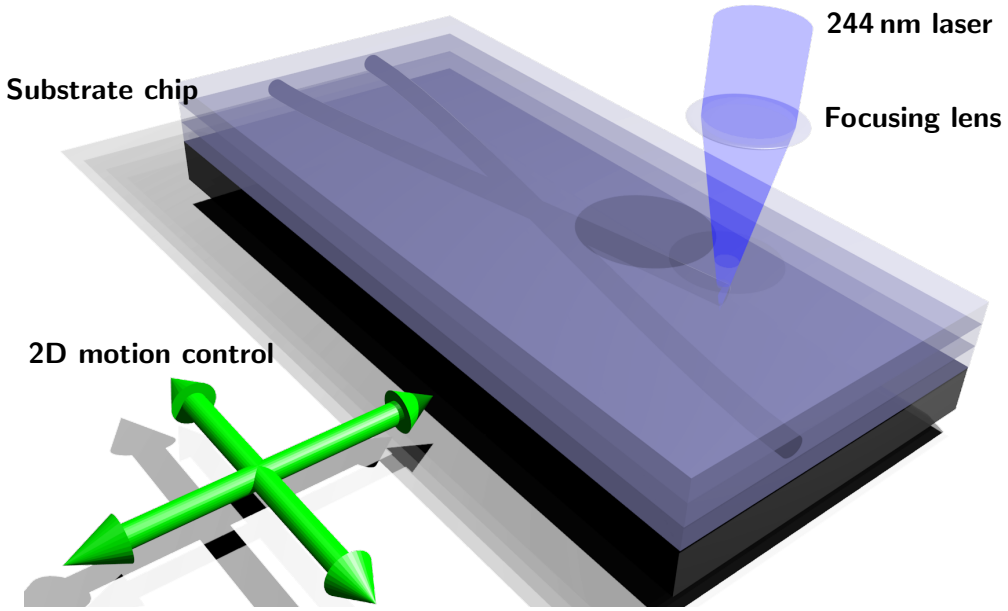

Figure 3.2: Schematic of the UV-waveguide writing process.

defined by the thickness of the Ge-doped layer while the transverse extent is defined by the beam waist of the UV beam. Since the thickness of the core layer is much less than the Rayleigh range of the writing beam, the core is rectangular in cross-section and has an effective step index. To ensure symmetric single transverse spatial mode operation of the waveguides at a wavelength of 830 nm, to match the photons produced by the photon source described in Section 2.1, care must be taken in choosing the core dimension, laser focusing and fluence[137,138]. The UV laser was focused to a spot size of approximately 4.5 μm to match the core thickness and ensure a circular guiding mode. The supported transverse waveguide mode is well matched to single-mode optical fibres, with measured butt-coupling efficiencies of up to 70% in a single channel.

The laser written waveguides discussed above allow creation of structures that are not viable using the lithographic etching techniques of standard integrated optics manufacturing, including x-couplers[137,138], and Bragg reflectors[139]. A second advantage is

that since there is no lithographic step, the waveguide writing process is relatively rapid, enabling quick development from prototype to completed device.

3.1.2 Beamsplitters

Beamsplitters in integrated optical devices can be constructed using evanescent couplers [140,141], x-couplers [36], or multimode interference devices [142]. Evanescent couplers are fabricated by bringing together two waveguides so that the evanescent fields of the two modes overlap, creating a coupling between them. The field then oscillates back and forth between the waveguides as they propagate in parallel. The rate of this oscillation is determined by the overlap of the two modes, which is dependent on the separation of the waveguides, and their relative propagation constants. For such a device with a given waveguide separation, the splitting ratio is determined by the length of the coupling region, and the wavelength being used. They can be produced using either lithographic or direct-write techniques. Multimode interference devices are constructed by creating a multimode region with multiple input waveguides. Light propagating into this region periodically re-phases along its length into multiple localized regions of high intensity. If output waveguides are positioned at these points, the light is split into a number of outputs. The coupling ratio and number of modes depends significantly upon the particular geometry chosen for the device.

X-couplers, the beamsplitter technology employed here, are produced by physically crossing the waveguides at a shallow angle. Photolithography methods cannot be used to construct x-couplers as this technique leaves under-etched segments in the crossing area, resulting in coupling ratios which are difficult to reproduce and high scattering losses. The effective beam splitter reflectivity of the x-couplers is primarily governed by

the intersection angle of the guides[137,143] (2.45° for 50:50 coupling) and the balance of the UV-light fluence (and thus the index change δn) between both waveguides at the crossing region. The x-couplers discussed here were formed by writing one channel at a time taking care to decrease the UV laser flux at the crossing point to ensure a continuous refractive index profile. Due to the dependence of the coupling ratio on geometry as opposed to optical interference, which occurs in evanescent couplers, x-couplers are less sensitive to fabrication imperfections, thermal fluctuations, and polarization state at the coupling junction[137,138].

3.1.3 Phase shifters

Integrated optical phase shifting can also be achieved in several different ways. The most common are implemented by thermo-optic[36,38] or electro-optic[144] means, however stress-induced phase shifting has also been demonstrated[145]. Electro-optic phase shifting is extremely common in commercially available LN devices for telecommunications wavelengths where it has been used, for example, in amplitude modulators and frequency converters for many years. In these devices, the refractive index of the material has a linear dependence on the applied electric field. The electro-optic effect, defined by the electro-optic tensor, can therefore be used to modulate the phase of one polarization with respect to another. By applying an electric field across a crystal with a non-zero electro-optic tensor, one that is non centro-symmetric or lacks inversion symmetry, the refractive index along one or more crystal axes can be altered, thereby changing the phase of light which is polarized along those axes. State of the art devices can modulate at many tens of GHz. Speeds at this level are in principle sufficient, when combined with a quantum memory

of sufficient time-bandwidth product [146–148], to realise true feed-forward measurements, a critical component of one-way quantum computation [149].

Since the silica-on-silicon devices used have an electro-optic tensor of zero to first order, phase control is implemented through a thermo-optic phase shifter. Again, the technology for these devices is extremely advanced in the telecommunications industry and has been used for many years [150]. Such devices operate via the thermo-optic effect governed by the thermo-optic coefficient. The effect of temperature on the thermo-optic coefficient, dn/dT, has two origins. First, the increased temperature results in material expansion, making it less dense which tends to make dn/dT negative. Second, changes in T result in changes in the thermal occupancies and spectra of the material energy levels. This tends to increase n making dn/dT positive. For silica, this second effect dominates, resulting in $dn/dT \approx 10^{-5}$ [151]. Due to the diffusion-speed limited thermal propagation, thermo-optic phase shifters operate on milli to microsecond timescales rather than the nano to picosecond timescales achievable by electro-optic devices. This potentially limits their use in feed-forward measurements, however, they have been demonstrated to be robust and repeatable in classical integrated photonics and hence are a promising technology, for example, in 'programming' a general quantum photonic circuit.

In the devices considered in this thesis, thermo-optic phase shifting was achieved through the use of small NiCr electrodes of dimensions $0.4\,\mu$m $\times$ $50\,\mu$m $\times$ $2.5\,$mm (height $\times$ width $\times$ length) and $0.85\,\mathrm{k}\Omega$ electrical resistance. These electrodes were deposited directly over one of the waveguides and current was passed through it. Local Ohmic heating causes the refractive index to change, thus inducing an optical phase difference between two different waveguides. The inherent stability and low propagation loss of the

integrated devices paired with the ability to control the phase between different optical paths and high quality mode matching allows observation of phase-dependent quantum effects[31,35,152,153].

3.2 Hong-Ou-Mandel interference at an integrated Mach-Zehnder interferometer

The first question that must be answered is whether the UV-written waveguide devices discussed above are capable of operating in the quantum regime. In order for this to be the case, they must preserve quantum coherences and therefore quantum interference effects. The clearest indication of this is by observing high visibility HOM interference between two indistinguishable photons. Such interference is inherently quantum mechanical and so observation of it in a waveguide device constitutes strong evidence that this platform is suitable for quantum-enhanced photonic technologies, including metrology.

3.2.1 The MZI as a programmable beamsplitter

The device under test in this experiment was a fully integrated MZI. In order to observe HOM interference, the MZI must behave as a beam splitter with reflectivity $\eta = 1/2$. In fact, the MZI as shown in Figure 1.2 with ideal beam splitter reflectivities of $\eta_1 = \eta_2 = 1/2$ can in principle achieve any effective beamsplitting ratio by adjusting the phase ϕ. This is analogous to the effect used in Section 2.2.2 for HOM interference between two polarization modes through a polarization MZI. Consider the propagation of creation

operators through a MZI,

$$\hat{a}^\dagger \rightarrow \frac{1}{2}\left[(e^{i\phi}+1)\hat{a}^\dagger + (e^{i\phi}-1)\hat{b}^\dagger\right], \tag{3.1}$$

$$= e^{i\frac{\phi}{2}}\left[\cos\left(\frac{\phi}{2}\right)\hat{a}^\dagger + i\sin\left(\frac{\phi}{2}\right)\hat{b}^\dagger\right], \tag{3.2}$$

$$\hat{b}^\dagger \rightarrow \frac{1}{2}\left[(e^{i\phi}-1)\hat{a}^\dagger + (e^{i\phi}+1)\hat{b}^\dagger\right], \tag{3.3}$$

$$= e^{i\frac{\phi}{2}}\left[i\sin\left(\frac{\phi}{2}\right)\hat{a}^\dagger + \cos\left(\frac{\phi}{2}\right)\hat{b}^\dagger\right], \tag{3.4}$$

and compare them with the transformation which occurs at a beamsplitter of reflectivity η,

$$\hat{a}^\dagger \rightarrow \sqrt{\eta}\hat{a}^\dagger + \sqrt{1-\eta}\hat{b}^\dagger, \tag{3.5}$$

$$\hat{b}^\dagger \rightarrow \sqrt{1-\eta}\hat{a}^\dagger - \sqrt{\eta}\hat{b}^\dagger. \tag{3.6}$$

It can be seen that with the addition of a $-\pi/2$ phase shift at the input and output of mode b, these two pairs of transformations can be made identical and, by tuning ϕ through the range $[0,\pi]$, an effective reflectivity with any magnitude can be obtained. It is sufficient, however, to set $\phi = \pi/2$ without the additional $-\pi/2$ phase shifts in order to observe the desired HOM interference. This can be seen by propagating the state $\hat{a}^\dagger\hat{b}^\dagger|\text{vac}\rangle$ through the MZI with the correct phase setting which results in the output state $ie^{i\phi}(|2,0\rangle_{\text{a,b}} + |0,2\rangle_{\text{a,b}})/\sqrt{2}$. This output state contains only terms where the photons have bunched together into the same mode due to HOM interference. Note that in more complex cases, where $\eta_1 \neq \eta_2 \neq 1/2$ and multiple programmable beamsplitters are required across more than two modes, care must be taken to ensure that optical phases are matched.

3.2.2 Observing Hong-Ou-Mandel interference

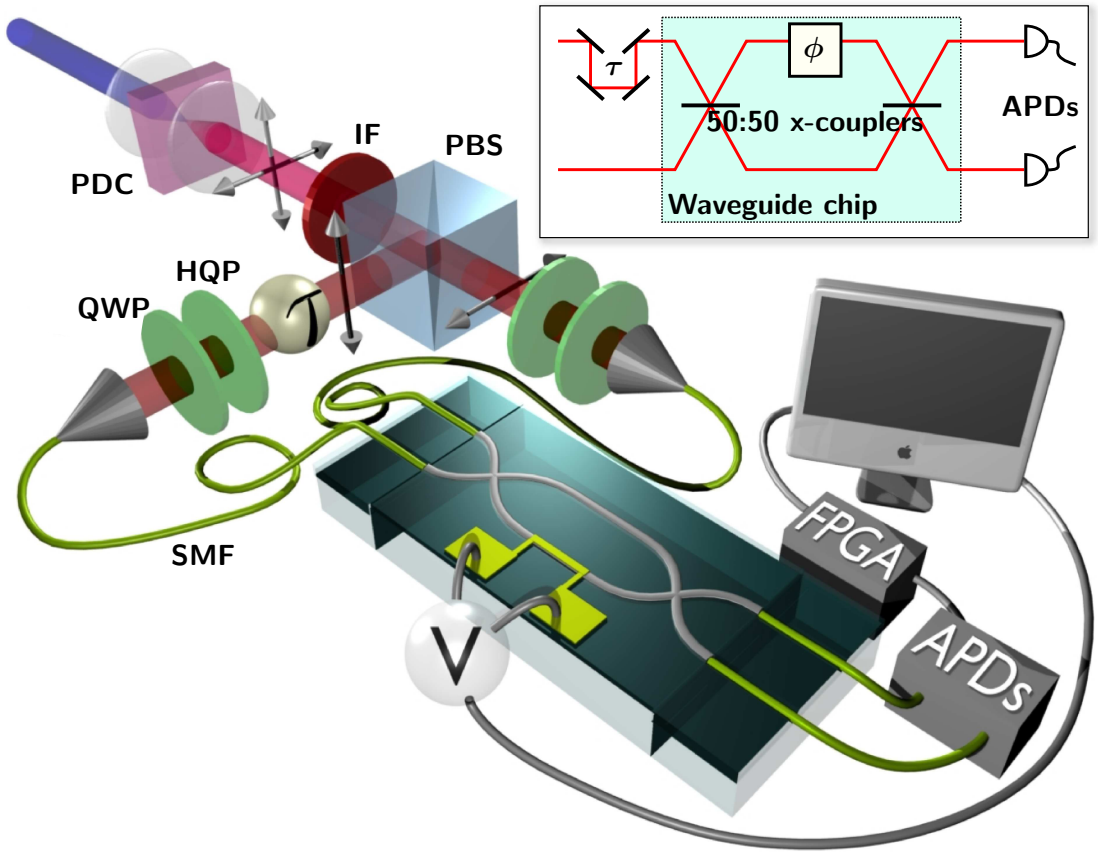

Figure 3.3: Experimental scheme. Horizontally and vertically polarized photon pairs created by a parametric downconverter (**PDC**) passed through an interference filter (**IF**) prior to being separated by a polarizing beamsplitter (**PBS**). A temporal delay line (τ) in one of the photon paths controlled the relative arrival time of the photons to the MZI. A half- (**HWP**) and quarter-wave plate (**QWP**) combination ensured the photons coupled into the single mode fibre (**SMF**) arrived at the waveguide chip with identical polarization states. A computer-controlled voltage supply (**V**) controlled the relative phase (ϕ) between the interferometer arms. The outputs of the interferometer were sent to avalanche photodiodes (**APDs**). The single and coincidence count rates were monitored by computer-interfaced **FPGA** electronics. Inset shows a schematic of the waveguide chip.

The photon source used to observe HOM interference in the integrated MZI depicted in Figure 3.3 is similar to that described in Section 2.1. In this configuration, since it is the behaviour of the integrated device which is of interest, a single PDC was used and measurements were performed in post-selection. The photons, centred at 830 nm

wavelength, were created from a degenerate, collinear, type-II PDC[56,82]. The 5 mm thick KDP crystal was pumped with 600 mW of 80 MHz pulsed, 415 nm centred, 3.5 nm bandwidth light. This UV pump was obtained by frequency doubling a mode-locked, 80 MHz repetition rate Ti:Sapphire laser with 830 nm central wavelength and a bandwidth of ∼15 nm in a 0.7 mm thick BBO crystal. The focussing into both the BBO and KDP crystals was chosen to produce spectrally decorrelated photon pairs[81], however, this configuration leads to generated photons of different bandwidths. The downconverted light was therefore passed through an interference filter (IF) centred at a wavelength of 830 nm with a bandwidth of 3 nm to ensure good spectral overlap of the photons. The orthogonally polarized photons were then separated using a PBS before a QWP and HWP were used prior to launching each polarization state into SMFs to ensure that each photon reached the MZI chip with the same polarization. A temporal delay line (τ) in the path of one of the photons allowed control of the relative arrival time of the photons at the MZI. The SMFs were directly coupled to the waveguides using a v-groove assembly (VGA) from Oz Optics and fixed by a UV curing index-matched epoxy (Dymax Op-52). The pitch of the waveguides (250 μm) was chosen to match the commercially available fibre array used in the experiments.

The throughput of a single channel was maximized by measuring the output power in each channel with a free-space power meter while adjusting the input coupling, giving a value of ≈70%. This includes one coupling interface and propagation loss. Assuming a coupling efficiency of 80%, which is consistent with theoretically modelled values, this leads to a propagation loss of 0.3 dB cm^{-1}. Using this estimate of the propagation loss, typical coupling efficiencies of ≈60% at the inputs and outputs can be calculated for the

experiments presented here. This reduction from the maximum observed value was due to the difficulty of coupling multiple channels simultaneously. Such difficulty occurred for two reasons. First, coupling of the VGA to the waveguide chip was achieved by mounting the chip on a fixed stage while mounting the VGA on a five axis stage. In this configuration, unless the point of common rotation of the stage is at the output facet of the VGA overlapping with one of the fibre cores, the positions of the two fibre cores of interest are not independently adjustable. This fact makes practical optimization difficult. Second, although the position of the waveguides is both accurate and precise to a fraction of a micron due to the high precision Aerotech translation stage used in writing, the tolerance of the fibre core position in the VGA is $\pm 1\,\mu m$ both horizontally and vertically resulting in a $\pm\sqrt{2}\,\mu m$ uncertainty radially. The mode field diameter of the SMF fibres used in the VGA is $\sim 4\,\mu m$ so this core position uncertainty can lead to a significant decrease in coupling efficiency.

As previously mentioned, in order to observe HOM interference, the phase in the MZI must be adjusted so that the MZI behaves like a beamsplitter with an effective reflectivity of $\eta_{\text{eff}} = 1/2$. This phase setting was found using classical light by launching light into a single input of the MZI measuring the optical power at the output of the chip and adjusting the voltage across the phase shifter until the optical powers were balanced. The measured phase setting was verified by launching light into the second input and measuring the output optical power splitting ratio.

By setting the relative optical phase in the MZI so that it performed as a nearly 50:50 beam splitter and delaying the relative arrival time of the photons through zero delay by adjusting the optical delay line, a two-photon HOM interference dip was obtained.

The raw two-fold count rates measured per 10 s are shown in Figure 3.4a along with the theoretical fit. The raw visibility of the theoretical fit to the data is 79 $\pm$ 1%. This visibility beats the classical threshold of 50% by 29 standard deviations, however significantly higher visibilities have been obtained using free space propagation and bulk optics, including that reported in the original paper observing this effect by Hong, Ou, and Mandel [91]. The main reason for this low visibility is significant contamination arising from two or more pairs being produced by the PDC as a result of the high UV pump power being used. To determine this background, one of the MZI inputs was blocked and the number of coincidences in 300 seconds was counted. This was repeated with the other input blocked and the sum of the two measured backgrounds normalized by the counting time is the estimated total background ($\approx 75\,\mathrm{s}^{-1}$). Figure 3.4b shows the background-subtracted HOM interference with the theoretical fit. The visibility of the theoretical fit to the background-subtracted data is $95.0 \pm 1.4\%$, indicating the ability of the device and this technology to preserve quantum mechanical coherences and its potential for use in quantum-enhanced applications.

Since spectral indistinguishability is ensured by passing the central wavelength degenerate photons through the same filter, spatial indistinguishability is ensured by filtering at the input and output with SMFs, and the relative arrival time of the photons is the parameter being scanned, the remaining degree of freedom which can result in the residual 5% visibility is polarization. Distinguishability in this degree of freedom is likely to be a result of imperfect compensation for the birefringence in the input SMFs. As well as this, the waveguide chips display a small birefringence and, although the coupling ratio of the x-couplers is not very sensitive to polarization, an input-dependent rotation may occur

unless the photons are launched with their polarizations along one of the principal axes of the waveguide index ellipsoid.

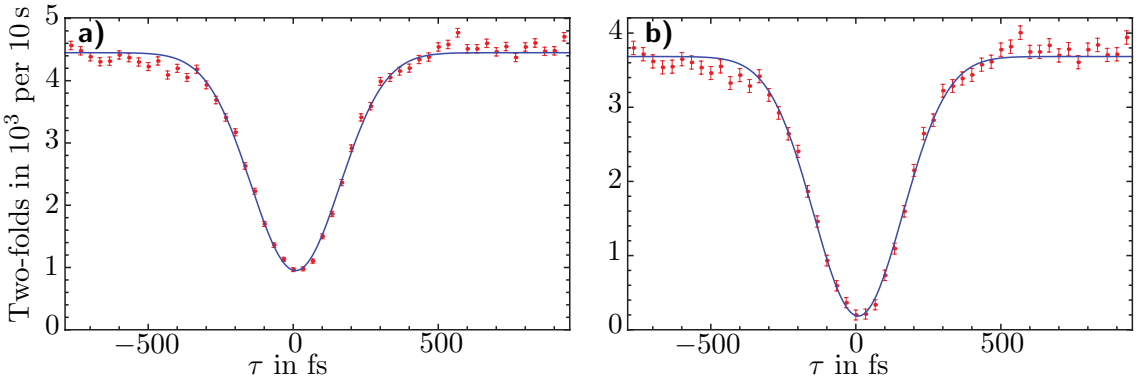

Figure 3.4: Two-photon Hong-Ou-Mandel interference through a waveguide Mach-Zehnder interferometer with the phase (ϕ) tuned so that it acts as a 50:50 beam splitter. Plots show a) measured coincidence count rate ($79 \pm 1\%$ visibility) and b) background subtracted coincidence count rate ($95.0 \pm 1.4\%$ visibility) as a function of the relative arrival time of photons to the beam splitter. Error bars are calculated assuming Poisson count statistics and propagating errors for the background subtraction.

3.3 Controllable quantum interference

As well as operating as a controllable reflectivity beamsplitter, the MZI, as previously discussed, is also the system required to produce HB states and perform optimal measurements on them. Demonstrating HB state interference over a range of phases is therefore a critical step in developing a complete quantum-enhanced metrology platform. As well as this, the introduction of a controllable optical phase in the arm of the MZI in which the sample is *not* sitting is a necessary requirement for adaptive phase estimation schemes [154,155].

In the previously presented experiment, the voltage across the thermo-optic phase shifter was adjusted such that the MZI behaved as an effective beamsplitter with reflectivity of $\eta_{\text{eff}} = 1/2$ while the relative arrival time between the photons was scanned through

zero delay. The complementary experiment is to set the relative arrival time at zero delay and scan the voltage across the thermo-optic phase shifter. Under these conditions, the interpretation is as follows. At the first beam splitter, which ideally has a beamsplitting ratio of $\eta_1 = 1/2$, two photon interference occurs between the two indistinguishable input photons. This creates an unheralded HB(2) state. The thermo-optic phase shifter then introduces a phase ϕ between the modes and the final beamsplitter, ideally of ratio $\eta_2 = 1/2$, followed by two APDs implements the ideal measurement to extract information about the phase shift from the state.

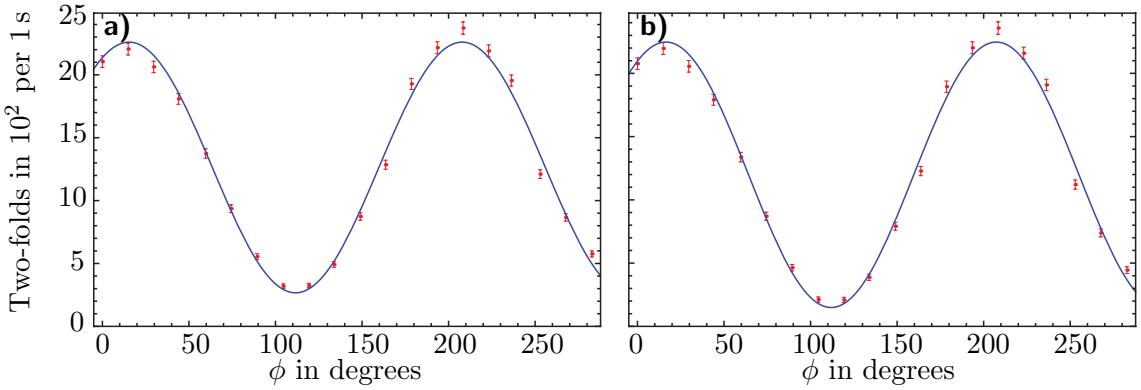

Figure 3.5: Two-photon Holland-Burnett state interference through a waveguide Mach-Zehnder interferometer as a function of the phase induced by the thermo-optic phase shifter. Plots show a) raw measured coincidence count rate ($78.9 \pm 3\%$ visibility) and b) background subtracted coincidence count rate ($88 \pm 3\%$ visibility) at zero time delay. Error bars are calculated assuming Poisson count statistics and propagating errors for the background subtraction.

The zero delay point was set by adjusting the optical delay to the position coinciding with the minimum point in the theoretical fit to the data shown in Figure 3.4. Once the time delay was set, the phase was scanned from 0° to 280°. A full 2π scan was not possible as the thermo-optic phase shifter on this device was fragile and likely to burn out if the voltage was increased further. The phase applied is proportional to the dissipated power, P, by $\phi = \alpha \mathrm{P}$. Here, the constant of proportionality, $\alpha = 0.579 \pm 0.006^\circ\,\mathrm{mW}^{-1}$ was determined from the classical fringe pattern. The power is then given by $\mathrm{P} = V^2/R$,

where V is the voltage drop across the phase shifter and $R = 850 \pm 5\,\Omega$ is its measured resistance. As in the observation of HOM interference, detection was achieved with APDs and FPGA based counting logic, as shown in Figure 3.3. Counting was performed for 1 s per phase setting. The raw two-fold coincidence rates as a function of the phase induced by the thermo-optic phase shifter, ϕ, are plotted in Figure 3.5a along with a theoretical fit to the data. The visibility of this fit is $79 \pm 3\%$. Again, however, there was a significant background coincidence contribution from multi-pair emission events, similar to those that occurred in the HOM interference experiment. This can be taken into account by measuring the two-fold coincidence count rates as the phase is varied for each of the SPDC modes blocked. These background count rates can then be subtracted from the raw data giving a fringe visibility of $88 \pm 3\%$ as shown in Figure 3.5b. The fringes show clear super-resolution, the double frequency oscillations which are characteristic of the two-photon state.

The visibility of the HB state interference should, in principle, be equal to the visibility of the HOM interference. The discrepancy can be attributed again to imperfect polarization compensation for the effect of the SMFs in the input VGA. The polarization compensation was performed with a bright alignment beam prior to the HOM and HB state experiments. During the time over which the experiments were performed, the temperature of the lab fluctuates due to the cyclic action of the air conditioning unit controlling the area with a period of $\sim$17 minutes. Both the axis and magnitude of any birefringence in the SMFs as a result of stresses in the fibre may also wander over this time, due to thermal expansion of the material, reducing the effectiveness of the previously aligned compensation and the indistinguishability of the photons.

In order to assess the ability of this configuration to outperform its classical counterpart, the analyses of Chapter 1 must be applied. The visibility of the HB state fringes is sufficient to beat the threshold of of $1/\sqrt{2}$ necessary to claim super-sensitivity under the assumption of no losses. The throughput of this device, however, is too low, so that it will in reality never be able to outperform its classical counterpart, even using HB(2) states where the constraints are at their least severe. For comparison with the previous chapter, employing Equation 1.55 setting $f = \xi_{\mathrm{g}}(\xi\xi_{\mathrm{d}})^N$ where $\xi_{\mathrm{g}} = 0.6^2$, the probability that two deterministically generated photons are coupled into the device, $\xi = 0.94$, the estimated propagation efficiency, and $\xi_{\mathrm{d}} = 0.6 \times 0.45$, the probability that a photon is coupled out of the device and detected by the APD, and assuming deterministic photon generation, $V_{\mathrm{th}} = 2.3$ so that the comparable classical device cannot be beaten. What the work presented here has demonstrated, however, is the ability to robustly control quantum interference through the mechanism of thermo-optic phase shifting and the ability of this technology platform to support and maintain quantum coherences.

These experiments demonstrate the viability of integrated devices to preserve and control quantum interference in a robust way. In the second part of this thesis the basic building blocks investigated here will be employed to increase the complexity of integrated devices, demonstrating its application in quantum information processing tasks. In addition, a major source of inefficiency in photonic experiments will be addressed - detection.

Part II

Information Processing

Chapter 4

Introduction

Although Moore's Law has held firm with the speed of computers doubling approximately every eighteen months, some problems in computation remain extremely difficult to solve. In fact, the computational time required to solve them often scales exponentially with the size of the problem, very quickly making them infeasible. Examples of such problems include factoring large numbers, searching an unsorted list, optimizing paths and many more. One of the most exciting potential applications of quantum mechanics to technology is the possibility of dramatically improving computational power [50]. The foundations of this idea are often credited to Feynman [156]. The power of quantum computation is thought to arise from the ability of quantum systems to both occupy a coherent superposition of multiple states and have stronger-than-classical correlations, or entanglement. The exact source of this computational improvement, however, is still an open question [157].

Quantum information processing splits into two practical sub-categories. The first applies to systems where information is encoded and manipulated using a discrete set of states, the so-called discrete variable regime, while the second applies when information is

encoded and manipulated in a continuous set of variables[158,159]. Although there is much promise in both approaches, the combination is too much to discuss here in any useful depth and so this thesis is restricted to the former.

4.1 Part II outline

This chapter will continue with a discussion of the necessary theoretical background of quantum information processing including an introduction to qubits and the controlled-NOT gate, two of the basic concepts required to look at the field. A brief round up of some broad theoretical and experimental results will be given followed by a discussion of the two major schemes for linear optics quantum computation: the KLM and one-way computing schemes. A review of the state of the art in linear optics quantum computation follows. Finally, a scheme for managing fabrication imperfections in integrated photonic devices will be presented.

Chapter 5 will discuss techniques for understanding the behaviour of integrated devices. It will introduce and demonstrate a loss independent method for characterizing beamsplitter reflectivities in integrated devices which can also be employed to calibrate phase shifting elements. The second half of the chapter will present a method for effectively simulating the behaviour of a linear optical circuit based on a parameterized model of its structure.

In Chapter 6, the issue of complexity in linear optical circuits for quantum information processing will addressed by experimentally investigating a circuit consisting of eight spatial modes with twelve beamsplitters and five phase shifting elements. Two interpretations of the theoretical operation of the circuit will be discussed. An experimental character-

ization based on the techniques presented in Chapter 5 will be presented followed by the observation of two- and three-photon interference beyond the classical limit. This limit will be found by using the simulation techniques presented in Chapter 5.

The penultimate chapter of this thesis will present a proof of concept integrated photon number resolving detector based on an evanescently-coupled superconducting transition edge sensor. The absorption of the structure will be modelled numerically and measured using a novel technique based on multiple bragg-reflectors. A proof of concept device will then be used to measure a weak coherent state and its detection efficiency will be characterized. Finally, routes to increasing the efficiency of the device will be investigated by simulating the effect of different device geometries. Conclusions and an outlook on future work follow in Chapter 8.

4.2 Background

4.2.1 Qubits and the controlled-NOT gate

In discrete quantum information processing, information is encoded in systems of two or more levels. The former is a quantum bit, referred to as a qubit [160], while a general d level system is similarly referred to as a qudit. Qudits show particular promise for violating Bell-type inequalities in tests of local hidden variable theories, as well as increasing security in quantum key distribution schemes [161], however, the discussion here will be centred around systems of qubits.

The state of a qubit can be represented in Dirac notation as the state vector

$$|\psi\rangle = \alpha\,|0\rangle + \beta\,|1\rangle\,, \tag{4.1}$$

where there is a normalization constraint on α and β, $|\alpha|^2+|\beta|^2 = 1$. Here, α and β are the usual complex probability amplitudes associated with the two orthonormal logical states $|0\rangle$ and $|1\rangle$. In general, a computation is carried out by implementing a physical operation on the system in which a register of logical states is encoded. This operation transforms the register into an input state dependent output, $|\psi\rangle \rightarrow |\psi'\rangle$. In fact, it is sufficient to be able to implement only one- and two- qubit operations to be able to construct all possible transformations[162]. Perhaps even more surprisingly, only a single two-qubit gate, the controlled-NOT (CNOT) gate, in combination with one-qubit Hadamard gates and phase rotations is necessary[50].

The CNOT is part of a class of operations called 'controlled' unitaries. That is, they implement a unitary on the target qubit(s) only if the control qubit(s) are in a particular state. The logical states can be represented by the vectors

$$|0\rangle = \begin{pmatrix} 1 \\ \\ 0 \end{pmatrix} ; \; |1\rangle = \begin{pmatrix} 0 \\ \\ 1 \end{pmatrix}, \tag{4.2}$$

while the unitary to be implemented is the NOT gate, represented by the matrix

$$U_{\mathrm{NOT}} \equiv \sigma_{\mathrm{x}} = \begin{pmatrix} 0 & 1 \\ \\ 1 & 0 \end{pmatrix}, \tag{4.3}$$

so that the CNOT operation can be written as

$$U_{\text{CNOT}} = |0\rangle\langle 0| \otimes \mathbb{1} + |1\rangle\langle 1| \otimes \sigma_{\text{x}}, \tag{4.4}$$

$$= \begin{pmatrix} 1 & & & \\ & 1 & & \\ & & 0 & 1 \\ & & 1 & 0 \end{pmatrix}, \tag{4.5}$$

where empty elements in a matrix are 0. Here, the unitary matrix representing the NOT operation has also been denoted with the Pauli matrix σ_{x}.

As a brief aside, it will be useful for later discussions to define the other Pauli matrices,

$$\begin{aligned} \sigma_0 &\equiv \mathbb{1} = \begin{pmatrix} 1 & 0 \\ 0 & 1 \end{pmatrix}, \\ \sigma_1 &\equiv \sigma_{\text{x}} = \begin{pmatrix} 0 & 1 \\ 1 & 0 \end{pmatrix}, \\ \sigma_2 &\equiv \sigma_{\text{y}} = \begin{pmatrix} 0 & -i \\ i & 0 \end{pmatrix}, \\ \sigma_3 &\equiv \sigma_{\text{z}} = \begin{pmatrix} 1 & 0 \\ 0 & -1 \end{pmatrix}. \end{aligned} \tag{4.6}$$

These matrices are unitary, Hermitian, and form a complete basis, making them extremely useful for expressing two-qubit operations.

The CNOT gate has the classical truth table as shown in Table 4.1. It can be seen

Input		Output	
Control	Target	Control	Target
0	0	0	0
0	1	0	1
1	0	1	1
1	1	1	0

Table 4.1: Classical truth table for the controlled-NOT gate.

Input		
Control	Target	Output
$\|D\rangle$	$\|0\rangle$	$\|\Phi^+\rangle = (\|00\rangle + \|11\rangle)/\sqrt{2}$
$\|D\rangle$	$\|1\rangle$	$\|\Phi^-\rangle = (\|00\rangle - \|11\rangle)/\sqrt{2}$
$\|A\rangle$	$\|0\rangle$	$\|\Psi^+\rangle = (\|01\rangle + \|10\rangle)/\sqrt{2}$
$\|A\rangle$	$\|1\rangle$	$\|\Psi^-\rangle = (\|01\rangle - \|10\rangle)/\sqrt{2}$

Table 4.2: Truth table for the controlled-NOT gate with superposition inputs as the control.

that in the classical situation, where the control and target bits can take the values 0 and 1 only, the state of the target bit is flipped only when the control bit has the value 1. The operation of this gate is significantly more interesting in the quantum case, however, where qubits can occupy a superposition of $|0\rangle$ and $|1\rangle$. Table 4.2 shows the two-qubit output state if the control qubit is in the superposition $|D\rangle = (|0\rangle+|1\rangle)/\sqrt{2}$ or $|A\rangle = (|0\rangle-|1\rangle)/\sqrt{2}$. In contrast to the output of the CNOT gate with classical inputs where the state of each output bit can be separately written, in the quantum case the states of the two qubits at the output cannot be written separately. In fact, the four two-qubit states generated in this way are the maximally entangled Bell states. The ability of the CNOT gate to produce this non-classical resource is central to its importance in quantum computation as it is precisely states of this type, and their associated properties, that classical computers do not have access to.

4.2.2 Results in the field

Some of the broad theoretical advances in the field include the discovery of algorithms which are computationally more efficient than their classical equivalents, including both for factoring (Shor's algorithm [163]) and searching (Grover's algorithm [164]). These algorithms scale $O((\log N)^3)$ and $O(N^{1/2})$ in time respectively, where N is the number to be factored in the first case and the size of the database in the second. In contrast, the best known classical algorithm for searching an unstructured database is $O(N)$ in time while there is no known classical algorithm which can factor in time $O((\log N)^k)$ for any k. As well as these theoretical demonstrations of the power of quantum computation, the discovery of quantum error correcting codes by Shor [165] and Steane [166] has enabled experimental progress to continue with the knowledge that, at least in principle, methods exist for dealing with the inevitable imperfections that occur in the real world. Fundamentally, error detection and correction is difficult in the quantum regime for two reasons. First, any measurement on a qubit projects the state onto the eigenbasis of the measurement operator and collapses the wavefunction into one of the eigenmodes, thereby potentially destroying the information it previously contained. Second, the no-cloning theorem [167] says that an unknown quantum state cannot be perfectly copied. This makes classical error correction schemes, which rely on multiple copies or measurement results being sent, impossible to implement.

In analogy with quantum-enhanced metrology, there are a range of physical systems which are suitable for implementing the requirements for quantum information processing [168], each with advantages and disadvantages. Trapped atomic ions, currently perhaps the most advanced platform, were proposed as a system for quantum compu-

tation by Cirac and Zoller[169] and since then much progress has been made[3,170]. All of the fundamental requirements have been demonstrated including high-fidelity read-out of multiple qubits[171], multi-qubit entangling operations[14,172], teleportation[173,174], and the implementation of small algorithms including a Fourier transform[175] and an error correcting protocol[176]. Miniaturised chip-scale traps are already established[177], providing a route to scalability with optical manipulations, however, recent developments[178,179] employ microwave transitions driven with the evanescent field from a transmission line. This potentially simplifies the technical requirements for ion trap quantum computing as extremely high quality microwave sources are already commercially available. Solid state systems have also been proposed for quantum computing including quantum dots[180,181] and superconducting circuitry[182,183]. Both of these platforms are at an earlier stage in their development than ion traps. Conditional evolution has only recently been demonstrated in quantum dots[184] although a single quantum dot has also been used to boost the strength of photon-photon interactions[185]. Perhaps their greatest strength currently, however, is their use as single photon sources[186–188]. Superconducting circuits have been used to demonstrate coherent dynamics[189], a controlled-NOT gate[190], and even a two-qubit processor[191]. Further advances with superconducting qubits have been claimed by the commercial company D-Wave who have used flux qubits to simulate systems of eight spins with programmable spin-spin couplings[192].

4.3 Linear optics quantum computation

Although there are several promising systems with the physical characteristics necessary to implement general quantum information processing schemes, certain tasks naturally lend

themselves to optical implementations. These include small-scale quantum computing and quantum repeaters[193–197], and quantum cryptography[198–201] as well as metrology as discussed in Part I of this thesis. This is a result of the ease and speed with which light can traverse long distances with low loss and decoherence as well as its potential as a medium for high bandwidth transmission.

As discussed in the previous section, the starting point for using a system to implement quantum information processing is to identify a suitable two-level system in which a qubit can be encoded. For photons there are several possible choices, however the two most common are polarization and path encodings. Polarization naturally forms a two level orthogonal basis where the logical states of the qubit can be encoded as, for example, H and V. In path or 'dual rail' encodings, a pair of spatial modes forms the physical system and the logical states are encoded in the presence of a single photon in one mode or the other. A second requirement is single-qubit phase gates. These are easily implementable in both polarization and path encodings where relative phase rotations between the logical states can be performed using wave plates and a path length delay respectively. To complete the toolbox for single qubit operations, the single-qubit Hadamard gate is required. This gate, the unitary of which is

$$U_{\mathrm{H}} = \frac{1}{\sqrt{2}} \begin{pmatrix} 1 & 1 \\ 1 & -1 \end{pmatrix}, \tag{4.7}$$

performs the transformation $|0\rangle \rightarrow |D\rangle$ and $|1\rangle \rightarrow |A\rangle$. For polarization encodings, it can be implemented by a HWP aligned at 22.5° while a simple beamsplitter with reflectivity $\eta = 1/2$ is sufficient for path encodings. Finally, we need the CNOT gate. As discussed, this gate applies an operation dependent upon the state of the control qubit, but the state

of the control qubit cannot be measured. It therefore necessarily requires a two photon interaction. In fact, it can be shown that a CNOT gate can be written as a Hadamard applied to the target qubit followed by a controlled-σ_z (CZ) and finally a second Hadamard applied to the target qubit. This is easy to see either by multiplying out the operators or noting that a Hadamard gate is unitary and Hermitian so that two consecutive applications are the identity operator while $U_{\mathrm{H}}\sigma_{\mathrm{z}}U_{\mathrm{H}} = \sigma_x$. Hence, a CNOT gate amounts to being able to implement the necessary controlled sign flip operation, which is equivalent to a CZ. It is possible to realise a system where one light beam deterministically undergoes a phase shift conditional of the presence of a second beam, mediated by a material. Such interactions are known as the cross-Kerr effect [202]. This non-linear effect is proportional to the square of the electric field, however, and is extremely small for all known naturally occurring materials. Hence, designing a system in which the requisite π phase shift is obtained due to the presence of a single photon is extremely challenging.

Perhaps because of the difficulty in obtaining the required two-photon interaction, many proposals for quantum information processing systems exist which involve photons interacting with matter based systems including atoms in cavities [203,204] and optomechanical resonators [205,206]. It is, however, possible to achieve these conditional phase shifts using only linear optics if one is prepared to give up determinism and accept an implementation which is only probabilistically successful.

4.3.1 The KLM scheme

Until the work of Knill, Laflamme, and Milburn (KLM) [207] it was commonly thought that linear optics was not sufficient to realise a scalable quantum computer due to the

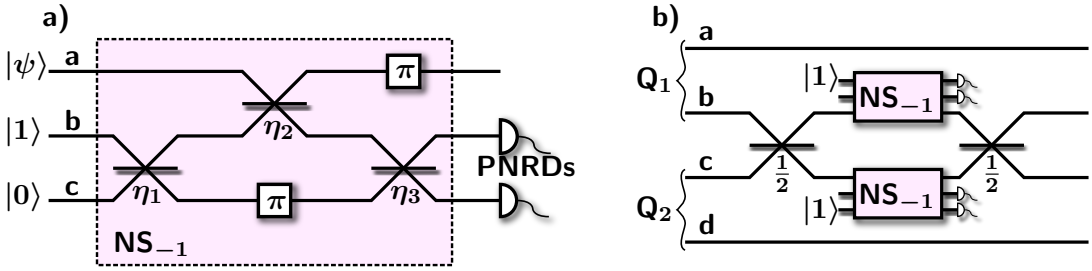

Figure 4.1: Linear optical networks to implement a) a nonlinear sign flip and b) a controlled sign flip. The convention of photons undergoing a sign flip upon reflection from the bottom of a beamsplitter is adopted. The nonlinear sign flip requires $\boldsymbol{\eta_1 = \eta_3 = 1/2 - 1/(2\sqrt{2})}$ and $\boldsymbol{\eta_2 = (\sqrt{2}-1)^2}$ and implements the transformation $\alpha|0\rangle + \beta|1\rangle + \gamma|2\rangle \rightarrow -\alpha|0\rangle - \beta|1\rangle + \gamma|2\rangle$. This is not identical to the one proposed by Knill, Laflamme, and Milburn but it is sufficient to implement the controlled sign flip operation shown in b) where qubits 1 (**Q1**) and 2 (**Q2**) are encoded using mode pairs {**a**,**b**} and {**c**,**d**} respectively with modes **b** and **c** the logical 1 rails.

probabilistic nature of the necessary two-qubit gates. Using a system built from these gates, it was thought that for increasingly complex computations the probability of success of the entire scheme would exponentially decrease, rendering any computational speed increase due to quantum mechanics irrelevant.

KLM constructed a linear optical network to produce a nonlinear sign shift, applying the transformation $\alpha|0\rangle + \beta|1\rangle + \gamma|2\rangle \rightarrow \alpha|0\rangle + \beta|1\rangle - \gamma|2\rangle$, where $|n\rangle$ here represents n photons in a single mode. Figure 4.1a shows a network which implements the negative of this transformation. Although not identical to the one proposed by KLM, it is sufficient to achieve conditional phase shifts. It consists of three spatial modes: the mode which will undergo the phase shift and two ancillary modes. At the first ancillary mode a single photon is input while at the second there is vacuum. At the output of the network, the success of the gate is determined by the result of measurements on the ancillary modes. There must be one and only one photon detected in mode two and zero photons detected in mode three for the operation to be judged successful. This is still probabilistic and occurs with probability 1/4 but, critically, *whether* it has succeeded on any given attempt

is known. In fact, the linear optical network proposed is capable of applying any phase shift to the two photon component of the state.

Since there are no nonlinear elements in the network, this result is surprising. However, although there are no non-linear optical elements, the projective measurement applied to the two ancillary modes is an inherently nonlinear process. For this reason, it is often referred to as a measurement-induced nonlinearity.

Figure 4.1b shows the incorporation of the nonlinear sign flip into a controlled sign flip or CZ gate. It operates on photonic qubits formed with dual rail encoding. The operation of this gate is more intuitive to understand. Qubit 1 is encoded in modes a and b, and qubit 2 is encoded in modes c and d. The other modes shown are the ancillary modes necessary for operating the nonlinear sign flip gates. The only way for the nonlinear sign flip gates to apply a phase is for the photons to be in modes b and c, which is the logical state $|11\rangle$. With this input, HOM interference occurs at the first beamsplitter, creating the state $(|20\rangle_{\mathrm{b,c}} - |02\rangle_{\mathrm{b,c}})/\sqrt{2}$. On passing through the two nonlinear sign flip gates, this state acquires an overall π phase. This is the probabilistic operation and succeeds with probability 1/16. Finally, the two modes of the sign-flipped state are interfered at the second beamsplitter, deterministically returning the logical state $|11\rangle$.

The second realisation by KLM was that the CZ operation can be performed on two ancillary qubits without potentially 'wasting' previously successful operations. Once the CZ is successful, the state of the control and target qubits can be teleported onto the ancillary qubits. Since the CZ and teleportation operations commute, this is equivalent to having performed the CZ operation on the control and target qubits. Moreover, the teleportation can be made asymptotically close to deterministic using linear resources and

be done in a way which enables photon loss detection. The advantage is that the operations on the ancillary qubits can be performed offline in a massively parallel architecture, reducing two qubit CZ gates to a problem of state preparation. These results raised the prospects of linear optics quantum computation (LOQC) to a credible level, in stark contrast to the belief that such schemes would not be scalable and were therefore unsuitable for all but the simplest of operations.

Although the results of KLM are remarkable, it is important to note the implicit requirements of the system they envisaged. The first is that they require multiple single photon sources that produce photons in indistinguishable pure states with high efficiency. These are still very much under development across a range of physical platforms and none have so far been demonstrated which fulfil the requirements of the KLM scheme. Secondly, since the state generation aspect of the scheme is still essentially repeat until success, it is necessary to have a device which enables the synchronisation of multiple parts of a larger protocol. Such a device is a quantum memory and must operate with high fidelity and efficiency. They must also operate with a high time-bandwidth product to enable many repetitions of the state preparation, thereby increasing the probability of success. Again, these are the subject of much research. Finally, photon number resolving detectors are a critical element of this scheme, since they must be able to distinguish accurately between states of one and two photons. Such detectors do exist [79], however they currently operate too slowly to implement feed-forward adjustments.

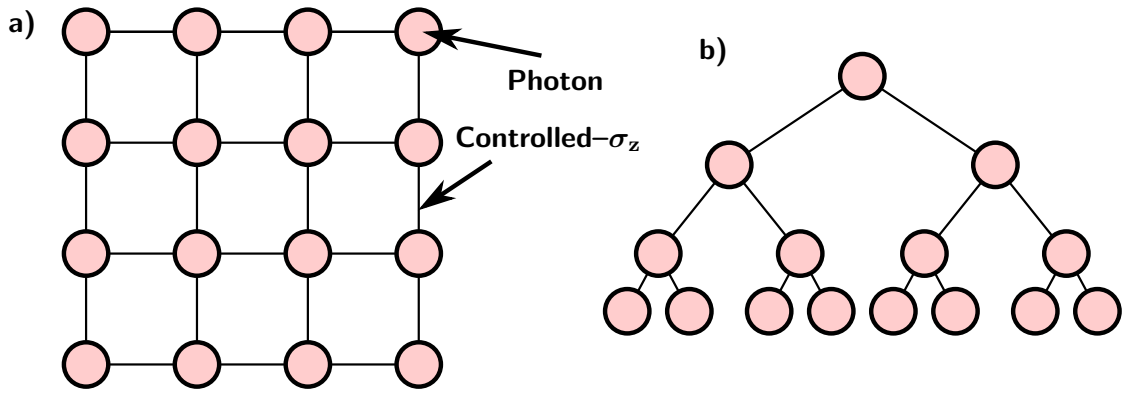

Figure 4.2: Two examples of cluster states. Each node represents a qubit while each edge represents the application of a controlled-$\boldsymbol{\sigma_z}$ operation. a) The basic lattice cluster. b) A tree cluster used in error correction schemes to encode against photon loss [208].

4.3.2 One-way quantum computing

An alternative scheme exists for quantum computation which can be implemented in photonic architectures. It is called one-way or cluster state computation [149,209–211]. One-way quantum computation begins with the creation of a cluster or graph state, depicted in Figure 4.2. These states are highly entangled states of many qubits, conceptually created by performing CZ gates between the qubits to form a two or three dimensional array of entangled qubits. The most common arrangement is a regular rectangular grid in two or three dimensions with CZ operations between nearest neighbours. This is as a result of the schemes original inception as a route to quantum computation with atoms trapped in optical lattices. In that situation, it is possible to create an interaction which applies a CZ between nearest neighbours across the entire lattice at once while interactions between non-nearest neighbours are difficult to engineer. For photons, the nearest neighbour restriction is lifted and graph states with complex layouts can be created. This is useful in producing states which are tolerant to photon loss [208]. In contrast, however, each two-qubit interaction must be individually applied. The difficulty of producing a linear optical

CZ interaction therefore still remains, however, even with a probabilistic interaction an efficient cluster state generation scheme exists [212].

Once a cluster state has been produced, information is routed, manipulated, and processed using single qubit operations only, including projective measurement and feed forward local operations. This is the real power of cluster state quantum computing. The cluster state is a universal resource for quantum computation independent of the specific algorithm that is to be implemented. It can therefore be prepared in exactly the same way for each use. As well as this, 'gates' in cluster-state computing are deterministic rather than asymptotically deterministic in the KLM scheme. In most physical implementations of qubit systems, single qubit operations are significantly more straightforward than two qubit operations. Unfortunately, however, this is not the case for atoms in optical lattices where single qubit addressability is still a practical challenge.

Cluster state computation has also reduced the efficiency thresholds for loss tolerance and the resource requirements in comparison with the KLM scheme [213]. If gate errors can be neglected, it has been shown that the product of source and detector efficiencies must be greater than $2/3$ [212] in order to be efficient. With the inclusion of encoding against gate errors, a trade-off can be found with a region of gate error rates and photon loss rates within which an efficient scheme is possible [214].

Although the one-way quantum computation paradigm has improved resource usage, error tolerance thresholds, and complexity for LOQC, the practical requirements are still challenging. Tens of optical elements are necessary per logical operation using tens of photons. The current state of the art is the generation of a post-selected eight photon linear cluster state [215] using bulk optics and free space propagation. This result provides

hope that the significant increase in complexities required to truly implement LOQC are feasible.

4.3.3 The state of the art in linear optics quantum computation

Until recently, the only demonstrations of the necessary elements for a quantum information processing device have been performed using free space propagation and bulk optics. These include demonstration of post-selected [216–220] and heralded two [221,222] and three [223] qubit gates. There have also been proof of principle demonstrations of cluster state generation for one way computation [224–227] including classical feedforward [228]. Finally, proof of principle demonstrations of small algorithms and protocols have also been performed including a compiled version of Shor's factoring algorithm [229], and teleportation of a two-qubit system [230]. Despite the significant success demonstrated using bulk optics, this is not a practicable approach to scalable implementations of more powerful quantum protocols. This is due in part to the difficulty associated with aligning and stabilizing the bulk optical elements that are necessary to create and maintain optimal mode matching in several sequential interferometers. The sheer size of bulk devices is also impractical for scalable manipulation of many photons. Approaches based on integrated optics minimize alignment considerations, are inherently stable because of their small size and monolithic structure, and allow straightforward construction of complex interferometric networks on the micro-scale. These characteristics, in combination with the control over the electric field integrated devices enable, makes them well positioned to overcome the limitations of bulk optics [231,232].

First steps toward integrated photonic quantum circuits were recently reported based

on etched planar silica-on-silicon waveguides[141,233] and femtosecond-pulse-written waveguides in bulk silica[140]. Optical-fibre-based quantum logic gates have also recently been demonstrated[234,235]. Such gates will play an important role in quantum communications, but seem limited to a few gates, due to classical phase stability, rather than computational tasks with several cascaded gate operations. The experiments with silica-on-silicon etched waveguides demonstrated that integrated optical devices can be used to perform high-visibility classical[233] and quantum interference[141] at the few-photon level. HOM interference at an evanescent coupler with a visibility of $94.8 \pm 0.5\%$, and the implementation of a controlled-NOT (CNOT) quantum logic gate in the logical basis[141] show the feasibility of integrated optics for quantum interference.

4.4 Coping with imperfections

As with quantum-enhanced metrology, in order to be a viable technology, photonic quantum information processing devices must be able to cope with fabrication imperfections. This is especially true given that gate error rates in the 10^{-4} range are necessary before efficient LOQC is possible[214]. By utilizing the controllability of quantum interference discussed in Chapter 3, the tunability required to reach this level can be achieved.

4.4.1 Programmable beamsplitters revisited

As previously shown, each linear optics implementation of a two qubit gate can involve many beamsplitters (see Figure 4.1). Imperfections in these beamsplitters will increase gate errors which exponentially decrease the probability of overall computation success. While integrated devices promise stability, reduced loss, and increased compactness com-

pared with bulk optics, they can also reduce flexibility as a single faulty component 'on chip' cannot be replaced. It is, however, possible to plan ahead and allow for post-fabrication compensation of device imperfections.

Gate errors in integrated photonics arise primarily from fabrication imperfections in beamsplitters, meaning that their true reflectivity is not their designed reflectivity. Highly accurate gates therefore require precise control over the reflectivity of the beamsplitters from which it is composed. Fortunately, the MZI provides a solution, since the combination of two beam splitters and a phase shifter can be thought of as a single beam splitter whose reflectivity, η_{eff}, is a function of the applied phase. In Section 3.2.1 it was shown how a perfect MZI with beamsplitter reflectivities $\eta_1 = \eta_2 = 1/2$ can be tuned to reach any effective beamsplitting ratio. For tolerance to fabrication imperfections, the converse question is important: for what combinations of η_1 and η_2 can a particular effective beamsplitting ratio be reached?

Consider the lossless MZI shown in Figure 1.2. For general η_1 and η_2, the evolution of the creation operators for the two input modes is given by the transformations

$$\begin{aligned} \hat{\mathrm{a}}^\dagger \;\rightarrow\; & (e^{i\phi}\sqrt{\eta_1\eta_2} + \sqrt{(1-\eta_1)(1-\eta_2)})\hat{\mathrm{a}}^\dagger + \\ & (e^{i\phi}\sqrt{\eta_1(1-\eta_2)} - \sqrt{(1-\eta_1)\eta_2})\hat{\mathrm{b}}^\dagger, \end{aligned} \tag{4.8}$$

$$\begin{aligned} \hat{\mathrm{b}}^\dagger \;\rightarrow\; & (e^{i\phi}\sqrt{(1-\eta_1)\eta_2} - \sqrt{\eta_1(1-\eta_2)})\hat{\mathrm{a}}^\dagger + \\ & (e^{i\phi}\sqrt{(1-\eta_1)(1-\eta_2)} + \sqrt{\eta_1\eta_2})\hat{\mathrm{b}}^\dagger. \end{aligned} \tag{4.9}$$

Any phase differences between the rails can be corrected with a phase shift before and after the MZI, however, it is the magnitude of the effective reflectivity, $|\eta_{\text{eff}}|$, which is of

concern here. This is calculated from the modulus squared of the coefficient of $\hat{a}^\dagger$ in the first transformation above or the modulus squared of the coefficient of $\hat{b}^\dagger$ in the second transformation above. These are equal to each other and given by

$$|\eta_{\text{eff}}| = \eta_1\eta_2 + (1-\eta_1)(1-\eta_2) + 2\sqrt{\eta_1(1-\eta_1)\eta_2(1-\eta_2)}\cos\phi. \tag{4.10}$$

In the case $\eta_1 = \eta_2 = \eta$, the effective reflectivity becomes

$$|\eta_{\text{eff}}| = 1 - 4\eta(1-\eta)\sin^2(\phi/2). \tag{4.11}$$

The minimum effective reflectivity that can be reached in this case is

$$|\eta_{\text{eff}}^{(\text{min})}| = 1 - 4\eta(1-\eta), \tag{4.12}$$

while the maximum reflectivity which can be reached is always 1. If both beam splitters have a splitting ratio of 1/2 then $|\eta_{\text{eff}}^{(\text{min})}| = 0$ and, by adjusting the phase, the full range of reflectivities from perfectly reflective to perfectly transmissive can be realised. As η deviates away from 1/2, the fraction of effective reflectivities that can be reached is given by $4\eta(1-\eta)$. This is true for deviations away from 1/2 in either direction due to the symmetry of Equation 4.12.

Figure 4.3 shows values of η_1 and η_2 for which a range of desired effective reflectivity magnitudes can be reached through the tuning of ϕ. In each plot, combinations outside the ellipse do not allow tuning to the desired point. For an effective reflectivity magnitude of 1/2, the maximum tolerance is obtained, as shown by the size of the circle. As the desired

$|\eta_{\text{eff}}|$ is decreased, the circle deforms into an ellipse with its major axis along the line $\eta_2 = 1 - \eta_1$ and shrinking minor axis. For increasing $|\eta_{\text{eff}}|$, the same occurs but with the major axis aligned along $\eta_2 = \eta_1$. This shrinking indicates that for a fully programmable circuit, extremely tight fabrication tolerances are necessary in order to reach effective reflectivities of 0 using this scheme.

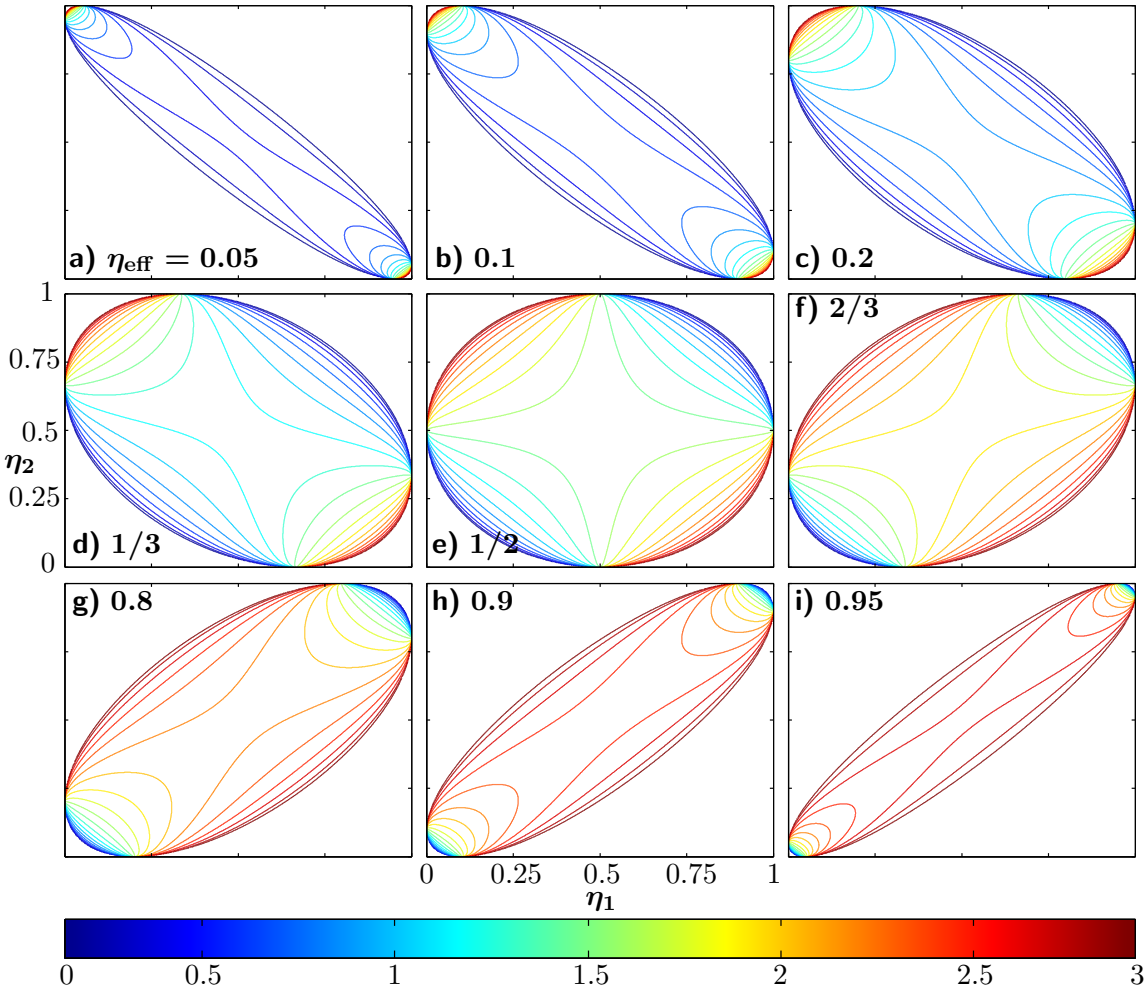

Figure 4.3: Values of the beamsplitter reflectivities in a Mach-Zehnder interferometer for which a specified effective reflectivity can be reached. Contour plots a) to i) correspond to effective reflectivities, $|\eta_{\text{eff}}|$, of 0.05, 0.1, 0.2, 1/3, 1/5, 2/3, 0.8, 0.9, and 0.95 respectively. Points outside the ellipse in each case cannot be reached by tuning ϕ. For points inside the ellipse, contours of constant ϕ are given where the colour denotes the value of the phase in radians as shown by the colour bar.

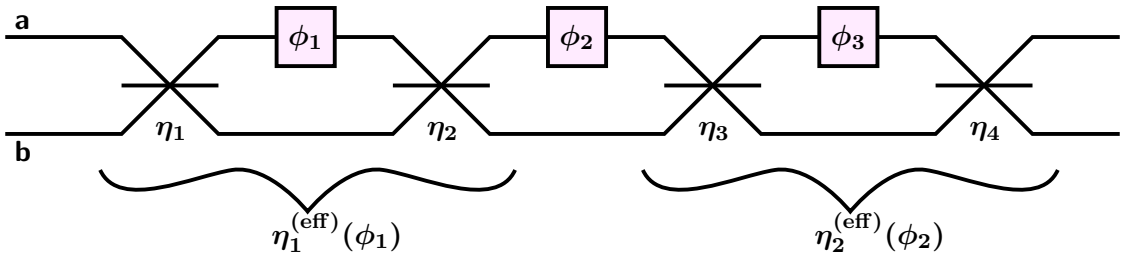

Figure 4.4: A perfectly programmable beamsplitter constructed from four imperfect beamsplitters, with nominal reflectivities $\boldsymbol{\eta_1 = \eta_2 = \eta_3 = \eta_4 = 1/2}$, and three phase shifting elements $\boldsymbol{\phi_1}$, $\boldsymbol{\phi_2}$, and $\boldsymbol{\phi_3}$.

4.4.2 Perfectly programmable beamsplitters

Ultimately, if LOQC is to be viable, a network must be produced that can be programmed to implement a range of operations. In principle this could be implemented using programmable beamsplitters in the form of MZIs, where the beamsplitters comprising each MZI have reflectivities of 1/2. In practice, however, the ability of these MZI-based beamsplitters to reach extreme effective reflectivities is quickly lost as a result of fabrication imperfections. Fortunately, the MZI again provides the solution. A MZI comprised of two perfectly 1/2 reflectivity beamsplitters allows the full range of effective reflectivities to be reached. This can be constructed as shown in Figure 4.4 from two further MZI, each comprised of beamsplitters which have a nominal reflectivity of 1/2. Phases ϕ_1 and ϕ_3 must be tuned to achieve $\eta_1^{(\mathrm{eff})}(\phi_1) = \eta_2^{(\mathrm{eff})}(\phi_3) = 1/2$. Once set, the full range of effective reflectivities from 0 to 1 can be obtained by tuning ϕ_2.

By replacing single beamsplitters with MZIs as detailed above, any linear optical network can be made significantly more robust to fabrication imperfections. Not only can imperfections be tuned away but fabrication is simplified by writing beamsplitters of a single reflectivity only. The behaviour of a linear optical circuit can also be tuned, enabling programmable operation across the whole range of possible operations. The ability

to achieve this, however, relies upon accurate characterization of the elements which comprise the circuit. This is not trivial in an integrated optical device, since it is difficult to gain access to individual modes at different locations within it. In the next chapter, a method of characterizing individual elements in a linear optical integrated circuit will be introduced along with a method for simulating the behaviour of such a circuit.

Chapter 5

Characterization and simulation of linear optical circuits

As the complexity of linear optical networks increases, it becomes increasingly critical to be able to accurately model their behaviour, both to verify that they are well understood and to ensure accurate fabrication. It is possible to accomplish this by taking a 'black-box' approach, that is, without assuming anything about the network. Such an approach is called quantum process tomography [217,236,237]. The distinct advantages of this approach are that it is completely general and provides an accurate description of the exact operation that a linear optical circuit is performing. The down sides, however, are that in order to create a predictive model of the operation across multiple photon-number subspaces, a complete set of tomographic measurements must be performed in each of the subspaces. As well as this, an exponentially larger set of measurements must be performed as the system increases in size, $O(2^{2n})$ for an n qubit operation. This situation has been significantly improved for processes that can be described using sparse matrices by compressive

sensing techniques[238–240]. In this case, the process matrix can be estimated in $O(n)$ measurements.

Instead of these black-box approaches, a model-driven approach can be taken. Here, *a priori* information about the structure of the circuit allows its behaviour to be parameterized. Such an approach is obviously linear in the number of circuit elements and, if the elements can be straightforwardly parameterized as in the case of beam splitting ratios, can be predictive across multiple photon number subspaces without additional measurements. In order to be predictive, it is necessary not only to have precise estimates of the parameters but to be able to simulate the behaviour of the circuit. Linear optical circuits are sufficient to realise quantum computation, however, and so the quantum behaviour of photons in them cannot be efficiently simulated by a classical computer. If it could, a quantum computer could be efficiently simulated on a classical computer and they would fundamentally be no different. In this chapter, methods of characterizing individual elements of an integrated photonic circuit will be discussed and a loss-free characterization method will be demonstrated. Subsequently, a method of simulating the behaviour of a linear optical network will be presented.

5.1 Estimating reflectivity

As discussed in the previous chapter, only two devices are required to implement unitary operations in LOQC: beamsplitters and phase shifters. In fact, as shown in Section 4.4, only beamsplitters with a reflectivity of 1/2 in combination with phase shifters are necessary. Furthermore, the behaviour of phase shifters is also only significant in a linear optical circuit when they are part of a MZI. Unless this is the case, a phase shifter will

not change the probability of a photon being found at a particular output and so, for the purposes of quantum computation, can be ignored. Since a MZI can be thought of as a programmable reflectivity beamsplitter, it is enough to be able to characterize the effective reflectivity of the MZI in order to have calibrated the phase shifter.

5.1.1 Naive reflectivity characterization

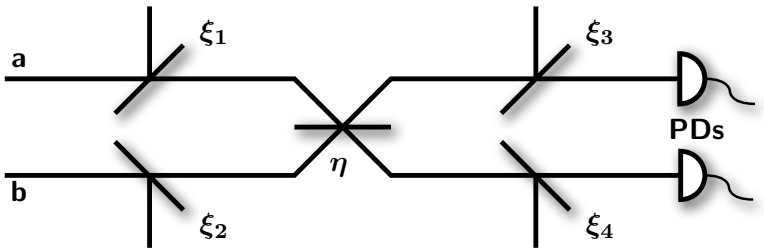

Figure 5.1: Schematic of a device consisting of a single beam splitter of reflectivity $\boldsymbol{\eta}$ with input and output coupling efficiencies modelled by beam splitters with transmissivities $\boldsymbol{\xi_1, \xi_2}$ for input coupling efficiencies, and $\boldsymbol{\xi_3, \xi_4}$ for output coupling efficiencies. The spatial modes are labelled **a** and **b**. Detection is performed by photodiodes (**PD**).

Consider the single beamsplitter shown in Figure 5.1. Here, a single beamsplitter of unknown reflectivity η is to be characterized, however, losses ξ_1, ξ_2, ξ_3, ξ_4 are present at the four input and output modes.

The naive characterization method of the reflectivity of this beamsplitter is as follows. Light of intensity I_1 is launched into mode a. At the output of the beamsplitter, the two intensities are measured. Expressed in terms of the input intensity, efficiencies, and beamsplitter reflectivity, they are given by

$$I_a = \xi_1 \xi_3 \eta I_1, \tag{5.1}$$

$$I_b = \xi_1 \xi_4 (1 - \eta) I_1. \tag{5.2}$$

The value of η is then estimated by

$$\eta_{\text{est}} = \frac{I_a}{I_a + I_b} \tag{5.3}$$

$$= \frac{\xi_3 \eta}{\xi_4 + (\xi_3 - \xi_4)\eta}. \tag{5.4}$$

Clearly, unless $\xi_3 = \xi_4$, $\eta_{\text{est}} \neq \eta$. For polarization-based schemes in free space, it is a reasonable approximation that there is no polarization dependent loss. In situations where the transverse spatial mode of orthogonal polarizations can differ, however, losses can be significantly different for each polarization. This is the case in some integrated optical platforms, for example with titanium in-diffused waveguides in lithium niobate. For path encoded schemes in integrated devices, it is perhaps more of a stretch to assume equal losses. Even if the propagation losses in the waveguides are equal, the difficulty of coupling into and out of multiple waveguides at the same time makes it unlikely to be true overall. Finally, if the beamsplitter to be characterized is inside a larger optical network then other beamsplitters will act as effective losses. Unless all the beamsplitters in each path sum to the same effective loss, a fact that is reliant upon both extremely tight fabrication tolerances and a favourable network design, the error introduced to the reflectivity estimate is likely to be large.

5.1.2 Loss independent reflectivity characterization

Here, a ratiometric characterization technique is presented which allows measurement of the splitting ratio independently of the input and output coupling efficiencies associated with launching light into and collecting light from the device. Again, the situation being

considered is shown schematically in figure 5.1. Although only a single beam splitter is shown, this technique can be applied to any beam splitter embedded in a larger circuit as long as both inputs to and both outputs from the beam splitter can be accessed independently. This applies even if the inputs or outputs can only be accessed through other beamsplitters, as long as the path from the input mode to the beamsplitter doesn't introduce light at both input ports and the paths from the detectors to the output modes of the beamsplitter never meet.

As in the previous section, coherent light with intensity I_1 is coupled into mode a but in addition, light with intensity I_2 is coupled into mode b in a separate measurement. For each of these two measurements light propagates through the circuit and is detected at the outputs, having experienced propagation, coupling, and detection losses. At the outputs, two intensities are measured in each case, I_{1a} and I_{1b} in modes a and b respectively for the first case and I_{2a} and I_{2b} for the second case. These intensities can be written as

$$I_{1a} = \xi_1 \xi_3 \eta I_1, \tag{5.5}$$

$$I_{1b} = \xi_1 \xi_4 (1-\eta) I_1, \tag{5.6}$$

$$I_{2a} = \xi_2 \xi_3 (1-\eta) I_2, \tag{5.7}$$

$$I_{2b} = \xi_2 \xi_4 \eta I_2. \tag{5.8}$$

Now, taking the ratio $r = I_{1b} I_{2a} / I_{1a} I_{2b}$ gives

$$r = \frac{I_{1b} I_{2a}}{I_{1a} I_{2b}} \tag{5.9}$$

$$= \left(\frac{1-\eta}{\eta} \right)^2, \tag{5.10}$$

a ratio which is independent of all coupling and propagation efficiencies. Solving for η and taking the solution which gives $0 \leq \eta \leq 1$ yields a loss independent estimate of the reflectivity.

$$\eta_{\text{est}} = \frac{1}{1+\sqrt{r}}. \tag{5.11}$$

The only underlying assumptions made here are that the detectors used to measure the intensity at the outputs are linear and have zero offset. The response coefficient does not have to be the same for each detector since it would drop out in the expression for r and any systematic zero offsets can be easily characterized and subtracted from the measurements.

Although this technique provides an efficiency free estimate of a beamsplitters reflectivity, the requirement of being able to isolate both input and output modes independently is practically difficult, even for moderately sized circuits. In general, the individual inputs and outputs of some beamsplitters in LOQC circuits are not independently accessible, for example in a CNOT gate where only three beam splitters may be characterized in this way[241].

5.1.3 Camera-based characterization

The issue of requiring independent access to the output modes of beamsplitters can be alleviated by using a camera to collect light scattered out of the mode in the transverse direction. The outputs of a particular beam splitter can then always be independently accessed, drastically increasing the applicability of the technique described in the previous section. Light observed at the camera is a proportion of the light propagating in the mode. As with the ratiometric technique discussed in the previous section for output intensities

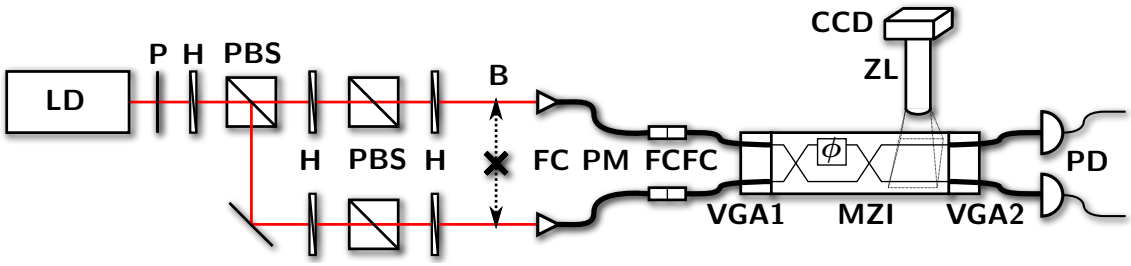

Figure 5.2: Experimental scheme used to compare reflectivity characterization techniques. A continuous wave laser diode (**LD**) was passed through a polarizer (**P**), half-wave plate (**H**), and polarizing beamsplitter (**PBS**) to produce two beams. These were then passed through a **H** and a **PBS** for individual power control before a further **H** rotated the polarization to match the polarization maintaining fibre (**PM**) at the fibre coupling stage (**FC**). A movable beam-block (**B**) allowed each input to be launched individually. Polarization maintaining FCFC connectors (**FCFC**) coupled the light into a polarization maintaining v-groove assembly (**VGA1**). This was butt coupled to a direct-UV written Mach-Zehnder interferometer (**MZI**) using a six-axis translation stage. The **MZI** was placed on a thermo-electrically stabilised mount (not shown) and kept at 20°. Output coupling was achieved with a second v-groove assembly (**VGA2**), whose single mode fibres were connected to two photodiodes (**PD**). A camera (**CCD**) was used to simultaneously capture light scattered in the transverse direction via a zoom lens (**ZL**) system. The effective reflectivity of the (**MZI**) was tuned by setting the phase ϕ using a thermo-optic element connected to a programmable voltage supply (not shown).

measured with linear detectors, the proportion scattered does not need to be constant for different paths since the ratiometric analysis gives a reflectivity which is independent of the scattering ratio and coupling efficiency. Consequently, however, the camera pixels must display a linear response and the image of the output modes must not change position on the camera sensor so that the pixel efficiency is constant when coupling into each input.

Figure 5.2 shows the experimental scheme used to compare the loss independent and naive reflectivity characterization techniques. A diode laser capable of emitting 300 mW at a wavelength of 825 nm was coupled into two polarization maintaining single mode fibres. A QWP and HWP combination before the coupling stages allowed the polarization of the light to be aligned along one of the same principle axis of the fibres by minimizing the transmission through a PBS placed at the fibre output (not shown). Once aligned, the polarization maintaining fibres (PMFs) were connected to two PMFs mounted in a

VGA (Oz Optics) using two polarization maintaining FC-FC connectors. This VGA was butt-coupled to an integrated MZI as described in Chapter 3. A thermo-electric element, temperature transducer (AD 590), and PID controller (Newport 350B) were used to stabilize the temperature of the device, to ensure constant conditions for all measurements. Coupling was achieved by mounting the VGA on a computer interfaced six-axis stage (Thorlabs NanoMax 603D and APT MPZ601). Index matching oil (Cargille AA 1.450) was applied to the interface to reduce Fresnel reflections due to a small air gap.

Initial coupling was achieved manually by positioning a microscope objective (40x Olympus Plan n) at its focal length from the output face of the chip. The movable camera (Spiricon SP620U) and zoom lens (Navitar 12x system) allowed the waveguides and cores of the fibres in the VGA to be located by eye, enabling rough alignment in the plane. From this position, the vertical position of the VGA was adjusted until two bright spots could be seen after the microscope objective using an infrared sensitive card. Once located, the brightness of these spots was maximized by adjusting the position of the VGA in both transverse dimensions. The final part of rough alignment was to move the camera to the output face of the MZI chip and double check the coupling, optimizing if necessary. This was necessary since the act of moving the camera would sometimes disturb the coupling, due to unavoidable vibrations.

The second stage of coupling involved mounting the output VGA on the second six axis stage, again using the camera to roughly position the face of the VGA with respect to the output face of the MZI. The output fibres of the VGA were connected to photodiodes. Manual coupling of the output was performed by adjusting the vertical position of the output VGA until coupling of a few percent was achieved. From this point, an iterative

algorithm was followed, maximizing the coupling by adjusting all three positions, first on one stage and then on the other. Once a maximum was obtained, the angles of the VGAs were optimized individually. The algorithm followed was a simple beam walk, using three axes instead of the usual two.

With coupling optimized, the voltage across the thermo-optic phase shifter was set and then left for $\sim$2 mins to ensure that any thermal transients had dissipated. 100 currents from the photodiodes were recorded first with one input unblocked and then with the other. The same was performed again for the camera, recording 100 images of the output modes from the transverse direction. The voltage was then adjusted and the process repeated. Since the photodiodes displayed negligible offset, the analyses outlined in the previous two sections could be directly applied to obtain both a naive and loss-independent estimate of the beamsplitter reflectivities as a function of the applied power.

Figure 5.3 shows the sequence of analysis which was applied to images of the transverse scatter. The analysis was applied to two images for each estimate of the reflectivity, one image taken with the first input fibre unblocked, and one image taken with the second fibre unblocked. Figures a, b, and c show the analysis for a single image only. Figure 5.3a shows the raw image. The exposure of the camera was adjusted so that as much of the dynamic range of the camera as possible was used. Once taken, a region of interest (ROI) was selected, as shown by the white rectangle superimposed on the image. This ROI was selected to contain both waveguides and no bright scatter points due to dust on the surface of the device. The selected area remained the same for the analysis of both images.

An enlargement of the ROI denoted by the white rectangle in Figure 5.3a is shown in Figure 5.3b. A second rectangle was then selected from within the ROI but which did not

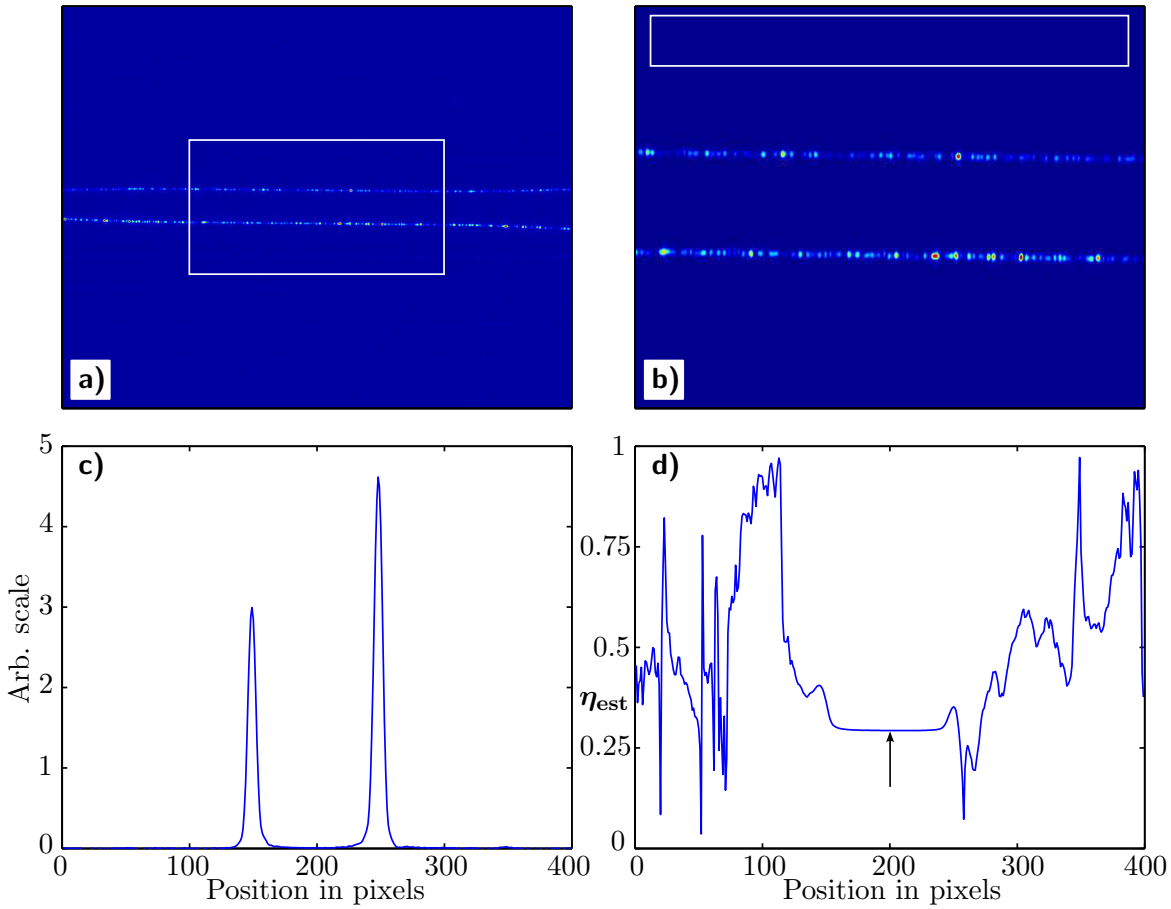

Figure 5.3: The sequence of image analysis applied to the images of scatter from the output modes of the beamsplitter to be characterized. a) The raw image. The white rectangle indicates a selected region of interest. b) An enlargement of the region of interest. The white rectangle indicates a region used to estimate the mean background pixel noise. c) The region of interest after integration along the waveguide direction and background subtraction. Steps a, b, and c were applied to two images of the output of a beamsplitter. d) The estimated beamsplitter reflectivity as a function of the position of the dividing line (see text). The arrow shows the region of stability, the minimum of which gives the reflectivity estimate.

overlap with any of the scattered light. The pixel values in this rectangle were averaged to give an estimate of the mean noise and this value was subtracted from every pixel in the ROI. The background subtracted ROI was then integrated along the direction of propagation in the waveguides, giving the data shown in Figure 5.3c.

Finally, the ratio of I_{1a}/I_{1b} was given by the ratio of areas underneath the two peaks in the background subtracted integrated ROI. Once the ratios for the two images were found, the ratio $r = (I_{1b}I_{2a})/(I_{1a}I_{2b})$ could be calculated, allowing the reflectivity to be estimated. One method of obtaining the two areas would be to fit to a Gaussian function to each peak, integrate them analytically, and take ratio of analytic areas, however, the true function is not necessarily a Gaussian, especially if the waveguides are tilted in the frame of the ROI. Instead, a dividing line can be inserted and the pixel values can be summed from the left edge to the line and from the line to the right hand edge, giving numerical estimates of the areas under the peaks. This leaves some ambiguity about where the dividing line should be placed, although it should be the same for each input. Figure 5.3d shows the effect on the estimated reflectivity as a function of the position of this dividing line. As long as the division is made near the centre of the integrated ROI, as shown by the arrow, the estimate of the reflectivity is not very sensitive to its precise position, however, positioning it at the maximum or minimum value of this region does provide an objective way to choose its position.

Figure 5.4 shows the estimated effective reflectivity of the MZI for each of the three techniques discussed above as the voltage across the thermo-optic phase shifter is scanned. The red curve shows the reflectivity estimate when using the naive characterization technique and photodiodes, the blue curve shows the results of the loss-independent pho-

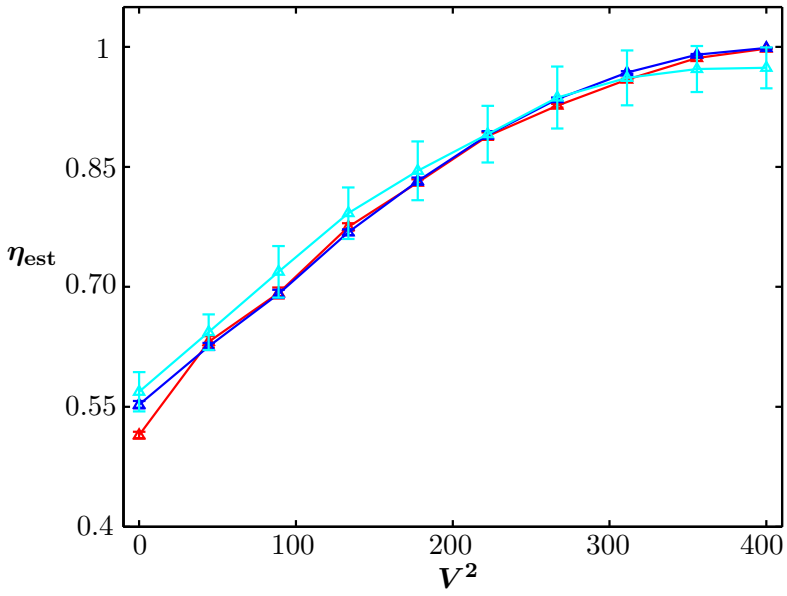

Figure 5.4: A direct comparison of naive photodiode, loss-independent photodiode, and loss-independent camera reflectivity characterization techniques. The effective reflectivity of a MZI, η_{est}, was estimated as the phase was scanned. The phase is proportional to V^2. Measurements were made using the naive photodiode characterization technique (red), the loss independent photodiode technique (blue), and the loss independent camera technique (cyan). The error bars are the standard deviation of one hundred measurements.

todiode method, and the cyan curve shows the results of the loss-independent camera technique. For each data point, the error bars are given by the standard deviation of 100 measurements. Apart from the first point, the two photodiode techniques agree within experimental error. This is as a result of balanced losses, both on the device itself and at input and output coupling. Note, however, that while the loss-independent technique is robust to imbalances in these losses, the naive technique is not. More importantly, the loss-independent camera and photodiode measurements also agree within experimental error. The error is significantly larger in the case of the camera, however, as a result of a relatively low signal to noise. This could be improved by averaging many images but this was not done here as the aim was to compare single-shot measurements. As well as this, the reflectivity from the camera images tends to be an underestimate as the reflectivity

approaches 1. The analysis applied to the data forces the value to be in the range $[0, 1]$ so that any noise on the measured intensities acts to push the estimate away from the boundaries. This effect can also be reduced, however, by averaging multiple images.

The loss independent characterization techniques presented here allow the characterzation of complex circuits consisting of many elements using *a priori* information about the structure of the circuit. These techniques will become increasingly important as circuits increase in complexity. Once the elements of a circuit are characterized, the circuit can be simulated in order to understand the effects of imperfections and errors, predict interference patterns and visibilities, as well as to provide a check on the behaviour of the circuit as a whole. A method for implementing such a circuit simulator is presented in the subsequent section.

5.2 Linear optical circuit simulation

In general, a linear optical circuit can be thought of as mapping inputs to outputs, as shown in Figure 5.5. This mapping is described by a unitary operation, U_{circ}, since linear optical elements preserve photon number. The aim of a circuit simulator is to provide a prediction of the outcome of measurements on the output state of a circuit when a particular state is launched into the input. In general, the input state may be any physically allowed state including those which are pure, mixed, separable, and entangled. Here, however, only input states which are products of coherent superpositions of Fock states in each mode are considered. If these can be successfully simulated, then mixed states can be introduced using beamsplitters of which one output is not monitored and entangled states can be introduced by simulating a CNOT operation.

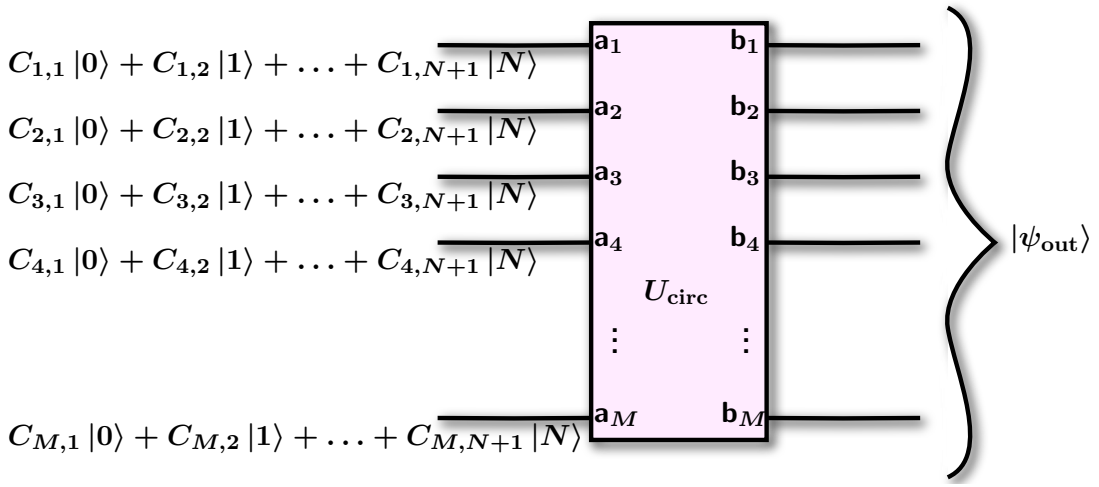

Figure 5.5: A generic linear optical circuit. The $\boldsymbol{M}$ input modes $\mathbf{a_1}$ to $\mathbf{a}_M$, with creation operators $\hat{\mathbf{a}}_1^\dagger$ to $\hat{\mathbf{a}}_M^\dagger$, are mapped to the outputs, with creation operators $\hat{\mathbf{b}}_1^\dagger$ to $\hat{\mathbf{b}}_M^\dagger$, by the unitary operation $\boldsymbol{U}_{\mathbf{circ}}$. Each input mode contains a superposition of Fock states up to a photon number of $\boldsymbol{N}$ so that the total input state is a product state of each input mode. The output state, $|\boldsymbol{\psi}_{\mathbf{out}}\rangle$ is pure but is not in general a product state.

5.2.1 Method

Before describing the method used to simulate a general linear optical circuit, it is useful to define some notation. Throughout this section, lowercase bold letters will signify vectors while uppercase bold letters will denote matrices.

M - The number of modes, beginning with 1.

N - The number of photons in the highest photon number Fock state in any of the input modes.

$\mathbf{C}$ - Matrix of coefficients of Fock states with dimensions M and $(N+1)$. Each row contains the coefficients for a given input mode and therefore must be correctly normalized. The first column are the coefficients of the vacuum for each input, the second column are the coefficients of the Fock state $|1\rangle$ and so on.

$\mathbf{n}_{\text{in}}$ - Vector of the highest photon number Fock states at each input mode.

$\mathbf{U}_{\text{BS}}(i, j, \eta)$ - Unitary matrix of a beamsplitter with reflectivity η between modes i and j.

$\mathbf{U}_{\mathrm{PS}}(i,\phi)$ - Unitary matrix of a phase shifter applying a phase ϕ to mode i.

Defining the input state

The state at the input of the circuit is specified by the matrix of coefficients $\mathbf{C}$. To be explicit, the input state is the pure state

$$|\psi_{\mathrm{in}}\rangle = \bigotimes_{i=1}^{M} \left(\sum_{j=1}^{N+1} C_{i,j} \, |j-1\rangle_i \right) \tag{5.12}$$

$$= \prod_{i=1}^{M} \left(\sum_{j=1}^{N+1} C_{i,j} \frac{(\hat{\mathrm{a}}_i^\dagger)^{(j-1)}}{\sqrt{(j-1)!}} \right) |\mathrm{vac}\rangle \, . \tag{5.13}$$

And the rows of the matrix $\mathbf{C}$ must each satisfy the normalization condition

$$\sum_{j=1}^{N+1} |C_{i,j}|^2 = 1. \tag{5.14}$$

Constructing the circuit unitary

The circuit performs the linear mapping $\mathbf{U}_{\mathrm{circ}}$ so that the input mode creation operators can be expressed in terms of the output mode creation operators by the matrix equation

$$\hat{\mathbf{a}}^\dagger = \mathbf{U}_{\mathrm{circ}} \hat{\mathbf{b}}^\dagger. \tag{5.15}$$

Here, $\hat{\mathbf{a}}^\dagger$ is the vector of creation operators in the input modes 1 to M and $\hat{\mathbf{b}}^\dagger$ is the vector of creation operators in the output modes 1 to M. With the $\hat{\mathrm{a}}_i^\dagger$ expressed in terms of linear combinations of $\hat{\mathrm{b}}_i^\dagger$, a substitution can be made in Equation 5.13, allowing the output state to be calculated.

First, then, the matrix $\mathbf{U}_{\mathrm{circ}}$ must be constructed. As previously discussed, only two

optical elements are necessary for LOQC, beamsplitters and phase shifters. In order to specify a beamsplitter, the two modes upon which it acts must be stated, along with its reflectivity. Its elements are then given by the equation

$$(\mathbf{U}_{\mathrm{BS}}(i,j,\eta))_{k,l} = \delta_{k,l}(1-\delta_{k,i})(1-\delta_{k,j}) + \sqrt{\eta}(\delta_{k,i}\delta_{l,i} - \delta_{k,j}\delta_{l,j}) \tag{5.16}$$

$$+\sqrt{1-\eta}(\delta_{k,i}\delta_{l,j} + \delta_{k,j}\delta_{l,i}), \tag{5.17}$$

where $\delta_{m,n}$ is a Kronecker delta function with a value of 1 if $m = n$ and 0 otherwise. This is simply the identity matrix with the diagonal matrix elements (i,i) and (j,j) replaced by $\sqrt{\eta}$ and $-\sqrt{\eta}$ respectively and the off-diagonal elements (i,j) and (j,i) replaced by $\sqrt{1-\eta}$. For example, in a three mode system, the matrix representing a beamsplitter between modes 1 and 2 is

$$\mathbf{U}_{\mathrm{BS}}(1,2,\eta) = \begin{pmatrix} \sqrt{\eta} & \sqrt{1-\eta} & 0 \\ \sqrt{1-\eta} & -\sqrt{\eta} & 0 \\ 0 & 0 & 1 \end{pmatrix} \tag{5.18}$$

Phase shifters are specified by the mode on which they operate and the phase applied. The matrix elements are given by the equation

$$(\mathbf{U}_{\mathrm{PS}}(i,\phi))_{k,l} = e^{i\phi}\delta_{k,i}\delta_{l,i} + \delta_{k,l}(1-\delta_{k,i}). \tag{5.19}$$

Again, this describes the identity matrix with the element (i,i) replaced by $e^{i\phi}$ so that in

the three mode system, a phase shifter applied to mode 2 is represented by the matrix

$$\mathbf{U}_{\mathrm{PS}}(2,\phi) = \begin{pmatrix} 1 & 0 & 0 \\ 0 & e^{i\phi} & 0 \\ 0 & 0 & 1 \end{pmatrix}. \tag{5.20}$$

For a circuit consisting of K elements, in correct time order, $\mathbf{U}_{\mathrm{circ}}$ is then given by

$$\mathbf{U}_{\mathrm{circ}} = \prod_{i=1}^{K} \mathbf{U}_{\alpha}^{(i)}, \tag{5.21}$$

where α is either PS or BS. This is the first opportunity for a computational speed improvement. The large string of matrix multiplications can be performed in parallel, pair-wise. That is that the first and second matrices can be multiplied together concurrently with the third and fourth and so on. This process can be recursively continued until a single matrix is obtained.

Calculating the size of the state space

The Fock basis in which the input state is written has a potentially infinite extent. In that basis, the creation operators become matrices of infinite size operating on the state vector representing the vacuum. Linear optical components conserve photon number, however, and knowledge of the input state can be used to truncate this space. One way to estimate the matrix size required is to sum up the photon numbers of the largest Fock states with non-zero coefficients in each input mode, giving the maximum total photon number,

$$n_{\mathrm{maxTot}} = \sum_{i=1}^{M} (\mathbf{n}_{\mathrm{in}})_i. \tag{5.22}$$

The creation operators are then square matrices of dimension $(n_{\text{maxTot}}+1)^M$. This is exponential in the number of modes, and hence matrices of this size rapidly become too large to handle. There is an implicit assumption here that every photon at every input can arrive at every output. In fact, this is frequently not the case. Instead, it is possible to use the matrix $\mathbf{U}_{\text{circ}}$ to calculate the dimension of the subspace associated with each output mode. This is obtained by forming the indicator matrix with elements

$$(\mathbf{I})_{k,l} = \begin{cases} 1 & \text{if} \quad (\mathbf{U}_{\text{circ}})_{k,l} \neq 0. \\ 0 & \text{otherwise.} \end{cases} \tag{5.23}$$

Finally, the maximum number of photons for a particular output is given by the sum of the maximum number of photons at each input that can reach it. The vector of maximum output photon numbers is therefore

$$\mathbf{n}_{\text{out}} = \mathbf{I} \cdot \mathbf{n}_{\text{in}}. \tag{5.24}$$

The dimension of each of the output mode subspaces is then given by the elements of $\mathbf{d} = \mathbf{n}_{\text{out}} + 1$, where one is added to include the vacuum for each mode. The dimension of the total output state, D, is then the product of the dimensions of the output mode subspaces. A state vector of this size allows the description of a superposition of Fock state components from zero photons in each output mode to $\mathbf{n}_{\text{out}}$ photons in each output mode. D is therefore given by

$$D = \prod_{i=1}^{M} d_i. \tag{5.25}$$

Each creation operator can therefore be represented as a square matrix of dimension D, constructed from a tensor product of a creation operator on a single mode with the identity operator on all others. In general, a creation operator, $\hat{\mathrm{O}}^\dagger$ operating on a mode of dimension d is given by

$$\hat{\mathbf{O}}^\dagger_{(d\times d)} = \begin{pmatrix} 0 & 0 & 0 & \dots & 0 \\ \sqrt{1} & 0 & 0 & \dots & 0 \\ 0 & \sqrt{2} & 0 & \dots & 0 \\ 0 & 0 & \sqrt{3} & \dots & 0 \\ \vdots & \vdots & \vdots & & \\ 0 & 0 & 0 & \sqrt{d-1} & 0 \end{pmatrix}. \tag{5.26}$$

Therefore, the creation operator which creates a single photon in output mode i can be written as the matrix

$$\hat{\mathbf{O}}^{\dagger(i)}_{(D\times D)} = \left(\bigotimes_{j=1}^{i-1} \mathbb{1}_{d_j}\right) \otimes \hat{\mathbf{O}}^\dagger_{(d_i\times d_i)} \otimes \left(\bigotimes_{k=i+1}^{M} \mathbb{1}_{d_k}\right). \tag{5.27}$$

Transforming the creation operator matrices

With each creation operator written as a truncated matrix in the Fock basis as above, Equation 5.15 becomes an equation relating a *vector of matrices* to another vector of matrices. In order to expand $\mathbf{U}_{\mathrm{circ}}$ to operate on this vector of matrices, a tensor product must be taken between it and a D dimensional identity matrix, $\mathbb{1}_{(D\times D)}$

$$\mathbf{U'}_{\mathrm{circ}} = \mathbf{U}_{\mathrm{circ}} \otimes \mathbb{1}_{(D\times D)}. \tag{5.28}$$

This square matrix has dimension $M \cdot D$, but has only a small number of non-zero elements. For this reason it can be stored in sparse form, dramatically reducing memory constraints and enabling the use of efficient matrix multiplication algorithms.

Having identified the size of each output mode subspace, the input creation operator matrices can be calculated in terms of the output mode creation operator matrices according to Equation 5.15, which now reads

$$\begin{pmatrix} \hat{\mathbf{A}}_1^\dagger \\ \vdots \\ \hat{\mathbf{A}}_M^\dagger \end{pmatrix} = \mathbf{U'}_{\text{circ}} \begin{pmatrix} \hat{\mathbf{B}}_1^\dagger \\ \vdots \\ \hat{\mathbf{B}}_M^\dagger \end{pmatrix}. \tag{5.29}$$

Note that each element in each of the two column vectors is a square matrix with dimension D. There are M elements, each representing one mode, and so the total number of elements in the two vectors is $D \cdot M$ vertically and D horizontally. All that remains is to perform the substitution of these creation operators into Equation 5.13. The sums can be performed in parallel since they are entirely independent and the multiplications can be performed in pairwise parallel. The resulting matrix then left multiplies the vector representing the vacuum, which is a vector of zeros with length D apart from the first element which is 1, giving the output state $|\psi_{\text{out}}\rangle$.

To summarise, a generic input state to a linear optical circuit was defined from a superposition of creation operators acting on the vacuum using Equation 5.13. These operators were then expressed as matrices and propagated through the chip, resulting in the input operators written in terms of the output operators. This was achieved using the unitary matrix describing the circuit, as shown in Equation 5.29. A substitution was then

made in Equation 5.13 to expresses the input state in terms of operators at the output of the chip, yielding $|\psi\rangle_{\text{out}}$. Three steps were taken to improve computational efficiency. First, knowledge of the input state and the circuit allows an upper bound to be placed on the size of the subspace at each output port, reducing the dimensionality of the overall problem. Second, many of the matrices are sparse and so could be stored and manipulated using efficient algorithms. Third, any opportunities to perform operations in parallel were taken.

Predicting measurement outcomes

With $|\psi_{\text{out}}\rangle$ calculated, the result of any measurement can be simulated. All that is required are the positive operator valued measure (POVM) elements associated with the measurement outcomes. The workhorse detector for quantum optics, the APD, is a binary detector that 'clicks' when one or more photons are incident upon it. The measurement outcomes for such a detector, assuming unit efficiency, are 'no click' and 'click' and their associated POVM elements are $|0\rangle\langle 0|$ and $\mathbb{1} - |0\rangle\langle 0|$ respectively. The matrix forms of these POVM elements with a single APD acting on mode i and no measurements on any other modes are

$$\hat{\mathbf{\Pi}}_i^{(\text{APD})}(\text{'no click'}) = \left(\bigotimes_{j=1}^{i-1} \mathbb{1}_{d_j}\right) \otimes \begin{pmatrix} 1 & 0 & \dots \\ 0 & 0 & \dots \\ \vdots & \vdots & \ddots \end{pmatrix}_{(d_i \times d_i)} \otimes \left(\bigotimes_{k=i+1}^{M} \mathbb{1}_{d_k}\right), \quad (5.30)$$

$$\hat{\mathbf{\Pi}}_i^{(\text{APD})}(\text{'click'}) = \mathbb{1}_{(D\times D)} - \hat{\mathbf{\Pi}}_i^{(\text{APD})}(\text{'no click'}). \quad (5.31)$$

The probability of these outcomes occurring is then given by

$$p(\text{`no click'}) = \langle\psi_{\text{out}}|\,\hat{\mathbf{\Pi}}_i^{(\text{APD})}(\text{`no click'})\,|\psi_{\text{out}}\rangle\,, \tag{5.32}$$

$$p(\text{`click'}) = \langle\psi_{\text{out}}|\,\hat{\mathbf{\Pi}}_i^{(\text{APD})}(\text{`click'})\,|\psi_{\text{out}}\rangle\,. \tag{5.33}$$

The POVM element for a particular multiple click pattern occurring can be calculated by multiplying together the POVM elements for the individual clicks before taking the expectation to calculate its probability of occurring.

There is a second measurement that is useful to model because of its use in calculating the intensity correlation functions that will be discussed in the next section. It is an intensity measurement. The operator representing this measurement on mode i is $\hat{\mathrm{I}}_i = \hat{\mathrm{b}}_i^\dagger\hat{\mathrm{b}}_i$ and its expectation gives the average photon number in mode i. It can be expanded to operate on the whole space by writing

$$\hat{\mathbf{I}}_i = \hat{\mathbf{B}}_i^\dagger\hat{\mathbf{B}}_i. \tag{5.34}$$

Although it is useful to be able to calculate the probability of a specific outcome, quantum optics experiments are often, as discussed in Part I of this thesis, based on observing an interference pattern, with special emphasis being placed on the visibility of that interference pattern. It is therefore important to be able to predict the expected visibility of interference occurring in a linear optical network.

5.2.2 Predicting interference visibilities

Interference effects in linear optical networks can be divided broadly into two categories. First, there are those which are observed as some parameter of the circuit itself is changed while the inputs remain the same. An example of this was seen in Part I of this thesis where the phase of a MZI was scanned in order to observe a sinusoidal interference pattern. Second, interference can also be observed when the circuit remains constant but the distinguishability of the input photons is changed, for example, in HOM interference. In each of these cases, one important question is what the visibility of the interference will be with classical versus quantum inputs.

Observing interference of the first kind can be thought of as observing either how the probability of a particular measurement outcome or the value of an intensity cross-correlation function, changes as a function of the parameter. Which it is depends on the detectors used since the binary nature of APDs means that they do not measure a true intensity cross-correlation function. It should be noted, however, that when true single-photon inputs are used and the outcome being monitored is a coincidence between the same number of detectors as input photons, these are equivalent. The expected interference pattern can be straightforwardly simulated by performing the method discussed in the previous section multiple times with the same input state but differing circuits and applying the correct detector POVM. The visibility is then calculated from the simulated interference pattern.

The classical equivalent is measuring an intensity cross-correlation function when phase averaged coherent states of the same average photon numbers as the quantum input states are used. For example, consider the case of a three mode network which is parameterized

by a phase, ϕ. The input is the state $|1,1,0\rangle$, representing 1 photon in each of modes 1 and 2 but the vacuum in mode 3. The measurement of interest is the intensity cross-correlation between output modes 2 and 3. This is given by

$$\Gamma^{(0)}_{2,3}(\phi) = \langle \psi_{\text{out}}(\phi)| \hat{\text{I}}_2 \hat{\text{I}}_3 |\psi_{\text{out}}(\phi)\rangle \,, \tag{5.35}$$

where the superscript in $\Gamma^{(0)}_{2,3}$ denotes that this is the intensity cross-correlation at zero delay. The visibility in this case is then given by

$$V_{\text{quant}} = \frac{\Gamma^{(0)}_{2,3}(\phi_{\max}) - \Gamma^{(0)}_{2,3}(\phi_{\min})}{\Gamma^{(0)}_{2,3}(\phi_{\max}) + \Gamma^{(0)}_{2,3}(\phi_{\min})}, \tag{5.36}$$

where $\phi_{\max}$ and $\phi_{\min}$ are the values of the parameter ϕ for which the cross-correlation takes its maximum and minimum values respectively. Note that this form for the visibility is used for interference patterns which are sinusoidal. If the pattern is not sinusoidal, as in the case of HOM interference, the $\phi_{\min}$ term in the denominator is omitted.

The corresponding classical case is to input two classical fields into modes 1 and 2, which have equal amplitude. The amplitude and phase of these fields can be expressed by a vector of complex numbers, $\mathbf{e}_{\text{in}}$. Only the relative amplitude will affect the visibility although their absolute values will affect the magnitude of the cross-correlations. As well as this, it is only necessary to specify the relative phase between the input fields, θ. The matrix $\mathbf{U}_{\text{circ}}$ contains all the information required to predict the resultant fields in each of the output modes and hence the intensity cross-correlation function for a particular value of the circuit parameter ϕ. The resultant fields in each of the output modes in this case

are given by

$$\mathbf{e}_{\text{out}} = \mathbf{U}_{\text{circ}}(\phi)\mathbf{e}_{\text{in}} \tag{5.37}$$

$$= \mathbf{U}_{\text{circ}}(\phi) \begin{pmatrix} 1 \\ e^{i\theta} \\ 0 \end{pmatrix}, \tag{5.38}$$

where $\mathbf{e}_{\text{out}}$ is the vector of time-independent electric fields in each of the output modes and similarly for $\mathbf{e}_{\text{in}}$. The θ dependent intensity cross-correlation function is then

$$\Gamma'^{(0)}_{2,3}(\phi,\theta) = |(\mathbf{e}_{\text{out}})_2|^2 |(\mathbf{e}_{\text{out}})_3|^2. \tag{5.39}$$

Recall, however, that it is the cross-correlation function for a phase averaged input state that is of interest and hence

$$\Gamma'^{(0)}_{2,3}(\phi) = \frac{1}{2\pi}\int_0^{2\pi} \Gamma'^{(0)}_{2,3}(\phi,\theta)\, d\theta, \tag{5.40}$$

so that the expected classical visibility is

$$V_{\text{class}} = \frac{\Gamma'^{(0)}_{2,3}(\phi'_{\max}) - \Gamma'^{(0)}_{2,3}(\phi'_{\min})}{\Gamma'^{(0)}_{2,3}(\phi'_{\max}) + \Gamma'^{(0)}_{2,3}(\phi'_{\min})}. \tag{5.41}$$

Note that the values of ϕ for which the quantum interference reaches its maximum and minimum value are not necessarily equal to the values for which the classical interference reaches its maximum and minimum values.

For interference of the second type, where the circuit stays constant but distinguishab-

ility is introduced in the input state, the situation can be thought of as one of the input modes being time delayed with respect to the others. The visibility of interference observed in this way is, as in the case of HOM interference, a function of only two points; when the time delay, τ, is very large compared with the coherence time of the inputs and when the time delay is zero. The exact form of the interference is a function of the temporal structure of the input modes, however, it is assumed here that the input modes have identical temporal structure but with one undergoing a temporal delay. At large delays, which will be denoted as $\tau = \infty$, the temporal modes are considered to be orthogonal, that is that their overlap is zero. At zero delay, they are considered to be indistinguishable. In the former case, it is the probabilities which are summed as there will be no interference, while in the latter case the probability amplitudes must be summed. Consider again the three mode system discussed above but with the input mode 2 being the subject of the delay. How to obtain $\Gamma^{(0)}_{2,3}$ in both quantum and classical cases has already been outlined although note that the circuit parameter ϕ is not being varied here.

To obtain the intensity cross-correlation for $\tau = \infty$, one must simulate the system twice, as the method outlined above cannot directly simulate a mixed state. First, the system must be simulated using the specified input state but with vacuum in mode 2 since it is the one being delayed. This results in the output state $\left|\psi^{(1,3)}_{\text{out}}\right\rangle$. Second, a simulation using only photons in mode 2 and vacuum in modes 1 and 3 must be performed. This results in $\left|\psi^{(2)}_{\text{out}}\right\rangle$. The total output state is a classical mixture of the two and must therefore be expressed in density matrix form as

$$\rho_{\text{out}} = \left|\psi^{(1,3)}_{\text{out}}\right\rangle\!\!\left\langle\psi^{(1,3)}_{\text{out}}\right| + \left|\psi^{(2)}_{\text{out}}\right\rangle\!\!\left\langle\psi^{(2)}_{\text{out}}\right|. \tag{5.42}$$

The intensity cross-correlation function at large delay is then given by

$$\Gamma_{2,3}^{(\infty)} = \mathrm{Tr}\{\rho_{\mathrm{out}}\hat{\mathrm{I}}_2\hat{\mathrm{I}}_3\}, \tag{5.43}$$

and the visibility is calculated as

$$V_{\mathrm{quant}} = \frac{\Gamma_{2,3}^{(\infty)} - \Gamma_{2,3}^{(0)}}{\Gamma_{2,3}^{(\infty)}}. \tag{5.44}$$

The classical cross-correlation function is calculated is a similar way, using $\mathbf{U}_{\mathrm{circ}}$ to calculate two sets of output fields, $\mathbf{e}_{\mathrm{out}}^{(1,3)}$ and $\mathbf{e}_{\mathrm{out}}^{(2)}$. The theta dependent intensity cross-correlation function in output modes 2 and 3 is then

$$\Gamma_{2,3}^{\prime(\infty)}(\theta) = \left(|(\mathbf{e}_{\mathrm{out}}^{(1,3)})_2|^2 + |(\mathbf{e}_{\mathrm{out}}^{(2)})_2|^2\right)\left(|(\mathbf{e}_{\mathrm{out}}^{(1,3)})_3|^2 + |(\mathbf{e}_{\mathrm{out}}^{(2)})_3|^2\right). \tag{5.45}$$

Again, in general it is necessary to average over the phase θ, however in this case there is no interference between the two temporal modes and hence θ can be safely set to 0 to achieve the same result. The classical visibility is then

$$V_{\mathrm{class}} = \frac{\Gamma_{2,3}^{\prime(\infty)} - \Gamma_{2,3}^{\prime(0)}}{\Gamma_{2,3}^{\prime(\infty)}}. \tag{5.46}$$

These methods allow the visibility of classical and quantum interference observed at the output of a linear optical network to be simulated. This is a critical ability as linear optical networks become increasingly complex. Ultimately, linear optical networks will reach such a complexity that the output cannot be simulated using a classical computer, however, while this technology is still in its infancy it is necessary to be able to verify both

our understanding and the behaviour of these networks.

Chapter 6

Three photon quantum interference in an integrated device: increasing complexity

Significant progress has been made in integrated linear optical quantum computation including proof of concept demonstrations of some of the basic building blocks. These demonstrations, however, have been limited to relatively simple circuits that have either already been demonstrated using bulk optics and free-space propagation, or would not be significantly more difficult to implement in this way. If integrated photonics is going to be a truly viable platform, the complexity of these circuits needs to be increased to a level where it is not practical to achieve the same results using bulk optics and free space propagation. This includes increasing the numbers of modes, photons, sources, and interference points. In this chapter, for the first time, a circuit with three photons generated by two separate sources propagating in eight spatial modes will be demonstrated. It incorporates three interlocking interferometers which must remain phase-stable and therefore represents a significant step in the level of complexity achievable in an integrated device. The device

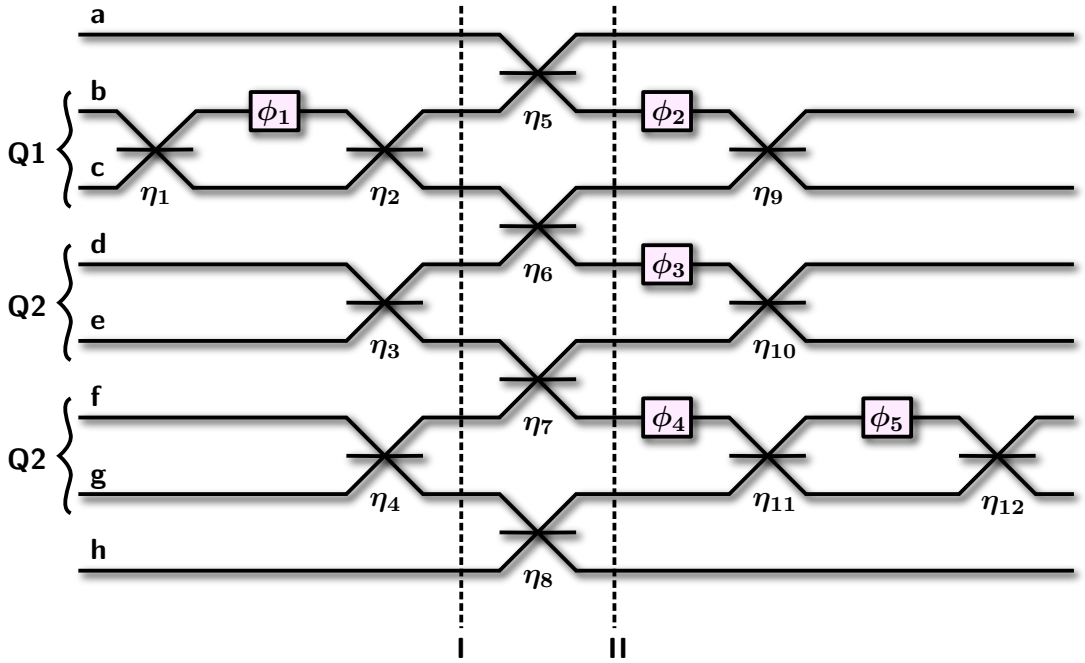

Figure 6.1: Schematic of the three qubit waveguide circuit. The circuit consists of eight modes, labelled **a** to **h**, twelve beamsplitters with reflectivities η_1 to η_{12}, and five phase shifters applying phases ϕ_1 to ϕ_5. Modes **a** and **h** are ancillary, while mode pairs (**b**, **c**), (**d**, **e**), and (**f**, **g**) are used to implement qubits **Q1**, **Q2**, and **Q3** respectively in dual rail encoding. For an explanation of its operation see text.

will be presented and its operation will be explained in detail. Its characterization will then be shown and both two and three photon quantum interference will be observed. Numerical simulations will reveal that the visibility of the latter of these is higher than that which could be obtained using three classical states and *any* comparable circuit. Finally, the estimated parameters of the circuit will be used to provide evidence that the device generates a tripartite entangled state from three initially separable photons.

6.1 The circuit

Figure 6.1a shows a schematic of the linear optical network with the qubit representation of this linear optical network shown in b. The circuit consists of six central modes, labelled

b-*g*, and two ancillary modes, labelled *a* and *h*. Modes *b*-*g* encode three qubits using dual-rail encoding. The beamsplitters are labelled 1 to 12 and their respective reflectivities are η_i. The phase shifters are labelled 1 to 5 and their respective phases are ϕ_i. All beamsplitters before I and after II ideally have a reflectivity of 1/2 while all beamsplitters between I and II ideally have a reflectivity of 1/3. Qubits are implemented using the path encoding in this device, with qubits Q1, Q2, and Q3 occupying mode pairs (*b*,*c*), (*d*,*e*), and (*f*,*g*) respectively.

A circuit similar to this was originally proposed by Ralph [242]. There are two possible interpretations of its operation. The first is that it creates a three qubit linear cluster state and performs an arbitrary single qubit X rotation by measurement while the second is that it performs a teleportation operation, teleporting the state of Q1 onto Q3. It should be noted that this circuit only operates correctly upon the post selection of a single photon in each pair of qubit rails at the output. It is therefore not scalable, however, its value for integrated photonics lies in the proof of concept and significant increase in complexity over previous devices. In either interpretation, it is also of interest to note that there is no entanglement at the beginning of this network as the input photons are in a product state.

In the cluster state interpretation, a three qubit cluster state is created by applying two controlled sign-flip (CS) gates, first between Q1 and Q2 and then between Q2 and Q3. The initial state of Q1 is set by the MZI which is implemented by beamsplitters 1, 2 and phase shifter 1. The initial states of Q2 and Q3 are a logical 0. The four 1/3 reflectivity beamsplitters between I and II implement the two CS operations, producing a three qubit linear cluster state. Q1 is then measured in the diagonal basis, $\{|D\rangle_{\mathrm{L}}, |A\rangle_{\mathrm{L}}\}$ and Q2 is

measured in a phase rotated or anti-rotated basis determined by the phase setting ϕ_3. The state of Q3 is then identical to the initial state of Q1 but with an X rotation. The logical basis in which this is the case is, however, is dependent upon the precise outcome of the measurements on Q1 and Q2.

In the teleportation interpretation, a CNOT operation is first applied to Q2 and Q3 with inputs of $|0\rangle_{\mathrm{L}}$ and $|D\rangle_{\mathrm{L}}$ respectively. This produces a Bell state, providing the necessary resource for teleportation. A single qubit superposition state is again prepared by the MZI operating on Q1. A second CNOT operation between Q1 and Q2 acts as a Bell state analyser, teleporting the state of Q1 onto Q3 up to a local unitary which depends on the exact outcome of the Bell state measurement.

The final elements of the circuit shown in Figure 6.1, phase shifters 4 and 5 along with beamsplitters 11 and 12, implement a single qubit unitary. This is sufficient to enable single qubit state tomography, ideally verifying the operation of the circuit.

6.1.1 The Ralph-White controlled sign-flip gate

The central element of the circuit depicted in Figure 6.1a is shown in Figure 6.2a along with its circuit model representation in 6.2b. It is a linear optic implementation of a CS gate which operates under the post-selection of one photon in each qubit rail pair, the 'coincidence basis,' with success probability $1/9$[243].

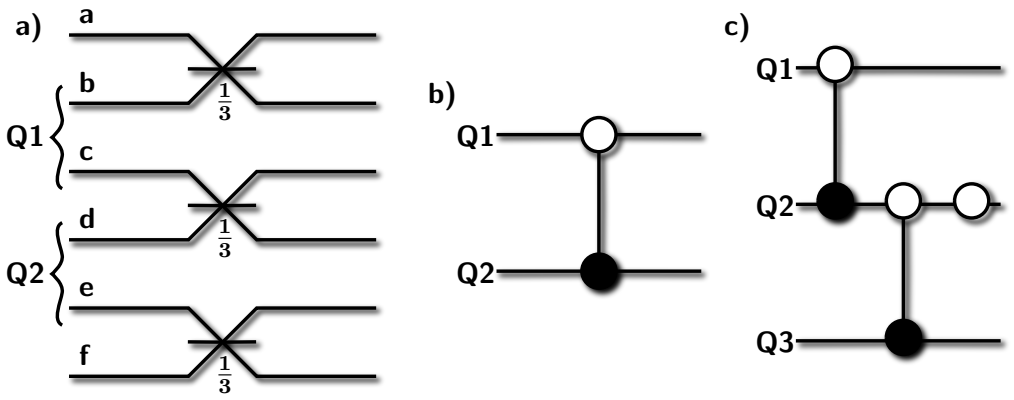

Figure 6.2: a) Schematic of the Ralph-White controlled sign-flip gate. The first qubit, **Q1**, is encoded in modes (**b**, **c**) while the second, **Q2**, is encoded in modes (**d**, **e**). Modes **a** and **f** are ancillary loss modes which are required to balance probability amplitudes. Each beam splitter has reflectivity $\boldsymbol{\eta = 1/3}$. b) Circuit model representation of the controlled sign-flip gate. The white circle indicates that it is the $\mathbf{|01\rangle_L}$ term that receives the sign flip. c) The circuit picture of the operation implemented when two Ralph-White gates are concatenated by re-using one ancilla mode. There is an additional sign flip to the $\mathbf{|0\rangle_L}$ term of **Q2**, as indicated by the open circle.

Represented in the computational basis, the traditional CS gate implements the unitary

$$U_{\mathrm{CS}} = \begin{pmatrix} 1 & & & \\ & 1 & & \\ & & 1 & \\ & & & -1 \end{pmatrix}. \tag{6.1}$$

That is, it flips the sign of the $|11\rangle_{\mathrm{L}}$ term of any input state. In fact, the linear optical network shown in Figure 6.2a implements an operation that is identical under local operations; it implements a controlled sign flip where it is the $|01\rangle_{\mathrm{L}}$ term whose coefficient undergoes the sign flip. This fact is denoted by the open circle on the first qubit in its circuit picture representation, shown in Figure 6.2b. The two can be made identical, for example, by applying a σ_{z} operation to the second qubit either before or after the gate.

In order to see that the linear optical circuit implements this operation, each input

state can be propagated in turn through the circuit. The output of this linear optical gate can then be written for each logical input as:

$$\begin{aligned}
|00\rangle_L &= \hat{b}^\dagger\hat{d}^\dagger|\text{vac}\rangle \rightarrow \frac{1}{3}\left(\hat{b}^\dagger\hat{d}^\dagger + 2\hat{a}^\dagger\hat{c}^\dagger - \sqrt{2}\hat{a}^\dagger\hat{d}^\dagger - \sqrt{2}\hat{b}^\dagger\hat{c}^\dagger\right)|\text{vac}\rangle\,, \\
|01\rangle_L &= \hat{b}^\dagger\hat{e}^\dagger|\text{vac}\rangle \rightarrow \frac{1}{3}\left(-\hat{b}^\dagger\hat{e}^\dagger + \sqrt{2}\hat{a}^\dagger\hat{e}^\dagger + 2\hat{a}^\dagger\hat{f}^\dagger - \sqrt{2}\hat{b}^\dagger\hat{f}^\dagger\right)|\text{vac}\rangle\,, \\
|10\rangle_L &= \hat{c}^\dagger\hat{d}^\dagger|\text{vac}\rangle \rightarrow \frac{1}{3}\left(\hat{c}^\dagger\hat{d}^\dagger + \sqrt{2}\hat{c}^\dagger\hat{c}^\dagger - \sqrt{2}\hat{d}^\dagger\hat{d}^\dagger\right)|\text{vac}\rangle\,, \\
|11\rangle_L &= \hat{c}^\dagger\hat{e}^\dagger|\text{vac}\rangle \rightarrow \frac{1}{3}\left(\hat{c}^\dagger\hat{e}^\dagger + \sqrt{2}\hat{c}^\dagger\hat{f}^\dagger + \sqrt{2}\hat{d}^\dagger\hat{e}^\dagger + 2\hat{d}^\dagger\hat{f}^\dagger\right)|\text{vac}\rangle\,. \qquad (6.2)
\end{aligned}$$

In each case, the output has been written so that the first term is the part of the state which would lead to a single photon ending up in each qubit. The input state $|10\rangle_{\text{L}}$ is the input for which two photons interfere at a beamsplitter. Since there are only two output modes involved rather than the four involved in the other cases, the number of terms in the output state is reduced. The square of the pre-factor of 1/3 in each case therefore gives the probability of the gate operating successfully, $(1/3)^2 = 1/9$. From Equation 6.2 it can be seen that, when only the coincidence basis terms in the output are retained, this circuit implements the transformation

$$\alpha_1|00\rangle_{\text{L}} + \alpha_2|01\rangle_{\text{L}} + \alpha_3|10\rangle_{\text{L}} + \alpha_4|11\rangle_{\text{L}} \rightarrow \alpha_1|00\rangle_{\text{L}} - \alpha_2|01\rangle_{\text{L}} + \alpha_3|10\rangle_{\text{L}} + \alpha_4|11\rangle_{\text{L}}\,. \quad (6.3)$$

As expected, the output state is identical to the input state but with the sign of the coefficient of the $|01\rangle_{\text{L}}$ term flipped.

If many of these gates are concatenated, one would expect the probability of success to scale as $1/9^n$ where n is the number of gates being concatenated. In fact, the ancillary modes can be used as one of the logical rails in additional qubits so that there are still

only two ancillary modes. If this approach is taken, the success probability scales as $1/3^{n+1}$ [242] so that the success probability of the two concatenated gates in the circuit shown in Figure 6.1, is 1/27. In using the ancillary modes in this way, however, an additional phase is accrued. To see this, each of the eight possible logical input states can be propagated through the linear optical circuit. Taking only the coincidence basis terms of the output, the two concatenated CS gates transforms a general input state as

$$\begin{aligned}
&\alpha_1 |000\rangle_{\mathrm{L}} + \alpha_2 |001\rangle_{\mathrm{L}} + \alpha_3 |010\rangle_{\mathrm{L}} + \alpha_4 |011\rangle_{\mathrm{L}} \\
&\quad + \alpha_5 |100\rangle_{\mathrm{L}} + \alpha_6 |101\rangle_{\mathrm{L}} + \alpha_7 |110\rangle_{\mathrm{L}} + \alpha_8 |111\rangle_{\mathrm{L}} \\
&\rightarrow \frac{1}{3\sqrt{3}}(-\alpha_1 |000\rangle_{\mathrm{L}} + \alpha_2 |001\rangle_{\mathrm{L}} - \alpha_3 |010\rangle_{\mathrm{L}} - \alpha_4 |011\rangle_{\mathrm{L}} \\
&\qquad - \alpha_5 |100\rangle_{\mathrm{L}} + \alpha_6 |101\rangle_{\mathrm{L}} + \alpha_7 |110\rangle_{\mathrm{L}} + \alpha_8 |111\rangle_{\mathrm{L}}). \qquad (6.4)
\end{aligned}$$

This transformation is not the same as applying the controlled sign flip operation implemented by the circuit shown in Figure 6.2 first between Q1 and Q2 and then between Q2 and Q3. In fact, the true operation being performed is shown in Figure 6.2c. The circuit implements an additional sign flip on the second qubit which is depicted by an open circle, indicating that it is the sign of the coefficient of the $|0\rangle_{\mathrm{L}}$ term which is flipped.

6.1.2 Operation under the cluster state single qubit rotation interpretation

Figure 6.3a shows the circuit picture of the linear optical network shown in Figure 6.1. Operations before I are thought of as state preparation while operations between I and IV create the three qubit cluster state. Finally, operations after IV implement the single

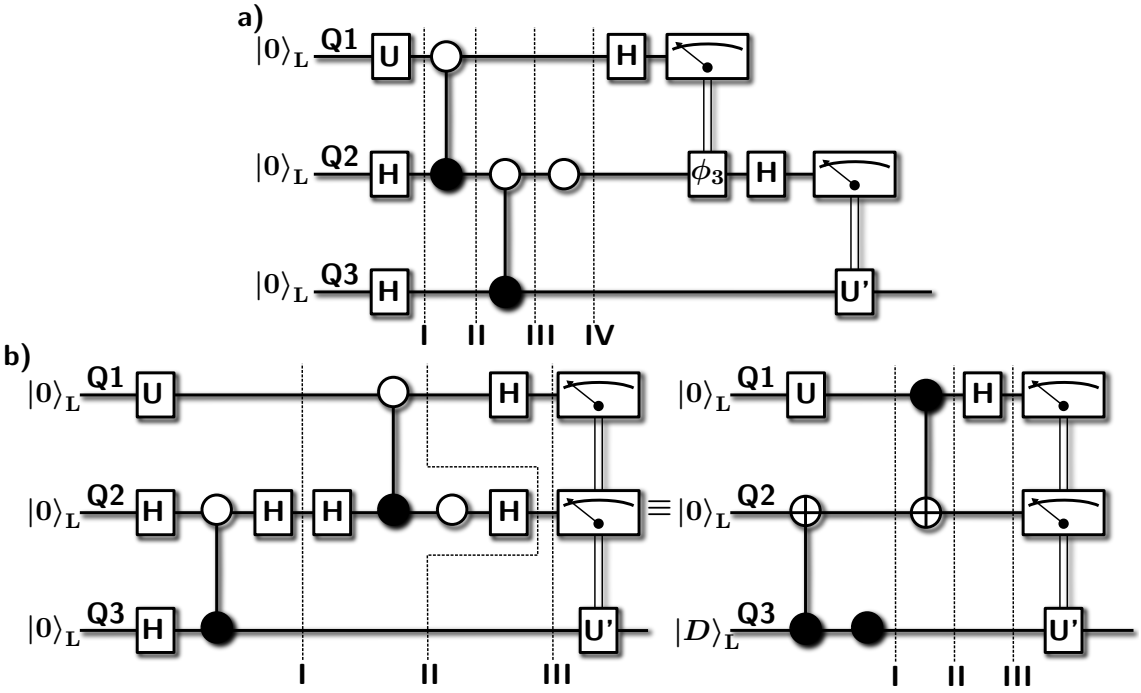

Figure 6.3: Circuit picture representations of the full linear optical circuit under the cluster state single qubit rotation and teleportation interpretations. a) Circuit picture of the linear optical circuit of Figure 6.1 under the cluster state single qubit rotation interpretation. b) Circuit picture of the same linear optical circuit but under the teleportation interpretation. Since Hadamard operations are unitary and Hermitian, fictional adjacent pairs of them can be inserted anywhere in the circuit without affecting the overall behaviour since these pairs are equivalent to the identity. The first circuit is then equivalent to the second circuit shown where lines joining two qubits with a filled circle at one end and an open circle containing a plus at the other represent a CNOT operation. All measurements are performed in the logical basis.

qubit measurements necessary to perform an arbitrary single qubit X rotation. The input state $|000\rangle$, where the 'L' denoting a logical state has been dropped for brevity, evolves so that at I, the state is

$$\begin{aligned} |\psi_{\mathrm{I}}\rangle &= (\alpha_1 |0\rangle + \alpha_2 |1\rangle) |DD\rangle \\ &= |\psi_{\mathrm{in}} DD\rangle . \end{aligned} \tag{6.5}$$

The input has now been prepared. Note that in general, it is not necessary to prepare one qubit in the state $|\psi_{\mathrm{in}}\rangle$ before the entangling operation as an arbitrary single qubit state can be prepared by single qubit measurements on a five qubit linear cluster [209]. Performing the operation in this way would push the experimental requirements beyond the current state of the art in LOQC, however, and hence the approach described was adopted. Next, the CS operations are applied, giving

$$|\psi_{\mathrm{II}}\rangle = (\alpha_1 |0A\rangle + \alpha_2 |1D\rangle) |D\rangle , \tag{6.6}$$

$$|\psi_{\mathrm{III}}\rangle = \frac{1}{\sqrt{2}} [\alpha_1 |0\rangle (|0A\rangle - |1D\rangle) + \alpha_2 |1\rangle (|0A\rangle + |1D\rangle)] , \tag{6.7}$$

$$|\psi_{\mathrm{IV}}\rangle = -\frac{1}{\sqrt{2}} (|\psi_{\mathrm{in}} 0A\rangle + |\psi^*_{\mathrm{in}} 1D\rangle) , \tag{6.8}$$

where $|\psi^*_{\mathrm{in}}\rangle = \alpha_1 |0\rangle - \alpha_2 |1\rangle$, which is a three qubit cluster state of the first type introduced by Raussendorf and Briegel [209]. Note that if U is set equal to a Hadamard operation, $\{|\psi_{\mathrm{in}}\rangle , |\psi^*_{\mathrm{in}}\rangle\} = \{|D\rangle , |A\rangle\}$ and state $|\psi_{\mathrm{IV}}\rangle$ is equivalent under local operations to a Greenberger-Horne-Zeilinger state [244]. This is a three-qubit linear cluster state of the second type introduced by Raussendorf and Briegel [209].

Performing the arbitrary single qubit X rotation begins with a measurement on Q1 in the diagonal basis, $\{|D\rangle, |A\rangle\}$. The correct basis of measurement on Q2 is then dependent upon the outcome of this measurement. If the outcome of the measurement on Q1 is $|D\rangle$ then Q2 must be measured in the phase anti-rotated basis $\{|-\theta\rangle, |-\theta^*\rangle\}$ where $|-\theta\rangle = |0\rangle + e^{-i\theta}|1\rangle$ and $|-\theta^*\rangle = |0\rangle - e^{-i\theta}|1\rangle$. If the outcome of the the Q1 measurement is $|A\rangle$, then Q2 must be measured in the phase rotated basis $\{|\theta\rangle, |\theta^*\rangle\}$ where $|\theta\rangle = |0\rangle + e^{i\theta}|1\rangle$ and $|\theta^*\rangle = |0\rangle - e^{i\theta}|1\rangle$. The measurement in the diagonal basis on Q1 is implemented in the linear optical circuit of Figure 6.1 by setting $\phi_2 = 0$ and performing a measurement on modes b and c after beamsplitter 9. Measurement in the phase rotated bases on Q2 can be achieved by setting $\phi_3 = -\theta$ and performing a measurement on modes d and e after beamsplitter 10. The minus sign in this relation is due to the phase shifter being on the $|0\rangle$ rail of Q2. Expressing $|\psi_{\rm IV}\rangle$ in the appropriate bases for Q1 and Q2 and the logical basis for Q3 leads to

$$\begin{aligned}
|\psi_{\rm IV}\rangle = &-\frac{e^{i\theta/2}}{2}|D\rangle|-\theta\rangle\left\{(\alpha_1\cos\frac{\theta}{2} - i\alpha_2\sin\frac{\theta}{2})|0\rangle + (i\alpha_1\sin\frac{\theta}{2} - \alpha_2\cos\frac{\theta}{2})|1\rangle\right\} \\
&+\frac{e^{i\theta/2}}{2}|D\rangle|-\theta^*\rangle\left\{(\alpha_1\cos\frac{\theta}{2} - i\alpha_2\sin\frac{\theta}{2})|1\rangle + (i\alpha_1\sin\frac{\theta}{2} - \alpha_2\cos\frac{\theta}{2})|0\rangle\right\} \\
&-\frac{e^{-i\theta/2}}{2}|A\rangle|\theta\rangle\left\{(\alpha_1\cos\frac{\theta}{2} - i\alpha_2\sin\frac{\theta}{2})|0\rangle - (i\alpha_1\sin\frac{\theta}{2} - \alpha_2\cos\frac{\theta}{2})|1\rangle\right\} \\
&+\frac{e^{-i\theta/2}}{2}|A\rangle|\theta^*\rangle\left\{(\alpha_1\cos\frac{\theta}{2} - i\alpha_2\sin\frac{\theta}{2})|1\rangle - (i\alpha_1\sin\frac{\theta}{2} - \alpha_2\cos\frac{\theta}{2})|0\rangle\right\}. \quad (6.9)
\end{aligned}$$

It is now clear that for each outcome of the measurements on Q1 and Q2, the X rotation has been implemented, however, a single qubit operation is required in three of the four possible measurement outcomes to correct for a basis transformation. For the outcomes $|D\rangle|-\theta\rangle$, $|D\rangle|-\theta^*\rangle$, $|A\rangle|\theta\rangle$, and $|A\rangle|\theta^*\rangle$, the operations $\sigma_{\rm z}$, $\sigma_{\rm z}\sigma_{\rm x}$, $\mathbb{1}$, and $\sigma_{\rm x}$ respectively

should be applied to Q3 in order to realise the arbitrary X rotation.

6.1.3 Operation under the teleportation interpretation

The circuit picture for operating the circuit under the teleportation interpretation is shown in Figure 6.3b. Note that the order of the two CS gates has been reversed and a fictitious pairs of Hadamard operations have been inserted. This is possible because the two CS operations commute with each other and two consecutive Hadamard operations implement the identity due to their unitarity and so do not change the behaviour of the circuit. With the addition of the Hadamard operations, the circuit can be written as equivalent to the second circuit shown in Figure 6.3b. The equivalence is straightforwardly seen by considering the different regions in turn. In the region to the left of I, the unitary on Q1 remains unchanged and the Hadamard on Q3 has been combined with the input state $|0\rangle$ to form the input state of $|D\rangle$. The remaining CS gate with Hadamard gates before and after on Q2 implements the transformation

$$\alpha_1 |00\rangle + \alpha_2 |01\rangle + \alpha_3 |10\rangle + \alpha_4 |11\rangle \rightarrow \alpha_1 |00\rangle - \alpha_2 |11\rangle + \alpha_3 |10\rangle - \alpha_4 |01\rangle . \qquad (6.10)$$

This is equivalent to a CNOT operation with the second qubit as the control, followed by a σ_z operation on the second qubit. The gates between I and II implement the transformation

$$\alpha_1 |00\rangle + \alpha_2 |01\rangle + \alpha_3 |10\rangle + \alpha_4 |11\rangle \rightarrow -\alpha_1 |00\rangle - \alpha_2 |01\rangle - \alpha_3 |11\rangle - \alpha_4 |10\rangle . \qquad (6.11)$$

This is equivalent to a −CNOT operation with the first qubit as the control. The minus sign leads to a global phase shift in this case and can therefore be ignored. The second circuit in Figure 6.3b also shows the single qubit measurements in the logical basis and the classically controlled unitary, U', that must be applied to correct the final output state.

The teleportation protocol now proceeds in the usual way [50]. Operations to the left of I are thought of as state preparation so that the unitary on Q1 prepares a superposition state to be teleported onto Q3, while the CNOT gate between Q2 and Q3 with a $|0\rangle$ target input and $|D\rangle$ control input creates the Bell state $|\Phi^+\rangle = (|00\rangle + |11\rangle)/\sqrt{2}$ which is then turned into the Bell state $|\Phi^-\rangle = (|00\rangle - |11\rangle)/\sqrt{2}$ by the σ_z applied to Q3. The state at I in Figure 6.3b is therefore

$$|\psi_I\rangle = \frac{1}{\sqrt{2}}(\alpha_1 |0\rangle + \alpha_2 |1\rangle)(|00\rangle - |11\rangle). \tag{6.12}$$

Expressing this state in terms of Bell states in the first two qubits gives

$$\begin{aligned} |\psi_I\rangle =& \frac{1}{2} \left|\Phi^+\right\rangle (\alpha_1 |0\rangle - \alpha_2 |1\rangle) \\ &+ \frac{1}{2} \left|\Phi^-\right\rangle (\alpha_1 |0\rangle + \alpha_2 |1\rangle) \\ &- \frac{1}{2} \left|\Psi^+\right\rangle (\alpha_1 |1\rangle - \alpha_2 |0\rangle) \\ &- \frac{1}{2} \left|\Psi^-\right\rangle (\alpha_1 |1\rangle + \alpha_2 |0\rangle), \end{aligned} \tag{6.13}$$

where $|\Psi^+\rangle$ and $|\Psi^-\rangle$ are the Bell states $(|01\rangle + |10\rangle)/\sqrt{2}$ and $(|01\rangle - |10\rangle)/\sqrt{2}$ respectively. The second CNOT between Q1 and Q2 now acts as a Bell state analyser on their joint state, distinguishing between the four possibilities by disentangling the Bell states into $|\Phi^+\rangle \to |D0\rangle$, $|\Phi^-\rangle \to |A0\rangle$, $|\Psi^+\rangle \to |D1\rangle$, $|\Psi^-\rangle \to |A1\rangle$. The state of the first qubit is

measured in the diagonal basis, again by setting $\phi_2 = 0$ and performing a measurement on modes b and c after beamsplitter 9 in Figure 6.1 while Q2 is already in the logical basis. Once these measurements have been performed, the state of Q1 has been teleported onto Q3 with a basis change that is dependent upon the outcome of the Bell state measurement performed on Q1 and Q2. To complete the teleportation, the unitary U' must be σ_z, $\mathbb{1}$, $\sigma_z\sigma_x$, and σ_x for the outcomes $|\Phi^+\rangle$, $|\Phi^-\rangle$, $|\Psi^+\rangle$, and $|\Psi^-\rangle$ respectively.

6.2 The device

The linear optical circuit shown in Figure 6.1 was implemented using the same direct write UV silica-on-silicon platform described in Chapter 3. Beamsplitters were implemented using x-couplers and thermo-optic phase shifters were implemented by passing current through resistive elements deposited above the waveguides. Coupling into the device was achieved using a commercially available eight channel polarization-maintaining, single-mode-fibre VGA (Oz Optics, VGA-8-250-0-X-10.3-3.8-2.03-P-830-5.5/125-3U-1-1-0.25) at the input and a non-polarization-maintaining VGA at the output. These were coupled using a three-axis stage with a VGA mounted on it and a three angle stage for the waveguide chip. One coupling interface was optimized and glued using an index matched UV-cure epoxy (Dymax OP-52) before the second VGA was attached.

The device was fabricated with short waveguides for modes a and h. Initially, it was thought that these waveguides did not need to propagate from the beginning to the end of the device since their only function was as ancillary loss modes. In fact, this decision impacted the characterization of the device since the two inputs to beamsplitters 5 and 8 could not be independently accessed, making the ratiometric characterization technique

described in Section 5.1 impossible.

6.2.1 Characterization

Characterization of the device was carried out using a continuous wave 825 nm diode laser. This was chosen because of its similarity to the wavelength of the photons used in the main experiment, 830 nm, but much higher average powers could be coupled into the device without damaging it than could be achieved using a pulsed laser system. The higher average power ensured that light scattered out of the waveguides in the transverse direction occupied a larger fraction of the dynamic range of the CCD camera, thereby improving the signal to noise of the measurements.

The laser diode was coupled into a polarization maintaining single mode fibre and its polarization was fixed by passing it through a PBS to filter it before adjusting HWPs before and after the PMF to minimize the transmission through a second PBS at the output of the fibre and after the second HWP. This ensured that the laser was polarized along one of the principal axes of the PMF. The laser could then be coupled to any of the PMF inputs of the input VGA using a FC-FC connector designed for use with PMFs (Thorlabs). These connectors have a tighter tolerance on the keyhole width than non PM FC-FC connectors, reducing possible rotation of the fibre tips which would misalign the principal axes of the two fibres.

Throughput measurement

In order to characterize the throughput of the device, the diode laser was coupled into each input in turn and then the power at each output was measured with a power meter. The ratio of the sum of these output powers to the power at the output of the laser

diode fibre gives the total throughput for that input. Note that the coupling efficiency for each mode is likely to have varied and is likely to have been different at the input and output. This is due to core placement imperfections in the VGAs as a result of core concentricity in the fibres themselves and irregularities in the v-groove cross section, as well as imperfectly optimized coupling. As well as this, the expected coupling ratios to each output even with perfect input and output coupling and zero propagation loss depend on the beamsplitter reflectivities and phase shifter settings. Finally, since modes a and h were not accessible at either input or output, the throughput of input modes for which light can reach beamsplitters 5 and 8 (modes b, c, f, g) was reduced. Never the less, characterizing the throughput gives an indication of the average transmission of the device.

Figure 6.4a shows the total transmission for each input. The maximum throughput of 0.157 for input mode e is acceptable, however, the geometric mean of these efficiencies is 0.097. The probability of three photons being transmitted by the device is therefore $0.097^3 = 0.00073$. This is before taking into account detector efficiency, gate success probability, spectral filtering, and photon heralding efficiency. Throughputs at this level represent a significant challenge for integrated photonics since they are a long way from the level of 0.5 required to implement a scheme which is tolerant to photon loss only [212], and even further from the 3×10^{-3} level required implement a scheme tolerant to more general imperfections [214]. Not only that but even in this scenario, where particular output events are post-selected, the average rate of occurrence of these events becomes so low as to make proof of principle experiments extremely difficult.

Figure 6.4b shows the individual contributions to the values in a) and Figure 6.4c shows

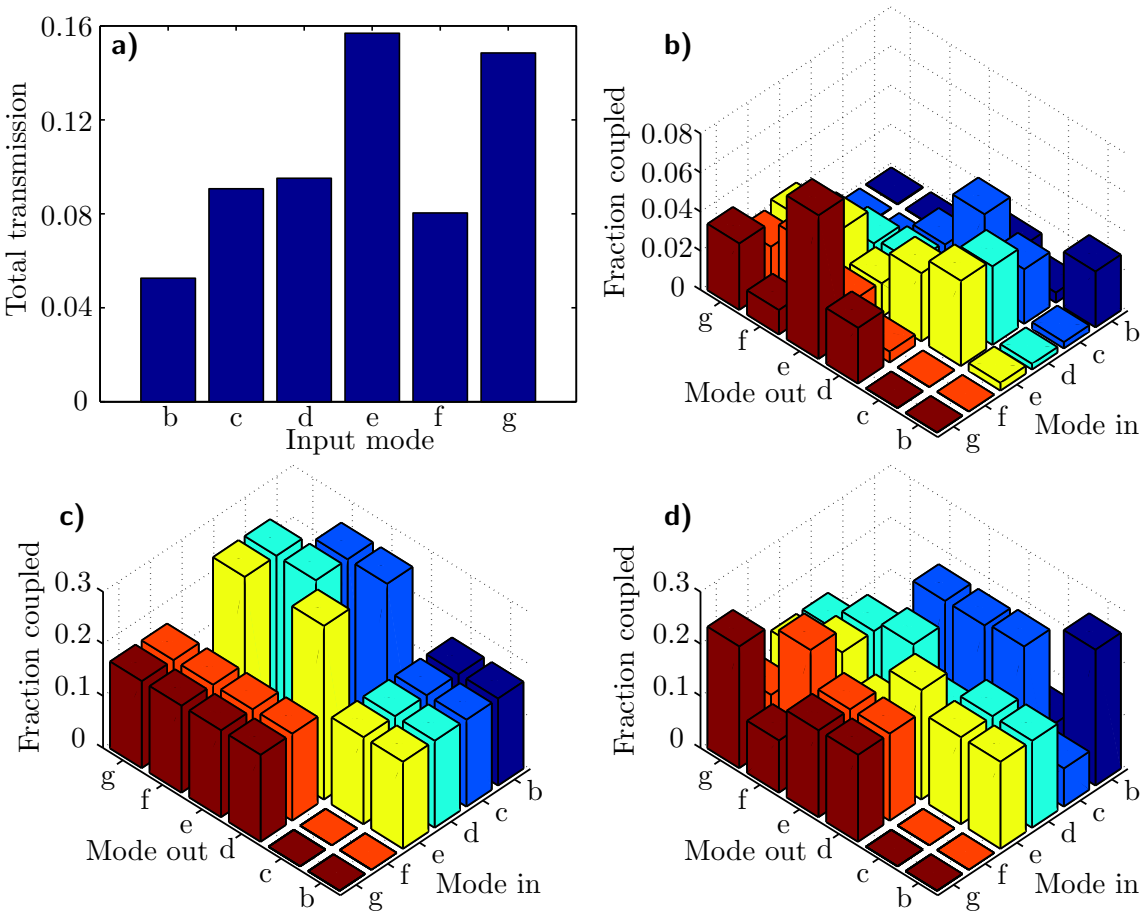

Figure 6.4: Transmission of the chip when light is coupled into each accessible input mode. a) Total transmission when light is coupled into each input mode in turn. Each bar is calculated by coupling light into the indicated input mode and measuring the power at each accessible output mode. The sum of the output powers divided by the input power gives the total transmission for that input. b) The matrix of measured transmissions for each accessible input/output combination. The values in a) were calculated by summing bars of the same colour in b). c) The theoretical matrix of transmissions assuming perfect coupling, ideal beamsplitter reflectivities, and $\phi_1 = \phi_2 = \phi_3 = \phi_4 = \phi_5 = 0$. d) The matrix of transmissions which gives the minimum sum of square differences between the elements of the measured and theoretical transmission matrix when the phases are optimized over. The optimization also had as a free parameter an overall scale factor to act like equally inefficient coupling across the modes at the input and output and uniform propagation loss, however, this was optimized analytically at each iteration.

their theoretical values assuming perfect coupling and transmission, ideal beamsplitter reflectivities, and all phase shifters in the circuit set to zero. The device clearly deviates from this ideal situation.

In order to assess whether this is due only to non-zero phases, the difference between the measured and simulated throughput matrices can be minimized as a function of the five phases in the circuit. First, the difference matrix, $\mathbf{D}$, is formed as

$$\mathbf{D} = \mathbf{T}_{\text{meas}} - x\mathbf{T}_{\text{sim}}, \tag{6.14}$$

where $\mathbf{T}_{\text{meas}}$ and $\mathbf{T}_{\text{sim}}$ are the measured and simulated throughput matrices respectively. The coefficient x is a scaling parameter on the simulated throughput matrix and acts like a global coupling efficiency, affecting all modes in the same way. The optimization therefore assumes that all coupling efficiencies are equal, but not necessarily perfect. This was done because if individual input and output coupling efficiencies were allowed to vary, the measured throughput matrix is reproducible for any set of phases which match the largest throughput in a row or column and give other throughput that are greater than the measured value. The value to be minimized is then the Frobenius norm of the matrix $\mathbf{D}$. This is equivalent to the Hilbert-Schmidt norm since $\mathbf{D}$ is real. The Frobenius norm, $\|\cdot\|_{\text{F}}$, is defined as

$$\|\mathbf{D}\|_{\text{F}} = \sqrt{\sum_{i,j} |D_{ij}|^2}, \tag{6.15}$$

$$= \sqrt{\text{Tr}\{\mathbf{D}\mathbf{D}^\dagger\}}, \tag{6.16}$$

$$\implies \|\mathbf{D}\|_{\text{F}}^2 = \text{Tr}\{\mathbf{T}_{\text{m}}\mathbf{T}_{\text{m}}^\dagger\} - x\text{Tr}\{\mathbf{T}_{\text{m}}\mathbf{T}_{\text{s}}^\dagger + \mathbf{T}_{\text{s}}\mathbf{T}_{\text{m}}^\dagger\} + x^2\text{Tr}\{\mathbf{T}_{\text{s}}\mathbf{T}_{\text{s}}^\dagger\}, \tag{6.17}$$

where the subscripts have been shortened for brevity. This quadratic in x has a single global minimum since the trace is positive and so $\|\mathbf{D}\|_{\mathrm{F}}^2$ can be analytically minimized over x for each chosen set of phases. This leads to an x independent value to be minimized which is a function of the five phases only,

$$\min_x \|\mathbf{D}\|_{\mathrm{F}}^2 = \mathrm{Tr}\{\mathbf{T}_{\mathrm{m}}\mathbf{T}_{\mathrm{m}}^\dagger\} - \frac{\mathrm{Tr}\{\mathbf{T}_{\mathrm{m}}\mathbf{T}_{\mathrm{s}}^\dagger + \mathbf{T}_{\mathrm{s}}\mathbf{T}_{\mathrm{m}}^\dagger\}^2}{2\mathrm{Tr}\{\mathbf{T}_{\mathrm{s}}\mathbf{T}_{\mathrm{s}}^\dagger\}}. \tag{6.18}$$

Figure 6.4d shows the results of this optimization over the five phases, which was performed in Matlab using a bounded nonlinear minimization algorithm. The discrepancy has indeed been reduced and some of the morphological features are reproduced, however, there is still a very definite difference. Since the discrepancy cannot be totally explained by a non-zero phase setting, the coupling efficiencies and losses cannot be uniform and/or the beamsplitting ratios are not ideal.

Beamsplitter characterization

In order to simulate the expected behaviour of the linear optical circuit, its elements must be characterized. The characterization method used was demonstrated in Section 5.1. Here it is applied to the elements of this circuit. Again, due to the short waveguides of mode a and g, beamsplitters 5 and 8 cannot be characterized using the ratiometric technique as the inputs cannot be independently addressed. As well as this, the MZI formed from beamsplitters 1 and 2 as well as the MZI formed from beamsplitters 11 and 12 can only be characterized as a single effective reflectivity beamsplitter due to the inability to access the input modes of both beamsplitters independently. For each beamsplitter that could be characterized using the ratiometric technique, the laser diode was coupled into an

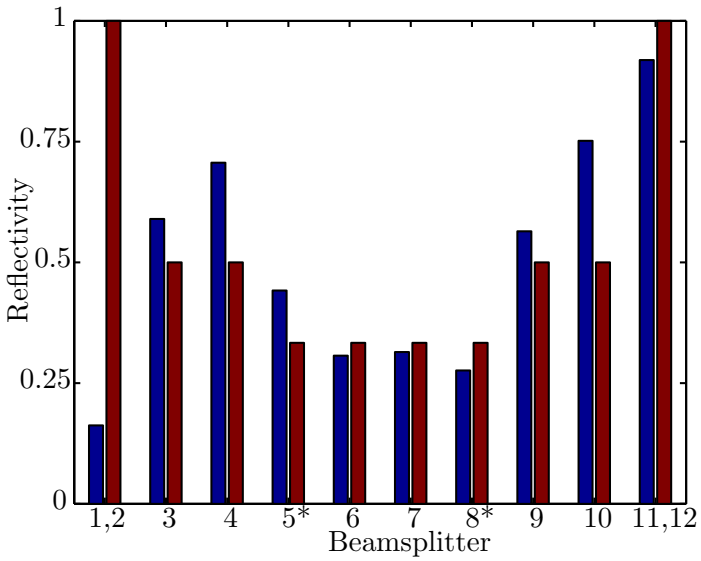

Figure 6.5: The characterized beamsplitter reflectivities (blue bars) and with their ideal values (red bars). The labels 1,2 and 11,12 denote that it is the effective reflectivity of the Mach-Zehnder interferometer made up by these beamsplitters that was characterized. The corresponding ideal reflectivity assumes $\phi_1 = \phi_5 = 0$. The asterisk on the bars for beamsplitters 5 and 8 indicate that these modes could not be characterized using the loss-independent technique. These measurements used the naive technique. The random error on each measurement was smaller than the width of the border of the bars.

input mode leading to only one of the beamsplitter inputs and images of the output were recorded using the same system described in Section 5.1.

Figure 6.5 shows a bar chart of the measured beamsplitter reflectivities, as characterized using the ratiometric technique, alongside their ideal values. There is clearly a significant difference between the intended reflectivities and the true reflectivities. This highlights the importance of improving fabrication techniques, developing circuit elements that are robust to fabrication imperfections, such as those discussed in Section 4.4, and designing circuits that are capable of being characterized.

Phase shifter calibration

There are two important characteristics of the phase shifters. First, it is important to know what phase shift is obtained for each power setting and second, what the phase shift

is when there is no voltage applied. This latter phase shift most likely arises from stress in the waveguide as a result of the deposition of the thin film which makes up the phase shifter.

In order to characterize these two quantities, the MZI in which each phase shifter is situated was treated as a single beamsplitter with an effective reflectivity. This reflectivity was characterized using the loss-independent technique as the voltage was scanned. The theoretical form was then fitted to the data, using the measured beamsplitter reflectivities as a seed for the least squares minimization. The lack of data on the individual reflectivities of beamsplitters 1, 2, 11, and 12, meant that phase shifters 1 and 5 could not be characterized. Again, if modes a and h had been accessible, calibration of these two phase shifters would have been possible.

Figure 6.6 shows the effective reflectivity of the three central MZIs in Figure 6.1 as a function of the square of the applied voltage. The theoretical least squares fits are shown in red (solid), as well as the fringes expected as a result of the beamsplitter reflectivity measurements, in cyan (dashed). Although the fits would be improved by measuring more of the fringe, this was not possible due to the robustness of the phase shifters. Nevertheless, the fits to the data are all very close and also match the expected fringes well in a) and b). In c), there is a discrepancy between the expected fringe and the data. This may arise for three reasons. First, beamsplitter 8 was characterized using the naive technique and so may not be accurate. Second, since the loss-independent camera technique is sensitive to noise when characterizing beamsplitters with reflectivities close to 0 or 1, and the final beamsplitter in the third central MZI has a measured reflectivity of 0.92, this may significantly underestimate the true reflectivity. Third, there may be significant loss

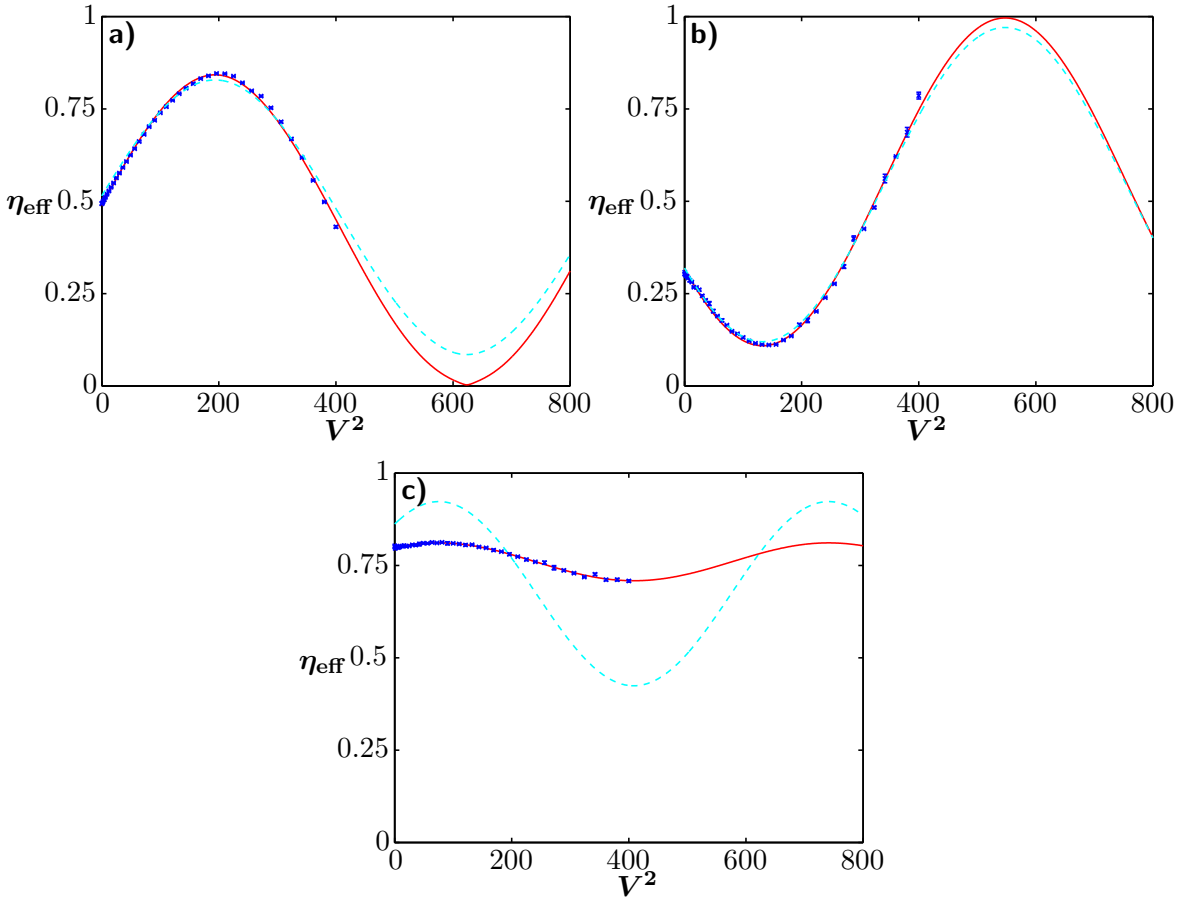

Figure 6.6: Measured effective reflectivity, (η_{eff}) of the three central Mach-Zehnder interferometers as a function of the square of the applied voltage (V^2). a) Applying a voltage to ϕ_2. b) Applying a voltage to ϕ_3. c) Applying a voltage to ϕ_4. In each case, the measured data (blue) is shown with its least squares theoretical fit (red, solid) and the expected fringe corresponding to the measured beamsplitter ratios but using the phase offset and period from the fit (cyan, dashed). The error bars on the data points are of the size of the markers.

Phase shifter	0 V Phase offset (radians)	Error (radians)	Phase per Volt^2 (radians/V^2)	Error (radians/V^2)
ϕ_2	-4.556	0.388	7.306×10^{-3}	2.000×10^{-3}
ϕ_3	-1.011	0.097	7.587×10^{-3}	0.716×10^{-3}
ϕ_4	-3.854	0.038	9.438×10^{-3}	0.375×10^{-3}

Table 6.1: Extracted phase shifter parameters. The error given is one quarter of the width of the 95% confidence interval on the parameter, as returned by the fit. All values are in radians.

occurring inside the interferometer. The loss independent technique produces an estimate that is free from input and output coupling inefficiencies, however, loss occurring inside the interferometer will, in this case, result in a different effective reflectivity of beamsplitters 7 and 8. The net effect is to change the visibility and position, although not the period or offset, of the interference fringe. Table 6.1 gives the zero voltage phase offsets and phase per V^2 extracted from the fits as well as their associated errors.

The characterization of the beamsplitter ratios and the zero voltage phase offsets enables the behaviour of the circuit to be simulated. This is especially important when observing HOM interference in the device as both the expected quantum visibility and the classical visibility limit can be calculated. Observing and analysing this interference is the subject of the next section.

6.3 Two-photon interference

The first step in demonstrating the linear optical circuit shown in Figure 6.1 is to demonstrate that two-photon HOM type interference can be observed. This is critical since it shows that the device preserves the quantum characteristics of the input state, enabling the interference effects on which its successful operation is dependent. As well as this, it provides a method for ensuring optimal temporal overlap between the input photons.

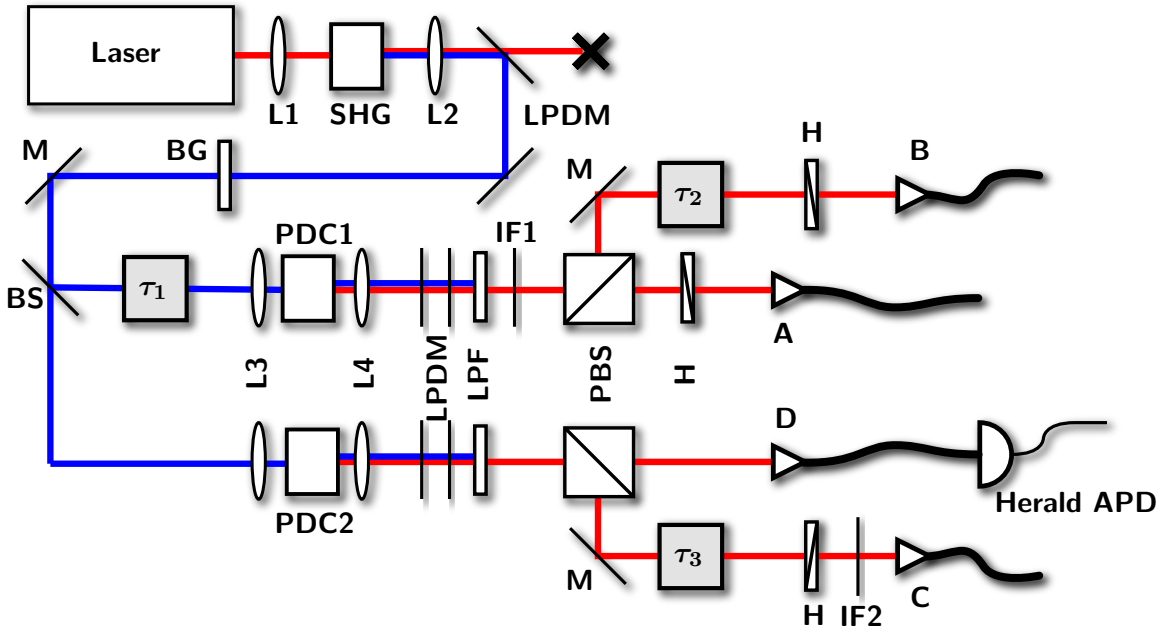

Figure 6.7: Experimental scheme for generating the photon pairs. A titanium sapphire laser, 830 nm central wavelength 80 MHz repetition rate (**Laser**) was focused (**L1**) into a BBO crystal (**SHG**) oriented for second harmonic generation. The resulting 415 nm pulses were collimated (**L2**) and filtered with two dichroic mirrors (**LPDM**) and a blue glass filter (**BG**) before being split at a 50:50 plate beamsplitter (**BS**). One arm was delayed with respect to the other by using an optical delay line, τ_1 before both were focused (**L3**) into KDP crystals aligned for type II, degenerate collinear parametric downconversion. The downconverted photons were collimated (**L4**) and filtered using two dichroic mirrors (**LPDM**) and an interference filter (**LPF**). Both photons from the first parametric downconverter (**PDC1**) were filtered using a 3 nm band pass filter (**IF1**) while only the narrowband photon from the second parametric downconverter (**PDC2**) was filtered (**IF2**). The orthogonally polarized photon pairs were split at a polarizing beamsplitter (**PBS**) before passing through half-wave plates (**HWP**) for polarization adjustment. The vertically polarized photons from each **PDC** were also delayed using optical delay lines, τ_2 and τ_3 before all photons were coupled into polarization maintaining fibre at coupling stages (**A**, **B**, **C**, and **D**).

To operate the device in the manner described in Section 6.1, the logical input state $|000\rangle$ is launched into the device, requiring three indistinguishable single photons. Figure 6.7 shows the source used to produce them. It is very similar to that used in Chapter 2 to generate heralded Holland-Burnett states in that it is based on parametric downconversion in two KDP crystals, generating spectrally disentangled photon pairs [56]. Rather than generating two heralded single photons, however, the required three-photon input is obtained by using both photons from one PDC and heralding a single photon from the second. Since the photons from one PDC have differing bandwidths, they were filtered using a 3 nm band pass filter at 830 nm (Semrock) to make them indistinguishable. A second filter was used on the narrowband photon from the second PDC, again in order to ensure spectral indistinguishability. Placing the filter only in the path of the photons which would be launched into the device enabled the herald photon count rates to be kept as high as possible, reducing the decrease in data rates as a result of the spectral filtering. A second difference to the source shown in Chapter 2 is that two additional optical delay lines were inserted in order to provide the ability to scan the arrival time of all three photons independently. Although it is only the relative arrival time of the photons that is important and hence only two delays are necessary, the extra range added by the third delay was useful in increasing the path differences that could be compensated for. Rough temporal alignment was achieved using a bright alignment beam derived from the residual infrared pump used in the second harmonic generation stage which was re-injected into the same spatial mode as the downconversion pump in order to put a bright beam into the same spatial mode as the downconverted photons. The temporal delay was then scanned while the output spectrum at a single output was measured. Spectral fringes were

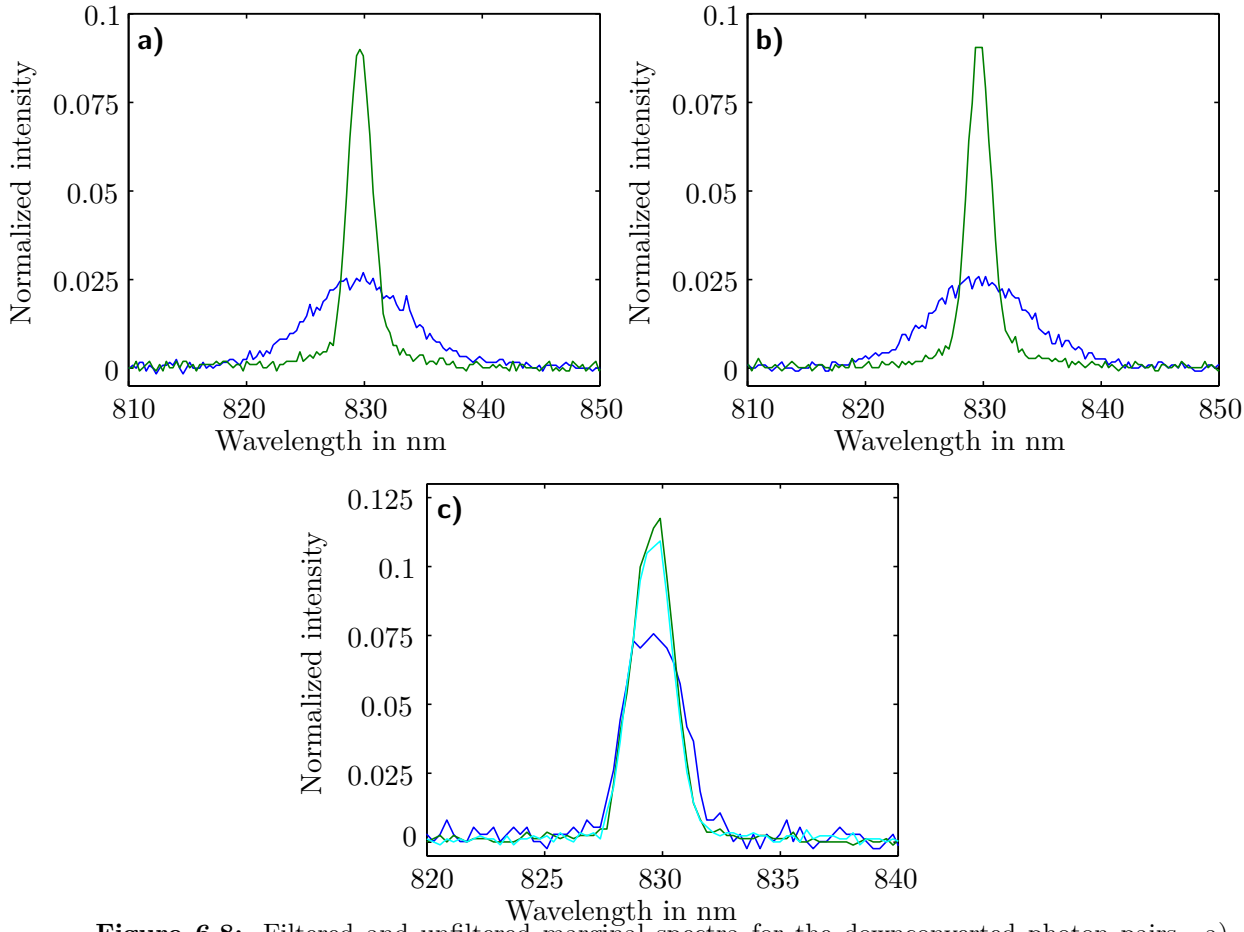

Figure 6.8: Filtered and unfiltered marginal spectra for the downconverted photon pairs. a) Unfiltered narrow (green) and broad (blue) band photons for PDC1. b) Unfiltered narrow (green) and broad (blue) band photons for PDC2. c) Filtered marginal spectra from PDC1 (green and blue), and the filtered narrow band photon from PDC2 (cyan). In each case, the spectra have had their background removed and have been normalized to a unit integral.

observed as the delay approached the zero point and a particular optical delay line was considered roughly aligned when a single fringe spanned the spectrum.

The photon pairs were split using PBSs and then coupled into PMF. The coupling was optimized through trial and error by trying different aspheric lens pairs (new focus), in each case optimizing the coincidence count rates. This resulted in unfiltered coincidence rates of 160 Kcounts s^{-1} and raw heralding efficiencies of 28% being observed by connecting the fibres directly to APDs when ~300 mW of 415 nm wavelength pump was used. The

polarization of the photons was adjusted to be along a principal axis of the PMF by adjusting a HWP before coupling into the PMF and a HWP after the PMF to minimize the transmission through a subsequent PBS. Once the second HWP was adjusted for one fibre, it was locked in place and only the HWPs before the PMFs were adjusted for the other modes. This ensured that all the photons would be launched with the same polarization.

Figure 6.8 shows the unfiltered and filtered marginal spectra for the downconverted spectra. The unfiltered marginal spectra for PDC1 are shown in a) while those for PDC2 are shown in b). These were obtained by connecting the PMFs in turn to a single-photon sensitive spectrometer (Andor Shamrock 163 with iDus camera). The crystal angles were then adjusted to ensure central wavelength degeneracy in the downconversion. Once the unfiltered reference spectra were taken, the filters were inserted and angle tuned in order to maximize the overlap. Figure 6.8c shows the filtered marginal spectra of the three photons to be sent to the device. Assuming flat spectral phase and spectral purity, the filtered spectra have fidelities of greater than 0.95 with each other.

There are three possible combinations of two-photon inputs to the device. Photons can either be launched into modes b and d, d and f, or b and f. With inputs b and d, two-photon interference effects can occur at beamsplitters 6, 9, and 10. Inputs b and f can lead to two-photon interference effects at beamsplitters 7, 10, and the effective beamsplitter formed by the MZI of beamsplitters 11 and 12. Depending on the zero offset of the phase shifters, either dips or anti-dips may be observed in particular output detector combinations. When photons are launched into modes b and f, however, two-photon interference can only occur at beamsplitter 10, leading to an expected dip in coincidence counts between the detectors

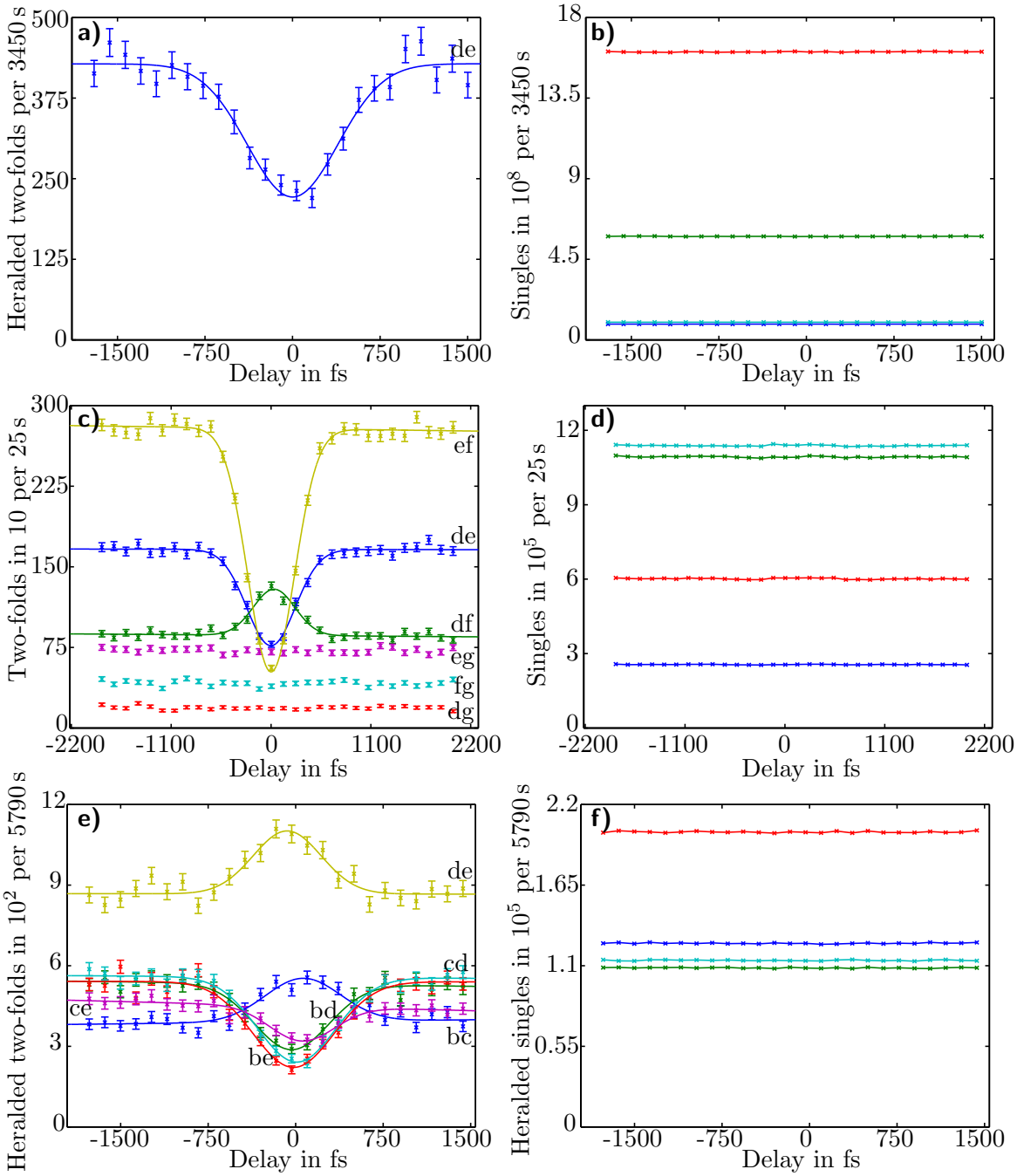

Figure 6.9: Two-photon coincidence rates measured at the output of the device when photons were launched into pairs of input modes while their relative arrival time was scanned. a) Heralded two-fold coincidences as a function of delay τ_1 with stage A connected to input f, stage D connected to input b, stages B and C used as herald signals, outputs d and e monitored. b) Singles rates as a function of τ_1, corresponding to the two heralds and the two signals used in a). c) Two-fold coincidences as a function of delay τ_2 with stage A connected to input f, stage B connected to input d, outputs d, e, f, and g monitored. d) Singles rates as a function of τ_2, corresponding to c). e) Heralded two-fold coincidences as a function of delay τ_2 with stage D connected to input b, stage B connected to input d, stages A and C used as herald signals, outputs b, c, d, and e monitored. f) Heralded singles rates as a function of τ_2, corresponding with e). In a), c), and e), where appropriate, the theoretical fit to the data is shown and the output mode combination corresponding to the data is indicated by the label.

monitoring the output modes d and e.

Figure 6.9 shows the resulting coincidence and singles rates as a function of relative time delay for the three situations. Figures 6.9a and b show the heralded two-fold and heralded singles rates respectively at outputs d and e when stages A and D are connected to inputs f and b respectively and stages B and C are connected directly to fibre-coupled APDs so that coincidences between them act as a herald signal. The relative arrival time was delayed using the optical delay line τ_1. Figures 6.9c and d show the two-fold coincidence and singles rates respectively when stages A and B are connected to inputs f and d respectively. Since both photons from a single crystal were used, there was no herald signal. Outputs d, e, f, and g were monitored and all pairwise combinations are shown. Finally, Figures 6.9e and f show heralded two-fold coincidence and heralded singles rates when stages B and D were connected to inputs d and b respectively and stages A and C were connected directly to APDs to provide a herald signal. Outputs b, c, d, and e were monitored and all pairwise combinations are shown.

Figure 6.10 shows a direct comparison of the measured interference visibilities with different theoretical visibilities. Charts a), b) and c) correspond to the three different two-input combinations: bf, df, and bd. The first bar in each group is the measured visibility; the second is the interference visibility expected as a result of using the circuit parameters obtained from characterization; the final bar is the expected classical visibility using the measured parameters. Theoretical visibilities were simulated using the techniques described in Section 5.2. The red section of each bar denotes the 95% confidence interval on the visibility. For the measured visibility, the confidence interval was retrieved from the fit to the data. For the theoretical visibilities, these were calculated by performing

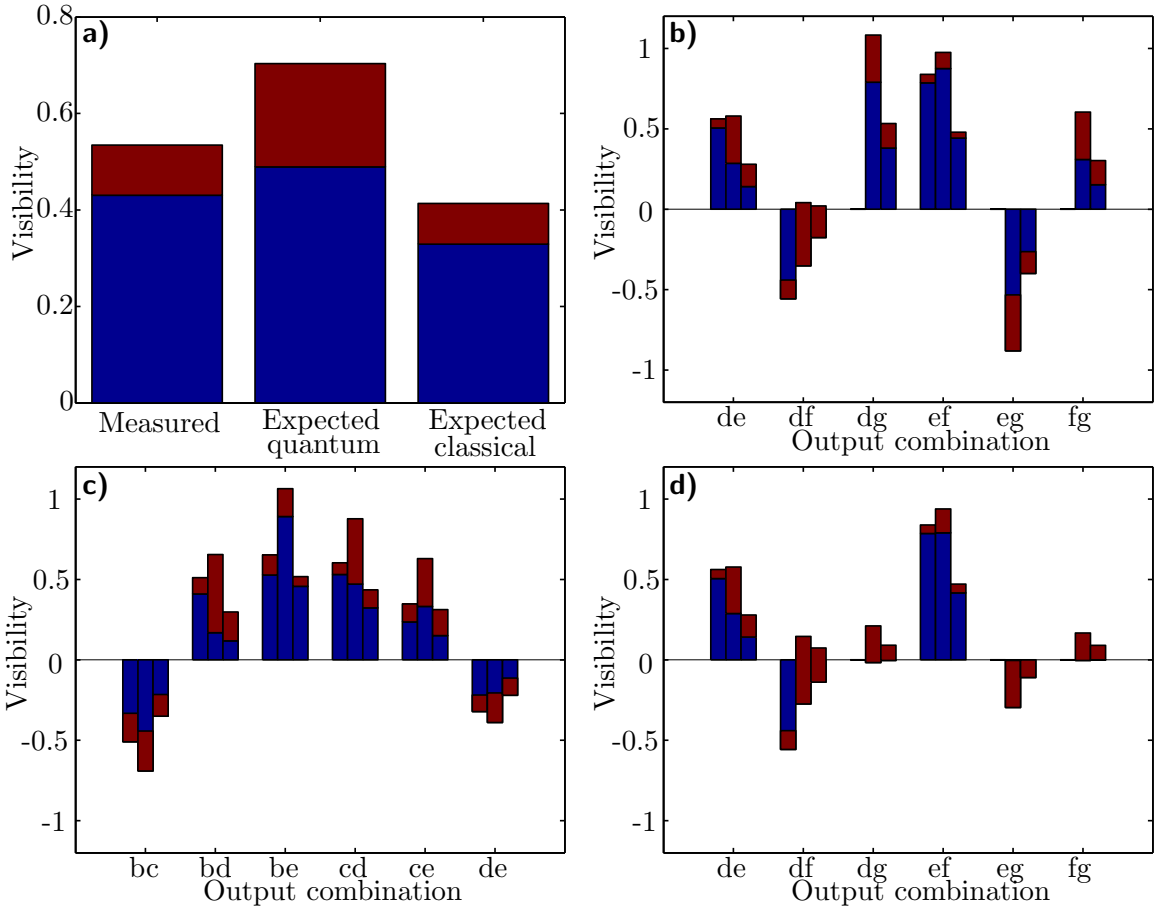

Figure 6.10: A comparison of measured two-photon interference visibilities with the expected two-photon interference visibilities based on the circuit characterization, and the classical limit on visibility. For each bar, the red region indicates the 95% confidence interval, obtained by Monte-Carlo simulation. a) The visibilities corresponding to Figure 6.9a, the coincidence rate at outputs d and e. In b), c), and d), the first bar of each group corresponds to the measured visibility, the second corresponds to the expected quantum visibility, and the third corresponds to the expected classical visibility. Where the first bar is missing, the fit to the data was unstable as a result of a negligible interference pattern. Since the confidence intervals are derived from this fit, there are also no confidence intervals in these cases. b) The visibilities corresponding to Figure 6.9c. c) The visibilities corresponding to Figure 6.9e. d) As in b) but with the effective reflectivity of the Mach-Zehnder interferometer formed by beamsplitters 11 and 12 set to 0.999.

Monte-Carlo simulations of the circuit where the circuit parameters were generated randomly from normal distributions, centred at their estimated values and with a standard deviation of 0.02 on the beamsplitter reflectivities and the errors on the zero voltage phase offsets shown in Table 6.1. The circuit was simulated 100 times, chosen empirically as the number by which the sample standard deviation had converged, and the sample standard deviation was calculated. The 95% confidence interval on the visibility was then simulated value using the estimated circuit parameters plus and minus twice the sample standard deviation.

Charts a) and c) show agreement between the measured and expected visibilities. The correct trends in visibility are observed: the 95% intervals for the measured and expected quantum visibilities overlap in all but one case, and the measured visibility never has a magnitude larger than the expected quantum visibility. In addition, the measured visibility outperforms the expected classical visibility in six of the seven measurements. Chart b) does not show the same agreement. Only the output combination *de* shows agreement between the measured and expected quantum visibilities. As well as this, the visibility of combination *df* outperforms its expected value. This lack of agreement may be due to inaccurate beamsplitter reflectivity characterizations. The most likely reflectivities to be poorly characterized are 8, due to the inaccessibility of both input modes, and the effective reflectivity of the MZI formed by beamsplitters 11 and 12, due to its proximity to a reflectivity of 1. Figure 6.10d is as in b), however, the effective reflectivity of the Mach-Zehnder interferometer formed by beamsplitters 11 and 12 was set to 0.999. This improves the situation considerably, with five out of the six combinations showing agreement, suggesting that this could indeed be a source of error.

These results show that the device is capable of operating in a manner which is inconsistent with classical predictions for two photon inputs. The characterization of the device has been, to some extent, validated due to its agreement with the data, however it is by no means perfect. It is clear that increasing the robustness of the phase shifters is critical to improving the accuracy of their characterization, as is having access to all inputs and outputs including ancillary loss modes.

6.4 Three-photon interference

In order to observe three-photon interference, stages A, B, and D were connected to inputs b, d, and f respectively so that the logical input state to the circuit was $|000\rangle$. The two-photon interference described in the previous section allowed the delays τ_1 and τ_2 to be set to zero relative delay by taking the mean minimum position of all observed interference. From this setting, three-photon interference effects could be observed by scanning τ_2, the relative arrival time of the photon coupled into stage B, through zero delay. Stage C was connected directly to an APD to act as a herald signal for a photon at stage D. Since photons at stage D were coupled into mode b and photons at this input cannot physically reach modes f or g, a three-fold coincidence where one photon is detected in each pair of qubit rails at the output of the device could only have been caused by at least one pair being generated in each PDC. Noise terms arising from multiple pair emissions are therefore a small contribution as they are a higher order process.

All six coupled outputs of the device were connected to APDs as well as the herald signal, so that seven APDs were used in total. Seven singles, six heralded singles, fifteen heralded two-fold, eight heralded three-fold, and twelve heralded four-fold rates were re-

corded using custom-built FPGA electronics. In the heralded two- and three-fold rates, only coincidences across qubits were recorded to mimic the behaviour of the circuit operating in the coincidence basis and the heralded four-fold rates were recorded in order to estimate the noise terms. The total number of heralded four-fold events was 23 in the entire experiment. Monitoring all combinations was not possible due to the limitations of the FPGA system that was used.

Data rates were extremely low as a result of the low throughput of the device. With stages A, B, C, and D plugged directly into APDs and the 3 nm bandpass filters in place, four-fold rates of $\sim 2\,\mathrm{s}^{-1}$ were observed. When coupled through the device, four-fold rates of $0.01\,\mathrm{s}^{-1}$ were observed across all monitored combinations. This low data rate resulted in an experimental duration on the order of 10 days. Over this timescale, fluctuations in the laboratory environment including temperature result in a wandering of the coupling efficiencies at the four stages. In order to mitigate this effect, the 11 points at which the interference was sampled were repeated many times for 60 s per point. This meant that laboratory conditions were approximately constant over the duration of a single pass, allowing their effects to be averaged out in the final data.

Figure 6.11 shows the heralded three-fold rates recorded as the relative arrival time of photons in input mode d, τ_2, was scanned through zero delay. All monitored combinations show some interference, however, combinations involving mode g consistently have a lower count rate, making the uncertainty in those visibilities larger. One interesting feature is that the minima of each fit to the data do not overlap. This suggests imperfect temporal alignment of the photons launched into modes b and f, however, a closer inspection of the errors on the fit parameters indicates that the minima agree within error.

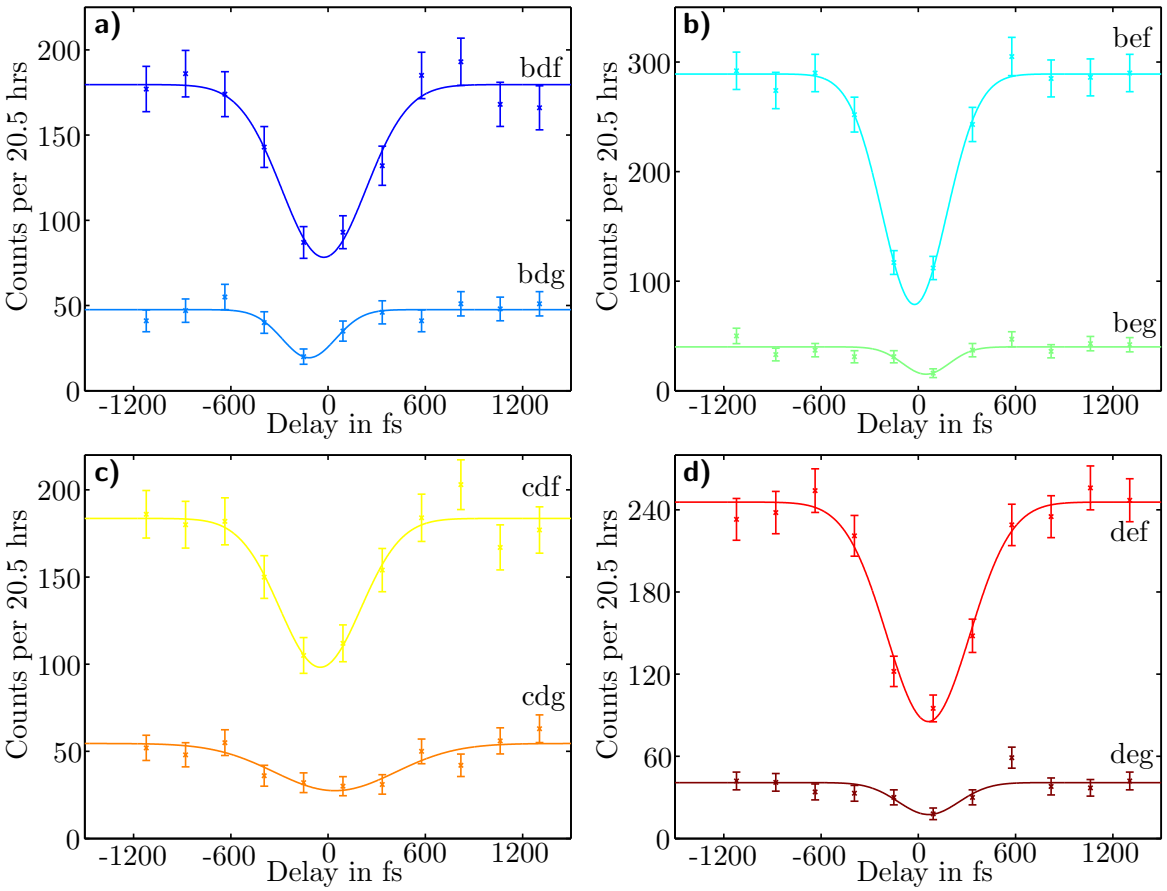

Figure 6.11: Heralded three-fold rates as a function of the time delay τ_2. In each graph the data for a particular output mode combination, denoted by the label, is shown along with its theoretical best fit. The error bars on the data points are Poissonian. The zero point on the x-axes is the mean of the delays corresponding to the minima of the fits to the data.

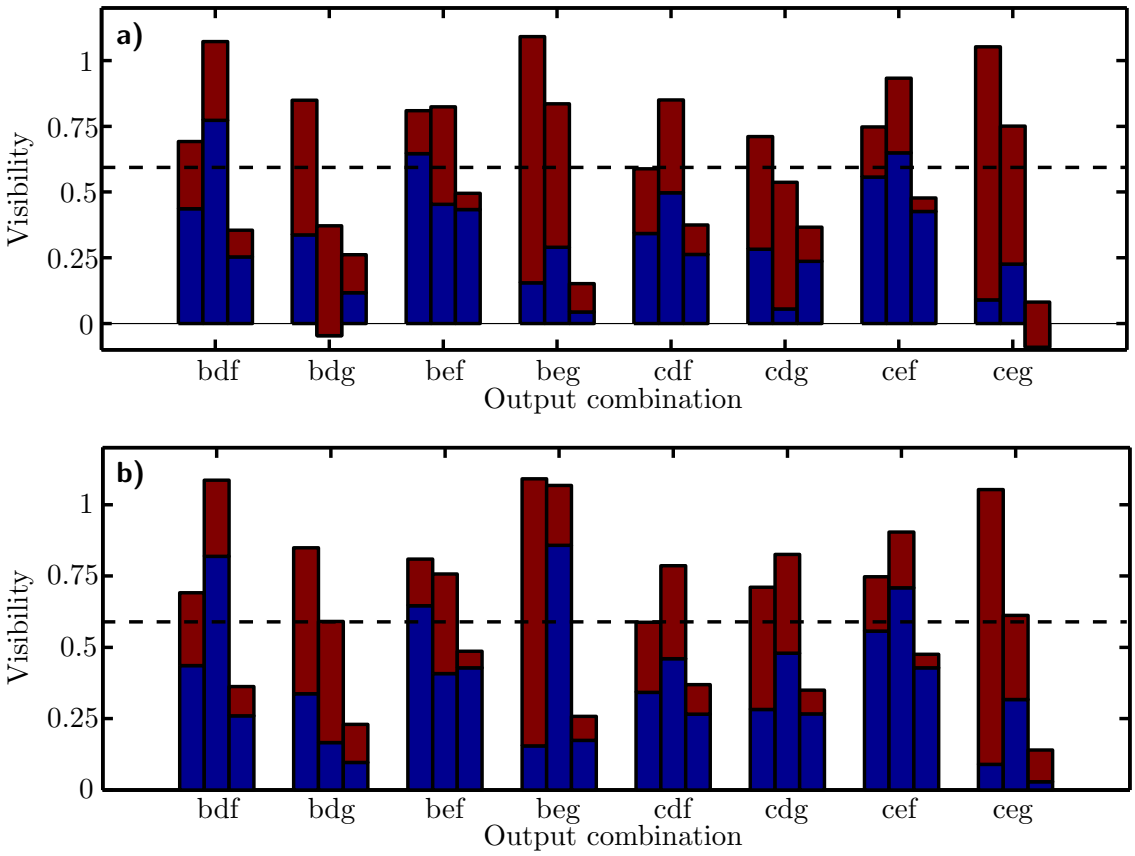

Figure 6.12: Comparison of the measured, theoretically expected, and classical three photon interference visibilities. In both charts, the first bar in each group is the measured visibility, the second is the expected quantum visibility given the measured circuit parameters, and the third is the classical visibility given the circuit parameters. The red sections of each bar denote the 95% confidence interval given by the fit, in the case of the first bar, or Monte-Carlo simulation, in the case of the second and third bars. a) Using the measured beamsplitter reflectivities with an uncertainty of 0.02 and the measured phase shifter offsets and uncertainties. The dashed line denotes the classical limit on three-input visibility, found by optimizing over all beamsplitter reflectivities and phase settings. b) As in a) but replacing the effective reflectivity of the Mach-Zehnder interferometer formed by beamsplitters 11 and 12 with 0.999.

A comparison of the measured and theoretical visibilities are shown in Figure 6.12a. As in Figure 6.10, the first bar in each group is the measured visibility for a given output mode combination, the second is the expected quantum visibility, and the third is the expected classical visibility. The red section of each bar indicates the 95% confidence interval on the value which is obtained either from the fit directly, or by Monte-Carlo simulation. Figure 6.12b shows the comparison again, but using an effective reflectivity of 0.999 for the MZI formed by beamsplitters 11 and 12, in analogy with Figure 6.10d. The difference is less pronounced in this case, demonstrating a reduced impact of this possible mis-characterization on the final analysis.

There is good agreement between the measured and expected values for all output combinations apart from bdf. As well as this, the measured visibility is beyond the 95% confidence interval on the expected classical visibility for all eight combinations and there is no overlap between the confidence intervals in six of them. This constitutes strong evidence that the device is able to support non-classical interference and behave in a manner which is inconsistent with classical predictions for three input photons. Finally, numerical optimizations reveal an upper limit on the classical three-input interference visibility of 0.593 which is shown by the dashed line. This was found by allowing a global optimization algorithm to vary all of the beamsplitter reflectivities and phase settings in order to maximize the three-photon interference visibility. Output combinations bef and cef have a measured visibility greater than this maximum value, beating it by 2.9 and 1.66 standard deviations respectively, conclusively demonstrating the ability of this device to support quantum behaviour.

In addition to observing a three-photon interference visibility greater than that which

can be explained classically, what can be said about the entanglement of the photons in the device? If the phase shifters were robust enough for extended operation and/or the data rates were higher, it would be possible to implement an entanglement witness [245,246] on the three qubit state at IV in Figure 6.3a by using phase shifters 2, 3, 4, and 5, as labelled in Figure 6.1, to measure in different bases. The data rates and lack of phase shifter robustness made this impossible. It is possible, however to perform a Monte-Carlo simulation, as described in Section 6.3, of the state at IV in Figure 6.3a, given an input of three indistinguishable photons. Since beamsplitters 9, 10, 11, and 12 and phase shifters 2, 3, 4, and 5 implement local operations on the qubits, their reflectivities and phase settings will not affect the entanglement of the state. They will therefore be ignored and only the effect of varying the first eight beamsplitter reflectivities along with the value of phase 1 will be considered in the simulation. For each set of circuit parameters, the state at IV in the coincidence basis was simulated and the tangle [247] of the state was calculated. The tangle is an entanglement monotone, that is, a value which ranges monotonically between 0 and 1, where a state with a tangle of 1 is maximally entangled and a state with a tangle of 0 is somehow disentangled. Critically, the tangle distinguishes between bipartite and tripartite entanglement so that tripartite states which are separable under any division have a tangle of 0. Hence a non-zero tangle indicates genuine tripartite entanglement. Given the estimated reflectivities of beamsplitters 1 to 8 and an ideal input of three indistinguishable input photons into modes b, d, and f, the expected tangle of the state at IV is 0.40 ± 0.07. This is larger than zero by 5.7 standard deviations, providing evidence that the experimentally generated state also displays genuine tripartite entanglement.

This work shows, for the first time, a four-photon experiment in an integrated device

demonstrating non-classical behaviour and provides some evidence that from three initially separable photons, a state with tripartite entanglement is generated. The multiple interlocking interferometers in this device would be difficult to realise using bulk optics due to the fraction of a wavelength stability which is necessary in such a scheme. The low data rates in the experiments presented here ultimately meant that it was impossible to operate the device in its originally intended form by demonstrating a single qubit teleportation or cluster state based X rotation. The experimental duration made such experiments infeasible since the coupling of the PDCs wandered over time and correcting the beam pointing error resulted in misaligning the optical delay lines. This could perhaps be improved in future experiments by using an active pointing stabilisation scheme but a more promising route is to use integrated and pig-tailed sources whose alignment will not drift. In addition, the thermo-optic phase shifting elements were not robust enough to be in continuous operation over the experimental duration. Although the exact failure mode of the phase shifters is unknown, the thermal stress on it could be reduced in future work by adjusting the dimensions of both the phase shifting element and the planar structure of the device to make the over-clad layer thinner and the resistive element thicker and longer. This would place a larger resistive element closer to the waveguide resulting in a lower voltage, and hence heat build up, for the same phase shift.

The observation of three photon interference in a waveguide device with a visibility beyond that which can be explained by classical physics represents a critical step forward for integrated photonics. As previous discussed, however, the approach taken here is not scalable. Fundamentally, the linear optical gates used in the device demonstrated here do not scale, however, there is a more practical reason. The probabilistic method of

generating the necessary single photons and the low throughput of the device itself results in an extremely low data rate. A practical device must be able to generate high quality input states in polynomial time otherwise any computational enhancement is rendered useless. Ultimately, this is likely to require quantum memories for the synchronisation of multiple probabilistic sources, as well as extremely high efficiency detection with photon number resolution. The former is beyond the scope of this thesis, however, the latter will be investigated in the next chapter.

Chapter 7

Integrated Transition Edge Sensors

Detection is a critical step in any experiment involving photons: in the KLM scheme of LOQC it is the means by which two-photon interactions are achieved; in one-way quantum computation schemes, measurements manipulate the encoded information; in precision measurement they provide a way of extracting information about the parameter of interest; in state generation, they can be used to conditionally prepare photons. In all of these areas, the key requirements are high efficiency, low noise, photon number resolution, and high speed. No detector technology to date has demonstrated all of these characteristics but all apart from the latter have been demonstrated by one, the superconducting transition edge sensor (TES). In this chapter, a proof of principle waveguide-coupled TES that can be directly integrated with chip-based waveguides and operates at telecommunication wavelengths will be demonstrated. Routes towards increasing the efficiency of the devices towards those which have been achieved in non-waveguide coupled versions will also be discussed.

As discussed throughout this thesis, photonics provides a promising path for building

and using complex quantum systems for both exploring fundamental physics and delivering quantum-enhanced technologies in information processing, metrology, and communications. Currently, the only feasible route towards sufficient complexity is integration, due to the high density of optical modes that can be contained within a single device and the extraordinary level of control that can be exercised over them. Although much research has gone into developing integrated elements at telecommunication wavelengths for classical applications, their use in the quantum regime has been limited, in large part because of intrinsic inefficiencies in input coupling, detector coupling, and propagation. The effect of these inefficiencies, as shown explicitly in Part I of this thesis with respect to metrology, is to reduce or remove any quantum advantage attainable with a given device[41,141,208,212,248–250]. Developing high-efficiency detectors that are compatible with these complex, high-density systems is therefore a critical enabling step for quantum photonics.

7.1 Superconducting transition edge sensors

Current single-photon-sensitive detectors for telecom wavelengths include APDs[251], superconducting nanowires[252], and superconducting TESs[253,254]. Of these, indium gallium arsenide (InGaAs) APDs are the only commercially available telecom-band, single-photon-sensitive detector, however, they suffer from low efficiencies and high dark-count rates. Superconducting nanowire detectors offer extremely fast detection with timing jitter reported in the tens of picoseconds[252] and can have relatively high quantum efficiencies compared to that of InGaAs APDs[125,255]. Neither of these detector technologies, however, has the ability to intrinsically resolve photon number and either spatial[256] or temporal[89] multi-

plexing must be employed in order to achieve even pseudo photon number resolution. In contrast, TESs, which function well across a very broad range of wavelengths, have been used to demonstrate the highest recorded detection efficiencies and number resolution, reaching 98%[257] and can determining the photon number of pulses of light containing up to between 10 and 30 photons depending upon the design[253].

TESs are sensitive detectors that use the electrical/thermal properties of a superconducting thin film to distinguish the energy of a discrete number of photons. Superconducting metals exhibit a resistance change from a high-temperature value of several ohms to negligible material resistance values at temperatures below the critical transition temperature, T_c. Materials used to make detectors sensitive to optical photon energy have transition temperatures on the order of 100 mK with transition widths as narrow as 1 mK. By thermally positioning the metal in its superconducting transition via voltage biasing, single absorbed photons create a detectable resistance change[258]. By use of this technique, materials such as tungsten or titanium can be fabricated into microcalorimeters sensitive enough to resolve the absorption of a single optical photon. These detectors have advantages over other types of single-photon detectors which make them ideal for integration into quantum optical systems. Efficiencies have been reported as high as 95 % at 1550 nm and they have a wavelength range exhibiting high quantum efficiency from the visible to the infrared. This makes them more efficient and wavelength-expansive than any silicon or InGaAs detector[254,259]. Additionally, TES detectors exhibit a thermal recovery time as short as 1 μs[259], and arrival-time jitter of less than 100 ns full width half maximum. Unlike most conventional high temperature photodetectors, TESs are intrinsically number-resolving, meaning that they can distinguish the energy correlated to the

absorption of not only a single photon, but to the absorption of several photons. In combination with the high efficiencies that have been demonstrated, this enables projection onto a particular Fock state with extremely high fidelities, something that is crucial for LOQC.

To operate a TES, the bath temperature of the whole system is held below the critical temperature of the TES and a voltage bias is applied to the TES itself. Joule heating produced by this voltage bias is carefully controlled to increase the TES temperature in order to position it within its sharp transition region. The TES will remain in a steady-state at this temperature due to electrothermal feedback [258] until a photon is absorbed. In a properly thermally engineered TES, the absorption of a photon will result in an increase of the TES temperature, with a corresponding increase in the TES resistance and therefore a decrease in the current. Under constant-voltage bias, the drop in the TES current is proportional to the absorbed energy, and this current change is measured by using DC-superconducting quantum interference device (SQUID) amplifier circuits.

All of the detector technologies discussed above typically employ designs in which the detected photons are normally incident on the detector. In order to achieve high efficiencies in this situation, care must be taken to impedance-match the incident field to the detector in order to avoid reflections of the optical signal. This typically involves fabricating a high reflecting layer behind the detector to reflect any light that passes through it unabsorbed and an anti-reflection coating in front of the detector to minimize reflections at the front face. Moreover, normal incidence-detection schemes are intrinsically limited to monitoring the modes that emerge from the end facet of the device. By using this detection scheme, inferring information about a quantum state or circuit element inside a device will only

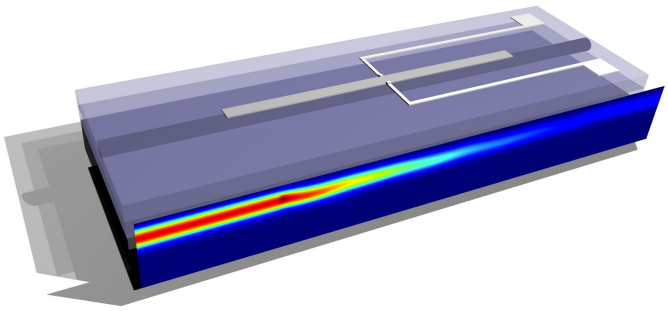

Figure 7.1: Schematic of the evanescently coupled photon counting detector. The detection layer is deposited on top of a UV-laser written silica waveguide structure. The simulated intensity distribution along the length of the device can also be seen at the front of the device schematic.

become more problematic as circuits move towards the complexities required to study effects beyond the scope of classical computational power [142,241,250].

7.2 Evanescently-coupled photon counting detectors

In this chapter, the operation of a new concept for broadband, efficient, single-photon detection is demonstrated, the evanescently-coupled photon counting detector (ECPCD), by merging two well-established technologies: photonic circuits and photon-number-resolving TESs. A conceptual schematic of such a device is shown in Figure 7.1. ECPCDs display the low noise and single-photon sensitivity required to operate in the quantum regime and, due to the evanescent coupling concept, are integration compatible as they target a single guided mode at an embedded location within the circuit and maintain a fixed alignment. The photon absorber, in this case a tungsten TES, is placed in the evanescent field of the guided mode of a waveguide passing underneath the detector. As the mode propagates through the detection region, it is coupled continuously into the detector via absorption. The continuous, evanescent coupling and the confinement of the waveguide mode enables

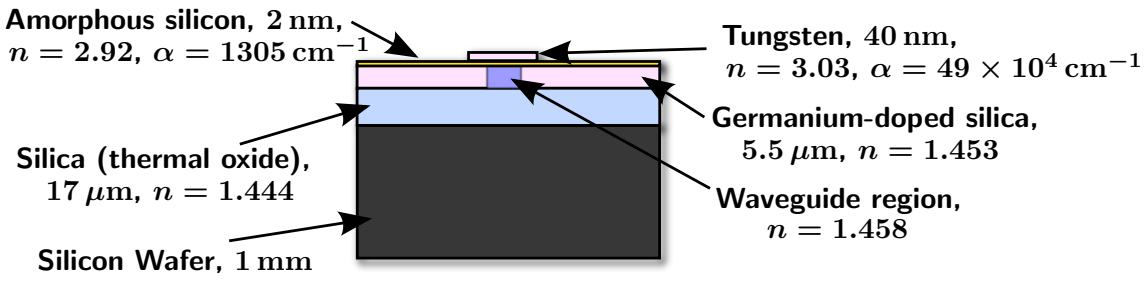

Figure 7.2: The cross sectional structure of the tungsten transition edge sensor based evanescently-coupled photon counting detector. The refractive indices and material α values shown were those necessary for simulation purposes. Those not shown were assumed to be zero.

extended interaction regions, providing a straightforward way to increase efficiency even when the coupling is weak, without limiting the detector acceptance bandwidth. As will be shown, a key feature of such a configuration is that the weak coupling allows use of a detector design that does not significantly modify the effective index and spatial profile of the guided mode, minimizing reflections at the beginning of the detection region. The detector is therefore intrinsically almost fully impedance-matched. Finally, the lithographic construction makes this concept compatible with fabrication techniques for conventional telecommunications planar lightwave circuits, enabling sufficiently high detector densities to be useful with complex circuit designs.

7.3 Device structure

A cross section of the structure of the devices that were fabricated and tested is shown in Figure 7.2. The waveguide structure is similar in form to that described in Chapter 3 and the actual waveguide was produced using the same method of focusing a UV laser into the photosensitive germanium-doped silica core layer. Here, a 5.5 μm core layer was deposited on top of a 17 μm underclad layer. No overclad was deposited so that the evanescent coup-

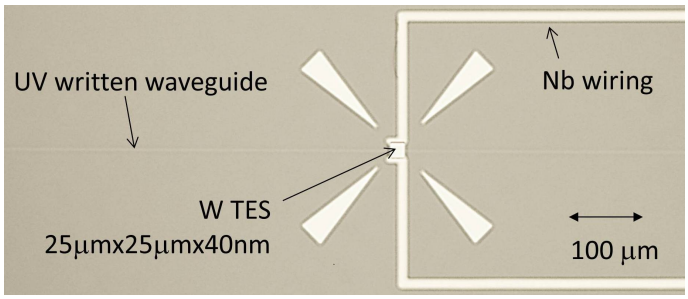

Figure 7.3: Microscope image of the fabricated TES on the optical waveguide. The TES dimension is $25\,\mu\text{m} \times 25\,\mu\text{m} \times 40\,\text{nm}$. The tungsten TES bisects the waveguide in the centre. The niobium wiring attaches top and bottom of the TES and exits off the chip to the right. Additional arrows simply serve as alignment marks and guide.

ling to the TES could be maximized. The refractive index contrast between the core layer and the underclad was 0.6 %. These layers were deposited onto a silicon wafer by FHD as with the device discussed in Chapter 3. The waveguide itself was of width $\sim 6\,\mu$m with a gaussian horizontal refractive index profile and step vertical refractive index profile. The index contrast between the waveguide and the core layer was 0.3 %. The optical properties of the tungsten and amorphous-silicon films were measured at NIST for a thickness of 25 nm. A critical feature of this structure is that the surface roughness is typically less than 1 nm, making it suitable for deposition of the TES structures. High surface roughness increases thermal stresses in the TES at cryogenic temperatures, suppressing its transition temperature. Although these stresses can be relieved to some extent by depositing an amorphous silicon layer underneath the TES, this material has unfavourable optical characteristics, namely high real and imaginary parts of the refractive index, and so must be kept to a minimum.

After waveguide fabrication, the TES structure was deposited on the top surface of the chip. The deposition process was equivalent to the process used in other studies [79,254]. First, a 2 nm thick layer of amorphous silicon was deposited followed by a tungsten layer

that was DC sputtered. The tungsten was then patterned and etched to produce the final TES geometry. Wiring to the tungsten TES was established using niobium, which was sputtered and lifted off. Due to the significantly higher superconducting transition temperature of niobium compared to tungsten, these wires are superconducting during TES operation. Figure 7.3 shows an image of a finished device, taken with a microscope.

7.4 Modelling a simple device

Several effects can affect the efficiency of the ECPCD. First, the transverse spatial mode supported by the waveguide with no TES over it will be different from the mode supported by the waveguide under the TES due to the presence of the tungsten which has a relatively high refractive index. These two regions will be referred to as the 'propagation' and 'detection' regions respectively. At the interface between the two regions, two effects can occur. First, the two modes may have different effective indices. If this is the case, a Fresnel-type reflection will occur, introducing loss. Second, the overlap of the transverse spatial mode may be reduced from unity. This can result in an imperfect transfer of light from the fundamental mode of the propagation region to the fundamental mode of the detection region. Since the waveguide is single mode in both regions, light not coupled into the fundamental mode is coupled to radiative modes and can be lost without being detected. In addition to these modal effects, the total absorption into the detector is governed by the size and shape of the tungsten layer. The volume of a single detector is, however, constrained by the detection mechanism. Absorbed photons create a temperature change that can be measured via the resulting change in resistance [258]. To resolve this temperature change, the heat capacity of the device must be carefully specified. This

in turn limits the volume of superconducting material that may be used. The choice of detector geometry is therefore critical to ensure good energy resolution and high-efficiency absorption.

Fimmwave and Fimmprop (Photon Design Ltd), commercial numerical mode-solver and propagation tools based on film mode matching and eigenmode expansion respectively, were used to model the device and investigate suitable design parameters. The mode-solver allows the mode overlaps between the two regions to be calculated so that mode mismatch can be evaluated. The eigenmode expansion method implemented by Fimmprop was used to propagate the modes through the device and obtain its overall scattering matrix, from which the absorption coefficients due to the detector layer were deduced. This approach takes account of any reflections and mode mismatches at the interfaces to give an estimate of the modal absorption coefficients, α, at the detector region.

Figure 7.4a shows the calculated absorption coefficient for the transverse electric field (TE) and transverse magnetic field (TM) modes of the waveguide as the thickness of a tungsten layer 25 μm wide is increased. This calculated absorption coefficient includes both the absorption in the tungsten TES and leakage from the propagating mode, as our modelling does not discriminate between them. A clear peak in the absorption coefficient for the TM mode is visible at around 45 nm thickness. Initially, the absorption coefficient increases, due to the increase in volume of absorbing material interacting with the propagating field, but as the layer thickness increases beyond the skin depth of tungsten and the field no longer penetrates through the layer, the guided mode begins to be pushed away from the tungsten, and the total flow of energy into the tungsten starts to be reduced.

Figure 7.4b shows the overlap of the TE and TM modes in the detection region with

those in the propagation region. The TM mode is affected more than the TE mode, however even for a 100 nm thick tungsten layer, the overlap is still ~ 0.98, clearly demonstrating how little the spatial mode is perturbed by the presence of the detector.

The peak in absorption and lack of mode mismatch suggested that a 45 nm thick layer of tungsten should be used. A thickness of 40 nm has previously been shown to work for fibre coupled detectors in the geometry $25\,\mu\text{m} \times 25\,\mu\text{m} \times 40\,\text{nm}$ [253]. This geometry provided number resolution of tens of photons while still exhibiting an easily accessible superconducting transition temperature. As this geometry is both known to work and is close to the optimal thickness for maximum modal α, it was chosen for the initial tests presented here. The intensity distribution of the TM mode in the propagation region is shown in Figure 7.4c while the intensity distribution of the TM mode in the detection region for a tungsten thickness of 40 nm is shown in Figure 7.4d. The similarity of these distributions highlights the high overlap of the modes in the two regions. Only a slight distortion in the vertical profile of the mode in the detection region can be seen along with a small clustering of intensity just under the detector.

The reflection at the interface between the regions due to effective index mismatch was found to be small, at only 0.01 % and 0.03 % for the TE and TM modes respectively. Finally, the simulated modal α for 40 nm thickness of tungsten are $2.3\,\text{cm}^{-1}$ and $54.6\,\text{cm}^{-1}$ for the TE and TM modes. This gives a calculated total absorption for the geometry $25\,\mu\text{m} \times 25\,\mu\text{m} \times 40\,\text{nm}$ of 13.2 % for the TM and 1.2 % for the TE mode, a ratio of 0.0909.

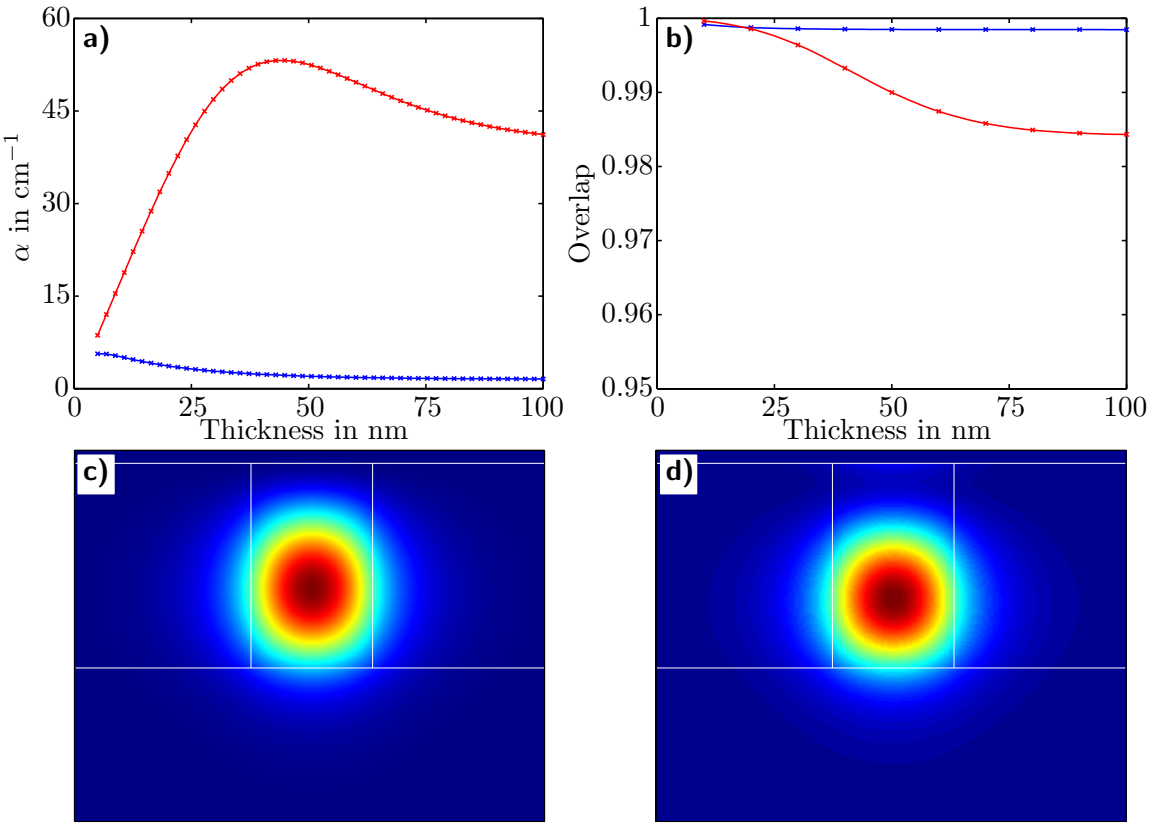

Figure 7.4: Simulated mode parameters for a simple superconducting transition edge sensor based evanescently coupled photon counting detector. a) The absorption coefficient, α, of both the TE (blue) and TM (red) as a function of the thickness of the tungsten layer for a 25 μm wide detector. The maximum absorption coefficient for the TM mode occurs at around 45 nm. b) The numerical overlap between TE (blue) and TM (red) modes at the point where the transition edge sensor begins as a function of tungsten thickness. c) The simulated intensity distribution of the TM mode in the region without the detector. d) The simulated intensity distribution of the TM mode in the region with the detector for a 40 nm tungsten thickness. A slight distortion in the vertical direction can be seen along with a small amount of intensity near the detector layer.

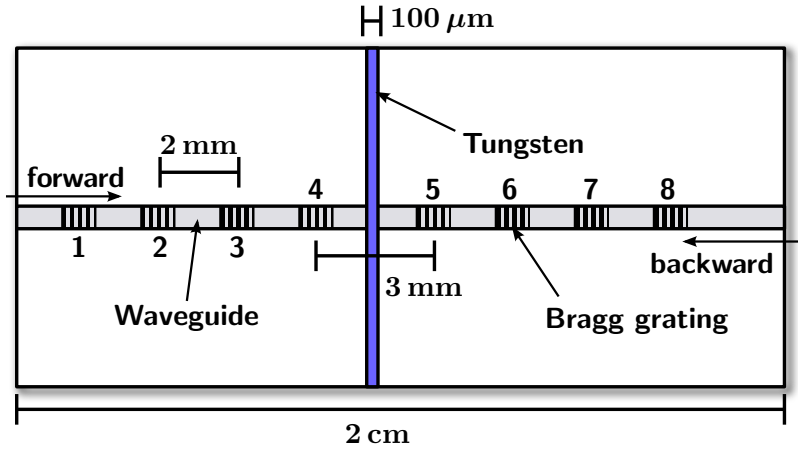

Figure 7.5: Schematic of a sample fabricated in order to measure the modal alpha underneath the tungsten, testing the validity of the predictions of the model. A 40 nm thick strip of tungsten 100 μm long was fabricated across the centre of a 2 cm long sample with a waveguide in it. Four Bragg reflectors were written into the waveguide at 2 mm intervals before and after the tungsten strip with a 3 mm gap in between. The reflection spectra of the reflectors, labelled 1–8, were centred at wavelengths of 1555, 1560, 1565, 1570, 1575, 1580, 1585, and 1595 nm respectively, with no overlap.

7.5 Experimental testing

7.5.1 Model verification by absorption measurement

To test the validity of the predicted modal α, a sample, shown schematically in Figure 7.5, was fabricated with a 100 μm long, 40 nm thick strip of tungsten across the waveguide. In addition, four weak Bragg reflectors were written at 2 mm intervals both before and after the tungsten with a 3 mm gap in between. The position of these Bragg reflectors was accurate to better than 1 μm due to the accuracy of the Aerotech stages used in the writing process. The central wavelength of each of these reflectors was separated by 5 nm, providing a reflection at 1555, 1560, 1565, 1570, 1575, 1580, 1585, and 1590 nm. These reflectors are labelled 1 to 8 respectively.

The presence of the weak Bragg reflectors in the waveguide allows the absorption of the tungsten to be characterized in a way that is independent of both coupling efficiency

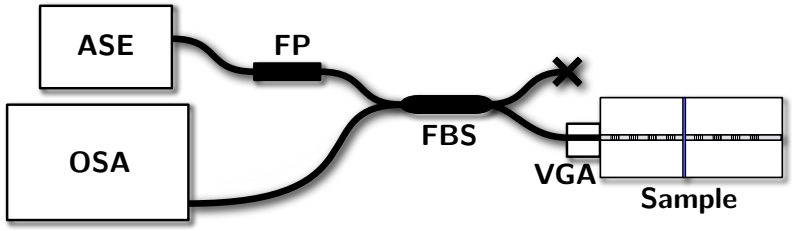

Figure 7.6: Schematic of experimental scheme for characterizing the absorption of a waveguide with a strip of tungsten above it. A single-mode fibre coupled amplified spontaneous emission source (**ASE**) was connected by an FC-FC connector to fibre polarizer (**FP**) followed by a fibre beamsplitter (**FBS**) with reflectivity of 1/2. One output of the fibre beamsplitter was terminated to avoid reflections while the other was coupled into the waveguide chip (**Sample**) using a v-groove assembly (**VGA**). Index matching oil was applied to the back face of the chip, to suppress unwanted back reflections. Light reflected by Bragg reflectors in the waveguide was directed into an optical spectrum analyser (**OSA**) for analysis.

and propagation loss. The approach is based on a previously demonstrated method [260], which was employed for in situ characterization of propagation losses. A schematic of the experimental apparatus used is shown in Figure 7.6. A fibre coupled amplified spontaneous emission (ASE) source was used as it emits an approximately flat power spectrum across a broad spectral range, enabling the reflections from all of the Bragg reflectors to be collected simultaneously. The polarization of the ASE source was filtered using a fibre polarizer before being connected to a polarization maintaining fibre beamsplitter with reflectivity 1/2. One output of the fibre beamsplitter was terminated while the other was connected, using an FC-FC connector, to a polarization maintaining v-groove assembly. A three axis stage enabled the v-groove to be butt coupled to the chip with the addition of index matching oil. An aspheric lens was used to image the output of the chip onto a 1550 nm sensitive CCD camera which allowed coupling to be roughly optimized. Once coupling had been roughly optimized, index matching oil was applied to the output face of the device, suppressing back reflections at it. Reflections from the Bragg reflectors in the waveguide propagated back through the fibre beamsplitter and were directed to an optical

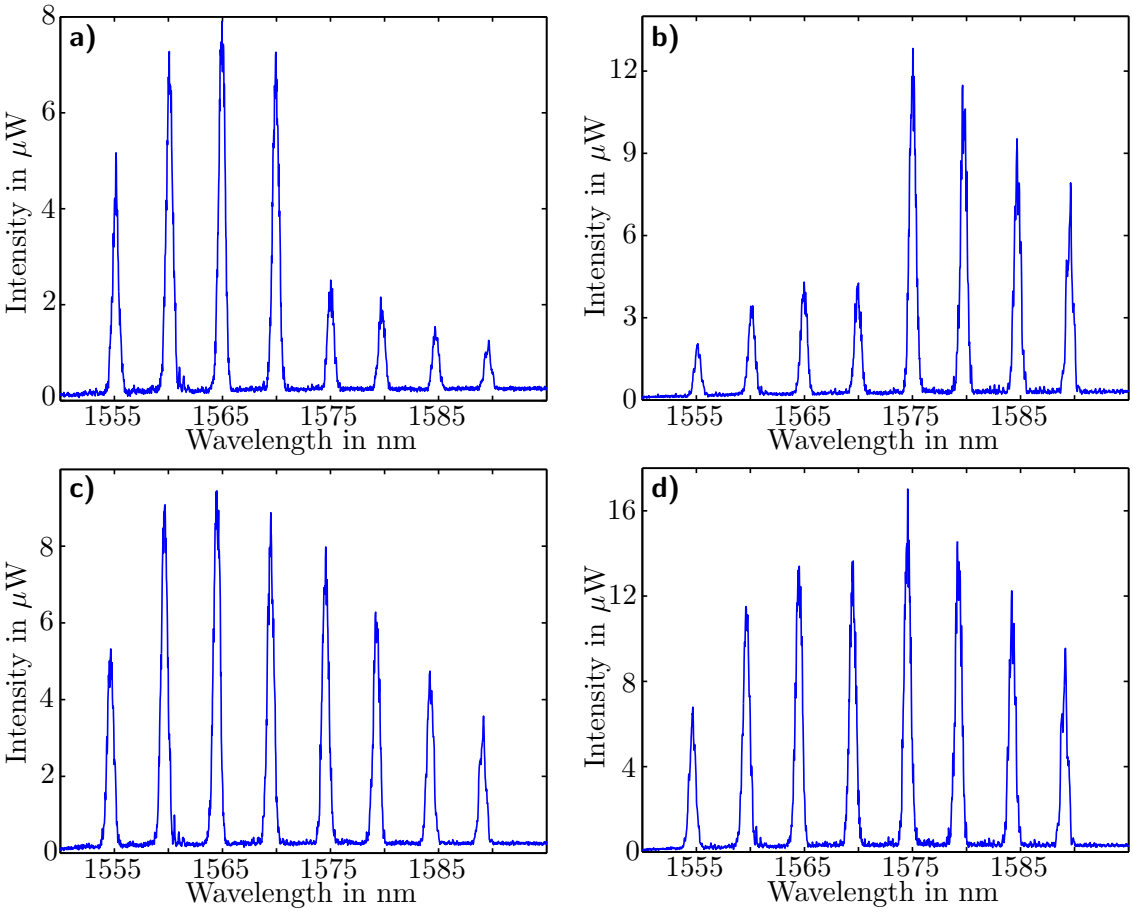

Figure 7.7: Reflected spectra for the a) TM mode, coupling in the forward direction. b) TM mode, backward direction. c) TE mode, forward direction. d) TE mode, backward direction.

spectrum analyser for analysis. The coupling was further optimized by maximizing the reflected signal.

Figure 7.7 shows the reflected spectra for the TE and TM modes when coupling first in the forward direction and then in the backward direction. When coupling in the forward direction, the four higher wavelength reflection peaks are clearly reduced in height compared to the four lower wavelength peaks for the TM mode which is indicative of the strong absorption of this mode in comparison with the TE mode. When coupling in the backward direction the four lower wavelength peaks are reduced in height since only light reflected from these Bragg reflectors had passed underneath the tungsten.

In order to extract the propagation loss of the mode underneath the tungsten, α_{w}, the reflection spectra were analysed as follows. First, it is assumed that the spectrum, $I(\omega)$, coupled into the chip in both directions was the same. It is also assumed that the coupling efficiency in the forward direction, ξ_{f}, and the backward direction, ξ_{b}, as well as the propagation loss in the waveguide not underneath the tungsten, α, are wavelength independent. Finally, it is assumed that the reflectivity of the Bragg reflectors, $\eta_i(\omega)$, is the same when coupling in each direction. This corresponds to the case here where the reflector is weak. The length of the chip will be denoted as L and the length of the tungsten as d. It is not assumed that the spectrum coupled into the device was uniform and neither is it assumed that the coupling efficiency was the same in each direction.

The reflected spectra for each of the 8 Bragg gratings can be written as

$$I_i^{(\mathrm{f})}(\omega) = \begin{cases} \xi_{\mathrm{f}}^2 e^{-2\alpha x_i} \eta_i(\omega) I(\omega) & \text{for} \quad i = [1,4] \\ \xi_{\mathrm{f}}^2 e^{-2\alpha(x_i - d) - 2\alpha_{\mathrm{w}} d} \eta_i(\omega) I(\omega) & \text{for} \quad i = [5,8] \end{cases}, \tag{7.1}$$

where $I_i^{(\mathrm{f})}(\omega)$ denotes the reflection spectrum from Bragg reflector i when coupling in the forward direction. Similarly, the reflection spectra when coupling in the backward direction, $I_i^{(\mathrm{b})}(\omega)$, can be written as

$$I_i^{(\mathrm{b})}(\omega) = \begin{cases} \xi_{\mathrm{b}}^2 e^{-2\alpha(L - x_i - d) - 2\alpha_{\mathrm{w}} d} \eta_i(\omega) I(\omega) & \text{for} \quad i = [1,4] \\ \xi_{\mathrm{b}}^2 e^{-2\alpha(L - x_i)} \eta_i(\omega) I(\omega) & \text{for} \quad i = [5,8] \end{cases}. \tag{7.2}$$

The reflection spectra can be integrated to give the total reflected intensities, $I_i^{(\mathrm{f})}$ and $I_i^{(\mathrm{b})}$.

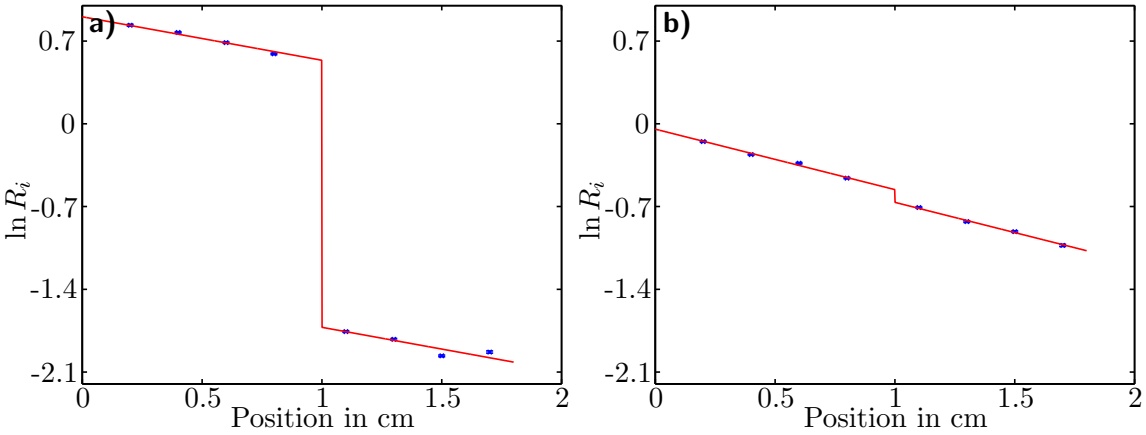

Figure 7.8: Logarithm of the ratio of forward- and backward-coupling reflected intensities for each Bragg grating with the theoretical fit. a) The TM mode. b) The TE mode. The error bars on the data were derived from the 95% confidence intervals on the parameters of Gaussian fits to the peaks in Figure 7.7. The graphs are plotted on axes of the same scale to highlight the difference in the step size between the TM and TE modes.

The logarithm of the ratio $R_i = I_i^{(\mathrm{f})}/I_i^{(\mathrm{b})}$ is then taken, giving

$$\ln R_i = \begin{cases} 2\ln\frac{\xi_\mathrm{f}}{\xi_\mathrm{b}} + 2\alpha(L-d) + 2\alpha_\mathrm{w}d - 4\alpha x_i & \text{for} \quad i = [1,4] \\ 2\ln\frac{\xi_\mathrm{f}}{\xi_\mathrm{b}} + 2\alpha(L+d) - 2\alpha_\mathrm{w}d - 4\alpha x_i & \text{for} \quad i = [5,8] \end{cases} . \tag{7.3}$$

These two equations describe straight lines with the same gradient but different intercepts. The gradient provides a coupling efficiency independent estimate of the propagation loss in the waveguide, α, while the difference between the intercepts, $4(\alpha_\mathrm{w} - \alpha)d$, allows α_w to be estimated.

Figure 7.8 shows the logarithm of the ratio of forwards and backwards intensities along with the least squares fit to the data. The function used to fit is a straight line minus a step function to ensure that the best gradient that fits all eight reflected intensities was obtained. For the TE mode, $\alpha = 0.128 \pm 0.005\mathrm{cm}^{-1}$ and $\alpha_\mathrm{W} = 2.8 \pm 0.5\mathrm{cm}^{-1}$. For the TM mode, $\alpha = 0.092 \pm 0.015\mathrm{cm}^{-1}$ and $\alpha_\mathrm{W} = 56.5 \pm 1.6\mathrm{cm}^{-1}$. These are in good agreement

with the predicted values of $2.3\,\mathrm{cm}^{-1}$ and $54.6\,\mathrm{cm}^{-1}$.

7.5.2 Measurement of a weak coherent state and efficiency characterization

In order to test the concept of the ECPCD, two TES detectors were fabricated, one positioned directly over the waveguide, as shown in Figure 7.3, and one 800 μm away from it (not shown). The former was the main interest of the study, while the latter provided a useful reference and allowed the effects of scattered light to be observed.

Figure 7.9 shows the experimental schematic for measuring weak coherent pulses of light with the ECPCD and characterizing its detection efficiency. The device was pigtailed with SMF-28 v-groove arrays at both input and output. This allowed the device to be tested in both directions and the overall throughput to be measured with a bright beam. A dilution refrigerator (DR) was used to cool the device down to $\sim 12\,\mathrm{mK}$, far below its transition temperature of $\sim 90\,\mathrm{mK}$. Voltage biasing allowed the ECPCD to be positioned in its superconducting transition region. A pulsed laser diode (driven with a pulse generator) produced coherent state pulses at a wavelength of 1550 nm with a temporal width of 10 ns and a repetition rate of $\sim 35\,\mathrm{kHz}$. The laser pulses were sent through an array of two fibre attenuators (A), a polarization controller (PC), and an optical fibre switch (S). The attenuators were calibrated before each measurement by individually measuring the un-attenuated and attenuated average laser power for each of the two attenuator settings[261]. Typically, the laser pulses were attenuated by approximately 60 dB to reach a mean photon number $\langle n \rangle = 28.5 \pm 0.8$ at the input fibre after the optical switch. The fibre polarization controller was used to modify the input polarization to the waveguide chip to

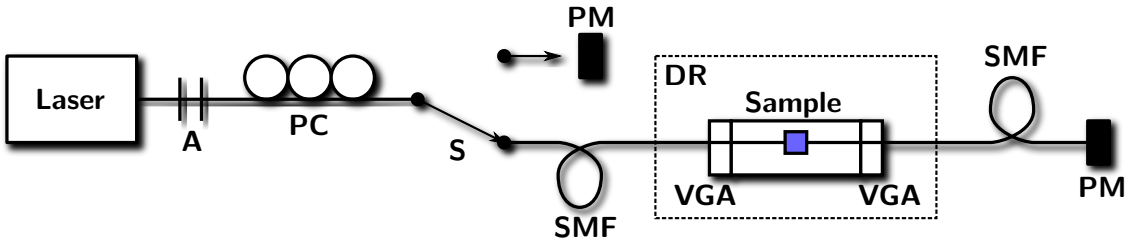

Figure 7.9: Experimental scheme. A 35 kHz pulsed laser at 1550 nm (**Laser**) delivers attenuated (**A**) weak coherent state pulses to the waveguide device (**Sample**) which is situated inside a dilution refrigerator (**DR**). The polarization of the input light could be modified via a fibre polarization controller (**PC**). A fibre switch (**S**) allowed the laser pulses to be directed to a calibrated power meter (**PM**) or to the device. Coupling to the device was achieved using SMF-28 (**SMF**) v-groove assemblies (**VGA**). The waveguide device along with the TES was cooled to about 12 mK. The TES is voltage biased and the electrical output is fed into a SQUID circuit (not shown). The SQUID output was amplified at room temperature and the signal was measured with data acquisition electronics.

allow the TE or TM mode behaviour to be observed. The switch allowed either the output power to be directly measured with a calibrated power meter (PM) or the attenuated laser pulses to be sent to the waveguide chip. The electrical output of the TES was fed into a SQUID circuit and amplified with a $\times 100$ amplifier outside the DR (not shown). This signal was recorded with data-acquisition electronics and post-processed to determine the pulse height of each of the individual photon traces[254,262].

By adjusting the input polarization of an unattenuated beam, a total device throughput of $19.1 \pm 0.4\,\%$ (maximum) and $17.7 \pm 0.4\,\%$ (minimum) was measured. These corresponded to launching into the chip with TE and TM modes, respectively. The total throughput was also measured in the opposite direction and these agreed within experimental error, as expected. The beam was then attenuated and the response of the ECPCD was recorded. The raw output pulses of the central TES for a TM input mode are shown overlaid on top of each other in Figure 7.10c, with a histogram of pulse heights shown in Figure 7.10a. The inset shows the histogram of pulse heights for a TE input mode. The clear separation

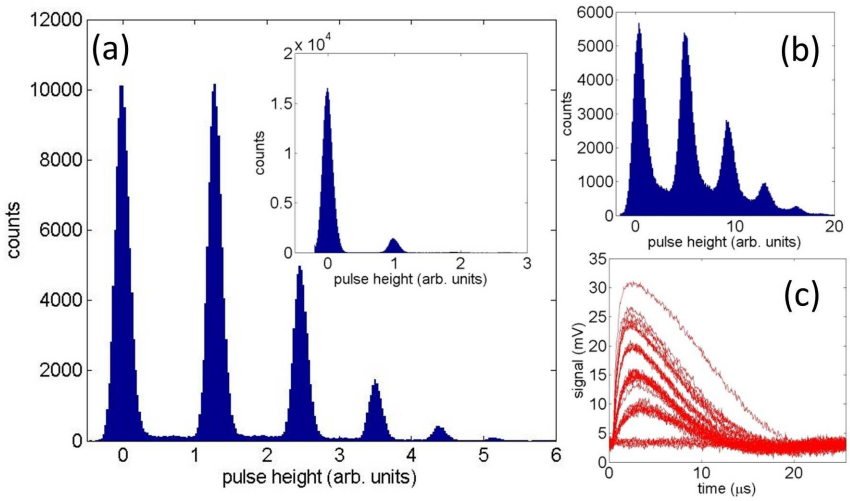

Figure 7.10: Experimental results. a) photon pulse height distribution for a measured coherent state with $\langle n \rangle = 0.986$ for the optimal TM polarization ($\eta_{det} = 7.2\,\%$). The inset shows the photon pulse-height distribution for the anti-optimal TE polarization. The measured mean photon number was 0.086 ($\eta_{det} = 0.65\,\%$). b) photon pulse height distribution for the TES not evanescently coupled to the waveguide ($\langle n \rangle = 1.03$; $\eta_{det} = 0.0056\,\%$). c) electrical TES output traces for different numbers of photons in the weak laser pulse; the photon number resolving capability is clearly visible. The TES recovery time is about $10\,\mu$s due to its low transition temperature. Note that this detector was optimized for its photon-number-resolving capability and the evanescent coupling strength, not for its recovery time.

between pulse heights, as demonstrated by the clearly resolved peaks in the histogram, shows the capability of this detector to resolve photon number and indicates that simple thresholding electronics are sufficient to determine the absorbed photon number. The measured mean photon number per pulse was $\langle n_{\text{detected}} \rangle = 0.986 \pm 0.02$ for a TM input mode and $\langle n_{\text{detected}} \rangle = 0.086 \pm 0.008$ for a TE input mode. These were obtained by adjusting the polarization control to maximize and minimize respectively the detected average photon number.

In order to characterize the efficiency of the ECPCD, three measurements are necessary for each input mode. First, the total throughput efficiency, ξ_{total}. Second and third, the device efficiency including coupling and propagation losses, from after the optical switch, measured in each direction. These are defined as the ratio of the average photon

number detected by the ECPCD to the average photon number at the input fibre after the optical switch, giving $\xi^{(1)}_{\text{device}}$ and $\xi^{(2)}_{\text{device}}$. As previously mentioned, the first of these can be measured using bright light and a calibrated power meter by first measuring the output power from mode 1 of the optical switch and then switching it and measuring the power transmitted all the way through the device. Since it is the efficiency after the optical switch that is of interest, however, the differential losses between the output modes the switch must be characterized. This is straightforwardly modelled by inserting a fictitious beamsplitter in the output of the switch that would be connected to the device. The transmissivity of this beamsplitter, ξ_{switch}, was measured to be $0.917 \pm 0.01\,\%$. The total throughput efficiency can then be written as

$$\xi_{\text{total}} = \xi_{\text{a}}(1 - \eta_{\text{int}})(1 - \xi_{\text{TES}})\xi_{\text{b}}, \tag{7.4}$$

where ξ_{a} and ξ_{b} are the coupling and propagation efficiencies from the optical switch to the TES and from the TES to the output respectively. η_{int} is the reflectivity of a fictitious beamsplitter modelling any reflections which occur at the interface between the propagation and detection regions in the device while ξ_{TES} is the efficiency of the TES itself. This latter efficiency is defined as the probability that a photon which successfully enters the detection region is detected.

There is a further efficiency term that enters into this measurement; a reflective loss is incurred at the air-silica interface of the fibre tip when used with a free space power meter. This reflection cannot be characterized in every situation and so the theoretical value of $\eta_{\text{fibre}} = 0.036$ is used. In this measurement, however, it occurs when measuring

both the input and output powers and hence cancels out when the ratio is taken. This is not the case when measuring the average photon number detected by the TES as there is no second air-silica interface. Hence, the input average photon number must be corrected for both the switch efficiency and the air-silica reflection, giving

$$\langle n_{\text{input}} \rangle = \langle n_{\text{measured}} \rangle \frac{\xi_{\text{switch}}}{(1 - \eta_{\text{fibre}})}. \tag{7.5}$$

The two remaining required measurements were then obtained by attenuating the input state using the calibrated fibre attenuators and measuring the detected average photon number when coupling in each direction. These measurements can be written as

$$\begin{aligned} \xi^{(1)}_{\text{device}} &= \frac{\langle n^{(1)}_{\text{detected}} \rangle}{\langle n_{\text{input}} \rangle} = \xi_{\text{a}}(1 - \eta_{\text{int}})\xi_{\text{TES}}, \\ \xi^{(2)}_{\text{device}} &= \frac{\langle n^{(2)}_{\text{detected}} \rangle}{\langle n_{\text{input}} \rangle} = \xi_{\text{b}}(1 - \eta_{\text{int}})\xi_{\text{TES}}. \end{aligned} \tag{7.6}$$

For the TM input mode these were measured to be $\xi^{(1)}_{\text{device}} = 2.9 \pm 0.2\,\%$ and $\xi^{(2)}_{\text{device}} = 3.5 \pm 0.2\,\%$. For the TE input mode they were measured to be $\xi^{(1)}_{\text{device}} = 0.26 \pm 0.02\,\%$ and $\xi^{(2)}_{\text{device}} 0.30 \pm 0.02\,\%$.

Equations 7.4 and 7.6 provide three equations for four unknowns, however, solving for ξ_{TES} and taking the positive solution leads to the expression

$$\xi_{\text{TES}} = \frac{\sqrt{K(K+4)} - K}{2}, \tag{7.7}$$

where

$$K = \frac{\xi^{(1)}_{\text{device}} \xi^{(2)}_{\text{device}}}{\xi_{\text{total}}(1 - \eta_{\text{int}})}. \tag{7.8}$$

η_{int}	ξ_{a}	ξ_{b}	ξ_{TES}
0.03 %	39.8 ± 4.4 %	47.9 ± 5.0	7.2 ± 0.4 %
1.00 %	40.0 ± 4.4 %	48.2 ± 5.0	7.3 ± 0.4 %

Table 7.1: Extracted fibre-pigtail-waveguide transmission $\eta_{A/B}$ and TES detection efficiency η_{TES}.

Although η_{int} cannot be measured experimentally, the theoretical prediction can be used in its place. In order to see its effect on the final value of η_{TES}, two values were taken, the theoretical prediction of 3×10^{-4} and a much higher value of 1×10^{-2}. The values of ξ_{a}, ξ_{b}, and ξ_{TES} that were obtained in each case are shown in Table 7.1. It is clear that the absolute value η_{int} does not have a large effect on the efficiency values obtained.

Applying this method for measurements taken with TM and TE input modes yielded an absolute detection efficiency of 7.2 ± 0.5 % and 0.65 ± 0.05 % respectively. In comparison, the modelling discussed in Section 7.4 predicted an absorption of 13.2 % and 1.2 % for this detector geometry. Although close, these do not agree within the experimental uncertainty of the measurements. Further exploration of the model showed a relatively weak dependence of the predicted absorption on the material parameters, suggesting that uncertainty in them was not the source of the discrepancy. One possible explanation is the fact that the model prediction does not discriminate between absorption into the tungsten TES and possible leakage of light from the waveguide structure, while the measurement provides only the absorption in the TES. A second possible explanation is that fibre-splice losses in the system contribute to a measured detection efficiency a few percent lower than predicted[261]. Even though the absolute values for the estimated absorption are higher than the measured detection efficiencies, the predicted ratio of the absorption of the TE to the TM mode of 0.909 is in very good agreement with the experimental result of 0.913.

Figure 7.10(b) shows a pulse-peak histogram for the reference detector after the input mean photon number was increased by ∼32 dB and the input polarization was adjusted to obtain the maximum detected mean photon number. This was 1.03 ± 0.02, implying a detection efficiency of 0.0056 %, which is expected for a detector that measures only the scattered photon contribution. From the scattered light signal it can be estimated that this contribution to the central TES detection signal is $\sim 8 \times 10^{-4}$ per pulse. The main peaks corresponding to direct photon number absorption are still present, however, there are also intermediate pulse heights that contribute to an exponential tail on what is usually a gaussian peak. These intermediate pulse heights could be caused by a parasitic absorption of photons in the silica itself. An absorbed photon will create a cloud of hot electrons that couple to the silica phonon system. A part of this heat diffuses into the tungsten, causing a partial warm-up [263]. The effect is less pronounced in the central TES, as the vast majority of the photon absorption is due to evanescent coupling into the tungsten directly. As well as this, a very small peak at half the photon energy was observed. This could be a possible indication of photon absorption in the niobium wiring [263]. These effects are expected to be suppressed in more optimized detector geometries with higher efficiency.

7.6 Geometry optimization

The experiments described above are a proof of principle demonstration of the ECPCD concept. In reality, however, the detection efficiency is significantly lower than that which has been demonstrated using standard normal-incidence TES technology. In order to be a viable technology, there must be a route towards improving the efficiency of TES-based ECPCD devices.

As previously discussed, the detection mechanism for TESs ensures that the heat capacity of the device, and hence its total volume, is a critical parameter. Here, the potential absorption achievable for a range of simple geometries is explored. Figure 7.11 shows nine plots, each of which models the absorption achievable for a device of fixed thickness but different lengths and widths using its TM mode. An estimate of the absorption is obtained by finding the α of the fundamental TM mode supported by the geometry. This was done using the Fimmprop mode solver. The fractional absorption is then $e^{-\alpha z}$, where z is the length of the device. Although this estimate does not include any reflections at the interface between the propagation and detection regions, the modelling performed in Section 7.4 suggests that this is a small effect.

In each case, the geometry is cuboid in shape and the colour indicates the expected absorption while the contours show the volume of the detector normalized to the volume used for the detector fabricated and tested in the work described in the previous section. Tungsten thicknesses of 5, 10, 15, 20, 25, 30, 40, 50, and 60 nm were modelled and correspond with figures a) to i) respectively. As expected, the fraction of power that can be absorbed in a single detector increases with the volume of that detector, however, it is much more sensitive to length than width, due to the exponential dependence of the absorption on propagation distance. Hence, for a fixed volume, as given by the contours, a longer and narrower device always outperforms a shorter and wider one. Unfortunately, increasing the length of the device is not trivial. Primarily, it is more difficult to keep an extended device in thermal equilibrium along its length, something which is critical to the operation of the TES. This issue could potentially be circumvented by constructing a multi-absorber 'segmented' detector, however, reading out multiple TESs in parallel is

also not straightforward. Despite these issues, this model indicates that with a five times increase in detector volume, absorption in the region of 80% is possible in a single pass.

In this chapter, the concept of an evanescently coupled photon-counting detector has been realised and its operational feasibility has been demonstrated by constructing a waveguide-based transition edge sensor, the first implementation of an on-chip, intrinsically photon number-resolving-detector. A clear and realistic route to high-efficiency detection using this scheme has been shown by engineering the aspect ratio of the detector. This wholly integrated solution for detection will be a key component of high efficiency integrated devices functioning in the quantum regime.

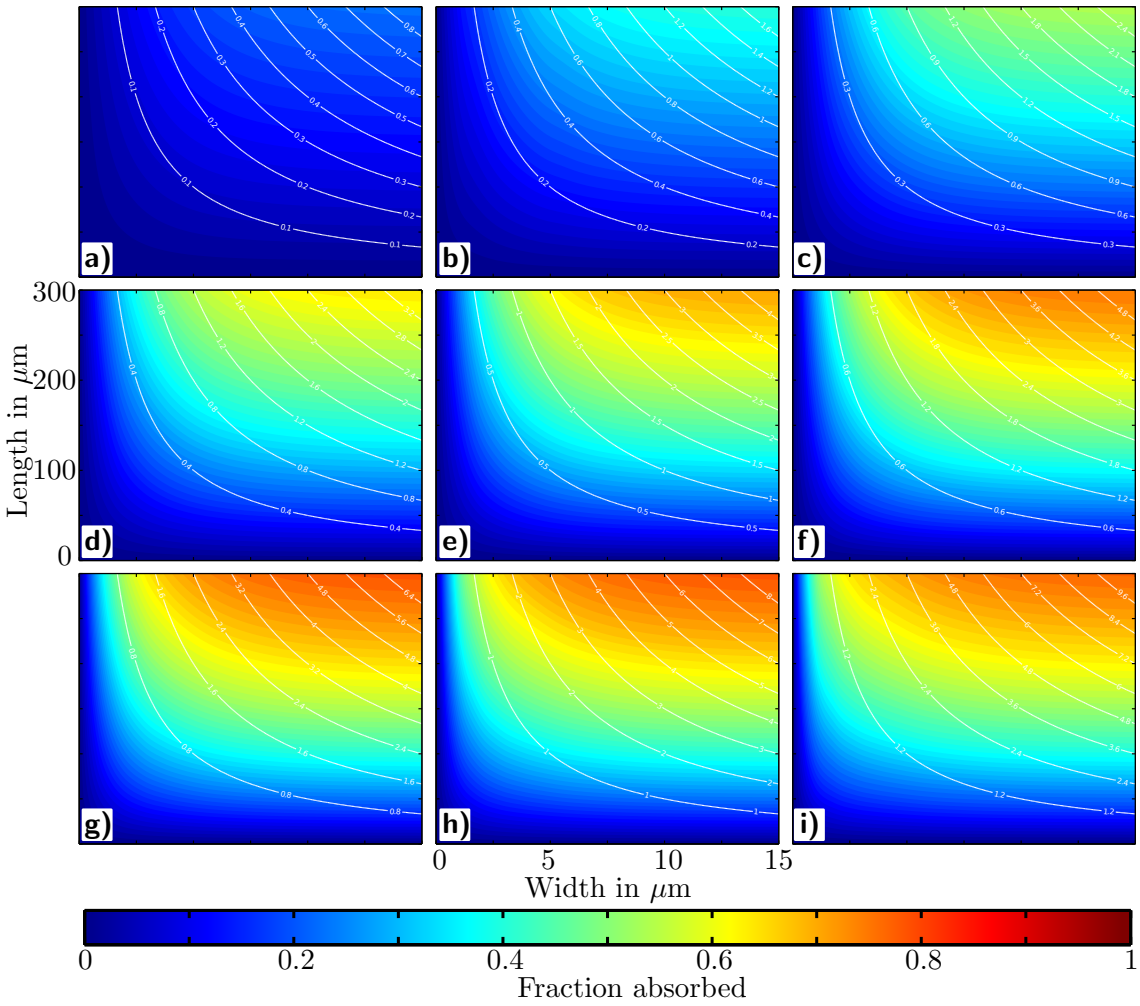

Figure 7.11: Estimated total absorption of the TM mode for different detector geometries. The thickness of the detector is constant for each scan while the width and length of the detector is varied. Colour represents the fraction of power absorbed for a detector of the indicated dimension. The contours indicate the volume of the detector normalized to a volume of 625 μm^2 $\times$ 40 nm, as used for the experiments described in the previous section. a) to i) correspond to tungsten layer thicknesses of 5, 10, 15, 20, 25, 30, 40, 50, and 60 nm respectively.

Chapter 8

Conclusion

Quantum optics has been a hugely productive area over recent decades. It has enabled relatively simple, experimentally speaking, tests of the foundations of quantum mechanics as well as proof of principle demonstrations of quantum-enhanced technologies. This is because it does not, in general, require large amounts of laboratory space, cryogenic facilities, or complex trapping and cooling apparatus. Photons do not interact strongly with their environment and so do not suffer from the same issues of decoherence as trapped ions, atoms, and solid state systems. Two issues do impact photonic systems, however. First, they suffer from loss. Second, up until recently, quantum optics was performed using bulk optics and free space propagation. This meant that large systems of modes was impractical due to space and stability constraints.

The work in this thesis discusses and experimentally demonstrates the importance of considering loss in comparing classical and quantum technologies. It also demonstrates the ability of an integrated approach to provide the necessary control, stability, and complexity in manipulation, as well as efficiency and photon-number-resolution in detection for larger

scale quantum metrology and quantum information processing tasks.

8.1 Summary

Chapter 1 introduced the problem of precision measurement. The theoretical tools used in assessing the precision with which a physical parameter can be estimated were introduced including Fisher information and the Cramér-Rao bound. Methods of comparing quantum and classical approaches to precision measurement were introduced, including commonly used limits and concepts such as the standard quantum limit, the standard interferometric limit, super-resolution, and super-sensitivity. A discussion of the effect of neglecting system inefficiencies in the quantum-classical comparison followed, including a discussion of the fragility of the well-studied N00N state. A more robust class of states, the Holland-Burnett or twin-Fock states was introduced and the effect of transmission, preparation, and detection inefficiencies as well as beamsplitter imperfections was theoretically investigated. The results showed the existence of a region of the transmission, preparation, and detection efficiencies for which a quantum device employing Holland-Burnett states can out-perform its classical counterpart in precision measurement. While these loss thresholds are stringent, and have not yet been attained by any group experimentally, there is a realistic hope of meeting them in the medium term.

The second chapter outlined a source of heralded Holland-Burnett states that, in principle, is capable of heralding high photon number states with high fidelity. It was based on heralded pure state generation in two parametric downconverters. These states used polarization as the two modes of the interferometer and the experimental methods of polarization interferometry were introduced. The quality of heralded single photons was

tested by means of polarization Hong-Ou-Mandel interference after which heralded but post-selected quantum interference fringes corresponding to Holland-Burnett state generation were observed. The concept of state tomography was introduced and a novel method for reconstructing the heralded Holland-Burnett state including all photon number subspaces, in contrast to a single photon number subspace, was presented. The heralded state was then characterized using this method and its density matrix was presented. The reconstructed density matrix was evaluated for precision measurement by applying several of the analyses outlined in Chapter 1. This resulted in a clear demonstration that ignoring system inefficiencies drastically over-estimates the utility of a state and can lead to the conclusion that a system out-performs its classical counterpart when, in reality, it does not.

Demonstrating the manipulation capabilities of an integrated approach to quantum-enhanced precision measurement formed the basis of Chapter 3. First, the direct UV written silica on silicon platform was introduced including a discussion of the way that beamsplitters and phase shifters are produced using this technology. Second, the integrated Mach-Zehnder interferometer was introduced and the concept of a Mach-Zehnder interferometer acting as a single, programmable beamsplitter was described. The effective reflectivity of the Mach-Zehnder interferometer was tuned to be nominally 1/2 and Hong-Ou-Mandel interference was observed at it using a single parametric downconversion source. Finally, in analogy with Chapter 2, post-selected quantum interference fringes consistent with two-photon Holland-Burnett state generation were observed. These experiments demonstrate the ability of the direct UV written silica on silicon integrated platform to support and manipulate quantum interference effects.

Chapter 4, the first of Part II of this thesis, introduced the concept of quantum information processing including a basic overview of the qubit and the efficiency gains that can be achieved using quantum algorithms that have been developed. The concept of quantum error correction was also introduced. Quantum information processing as applied to photonics was then discussed including an overview of the linear optics quantum computation scheme devised by Knill, Laflamme, and Milburn as well as one-way quantum computation using cluster states. The robustness of linear optical circuits based on Mach-Zehnder interferometers was then discussed and a simple scheme to produce programmable beamsplitters which can be tuned from a reflectivity of 0 to 1 based on the fabrication of nominally 1/2 reflectivity beamsplitters and phase shifters was outlined.

Methods of characterizing the individual elements of a complex linear optical circuit were presented in the first half of Chapter 5 as a route to model-driven circuit behaviour characterization. First, the problem of characterizing beamsplitter reflectivities and calibrating phase shifters was reduced to the same problem of reflectivity estimation. Second, a naive method of reflectivity estimation was presented followed by a method that is independent of coupling and propagation efficiencies. Third, the applicability of this technique was extended by utilizing a camera to observe light scattered in the transverse direction from the outputs of a particular beamsplitter. The three methods were compared by characterizing the effective reflectivity of a Mach-Zehnder interferometer. In the second half of this chapter, a method for simulating the behaviour of linear optical circuits with input states that consist of products of Fock state superpositons at each mode was presented. Opportunities for computational speed-up based on sparse matrix operations and parallelisation were identified.

In Chapter 6, integrated optics was used to increase complexity towards a level that is practically difficult to achieve using bulk optics and free space propagation. An integrated, linear optical device consisting of eight spatial modes, twelve beamsplitters, and five phase shifters forming five Mach-Zehnder interferometers of which three were interlinked was presented. Its operation on three photons to implement a post-selected cluster state single qubit X rotation or a teleportation in the coincidence basis was described. The device was characterized using the techniques described in Chapter 5 and it was found that there were significant deviations of the circuit elements away from their intended design. Nevertheless, two-photon interference effects were observed at the output of the device for each of three input combinations when the relative arrival time of the photons was scanned through zero delay. The visibility of this interference was found to be beyond what could be explained classically. Fitting a theoretical model to the observed interference allowed the three inputs to be accurately temporally overlapped. Subsequently, all three input photons, generated from two parametric downconversion sources, were launched into the device and the relative arrival time of one of the photons was scanned through zero delay. This time, three-photon interference effects were observed in the output and their visibility was found to be beyond that which can be explained classically. Moreover, the circuit characterization suggests that genuine tripartite entanglement was created from the three initially separable photons. The extremely low data rates and the robustness of the phase shifters over the resulting experimental duration meant that it was not possible to operate the device in its originally intended form to show either teleportation or a cluster state single qubit X rotation, however, the key barriers were identified and routes to overcoming them were discussed.

The penultimate chapter of this thesis contained the proposal of a novel integrated detector design, the evanescently coupled photon counting detector, and a proof of principle demonstration of its operation in the telecommunications band. First, superconducting transition edge sensors were introduced and briefly contrasted with other single-photon sensitive detectors. Then, the concept of an evanescently coupled photon counting detector was introduced including a qualitative discussion of its characteristics and their importance. The structure of the device was then described and its behaviour was modelled using a commercially available modelling suite. The predictions of the model were tested first by measuring the absorption coefficient of a mode propagating underneath a tungsten layer. This measurement was performed using a novel ratiometric technique based on Bragg reflectors making it coupling efficiency and propagation loss independent. The measurement and the prediction were found to agree. Next, a full proof of principle device was fabricated and tested by measuring the photon number statistics of a weak coherent state. By measuring the total throughput of the device as well as the photon number statistics with the weak coherent state propagating each way through the device, a coupling and propagation loss-free estimate of the device efficiency was obtained. This was less than the efficiency predicted by the model and reasons for the discrepancy were discussed. Finally, routes towards increasing the efficiency of the device through geometry optimization were discussed and modelled. It was found that there is a feasible route towards high efficiency devices, paving the way for further developments to use this newly demonstrated technology in quantum information processing or precision measurement applications.

8.2 Outlook

8.2.1 Femtosecond writing in bulk silica

For the three experiments presented in this thesis in which an integrated device is used, the platform is the same, namely direct UV written silica-on-silicon. This demonstrates the capability of this platform to support quantum phenomena, however, it is by no means the only integrated platform which is capable of such experiments. Its major advantages include: relatively low propagation loss at telecommunications wavelengths ($\sim$0.2 dB cm^{-1}), although this is still high compared to the best fibres; the ability to write Bragg reflectors without introducing additional losses to the waveguide; an extremely flat surface which makes it compatible with tungsten transition edge sensors. There are also significant downsides: no $\chi^{(2)}$ non-linearity, preventing both electro-optic phase shifting and parametric downconversion; a maximum theoretical coupling to SMF-28 of 87%, as modelled using Fimmwave; an intrinsically planar structure which is incompatible with writing three-dimensional structures.

Recent experiments not reported in this thesis have centred around fabrication of devices in bulk silica using an infrared pulsed laser system with 100 fs duration [131,264]. Devices have been fabricated using a writing system based around an adaptive optical element, a phase only spatial light modulator, leading to straight waveguides with published coupling efficiencies to single mode fibre of up to 95% and propagation losses lower than 0.4 dB cm^{-1} [265]. More recent results have reached 98% and 0.2 dB cm^{-1}. As well as this, the adaptability of the spatial light modulator enables Bragg structures to be fabricated as well as waveguides with a profile that varies along their length. The second

benefit of such a system is that it can be used to dynamically correct for aberration effects that occur as a result of focussing deep into a block of silica, something that is critical for large three dimensional structures. The flexibility and mode-matching capabilities already demonstrated by this platform make it a promising technology, despite the lack of an electro-optic coefficient.

8.2.2 Further work

Although the first steps have been taken for integrated quantum optics, there is an enormous amount still to be done. Continuing directly from the work presented here, it seems that loss is the single biggest barrier for photonic quantum-enhanced technologies to become viable. In the short to medium term, significant work is required to decrease the losses experienced at all stages of photonic experiments.

Specific sources of single photons have not been discussed in detail in this thesis, however, the preparation of high purity single photons with high heralding efficiencies must perhaps be the highest priority since heralding efficiencies of 20% for sources based on parametric downconversion are not uncommon. At this level, it is the single largest contributor to inefficiency. Significant progress has been made in this area, for example, using four-wave mixing in standard birefringent fibre[78]. In this experiment, an extremely impressive heralding efficiency of 85% was observed. Due to fluctuations in the material parameters of standard birefringent fibre, however, constructing two sources which interfere with high visibility is not trivial. It is intended to use the femtosecond writing techniques described above to develop heralded photon sources that are well mode-matched to both single mode fibre and other waveguide devices. The ability to write multiple waveguides with the cor-

rect birefringence will be a critical step towards fabricating multiple sources in a single device which produce single photons that interfere with high visibility. Initial experiments are promising, however. Waveguides have been produced with the correct birefringence and four-wave mixing has been observed.

In manipulation, the largest source of loss is at the interfaces of the device. As seen in Chapter 6, the difficulty of coupling multiple spatial modes at the same time led to data acquisition times on the order of 10 days. Again, the femtosecond writing system has the potential to alleviate this issue. The ability to shape and adiabatically alter the transverse profile of the waveguides and to write in three dimensions provides the possibility of fabricating high efficiency optical interconnects between, for example, a v-groove assembly and a waveguide chip. High efficiency optical interconnects between multiple material platforms would have a wider impact as they would enable a modular approach to constructing photonic information processing platforms. In such a scheme, the best platform is used and optimized for each individual task and then the interfaces between the platforms are optimized.

Finally, following on from the work presented on integrated detection schemes, it is clear that a second generation of devices must demonstrate significantly higher efficiencies. Work already being undertaken is investigating more complex geometries than the ones modelled in Chapter 7. It is anticipated that detection efficiencies of greater than 50% will be achieved. Once detection efficiencies of this level are obtained, work will have to be undertaken to improve the efficiency of coupling onto the device since that will then be the dominant source of loss. Pushing the detection efficiency further will have implications for other experiments. For example, a fully integrated implementation of an entanglement

distillation scheme may be possible. Low loss and high detection efficiency is a critical part of this scheme since high fidelity vacuum detection is necessary [266].

8.2.3 Future challenges

If loss is the most imminent hurdle to be crossed for photonic technologies, what are the longer term challenges? The simple answer is more photons in more modes. The difficulties in realising this goal lie in the nature of photon generation and manipulation. Many of the component elements of photonic systems are probabilistic and those which do show the promise of being deterministic, such as photon sources based on quantum dots, currently operate with low efficiency. Even when high efficiency heralded elements are used, the question of when they will succeed still has no answer. In order to realise a scalable source of states of large photon number or many probabilistic operations, it is therefore necessary to synchronise probabilistic events. The device required to do this is a quantum memory [147,267]. As with sources, manipulation, and detection, the quantum memories must operate with high efficiency and fidelity in order to be practically useful.

Much progress has been made in the development of quantum memories both in efficiency [268] and fidelity [269]. The next stage will be to further develop memories that are compatible with integrated photonic devices [270,271] and can be used to synchronise multiple probabilistic events with high efficiency. At that stage, all of the necessary elements for demonstrating fully fledged quantum enhanced technologies will have been demonstrated.

Bibliography

[1] V Giovannetti, S Lloyd, and L Maccone. Quantum-enhanced measurements: beating the standard quantum limit. *Science*, 306:1330, November 2004.

[2] V Giovannetti, S Lloyd, and L Maccone. Quantum Metrology. *Physical Review Letters*, 96:010401, January 2006.

[3] D J Wineland and D Leibfried. Quantum information processing and metrology with trapped ions. *Laser Physics Letters*, 8:175, March 2011.

[4] T Rosenband, D B Hume, P O Schmidt, C W Chou, A Brusch, L Lorini, W H Oskay, R E Drullinger, T M Fortier, J E Stalnaker, S A Diddams, W C Swann, N R Newbury, W M Itano, D J Wineland, and J C Bergquist. Frequency Ratio of Al^+ and Hg^+ Single-Ion Optical Clocks; Metrology at the 17th Decimal Place. *Science*, 319:1808, 2008.

[5] D J Wineland, J J Bollinger, W M Itano, F L Moore, and D J Heinzen. Spin squeezing and reduced quantum noise in spectroscopy. *Physical Review A*, 46:R6797, 1992.

[6] D J Wineland, J J Bollinger, W M Itano, and D J Heinzen. Squeezed atomic states and projection noise in spectroscopy. *Physical Review A*, 50:67, 1994.

[7] J J Bollinger, W M Itano, D J Wineland, and D J Heinzen. Optimal frequency measurements with maximally correlated states. *Physical Review A*, 54:R4649, 1996.

[8] D Leibfried, M D Barrett, T Schaetz, J Britton, J Chiaverini, W M Itano, J D Jost, C Langer, and D J Wineland. Toward Heisenberg-limited spectroscopy with multiparticle entangled states. *Science*, 304:1476, June 2004.

[9] C F Roos, M Chwalla, K Kim, M Riebe, and R Blatt. 'Designer atoms' for quantum metrology. *Nature*, 443:316, September 2006.

[10] G Goldstein, P Cappellaro, J R Maze, J S Hodges, L Jiang, A S Sørensen, and M D Lukin. Environment-Assisted Precision Measurement. *Physical Review Letters*, 106:140502, April 2011.

[11] D Leibfried, E Knill, S Seidelin, J Britton, R B Blakestad, J Chiaverini, D B Hume, W M Itano, J D Jost, C Langer, R Ozeri, R Reichle, and D J Wineland. Creation of a six-atom 'Schrödinger cat' state. *Nature*, 438:639, December 2005.

[12] V Meyer, M A Rowe, D Kielpinski, C A Sackett, W M Itano, C Monroe, and D J Wineland. Experimental Demonstration of Entanglement-Enhanced Rotation Angle Estimation Using Trapped Ions. *Physical Review Letters*, 86:5870, June 2001.

[13] I D Leroux, M H Schleier-Smith, and V Vuletić. Orientation-Dependent Entanglement Lifetime in a Squeezed Atomic Clock. *Physical Review Letters*, 104:250801, June 2010.

[14] T Monz, P Schindler, J T Barreiro, M Chwalla, D Nigg, W A Coish, M Harlander, W Hänsel, M Hennrich, and R Blatt. 14-Qubit Entanglement: Creation and Coherence. *Physical Review Letters*, 106:130506, March 2011.

[15] J A Dunningham, K Burnett, and S M Barnett. Interferometry below the Standard Quantum Limit with Bose-Einstein Condensates. *Physical Review Letters*, 89:150401, September 2002.

[16] J A Dunningham, K Burnett, and W D Phillips. Bose-Einstein condensates and precision measurements. *Philosophical Transactions of the Royal Society A*, 363:2165, September 2005.

[17] A B Tacla, S Boixo, A Datta, A Shaji, and C M Caves. Nonlinear interferometry with Bose-Einstein condensates. *Physical Review A*, 82:053636, November 2010.

[18] A O Jamison, J N Kutz, and S Gupta. Atomic interactions in precision interferometry using Bose-Einstein condensates. *Physical Review A*, 84:043643, October 2011.

[19] J Grond, U Hohenester, J Schmiedmayer, and A Smerzi. Mach-Zehnder interferometry with interacting trapped Bose-Einstein condensates. *Physical Review A*, 84:023619, August 2011.

[20] S Gupta, K Dieckmann, Z Hadzibabic, and D E Pritchard. Contrast Interferometry using Bose-Einstein Condensates to Measure h/m and α. *Physical Review Letters*, 89:140401, September 2002.

[21] O Garcia, B Deissler, K Hughes, J Reeves, and C A Sackett. Bose-Einstein-condensate interferometer with macroscopic arm separation. *Physical Review A*, 74(3):031601(R), September 2006.

[22] T Schumm, S Hofferberth, L M Andersson, S Wildermuth, S Groth, I Bar-Joseph, J Schmiedmayer, and P Krüger. Matter-wave interferometry in a double well on an atom chip. *Nature Physics*, 1:57, September 2005.

[23] M Albiez, R Gati, J Fölling, S Hunsmann, M Cristiani, and M K Oberthaler. Direct Observation of Tunneling and Nonlinear Self-Trapping in a Single Bosonic Josephson Junction. *Physical Review Letters*, 95:010402, June 2005.

[24] J Q You and F Nori. Atomic physics and quantum optics using superconducting circuits. *Nature*, 474:589, June 2011.

[25] W D Oliver, Y Yu, J C Lee, K K Berggren, L S Levitov, and T P Orlando. Mach-Zehnder interferometry in a strongly driven superconducting qubit. *Science*, 310:1653, December 2005.

[26] P Grangier, R E Slusher, and B Yurke. Squeezed-Light-Enhanced Polarization Interferometer. *Physical Review letters*, 59:2153, 1987.

[27] R E Slusher, P Grangier, A LaPorta, B Yurke, and M J Potasek. Pulsed Squeezed Light. *Physical Review Letters*, 59:2566, 1987.

[28] E S Polzik, J Carri, and H J Kimble. Spectroscopy with Squeezed Light. *Physical Review Letters*, 68:3020, 1992.

[29] M Xiao, L-A Wu, and H J Kimble. Precision Measurement beyond the Shot-Noise Limit. *Physical Review Letters*, 59:278, 1987.

[30] L K Shalm, R B A Adamson, and A M Steinberg. Squeezing and over-squeezing of triphotons. *Nature*, 457:67, January 2009.

[31] Morgan W Mitchell, Jeff S Lundeen, and Aephraim M Steinberg. Super-resolving phase measurements with a multiphoton entangled state. *Nature*, 429:161, May 2004.

[32] B L Higgins, D W Berry, S D Bartlett, H M Wiseman, and G J Pryde. Entanglement-free Heisenberg-limited phase estimation. *Nature*, 450:393, November 2007.

[33] H S Eisenberg, J F Hodelin, G Khoury, and D Bouwmeester. Multiphoton Path Entanglement by Nonlocal Bunching. *Physical Review Letters*, 94:090502, 2005.

[34] K J Resch, J L O'Brien, T J Weinhold, K Sanaka, B P Lanyon, N K Langford, and A G White. Entanglement Generation by Fock-State Filtration. *Physical Review Letters*, 98:203602, May 2007.

[35] T Nagata, R Okamoto, J L O'brien, K Sasaki, and S Takeuchi. Beating the standard quantum limit with four-entangled photons. *Science*, 316:726, May 2007.

[36] B J Smith, D O Kundys, N Thomas-Peter, P G R Smith, and I A Walmsley. Phase-controlled integrated photonic quantum circuits. *Optics Express*, 17:13516, 2009.

[37] H Kim, HS Park, and S-K Choi. Three-photon N00N states generated by photon subtraction from double photon pairs. *Optics express*, 17:19720, October 2009.

[38] J C F Matthews, A Politi, A Stefanov, and J L O'Brien. Manipulation of multiphoton entanglement in waveguide quantum circuits. *Nature Photonics*, 3:346, 2009.

[39] J C F Matthews, A Politi, D Bonneau, and J L O'Brien. Heralding Two-Photon and Four-Photon Path Entanglement on a Chip. *Physical Review Letters*, 107:163602, October 2011.

[40] U Dorner, R Demkowicz-Dobrzaski, B J Smith, J S Lundeen, W Wasilewski, K Banaszek, and I A Walmsley. Optimal Quantum Phase Estimation. *Physical Review Letters*, 102:040403, January 2009.

[41] A Datta, L Zhang, N Thomas-Peter, U Dorner, B J Smith, and I A Walmsley. Quantum metrology with imperfect states and detectors. *Physical Review A*, 83:063836, June 2011.

[42] S F Huelga, C Macchiavello, T Pellizzari, A K Ekert, M B Plenio, and J I Cirac. Improvement of Frequency Standards with Quantum Entanglement. *Physical Review Letters*, 79:3865, November 1997.

[43] A Shaji and C M Caves. Qubit metrology and decoherence. *Physical Review A*, 76:032111, September 2007.

[44] M A Rubin and S Kaushik. Loss-induced limits to phase measurement precision with maximally entangled states. *Physical Review A*, 75:053805, May 2007.

[45] S D Huver, C F Wildfeuer, and J P Dowling. Entangled Fock states for robust quantum optical metrology, imaging, and sensing. *Physical Review A*, 78:063828, December 2008.

[46] G Gilbert, M Hamrick, and Y S Weinstein. Use of maximally entangled N-photon states for practical quantum interferometry. *Journal of the Optical Society of America B*, 25:1336, July 2008.

[47] R A Fisher. Theory of statistical estimation. In *Mathematical Proceedings of the Cambridge Philosophical Society*, volume 22, pages 700–725, 1925.

[48] C. R Rao. Information and the Accuracy Attainable in the Estimation of Statistical Parameters. *Bulletin of the Calcutta Mathematical Society*, 37:81, 1945.

[49] H Cramér. *Mathematical Methods of Statistics*. Princeton Universtiy Press, Princeton, NJ, 1946.

[50] M A Nielsen and I L Chuang. *Quantum computation and quantum information*. Cambridge University Press, 2000.

[51] L A Wasserman. *All of Statistics: A Concise Course in Statistical Inference*. Springer, 2004.

[52] A S Holevo. *Probabilistic and Statistical Aspects of Quantum Theory*. North-Holland, 1982.

[53] C W Helstrom. *Quantum Detection and Estimation Theory*. Academic Press, 1976.

[54] S L Braunstein, C M Caves, and G J Milburn. Generalized Uncertainty Relations : Theory, Examples, and Lorentz Invariance. *Annals of Physics*, 247:135, 1996.

[55] S L Braunstein and C M Caves. Statistical distance and the geometry of quantum states. *Physical Review Letters*, 72:3439–3443, 1994.

[56] P J Mosley, J S Lundeen, B J Smith, P Wasylczyk, A B U'Ren, C Silberhorn, and I A Walmsley. Heralded Generation of Ultrafast Single Photons in Pure Quantum States. *Physical Review Letters*, 100:133601, April 2008.

[57] S Barz, G Cronenberg, A Zeilinger, and P Walther. Heralded generation of entangled photon pairs. *Nature Photonics*, 4:553, 2010.

[58] C Wagenknecht, C-M Li, A Reingruber, X-H Bao, A Goebel, Y-A Chen, Q Zhang, K Chen, and J-W Pan. Experimental demonstration of a heralded entanglement source. *Nature Photonics*, 4:549, 2010.

[59] R Loudon. *The Quantum Theory of Light*. Oxford University Press, Oxford, 1973.

[60] K J Resch, K L Pregnell, R Prevedel, A Gilchrist, G J Pryde, J L O'Brien, and A G White. Time-Reversal and Super-Resolving Phase Measurements. *Physical Review Letters*, 98:223601, May 2007.

[61] I Afek, O Ambar, and Y Silberberg. High-NOON States by Mixing Quantum and Classical Light. *Science*, 328:879–881, 2010.

[62] B C Sanders and G J Milburn. Optimal quantum measurements for phase estimation. *Physical Review Letters*, 75:2944, 1995.

[63] A N Boto, P Kok, D S Abrams, S L Braunstein, C P Williams, and J P Dowling. Quantum interferometric optical lithography: exploiting entanglement to beat the diffraction limit. *Physical Review Letters*, 85:2733, October 2000.

[64] R Okamoto, H F Hofmann, T Nagata, J L O'Brien, K Sasaki, and S Takeuchi. Beating the Standard Quantum Limit: Phase Super-Sensitivity of N-Photon Interferometers. *New Journal of Physics*, 10:073033, July 2008.

[65] P Kok, H Lee, and J P Dowling. Creation of large-photon-number path entanglement conditioned on photodetection. *Physical Review A*, 65:052104, April 2002.

[66] H F Hofmann. Generation of highly nonclassical n-photon polarization states by superbunching at a photon bottleneck. *Physical Review A*, 70:023812, August 2004.

[67] P Walther, M Aspelmeyer, and A Zeilinger. Heralded generation of multiphoton entanglement. *Physical Review A*, 75:012313, 2007.

[68] H Cable and J P Dowling. Efficient Generation of Large Number-Path Entanglement Using Only Linear Optics and Feed-Forward. *Physical Review Letters*, 99:163604, October 2007.

[69] K T Kapale and J P Dowling. Bootstrapping Approach for Generating Maximally Path-Entangled Photon States. *Physical Review Letters*, 99:053602, August 2007.

[70] K T McCusker and P G Kwiat. Efficient Optical Quantum State Engineering. *Physical Review Letters*, 103:163602, 2009.

[71] M Kacprowicz, R Demkowicz-Dobrzański, W Wasilewski, K Banaszek, and I A Walmsley. Experimental Quantum-Enhanced Estimation of a Lossy Phase Shift. *Nature Photonics*, 4:357–360, 2010.

[72] M J Holland and K Burnett. Interferometric detection of optical phase shifts at the Heisenberg limit. *Physical Review*, 71:1355, 1993.

[73] H Cable and G A Durkin. Parameter Estimation with Entangled Photons Produced by Parametric Down-Conversion. *Physical Review Letters*, 105:013603, 2010.

[74] J A Dunningham and K Burnett. Sub-shot-noise-limited measurements with Bose-Einstein condensates. *Physical Review A*, 70:033601, 2004.

[75] D Meiser and M J Holland. Robustness of Heisenberg-limited interferometry with balanced Fock states. *New Journal of Physics*, 11:033002, March 2009.

[76] F Wolfgramm, A Cerè, and M W Mitchell. NOON states from cavity-enhanced down-conversion: high quality and super-resolution. *Journal of the Optical Society of America B*, 27:A25, March 2010.

[77] B M Escher, R L de Matos Filho, and L Davidovich. General framework for estimating the ultimate precision limit in noisy quantum-enhanced metrology. *Nature Physics*, 7:406, 2011.

[78] C Soller, O Cohen, B J Smith, I A Walmsley, and C Silberhorn. High-performance single-photon generation with commercial-grade optical fiber. *Physical Review A*, 83:031806(R), 2011.

[79] A E Lita, B Calkins, L A Pellouchoud, A J Miller, and S W Nam. Superconducting transition-edge sensors optimized for high-efficiency photon-number resolving detectors. In *SPIE*, pages 7681, 76810D, 2010.

[80] B C Sanders, G J Milburn, and Z Zhang. Optimal quantum measurements for phase-shift estimation in optical interferometry. *Journal of Modern Optics*, 44:1309, July 1997.

[81] P J Mosley. *Generation of Heralded Single Photons in Pure Quantum States*. PhD thesis, University of Oxford, 2007.

[82] P J Mosley, J S Lundeen, B J Smith, and I A Walmsley. Conditional Preparation of Single Photons using Parametric Downconversion: a Recipe for Purity. *New Journal of Physics*, 10:093011, 2008.

[83] A B U'Ren, K Banaszek, and I A Walmsley. Photon engineering for quantum information processing. In *Quantum Information and Computation*, volume 3, page 480, October 2003.

[84] A B U'Ren, C Silberhorn, K Banaszek, and I A Walmsley. Efficient Conditional Preparation of High-Fidelity Single Photon States for Fiber-Optic Quantum Networks. *Physical Review Letters*, 93(9):93601, August 2004.

[85] A B U'Ren, C Silberhorn, R Erdmann, K Banaszek, W P Grice, I A Walmsley, and M G Raymer. Generation of Pure-State Single-Photon Wavepackets by Conditional Preparation Based on Spontaneous Parametric Downconversion. *Laser Physics*, 15:146, November 2005.

[86] W P Grice, A B U'Ren, and I A Walmsley. Eliminating frequency and space-time correlations in multiphoton states. *Physical Review A*, 64:063815, November 2001.

[87] A Christ, A Eckstein, P J Mosley, and C Silberhorn. Pure single photon generation by type-I PDC with backward-wave amplification. *Optics express*, 17:3441, March 2009.

[88] B J Smith, P Mahou, O Cohen, J S Lundeen, and I A Walmsley. Photon pair generation in birefringent optical fibers. *Optics Express*, 17(26):23589, 2009.

[89] D Achilles, C Silberhorn, C Śliwa, K Banaszek, and I A Walmsley. Fiber-assisted detection with photon number resolution. *Optics letters*, 28:2387, December 2003.

[90] J D Jackson. *Classical Electrodynamics*. Wiley, 3 edition, 1998.

[91] C K Hong, Z Y Ou, and L Mandel. Measurement of subpicosecond time intervals between two photons by interference. *Physical Review Letters*, 59:2044, 1987.

[92] R Ghosh and L Mandel. Observation of Nonclassical Effects in the Interference of Two Photons. *Physical Review Letters*, 59:1903, 1987.

[93] M Barbieri, T J Weinhold, B P Lanyon, A Gilchrist, K J Resch, M P Almeida, and A G White. Parametric downconversion and optical quantum gates: two's company, four's a crowd. *Journal of Modern Optics*, 56:209, January 2009.

[94] M A Broome, M P Almeida, A Fedrizzi, and A G White. Reducing multi-photon rates in pulsed down-conversion by temporal multiplexing. *Optics Express*, 19(23):22698, 2011.

[95] M D de Burgh, N K Langford, A C Doherty, and A Gilchrist. Choice of measurement sets in qubit tomography. *Physical Review A*, 78:052122, November 2008.

[96] R B A Adamson and A M Steinberg. Improving Quantum State Estimation with Mutually Unbiased Bases. *Physical Review Letters*, 105:030406, July 2010.

[97] A Ling, K P Soh, A Lamas-Linares, and C Kurtsiefer. Experimental polarization state tomography using optimal polarimeters. *Physical Review A*, 74:22309, 2006.

[98] J Nunn, B J Smith, G Puentes, and I A Walmsley. Optimal experiment design for quantum state tomography: Fair, precise, and minimal tomography. *Physical Review A*, 81:42109, 2010.

[99] D F V James, P G Kwiat, W J Munro, and A G White. Measurement of qubits. *Physical Review A*, 64:52312, 2001.

[100] Z Hradil, D Mogilevtsev, and J Rehacek. Biased tomography schemes: an objective approach. *Physical Review Letters*, 96:230401, 2006.

[101] S Boyd and L Vandenberghe. *Convex Optimization*. Cambridge, 2004.

[102] N K Langford. *Encoding , manipulating and measuring quantum information in optics*. PhD thesis, University of Queensland, 2007.

[103] D Achilles, C Silberhorn, C Sliwa, K Banaszek, I A Walmsley, M J Fitch, B C Jacobs, T B Pittman, and J D Franson. Photon-number-resolving detection using time-multiplexing. *Journal of Modern Optics*, 51:1499, June 2004.

[104] R B A Adamson, L K Shalm, M W Mitchell, and A M Steinberg. Multiparticle State Tomography: Hidden Differences. *Physical Review Letters*, 98:043601, January 2007.

[105] R B A Adamson, P S Turner, M W Mitchell, and A M Steinberg. Detecting Hidden Differences via Permutation Symmetries. *Physical Review A*, 78:033832, 2008.

[106] K Banaszek, G M D'Ariano, M G A Paris, and M F Sacchi. Maximum-likelihood estimation of the density matrix. *Physical Review A*, 61:010304(R), 1999.

[107] T Miya, Y Terunuma, T Hosaka, and T Miyashita. Ultimate low-loss single-mode fibre at $1.55\,\mu m$. *Electronics Letters*, 15:106, 1979.

[108] M E Anderson, D F McAlister, M G Raymer, and M C Gupta. Pulsed squeezed-light generation in $\chi^{(2)}$ nonlinear waveguides. *Journal of the Optical Society of America B*, 14:3180, November 1997.

[109] K Banaszek, A B U'ren, and I A Walmsley. Generation of correlated photons in controlled spatial modes by downconversion in nonlinear waveguides. *Optics letters*, 26:1367, September 2001.

[110] J Chen, L Xiaoying, and P Kumar. Two-Photon-State Generation via Four-Wave Mixing in Optical Fibers. *Physical Review A*, 72:033801, 2005.

[111] X Li, P L Voss, J E Sharping, and P Kumar. Optical-Fiber Source of Polarization-Entangled Photons in the 1550 nm Telecom Band. *Physical Review Letters*, 94(5):053601, February 2005.

[112] J E Sharping, K F Lee, M A Foster, A C Turner, B S Schmidt, M Lipson, A L Gaeta, and P Kumar. Generation of correlated photons in nanoscale silicon waveguides. *Optics Express*, 14:12388, February 2006.

[113] K Garay-Palmett, H J Mcguinness, O Cohen, J S Lundeen, R Rangel-Rojo, A B U'Ren, M G Raymer, C J McKinstrie, S Radic, and I A Walmsley. Photon pair-state preparation with tailored spectral properties by spontaneous four-wave mixing in photonic-crystal fiber. *Optics Express*, 15:14870, 2007.

[114] M Avenhaus, A Eckstein, P J Mosley, and C Silberhorn. Fiber-assisted single-photon spectrograph. *Optics letters*, 34:2873, September 2009.

[115] J Chen, A J Pearlman, A Ling, J Fan, and A L Migdall. A versatile waveguide source of photon pairs for chip-scale quantum information processing. *Optics Express*, 17:6727, April 2009.

[116] S Clemmen, K Phan Huy, W Bogaerts, R G Baets, P Emplit, and S Massar. Continuous wave photon pair generation in silicon-on-insulator waveguides and ring resonators. *Optics express*, 17:16558, September 2009.

[117] P J Mosley, A Christ, A Eckstein, and C Silberhorn. Direct Measurement of the Spatial-Spectral Structure of Waveguided Parametric Down-Conversion. *Physical Review Letters*, 103(23):233901, 2009.

[118] Z H Levine, J Fan, J Chen, A Ling, and A L Migdall. Heralded, pure-state single-photon source based on a Potassium Titanyl Phosphate waveguide. *Optics Express*, 18:3708, 2010.

[119] A M Brańczyk, T C Ralph, W Helwig, and C Silberhorn. Optimized generation of heralded Fock states using parametric down-conversion. *New Journal of Physics*, 12:063001, June 2010.

[120] A Eckstein, A Christ, P J Mosley, and C Silberhorn. Highly Efficient Single-Pass Source of Pulsed Single-Mode Twin Beams of Light. *Physical Review Letters*, 106:013603, January 2011.

[121] K Banaszek and I A Walmsley. Photon counting with a loop detector. *Optics letters*, 28:52, January 2003.

[122] D Achilles, C Silberhorn, and I A Walmsley. Direct, Loss-Tolerant Characterization of Nonclassical Photon Statistics. *Physical Review Letters*, 97:43602, 2006.

[123] C M Natarajan, A Peruzzo, S Miki, M Sasaki, Z Wang, B Baek, S Nam, R H Hadfield, and J L O'Brien. Operating quantum waveguide circuits with superconducting single-photon detectors. *Applied Physics Letters*, 96(21):211101, 2010.

[124] T Gerrits, N Thomas-Peter, J C Gates, A E Lita, B J Metcalf, B Calkins, N A Tomlin, A E Fox, A Lamas-Linares, J B Spring, N K Langford, R P Mirin, P G R Smith, I A Walmsley, and S W Nam. On-chip, photon-number-resolving, telecommunication-band detectors for scalable photonic information processing. *Physical Review A*, 84:060301(R), December 2011.

[125] J P Sprengers, A Gaggero, D Sahin, S Jahanmirinejad, G Frucci, F Mattioli, R Leoni, J Beetz, M Lermer, M Kamp, S Hofling, R Sanjines, and A Fiore. Waveguide superconducting single-photon detectors for integrated quantum photonic circuits. *Applied Physics Letters*, 99:181110, 2011.

[126] M Kawachi. Silica waveguides on silicon and their application to integrated-optic components. *Optical and Quantum Electronics*, 22:391, 1990.

[127] R C Alferness. Titanium-diffused Lithium Niobate waveguide devices. In *Applications of Ferroelectrics. 1986 Sixth IEEE International Symposium on*, page 1, 1986.

[128] J L Jackel, C E Rice, and J J Veselka. Proton exchange for high-index waveguides in LiNbO3. *Applied Physics Letters*, 41:607, 1982.

[129] M L Bortz and M M Fejer. Annealed proton-exchanged LiNbO(3) waveguides. *Optics letters*, 16:1844, December 1991.

[130] Y N Korkishko, V A Fedorov, T M Morozova, F Caccavale, F Gonella, and F Segato. Reverse proton exchange for buried waveguides in LiNbO3. *Journal of the Optical Society of America A*, 15:1838, 1998.

[131] G Della Valle, R Osellame, and P Laporta. Micromachining of photonic devices by femtosecond laser pulses. *Journal of Optics A: Pure and Applied Optics*, 11:013001, January 2009.

[132] M Ams, G D Marshall, P Dekker, M Dubov, V K Mezentsev, I Bennion, and M J Withford. Investigation of Ultrafast Laser–Photonic Material Interactions: Challenges for Directly Written Glass Photonics. *IEEE Journal of Selected Topics in Quantum Electronics*, 14:1370, 2008.

[133] M Svalgaard, C V Poulsen, A Bjarklev, and O Poulsen. Direct UV writing of buried singlemode channel waveguides in Ge-doped silica films. *Electronics Letters*, 30(17):1401, 1994.

[134] M Svalgaard and M Kristensen. Directly UV written silica-on-silicon planar waveguides with low. *Electronics Letters*, 33:861, 1997.

[135] P Tandon and H Boek. Experimental and theoretical studies of flame hydrolysis deposition process for making glasses for optical planar devices. *Journal of Non-Crystalline Solids*, 317:275, 2003.

[136] P J Lemaire, R M Atkins, V Mizrahi, and W A Reed. High pressure H2 loading as a technique for achieving ultrahigh UV photosensitivity and thermal sensitivity in GeO2 doped optical fibres. *Electronics Letters*, 29:1191, 1993.

[137] D O Kundys, J C Gates, S Dasgupta, C B E Gawith, and P G R Smith. Use of Cross-Couplers to Decrease Size of UV Written Photonic Circuits. *IEEE Photonics Technology Letters*, 21:947, 2009.

[138] F R M Adikan, C B E Gawith, P G R Smith, I J G Sparrow, G D Emmerson, C Riziotis, and H Ahmad. Design and demonstration of direct UV-written small angle X couplers in silica-on-silicon for broadband operation. *Applied optics*, 45(24):6113–8, August 2006.

[139] G D Emmerson, S P Watts, C B E Gawith, A V, M Ibsen, R J Williams, and P G R Smith. Fabrication of Directly UV-Written Channel Waveguides with Simultaneously Defined Integral Bragg Gratings. *Electronics Letters*, 38:1531, August 2002.

[140] G D Marshall, A Politi, J C F Matthews, P Dekker, M Ams, M J Withford, and J L O'Brien. Laser written waveguide photonic quantum circuits. *Optics Express*, 17:12546, 2009.

[141] A Politi, M J Cryan, J G Rarity, S Yu, and J L O'Brien. Silica-on-Silicon Waveguide Quantum Circuits. *Science*, 320:646, 2008.

[142] A Peruzzo, A Laing, A Politi, T Rudolph, and J L O'Brien. Multimode quantum interference of photons in multiport integrated devices. *arXiv:quant-ph*, 2010.

[143] F Dürr and H Renner. Analytical Design of X-Couplers. *Journal of Lightwave Technology*, 23:876, 2005.

[144] H Herrmann, K-D Büchter, R Ricken, and W Sohler. Tunable integrated electro-optic wavelength filter with programmable spectral response. *Journal of Lightwave Technology*, 28:1051, 2010.

[145] W N Ye, D X Xu, S Janz, P Waldron, and N G Tarr. Stress-induced SOI polarization splitter based on Mach-Zehnder interferometers (MZI). In *Group IV Photonics, 2006. 3rd IEEE International Conference on*, page 249. IEEE, 2006.

[146] J Nunn, I A Walmsley, M G Raymer, K Surmacz, F C Waldermann, Z Wang, and D Jaksch. Mapping broadband single-photon wave packets into an atomic memory. *Physical Review A*, 75:11401, 2007.

[147] K F Reim, J Nunn, V O Lorenz, B J Sussman, K C Lee, N K Langford, D Jaksch, and I A Walmsley. Towards high-speed optical quantum memories. *Nature Photonics*, 4:218, 2010.

[148] K F Reim, P Michelberger, K C Lee, J Nunn, N K Langford, and I A Walmsley. Single-photon-level quantum memory at room temperature. *Physical Review Letters*, 107:0533603, July 2011.

[149] H J Briegel, D E Browne, W Dür, R Raussendorf, and M Van den Nest. Measurement-based quantum computation. *Nature Physics*, 5(1):19–26, January 2009.

[150] K Watanabe, Y Hashizume, Y Nasu, M Kohtoku, M Itoh, and Y Inoue. Ultralow Power Consumption Silica-Based PLC-VOA/Switches. *Journal of Lightwave Technology*, 26:2235, July 2008.

[151] G Coppola, L Sirleto, I Rendina, and M Iodice. Advance in thermo-optical switches: principles, materials, design, and device structure. *Optical Engineering*, 50:071112, 2011.

[152] J G Rarity and P R Tapster. Experimental violation of Bell's inequality based on phase and momentum. *Physical Review Letters*, 64:2495, 1990.

[153] J G Rarity, P R Tapster, E Jakeman, T Larchuk, R A Campos, M C Teich, and B E A Saleh. Two-Photon Interference in a Mach-Zehnder Interferometer. *Physical Review Letters*, 65:1348, 1990.

[154] A Hentschel and B C Sanders. Machine Learning for Adaptive Quantum Measurement. In *Seventh International Conference on Information Technology: New Generations*, page 506. Ieee, 2010.

[155] T A Wheatley, D W Berry, H Yonezawa, D Nakane, H Arao, D T Pope, T C Ralph, H M Wiseman, A Furusawa, and E H Huntington. Adaptive Optical Phase Estimation Using Time-Symmetric Quantum Smoothing. *Physical Review Letters*, 104:093601, March 2010.

[156] R P Feynman. Simulating physics with computers. *International Journal of Theoretical Physics*, 21:467, June 1982.

[157] A Datta, A Shaji, and C M Caves. Quantum Discord and the Power of One Qubit. *Physical Review Letters*, 100:050502, February 2008.

[158] S L Braunstein and P van Loock. Quantum information with continuous variables. *Reviews of Modern Physics*, 77:513, 2005.

[159] U L Andersen, G Leuchs, and C Silberhorn. Continuous-variable quantum information processing. *Laser & Photonics Reviews*, 4:337, 2010.

[160] B Schumacher. Quantum coding. *Physical Review A*, 51:2738, 1995.

[161] M Genovese and P Traina. Review on qudits production and their application to quantum communication and studies on local realism. *Advanced Science Letters*, 1:153, 2008.

[162] D P DiVincenzo. Two-bit gates are universal for quantum computation. *Physical Review A*, 51:1015, February 1995.

[163] P W Shor. Polynomial-Time Algorithms for Prime Factorization and Discrete Logarithms on a Quantum Computer. In *35th Annual Symposium on Foundations of Computer Science*, page 124, Santa Fe, NM, 1994. IEEE Computer Society Press.

[164] L K Grover. A fast quantum mechanical algorithm for database search. In *28th Annual ACM Symposium on the Theory of Computing (STOC)*, page 212, Philadelphia, PA, 1996.

[165] P W Shor. Scheme for reducing decoherence in quantum computer memory. *Physical Review A*, 52:R2493, October 1995.

[166] A M Steane. Error Correcting Codes in Quantum Theory. *Physical Review Letters*, 77:793, 1996.

[167] W K Wootters and W H Zurek. A single quantum cannot be cloned. *Nature*, 299:802, 1982.

[168] D P DiVincenzo. The Physical Implementation of Quantum Computation. *Fortschritte der Physik*, 48:771, September 2000.

[169] J I Cirac and P Zoller. Quantum computations with cold trapped ions. *Physical Review Letters*, 74:4091, 1995.

[170] H Häffner, C F Roos, and R Blatt. Quantum computing with trapped ions. *Physics Reports*, 469:155, December 2008.

[171] A Myerson, D Szwer, S Webster, D Allcock, M Curtis, G Imreh, J Sherman, D Stacey, A M Steane, and D Lucas. High-Fidelity Readout of Trapped-Ion Qubits. *Physical Review Letters*, 100:200502, May 2008.

[172] D L Moehring, P Maunz, S Olmschenk, K C Younge, D N Matsukevich, L-M Duan, and C Monroe. Entanglement of single-atom quantum bits at a distance. *Nature*, 449:68, September 2007.

[173] M Riebe, H Häffner, C F Roos, W Hänsel, J Benhelm, G P T Lancaster, T W Körber, C Becher, F Schmidt-Kaler, D F V James, and R Blatt. Deterministic quantum teleportation with atoms. *Nature*, 429:734, 2004.

[174] M D Barrett, J Chiaverini, T Schaetz, J Britton, W M Itano, J D Jost, E Knill, C Langer, D Leibfried, R Ozeri, and D J Wineland. Deterministic quantum teleportation of atomic qubits. *Nature*, 429:737, June 2004.

[175] J Chiaverini, J Britton, D Leibfried, E Knill, M D Barrett, R B Blakestad, W M Itano, J D Jost, C Langer, R Ozeri, T Schaetz, and D J Wineland. Implementation of the semiclassical quantum Fourier transform in a scalable system. *Science*, 308:997, May 2005.

[176] J Chiaverini, D Leibfried, T Schaetz, M D Barrett, R B Blakestad, J Britton, W M Itano, J D Jost, E Knill, C Langer, R Ozeri, and D J Wineland. Realization of quantum error correction. *Nature*, 432:602, December 2004.

[177] D Stick, W K Hensinger, S Olmschenk, M J Madsen, K Schwab, and C Monroe. Ion trap in a semiconductor chip. *Nature Physics*, 2:36, December 2006.

[178] C Ospelkaus, U Warring, Y Colombe, K R Brown, J M Amini, D Leibfried, and D J Wineland. Microwave quantum logic gates for trapped ions. *Nature*, 476:181, August 2011.

[179] N Timoney, I Baumgart, M Johanning, A F Varón, M B Plenio, A Retzker, and C Wunderlich. Quantum gates and memory using microwave-dressed states. *Nature*, 476:185, August 2011.

[180] D Loss and D P DiVincenzo. Quantum computation with quantum dots. *Physical Review A*, 57:120, 1998.

[181] A Imamoğlu, D D Awschalom, G Burkard, D P DiVincenzo, D Loss, M Sherwin, and A Small. Quantum information processing using quantum dot spins and cavity QED. *Physical review letters*, 83:4204, 1999.

[182] M H Devoret and J M Martinis. Implementing Qubits with Superconducting Integrated Circuits. *Quantum Information Processing*, 3:163, 2004.

[183] J Clarke and F K Wilhelm. Superconducting quantum bits. *Nature*, 453:1031, June 2008.

[184] L Robledo, J Elzerman, G Jundt, M Atatüre, A Högele, S Fält, and A Imamoğlu. Conditional dynamics of interacting quantum dots. *Science*, 320:772, May 2008.

[185] I Fushman, D Englund, A Faraon, N G Stoltz, P Petroff, and J Vuckovic. Controlled phase shifts with a single quantum dot. *Science*, 320:769, May 2008.

[186] A J Shields. Semiconductor quantum light sources. *Nature Photonics*, 1:215, 2007.

[187] S Strauf, N G Stoltz, M T Rakher, L A Coldren, P M Petroff, and D Bouwmeester. High-frequency single-photon source with polarization control. *Nature Photonics*, 1:704, November 2007.

[188] E B Flagg, A Muller, S V Polyakov, A Ling, A L Migdall, and G S Solomon. Interference of Single Photons from Two Separate Semiconductor Quantum Dots. *Physical Review Letters*, 104:137401, April 2010.

[189] I Chiorescu, Y Nakamura, C J P M Harmans, and J E Mooij. Coherent quantum dynamics of a superconducting flux qubit. *Science*, 299:1869, March 2003.

[190] J H Plantenberg, P C de Groot, C J P M Harmans, and J E Mooij. Demonstration of controlled-NOT quantum gates on a pair of superconducting quantum bits. *Nature*, 447:836, June 2007.

[191] L DiCarlo, J M Chow, J M Gambetta, L S Bishop, B R Johnson, D I Schuster, J Majer, A Blais, L Frunzio, S M Girvin, and R J Schoelkopf. Demonstration of two-qubit algorithms with a superconducting quantum processor. *Nature*, 460:240, July 2009.

[192] M W Johnson, M H S Amin, S Gildert, T Lanting, F Hamze, N Dickson, R Harris, A J Berkley, J Johansson, P Bunyk, E M Chapple, C Enderud, J P Hilton, K Karimi, E Ladizinsky, N Ladizinsky, T Oh, I Perminov, C Rich, M C Thom, E Tolkacheva, C J S Truncik, S Uchaikin, J Wang, B Wilson, and G Rose. Quantum Annealing with Manufactured Spins. *Nature*, 473:194, 2011.

[193] P Kok, K Nemoto, T C Ralph, J P Dowling, and G J Milburn. Linear optical quantum computing with photonic qubits. *Reviews of Modern Physics*, 79:135, January 2007.

[194] J L O'Brien. Optical quantum computing. *Science*, 318(5856):1567–70, December 2007.

[195] L-M Duan, M D Lukin, J I Cirac, and P Zoller. Long-distance quantum communication with atomic ensembles and linear optics. *Nature*, 414(6862):413–8, November 2001.

[196] N Gisin and R Thew. Quantum Communication. *Nature Photonics*, 1:165, 2007.

[197] H J Kimble. The quantum internet. *Nature*, 453:1023, June 2008.

[198] S Wiesner. Conjugate Coding. *SIGACT News*, 15:78, 1983.

[199] C H Bennett and G Brassard. Quantum Cryptography: Public Key Distribution and Coin Tossing. In *IEEE International Conference on Computers, Systems, and Signal Processing*, page 175, Bangalore, 1984.

[200] A K Ekert. Quantum Cryptography Based on Bell's Theorem. *Physical Review Letters*, 67:661, 1991.

[201] N Gisin, G Ribordy, W Tittel, and H Zbinden. Quantum Cryptography. *Reviews of Modern Physics*, 74:145, May 2002.

[202] R Boyd. *Nonlinear optics*. Academic Press, 2008.

[203] A M Stephens, Z W E Evans, S J Devitt, A D Greentree, A G Fowler, W J Munro, J L O'Brien, K Nemoto, and L C L Hollenberg. Deterministic Optical Quantum Computer Using Photonic Modules. *Physical Review A*, 78:032318, 2008.

[204] L-M Duan, B Wang, and H J Kimble. Robust quantum gates on neutral atoms with cavity-assisted photon scattering. *Physical Review A*, 72:032333, September 2005.

[205] M Aspelmeyer, S Gröblacher, K Hammerer, and N Kiesel. Quantum Optomechanics Throwing a Glance. *Journal of the Optical Society of America B*, 27:A189, 2010.

[206] K Stannigel, P Rabl, A S Sørensen, P Zoller, and M D Lukin. Optomechanical Transducers for Long-Distance Quantum Communication. *Physical Review Letters*, 105:220501, November 2010.

[207] E Knill, R Laflamme, and Gerrard J Milburn. A scheme for efficient quantum computation with linear optics. *Nature*, 409:46, January 2001.

[208] M Varnava, D E Browne, and T Rudolph. Loss Tolerance in One-Way Quantum Computation via Counterfactual Error Correction. *Physical Review Letters*, 97:120501, 2006.

[209] R Raussendorf and H J Briegel. A One-Way Quantum Computer. *Physical Review Letters*, 86:5188, May 2001.

[210] R Raussendorf and H J Briegel. Computational model underlying the one-way quantum computer. *Quantum Information and Computation*, 2:433, 2002.

[211] R Raussendorf, D E Browne, and H J Briegel. Measurement-based quantum computation on cluster states. *Physical Review A*, 68:022312, August 2003.

[212] M Varnava, D E Browne, and T Rudolph. How Good Must Single Photon Sources and Detectors Be for Efficient Linear Optical Quantum Computation? *Physical Review Letters*, 100:060502, February 2008.

[213] D E Browne and T Rudolph. Resource-Efficient Linear Optical Quantum Computation. *Physical Review Letters*, 95:010501, June 2005.

[214] C M Dawson, H L Haselgrove, and M A Nielsen. Noise Thresholds for Optical Quantum Computers. *Physical Review Letters*, 96:020501, January 2006.

[215] Y-F Huang, B-H Liu, L Peng, Y-H Li, L Li, C-F Li, and G-C Guo. Experimental Generation of an Eight-Photon Greenberger-Horne-Zeilinger State. *Nature Communications*, 2:546, November 2011.

[216] J L O'Brien, G J Pryde, a G White, T C Ralph, and D Branning. Demonstration of an all-optical quantum controlled-NOT gate. *Nature*, 426(6964):264–7, November 2003.

[217] J L O'Brien, G J Pryde, A Gilchrist, D James, N K Langford, T C Ralph, and A G White. Quantum Process Tomography of a Controlled-NOT Gate. *Physical Review Letters*, 93(8):1–4, August 2004.

[218] N Kiesel, C Schmid, U Weber, R Ursin, and H Weinfurter. Linear Optics Controlled-Phase Gate Made Simple. *Physical Review Letters*, 95(21):1–4, November 2005.

[219] R Okamoto, H F Hofmann, S Takeuchi, and K Sasaki. Demonstration of an Optical Quantum Controlled-NOT Gate without Path Interference. *Physical Review Letters*, 95:210506, November 2005.

[220] N K Langford, T Weinhold, R Prevedel, K Resch, A Gilchrist, J L O'Brien, G J Pryde, and A G White. Demonstration of a Simple Entangling Optical Gate and Its Use in Bell-State Analysis. *Physical Review Letters*, 95(21):3–6, November 2005.

[221] T B Pittman, M J Fitch, B C Jacobs, and J D Franson. Experimental controlled-NOT logic gate for single photons in the coincidence basis. *Physical Review A*, 68(3):32316, September 2003.

[222] S Gasparoni, J-W Pan, P Walther, T Rudolph, and A Zeilinger. Realization of a Photonic Controlled-NOT Gate Sufficient for Quantum Computation. *Physical Review Letters*, 93:020504, July 2004.

[223] B P Lanyon, M Barbieri, M P Almeida, T Jennewein, T C Ralph, K J Resch, G J Pryde, J L O'Brien, A Gilchrist, and A G White. Simplifying quantum logic using higher-dimensional Hilbert spaces. *Nature Physics*, 5:134, December 2009.

[224] P Walther, K J Resch, T Rudolph, E Schenck, H Weinfurter, V Vedral, M Aspelmeyer, and A Zeilinger. Experimental one-way quantum computing. *Nature*, 434:169, 2005.

[225] N Kiesel, C Schmid, U Weber, G Tóth, O Gühne, R Ursin, and H Weinfurter. Experimental Analysis of a Four-Qubit Photon Cluster State. *Physical Review Letters*, 95(21):210502, November 2005.

[226] C-Y Lu, X-Q Zhou, O Gühne, W-B Gao, J Zhang, Z-S Yuan, A Goebel, T Yang, and J-W Pan. Experimental entanglement of six photons in graph states. *Nature Physics*, 3:91, January 2007.

[227] W-B Gao, P Xu, X-C Yao, O Gühne, A Cabello, C-Y Lu, C-Z Peng, Z-B Chen, and J-W Pan. Experimental Realization of a Controlled-NOT Gate with Four-Photon Six-Qubit Cluster States. *Physical Review Letters*, 104:020501, January 2010.

[228] R Prevedel, P Walther, F Tiefenbacher, P Böhi, R Kaltenbaek, T Jennewein, and A Zeilinger. High-speed linear optics quantum computing using active feed-forward. *Nature*, 445:65, 2007.

[229] B P Lanyon, T J Weinhold, N K Langford, M Barbieri, D F V James, A Gilchrist, and A G White. Experimental Demonstration of a Compiled Version of Shor's Algorithm with Quantum Entanglement. *Physical Review Letters*, 99(25):250505, 2007.

[230] Q Zhang, A Goebel, C Wagenknecht, Y-A Chen, B Zhao, T Yang, A Mair, J Schmiedmayer, and J-W Pan. Experimental quantum teleportation of a two-qubit composite system. *Nature Physics*, 2:678, 2006.

[231] I A Walmsley and M G Raymer. Applied physics. Toward quantum-information processing with photons. *Science*, 307:1733, March 2005.

[232] I A Walmsley. Looking to the future of quantum optics. *Science*, 319:1211, February 2008.

[233] H Takesue and K Inoue. Generation of 1.5-μm band time-bin entanglement using spontaneous fiber four-wave mixing and planar light-wave circuit interferometers. *Physical Review A*, 72(4):41804, October 2005.

[234] J Chen, J Altepeter, M Medic, K F Lee, B Gokden, R H Hadfield, S W Nam, and P Kumar. Demonstration of a Quantum Controlled-NOT Gate in the Telecommunications Band. *Physical Review Letters*, 100:133603, April 2008.

[235] A S Clark, J Fulconis, J G Rarity, W J Wadsworth, and J L O'Brien. All-Optical-Fiber Polarization-Based Quantum Logic Gate. *Physical Review A*, 79:030303(R), 2009.

[236] I L Chuang and M A Nielsen. Prescription for experimental determination of the dynamics of a quantum black box. *Journal of Modern Optics*, 44:2455, 1997.

[237] J F Poyatos, J I Cirac, and P Zoller. Complete Characterization of a Quantum Process : The Two-Bit Quantum Gate. *Physical Review Letters*, 78:390, 1997.

[238] R L Kosut. Quantum Process Tomography via L1 -norm Minimization. *arXiv:quant-ph*, page 0812.4323v2, 2009.

[239] E J Candès and M B Wakin. An introduction to compressive sampling. *Signal Processing Magazine, IEEE*, 25:21, 2008.

[240] A Shabani, R L Kosut, M Mohseni, H Rabitz, M A Broome, M P Almeida, A Fedrizzi, and A G White. Efficient Measurement of Quantum Dynamics via Compressive Sensing. *Physical Review Letters*, 106:100401, March 2011.

[241] A Laing, A Peruzzo, A Politi, M R Verde, M Halder, T C Ralph, M G Thompson, and J L O'Brien. High-fidelity operation of quantum photonic circuits. *Applied Physics Letters*, 97(21):211109, 2010.

[242] T C Ralph. Scaling of multiple postselected quantum gates in optics. *Physical Review A*, 70:012312, July 2004.

[243] T C Ralph, N K Langford, T B Bell, and A G White. Linear optical controlled-NOT gate in the coincidence basis. *Physical Review A*, 65(6):62324, 2002.

[244] D M Greenberger, M A Horne, and A Zeilinger. *Bell's Theorem, Quantum Theory, and Conceptions of the Universe*. Kluwer, Dordrecht, 1989.

[245] M Bourennane, M Eibl, C Kurtsiefer, S Gaertner, H Weinfurter, O Gühne, P Hyllus, D Bruß, M Lewenstein, and A Sanpera. Experimental Detection of Multipartite Entanglement using Witness Operators. *Physical Review Letters*, 92:087902, February 2004.

[246] G Tóth and O Gühne. Detecting Genuine Multipartite Entanglement with Two Local Measurements. *Physical Review Letters*, 94:060501, February 2005.

[247] V Coffman, J Kundu, and W K Wootters. Distributed entanglement. *Physical Review A*, 61:052306, 2000.

[248] A Politi, J C F Matthews, and J L O'Brien. Shors Quantum Factoring Algorithm on a Photonic Chip. *Science*, 325:1221, 2009.

[249] N Thomas-Peter, B J Smith, A Datta, L Zhang, U Dorner, and I A Walmsley. Real-World Quantum Sensors: Evaluating Resources for Precision Measurement. *Physical Review Letters*, 107:113603, September 2011.

[250] N Thomas-Peter, N K Langford, A Datta, L Zhang, B J Smith, J B Spring, B J Metcalf, H B Coldenstrodt-Ronge, M Hu, J Nunn, and I A Walmsley. Integrated Photonic Sensing. *New Journal of Physics*, 13:19, April 2011.

[251] J C Campbell, S Demiguel, F Ma, A Beck, X Guo, S Wang, X Zheng, X Li, J D Beck, M A Kinch, A Huntington, L A Coldren, J Decobert, and N Tscherptner. Recent Advances in Avalanche Photodiodes. *IEEE journal of selected topics in quantum electronics*, 10:777, July 2004.

[252] M J Stevens, R H Hadfield, R E Schwall, S W Nam, R P Mirin, and J A Gupta. Fast Lifetime Measurements of Infrared Emitters Using a Low-Jitter Superconducting Single-Photon Detector. *Applied Physics Letters*, 89:031109, 2006.

[253] A J Miller, S W Nam, J M Martinis, and A V Sergienko. Demonstration of a low-noise near-infrared photon counter with multiphoton discrimination. *Applied Physics Letters*, 83:791, 2003.

[254] A E Lita, A J Miller, and S W Nam. Counting near-infrared single-photons with 95 *Optics Express*, 16:3032, October 2008.

[255] S Miki, T Yamashita, M Fujiwara, M Sasaki, and Z Wang. Multichannel SNSPD system with high detection efficiency at telecommunication wavelength. *Optics letters*, 35:2133, July 2010.

[256] A Divochiy, F Marsili, D Bitauld, A Gaggero, R Leoni, F Mattioli, A Korneev, V Seleznev, N Kaurova, O Minaeva, G Gol'tsman, K G Lagoudakis, M Benkhaoul, F Lévy, and A Fiore. Superconducting nanowire photon-number-resolving detector at telecommunication wavelengths. *Nature Photonics*, 2:302, April 2008.

[257] D Fukuda, G Fujii, T Numata, K Amemiya, A Yoshizawa, H Tsuchida, H Fujino, H Ishii, T Itatani, S Inoue, and T Zama. Titanium-based transition-edge photon number resolving detector with 98 *Optics Express*, 19:870, January 2011.

[258] K D Irwin. An application of electrothermal feedback for high resolution cryogenic particle detection. *Applied Physics Letters*, 66:1998, 1995.

[259] R H Hadfield. Single-photon detectors for optical quantum information applications. *Nature Photonics*, 3:696, December 2009.

[260] H L Rogers, S Ambran, C Holmes, P G R Smith, and J C Gates. In situ loss measurement of direct UV-written waveguides using integrated Bragg gratings. *Optics letters*, 35:2849, 2010.

[261] A J Miller, A E Lita, B Calkins, I Vayshenker, S M Gruber, and S W Nam. Compact cryogenic self-aligning fiber-to-detector coupling with losses below one percent. *Optics Express*, 19:9102, May 2011.

[262] D Alberto, M Rajteri, E Taralli, L Lolli, C Portesi, E Monticone, Y Jia, R Garello, and M Greco. Optical Transition-Edge Sensors Single Photon Pulse Analysis. *Applied Superconductivity, IEEE Transactions on*, 21:285, 2011.

[263] B Cabrera, R M Clarke, P Colling, A J Miller, S Nam, and R W Romani. Detection of single infrared, optical, and ultraviolet photons using superconducting transition edge sensors. *Applied Physics Letters*, 73:735, 1998.

[264] K M Davis, K Miura, N Sugimoto, and K Hirao. Writing waveguides in glass with a femtosecond laser. *Optics Letters*, 21:1729, November 1996.

[265] P S Salter, A Jesacher, J B Spring, B J Metcalf, N Thomas-Peter, R D Simmonds, N K Langford, I A Walmsley, and M J Booth. Adaptive slit beam shaping for direct laser written waveguides. *Optics Letters*, 37:470, February 2012.

[266] D E Browne, J Eisert, S Scheel, and M B Plenio. Driving non-Gaussian to Gaussian states with linear optics. *Physical Review A*, 67:062320, June 2003.

[267] K F Reim, P Michelberger, K C Lee, J Nunn, N K Langford, and I A Walmsley. Single-Photon-Level Quantum Memory at Room Temperature. *Physical Review Letters*, 107:0533603, July 2011.

[268] M Hosseini, B M Sparkes, G Campbell, P K Lam, and B C Buchler. High efficiency coherent optical memory with warm rubidium vapour. *Nature Communications*, 2:174, January 2011.

[269] W Rosenfeld, S Berner, J Volz, M Weber, and H Weinfurter. Remote Preparation of an Atomic Quantum Memory. *Physical Review Letters*, 98:050504, February 2007.

[270] B Wu, J F Hulbert, E J Lunt, K Hurd, A R Hawkins, and H Schmidt. Slow light on a chip via atomic quantum state control. *Nature Photonics*, 4(11):776, 2010.

[271] N Sinclair, E Saglamyurek, M George, R Ricken, C La Mela, W Sohler, and W Tittel. Spectroscopic Investigations of a Ti:Tm:$LiNbO_3$ Waveguide for Photon-Echo Quantum Memory. *Journal of Luminescence*, 130:1586, 2010.